ANALYSIS OF IONOSPHERIC DISTURBANCES BEFORE AND DURING EARTHQUAKES OVER SUMATRA

ALINA MARIE HASBI

THESIS SUBMITTED IN FULFILMENT FOR THE DEGREE OF DOCTOR OF PHILOSOPHY

FACULTY OF ENGINEERING AND BUILT ENVIRONMENT
UNIVERSITI KEBANGSAAN MALAYSIA
BANGI

2011

ANALISIS GANGGUAN IONOSFERA SEBELUM DAN SEMASA GEMPA BUMI DI SUMATRA

ALINA MARIE HASBI

TESIS YANG DIKEMUKAKAN UNTUK MEMPEROLEH IJAZAH DOKTOR FALSAFAH

FAKULTI KEJURUTERAAN DAN ALAM BINA
UNIVERSITI KEBANGSAAN MALAYSIA
BANGI

2011

DECLARATION

I hereby declare that the work in this thesis is my own except for quotations and summaries which have been duly acknowledged.

8 July 2011

ALINA MARIE HASBI
P34996

ACKNOWLEDGMENTS

Alhamdulillah and thanks to Allah S.W.T for giving me the health, strength and determination and also for giving me the patience and perseverence to successfully complete this thesis. My deepest gratitute goes to my former supervisor, the late Assoc. Prof. Dr. Zainol Abidin Abdul Rashid for his supervision, suggestions, advice and tremendous support throughout the course of this research project, also to my current supervisors Prof. Dr. Mohd Alauddin Mohd Ali, Assoc. Prof. Dr. Norbahiah Misran and Dr. Muhammad Awad Momani for their valuable suggestions, discussions and ongoing support.

My sincere thanks goes to UKM for sponsoring this project under the Fundamental Research Grant Scheme (FRGS). Special thanks to the staff of the Malaysian Mapping and Surveying Department (JUPEM) for providing free GPS data. I would like to express my sincere gratitude to Prof. Yumoto from University of Kyushu, and also Prof. Shiokawa from Nagoya University for providing us the magnetometer data of Kototabang and for their fruitful suggestions. Special thank also goes to the former and current staff of Institute of Space Science (ANGKASA) for providing the necessary equipment, facilities and unlimited help for the completion of my work. Not to forget my friends in the Satellite Mobile Research Group (SMRG) laboratory for their support and for making my stay at UKM enjoyable.

My deepest appreaciation goes to my beloved husband, beloved mother for their love, support and encouragement, and not to forget my daughter Alisha and son Arman for their love and for making my life enjoyable throughout the duration of my study.

ANALYSIS OF IONOSPHERIC DISTURBANCES BEFORE AND DURING EARTHQUAKES OVER SUMATRA

ABSTRACT

Seismo-ionospheric coupling research has acclaimed specific attention from the scientific community due to the triggering of disastrous earthquakes that have claimed many lives and properties. However, due to the highly unpredictable behavior of the equatorial ionosphere as well as the lack of measurements over seismically active regions such as Sumatra, this research has often been a subject of debate. The advent of the Global Positioning System (GPS) sensing technology provides exciting prospects in seismology including detecting and analyzing signals in regions of seismic activity. This thesis aims to analyze the ionospheric disturbances during and prior to earthquake events in Sumatra. In order to achieve this objective, the thesis addresses several critical challenges in contributing to earthquake prediction research. First, to investigate the ionospheric disturbances during Sumatra earthquake event in the GPS TEC and geomagnetic field measurements and conduct a correlation between both measurements. Second, to analyze the characteristics of precursory signatures in the ionospheric Total Electron Content (TEC) prior to strong Sumatra earthquake events and validate them using CHAMP satellite electron density measurements. Finally, to perform a long-term statistical analysis of temporal and spatial correlation between irregular TEC and earthquake occurrence using the envelope, cross-correlation and the TEC variability index techniques. Data between 2004 and 2007 obtained from ground-based GPS stations located surrounding the earthquake epicentres, CHAMP satellite electron density and ground-based magnetometer were employed in the analyses. The study of ionospheric disturbances during earthquakes showed TEC oscillations with horizontal propagation velocities of 900-1200 m/s about 10-24 minutes after the events. The magnetic field measurements show rapid fluctuations of 4-5 seconds shortly after the earthquake, followed by magnetic pulsations about 8-11 minutes after the events. The GPS TEC disturbances and magnetic pulsations were well correlated, suggesting that the acoustic wave generated near the epicentre propagates upwards to ionospheric heights and induce disturbances in the ionosphere. The results prior to earthquakes showed significant TEC increases of up to 88% and decreases of up to 45% with respect to the upper and lower bound, respectively observed within few hours to six days before the earthquakes. These TEC anomalies were detected mostly during daytime and do not only depend on their distances from the epicentre but on their latitude positions in the equatorial anomaly region. This phenomenon is mainly due to the migration of ionospheric anomalies to the direction of meridional winds toward the equatorial anomaly crests and the ExB drift during the daytime. The precursory signatures also appeared in the form of equatorial anomaly modification during a few days before the events. The results also showed that both GPS TEC and CHAMP electron density measurements exhibit similar tendencies. The long-term statistical analysis of GPS TEC showed that anomalous TEC variations are observed prior to large earthquake events but they are also observed prior to non-earthquake periods and are subject to seasonal variations. Therefore, the statistical methods need to be improved in order to better distinguish between earthquake-related signals and non-earthquake related ones. In general, these results have proven the efficiency of joint measurement techniques to detect possible seismo-ionospheric disturbances as well as enhancing the understanding of the physical processes involved prior and during earthquakes. Hence, the results can further be used to improve the efficiency of future earthquake and tsunami warning systems.

ANALISIS GANGGUAN IONOSFERA SEBELUM DAN SEMASA GEMPA BUMI DI SUMATRA

ABSTRAK

Penyelidikan gandingan seismo-ionosferik telah mendapat perhatian khusus dari komuniti saintifik disebabkan cetusan gempa-gempa bumi besar yang telah meragut banyak nyawa dan harta. Walaupun begitu, disebabkan kelakuan ionosfera khatulistiwa yang tidak boleh diramal dan juga kekurangan pengukuran di kawasan aktif gempa bumi seperti Sumatra, penyelidikan ini sentiasa dipersoalkan. Kemunculan teknologi sistem penentudududukan global (*Global Positioning Satellite, GPS*) memberikan prospek yang baik dalam bidang seismologi termasuk mengesan, mengimej dan menganalisis isyarat-isyarat di kawasan gempa bumi. Matlamat utama tesis ini ialah untuk mengkaji gangguan ionosfera sebelum dan semasa peristiwa gempa bumi di Sumatera. Bagi mencapai matlamat ini, tesis ini mengemukakan beberapa cabaran kritikal bagi menyumbang kepada penyelidikan ramalan gempa. Pertama, mengkaji kesan ionosfera semasa peristiwa gempa bumi dalam bacaan-bacaan GPS TEC dan magnetik serta mendapatkan korelasi kedua-dua gangguan ini. Kedua, menganalisis ciri-ciri petanda awal dalam bacaan jumlah kandungan elektron (*Total Electron Content, TEC*) ionosfera sebelum peristiwa gempa bumi di Sumatera dan mengesahkannya dengan bacaan ketumpatan elektron dari satelit CHAMP. Akhirnya, membuat analisis statistik jangka panjang korelasi masa dan ruang di antara variasi TEC yang luar biasa dan kejadian gempa bumi menggunakan kaedah sampul, korelasi dan kebolehubahan indeks TEC. Data dari 2004 hingga 2007 yang diperoleh daripada stesen-stesen GPS bumi di sekeliling pusat gempa, ketumpatan elektron satelit CHAMP dan magnetometer bumi digunakan dalam analisis. Kajian gangguan ionosfera semasa gempa bumi menunjukkan ayunan TEC dengan halaju perambatan mengufuk 900-1200 m/s kira-kira 10-24 minit selepas peristiwa. Bacaan medan magnet menunjukkan ayunan 4-5 saat selepas peristiwa gempa bumi, diikuti oleh denyutan magnetik kira-kira 8-11 minit selepas peristiwa. Gangguan GPS TEC dan denyutan magnetik mempunyai korelasi yang baik, mencadangkan bahawa gelombang akustik yang berpunca di kawasan berhampiran pusat gempa merambat ke lapisan ionosfera dan seterusnya menyebabkan gangguan ionosfera. Hasil analisis sebelum gempa menunjukkan peningkatan sebanyak 88% dan pengurangan sebanyak 45% berbanding sempadan atas dan bawah masing-masing diperhati antara enam hari ke beberapa jam sebelum berlakunya gempa bumi. Kebanyakan anomali TEC dikesan pada waktu siang hari dan tidak semestinya bergantung kepada jarak dari pusat gempa tetapi juga kepada kedudukan latitudnya di kawasan anomali khatulistiwa. Fenomena ini disebabkan pemindahan anomali ionosfera mengikut arah angin meridian ke kawasan puncak anomali khatulistiwa and hanyutan ExB pada waktu siang. Petanda awal juga muncul dalam bentuk perubahan anomali khatulistiwa beberapa hari sebelum peristiwa. Hasil juga menunjukkan bahawa kedua-dua bacaan GPS TEC dan ketumpatan elektron mempamerkan kecenderungan yang serupa. Kaedah-kaedah analisis statistik jangka panjang GPS TEC menunjukkan bahawa variasi TEC luar biasa diperhatikan sebelum peristiwa gempa bumi besar tetapi juga semasa tempoh tiada gempa dan bergantung kepada perubahan musim. Oleh itu, kaedah-kaedah statistik ini perlu diperbaiki untuk membezakan antara isyarat gempa dan bukan gempa. Secara keseluruhannya, keputusan ini telah membuktikan kebolehan teknik pengukuran bersama untuk mengesan gangguan seismo-ionosfera serta mempertingkatkan pemahaman proses-proses fizikal yang terlibat sebelum dan semasa gempa bumi. Maka, hasil ini boleh digunakan bagi meningkatkan kecekapan sistem amaran awal gempa bumi dan tsunami.

CONTENT

LIST OF FIGURES

Figure no.

LIST OF TABLES

Table no.

LIST OF SYMBOLS

Symbol	Meaning
H	horizontal component
I	magnetic inclination
D	magnetic declination
Z	vertical component
X	north-south component
Y	east-west component
F	total field intensity
c	speed of light in free space
ρ_r^s	true geometric distance between satellite and receiver
c	speed of light in free space (3×10^8 m/s)
Δt^s, Δt_r	satellite and receiver clock offsets with respect to the GPS system time
$d^s_{r,\ trop}$	tropospheric delay
b^s, b_r	satellite and receiver biases
ε	random error
Φ_r^s	carrier phase between satellite and receiver
λ	carrier wavelength
L_r^s	phase measurements between satellite and receiver
λ	geographic longitude
φ	geographic latitude
λ_m	geomagnetic longitude
φ_m	geomagnetic latitude

N_e	electron density
e	charge of one electron, 1.602x10^{-19} C
m_e	mass of electron, 9.109x10^{-31} kg
ε_0	permittivity of free space, 8.854x10^{-12} Fm^{-1}
P_r^s	pseudorange measurements between staellite and receiver
T_e	electron temperature
R_E	mean radius of the Earth
h_m	height of the maximum electron density
E	elevation angle
$\%\Delta TEC$	percentage of TEC difference
TEC_{QD}	TEC during mean quiet day
z	satellite zenith angle

LIST OF ABBREVIATIONS

AIUB	Astronomical Institute of University of Berne, Switzerland
AGW	Acoustic Gravity Wave
Ap	Planetary index
ARAU	Arau station
AS	Anti-Spoofing
BGS	Bernese software
C/A-code	Coarse/Acquisition code (1.023 MHz)
CHAMP	Challenging Mini-Satellite Payload
CID	Coseismic Ionospheric Disturbance
CODE	Center for Orbit Determination in Europe, AIUB, Switzerland
DCB	Differential Code Bias
DoD	Department of Defense
DST	Disturbance Storm index
EM	Electromagnetic
F10.7	10.7 cm Solar Flux
GFC	Geometry Free Combination
GFZ	GeoForschungsZentrum, Potsdam, Germany
GLONASS	GLObal Navigation Satellite System
GNSS	Global Navigation Satellite System
GPS	Global Positioning System
IGS	International GNSS Service
IMF	Interplanetary Magnetic Field
INTERMAGNET	International Real Time Magnetic Observatory Network
IONEX	Ionosphere Map Exchange
IPP	Ionospheric Pierce Point
IPS	Ionospheric Prediction Service, Australia
Kp	3-hour Planetary Index
KTB	Kototabang Station
LB	Lower Bound
LEO	Low Earth Orbit
LOS	Line Of Sight
LT	Local Time

M-code	Military code
MCS	Master Conrol Station
MSTID	Medium Scale Travelling Ionospheric Disturbance
NAVSTAR	NAVigation Satellite Timing and Ranging
NGA	National Geospatial-Intelligence Agency
NOAA	National Oceanic and Atmospheric Administration, USA
P-code	Precision code (10.23 MHz)
PRN	Pseudo-Random Noise
PVT	Position, Velocity and Time
RINEX	Receiver-INdependent EXchange Format
SAMP	Sampali Station
SEC	Space Environment Center, NOAA
SLM	Single Layer Model
SNR	Signal-to-Noise Ratio
SOPAC	Scripps Orbit and Permanent Array Center
SSN	Sun Spot Number
STEC	Slant Total Electron Content
SUGAR	Sumatran GPS Array
SV	Satellite Vehicle
TEC	Total Electron Content (el/m^2)
TECU	Total Electron Content Unit (10^{16} el/m^2)
TEQC	Translate Edit Quality and Check Routine
UB	Upper Bound
ULF	Ultra Low Frequency
UNAVCO	University's NAVSTAR Consortium
UT	Universal Time
USGS	United States Geological Survey
USNO	United States Naval Observatory
VTEC	Vertical Total Electron Content
WDC	World Data Center
WGS	World Geodetic System

CHAPTER I

INTRODUCTION

1.1 BACKGROUND

Earthquakes pose a significant threat to many communities in the world, particularly in developing countries. Apart from causing fatalities in human lives, earthquakes can also have a large social and economic impact on society. Therefore, the physics of earthquakes is an urgent task for the modern studies in seismology and in related areas of geophysical and geochemical precursors of earthquakes (Krankowski et al. 2006). Earthquake prediction can be divided into four main categories according to their time period: long-term (years), medium-term (months), short-term (days) and operative (hours). At present, the short-term and operative earthquake predictions are the most important because earthquakes are supposed to specify the time and location of a forthcoming earthquake. Therefore, potential victims could be warned and take precautions, also enabling evacuation of areas of a forthcoming earthquake within days or several hours before its occurrence.

At present, there are many ongoing investigations in search for reliable earthquake precursors namely seismicity, changes in the ionosphere, various types of abnormal electromagnetic emissions, radon emissions and even unusual animal behavior (Gokhberg et al. 1995). Seismometer is the most conventional method used by scientists to predict the occurrence time and magnitude of earthquakes by recording the ground shaking onto a seismograph. However, this method is meant for prediction of very short time intervals (within minutes) before the occurrence of an earthquake.

Recently, space-borne observations for short-term earthquake prediction have provided exciting prospects in seismology including detecting, imaging and analyzing signals in regions of seismic activity. This branch of research is known as seismo-ionospheric coupling, which involves the interaction between the processes in the lithosphere, atmosphere and the Earth's upper atmosphere that subsequently cause significant effects in the ionosphere. Among the coupling effects that are involved before and during the occurrences of earthquakes are such as the pre-earthquake variation of electric and magnetic fields near the seismic source, pre-earthquake ultra low frequency (ULF), very low frequency (VLF) and very high frequency (VHF) electromagnetic emissions, pre-earthquake vertical total electron content (VTEC) and acoustic wave generation during earthquakes. The seismo-ionospheric coupling phenomenon has been investigated since the 1920s (Wilson 1922) and is far from new. Wilson (1922) analyzed the changes in magnetic susceptibility caused by compression and the application of magnetometric methods in seismology. The use of atmospheric electric potential variations as a possible earthquake precursor was then proposed by Kalashnikov and Bonchkovsky (1954). The first observation of ionospheric phenomenon induced by a seismic event was provided during March 1964, Alaskan earthquake (Davies & Barker 1965; Leonard & Barnes 1965; Row 1966). Since then, there has been widespread of research devoted to the study of lithosphere-atmosphere-ionosphere coupling in search of short-term earthquake precursors using both ground and space based measurements. Many efforts have been made to improve the overall knowledge surrounding earthquakes, from the physical mechanism to the main features of seismo-ionospheric phenomena (Gokhberg et al. 1995; Shalimov & Gokhberg 1998; Molchanov et al. 2004; Pulinets & Boyarchuk 2004; Hayakawa 2006; Ondoh 2009).

Many studies have reported the ionospheric disturbances before, during and after earthquakes (Liu et al. 2004; Artru et al. 2004; Hobara & Parrot 2005). The ionospheric disturbances during the occurrence of earthquakes are called coseismic ionospheric disturbances, which are vital for the prediction of Tsunami waves produced by undersea earthquakes of large magnitudes or volcano eruptions. The more important seismo-ionospheric anomalies are those observed before earthquake occurrences as they can be considered to act as precursors. Nevertheless, the pre-earthquake seismo-ionospheric coupling research has often been a subject of debate due to the lack of complete measurements over seismically active regions and also due to the lack of concrete physical framework to explain the origin of these anomalies (Geller et al. 1997; Wyss 1997). Despite the skepticisms about the impossibility of earthquake prediction, more and more countries have developed specialized scientific projects to investigate earthquake and volcano eruption effects in the atmosphere and ionosphere. These projects are the ground-based observation projects such as the FRONTIER in Japan, iSTEP in Taiwan, PREVENTION in Mexico, and satellite-based studies such as the DEMETER in France, COMPASS and Vulkan in Russia as well as ESPERIA in Italy (Pulinets & Boyarchuk 2004).

Indonesia is located in the Pacific ring of fire and is one of the most seismic active regions in the world as it is prone to many volcano eruptions and earthquakes. The frequent occurrences of large earthquakes in the Sumatra region in the recent years have provided a great opportunity to study the ionospheric disturbances before and during large earthquake events. During the period from 2004 - 2010, about 70 strong earthquake events with magnitude more than 6.0 Richter scale took place surrounding the Sumatra region (NEIC 2010). Moreover, the location of Sumatra in the highly dynamic and unpredictable equatorial ionosphere makes it a challenging region for the study of seismo-ionospheric coupling. Thus, improved knowledge on the characteristics and behavior of the ionospheric disturbance before and during strong earthquake events over the Sumatra region will be of high importance for the future of earthquake prediction modeling.

1.2 PROBLEM STATEMENT

Most of the coseismic ionospheric disturbances (CID) studies over Sumatra have been conducted during the great 26 December 2004, M9.3 earthquake (Heki et al. 2006a; Liu et al. 2006a; Astafyeva & Afraimovich 2006; Otsuka et al. 2006; Shinagawa et al. 2007). However, research during the earthquake events from 2004 - 2007 in Sumatra has not been done adequately although these events were strong and had direct impact on the ionosphere. The correlation between the ionospheric GPS VTEC and magnetic disturbances during earthquakes has not been reported too. During some of the major earthquake events in 2004 and 2005, different measurement techniques were used such as the infrasound data (e.g. Le Pichon et al. 2005), GRACE satellite gravity data (e.g. Panet et al. 2007) and satellite magnetometer (e.g. Balasis & Mandea 2007) but the GPS technique and ground-based magnetometer data have not been used to report these events.

Extensive studies on pre-earthquake seismo-ionospheric perturbations are highly concentrated in the middle and low latitude regions but have not been adequately investigated in the equatorial latitudes especially in Sumatra. Due to the lack of instrumentations over Sumatra, the physical processes of the pre-earthquake ionospheric perturbations are often not well understood. Most of the previous studies in Sumatra were conducted prior to only a single event and based on short time intervals (Dutta et al. 2007; Li & Parrot 2006; Zakharenkova et al. 2006; Saroso et al. 2009), which makes it difficult to clearly show the statistical significance of the results. It is also important to distinguish between earthquake and non-earthquake anomalous ionospheric variations during the absence of earthquakes. For this reason, it is necessary to conduct long-term statistical analyses using several methods to better quantify the ionospheric variability in the absence of earthquakes as well as to show statistically the temporal correlation between anomalous signals and earthquakes. Such an analysis using GPS VTEC has been conducted in the middle latitudes but it has not been reported before in the equatorial latitudes. As the behaviour of pre-earthquake ionospheric perturbations at the high, middle, low and equatorial latitudes is of different nature, it is important to understand the behaviour of these ionospheric perturbations by monitoring them at the same location for a substantial period. Therefore, further investigations in the equatorial region are still required.

1.3 OBJECTIVES

This thesis aims at achieving the following objectives:

i. To study the impact of the ionosphere during the occurrences of earthquakes in the GPS VTEC and magnetic measurements as well as the correlation between both of these disturbances.

ii. To investigate the precursory signatures in the GPS VTEC and the electron density measurements onboard CHAMP satellite associated with Sumatra earthquakes based on short-term analysis.

iii. To analyze and quantify ionospheric variations based on long-term analysis as well as to show the statistical temporal correlation between anomalous signals and earthquakes using several statistical analysis methods.

1.4 SCOPE OF WORK

This study focuses on the investigation of ionospheric disturbances before and during strong earthquake events surrounding the Sumatra region using primarily ground-based GPS VTEC measurements. The characteristics and behavior of these ionospheric disturbances are also studied and compared with satellite-based and ground-based magnetometer measurement techniques. Several statistical analysis techniques are used to identify the ionospheric disturbances. The results of the analyses are compared and verified with those of previous observations. The possible physical mechanisms of these ionospheric disturbances are also discussed. This research aims to enhance the understanding about the physical processes involved before and during earthquakes in the equatorial region. However, future research beyond the present study is required with the help of other reliable measurement techniques for the modeling of seismo-ionospheric disturbances. The research is divided in three major parts as follows:

i. Determination of ionospheric disturbances during earthquake events.
The GPS VTEC and magnetic measurements are determined during the 26 December 2004, 28 March 2005, 14 May 2005 and 12 September 2007 earthquake events at ten GPS and one magnetometer stations in the near zone of the epicentres. In the GPS VTEC analyses, the ionospheric response during these earthquake events is investigated by analyzing both VTEC measurements obtained from all satellites and the VTEC along individual satellite passes at each GPS station. The observed VTEC

disturbance during the event is then filtered and compared with the filtered VTEC variations for the day before and after the event during the same observation period. The occurrence time, amplitude, period and the horizontal propagation velocity of these oscillations are the main parameters determined in the analysis. The geomagnetic variations and the geomagnetic pulsations in the H, D, Z components obtained from ground-based magnetometer measurements are also analyzed. The ionospheric disturbances observed in the filtered GPS VTEC and geomagnetic pulsations are then correlated.

ii. Identification of pre-earthquake ionospheric perturbations in the GPS VTEC measurements before large earthquake events of 2004-2007 surrounding the Sumatra region based on short-term analysis.

The daily GPS VTEC measurements and the percentage of VTEC deviation are determined at seven GPS stations surrounding the epicentres of the 26 December 2004, 26 February 2005, 28 March 2005, 24 July 2005 and 12 September earthquake events. In the short-term analysis, the GPS VTEC measurements are analyzed for the period between seven days before and a day after the events. To identify pre-earthquake ionospheric anomalies, the envelope method is employed, whereby VTEC measurements are compared with their associated upper and lower bounds, respectively. Significant VTEC variations observed during very quiet geomagnetic conditions are identified as possible precursors, validated and further analyzed along individual satellite passes. These VTEC anomalies are then verified using the CHAMP electron density measurements.

iii. Determination of the long-term statistical relationship of temporal correlation between irregular VTEC and earthquake occurrence.

The statistical study of the temporal variations of continuous GPS VTEC measurements for the period between July 2004 - June 2006 and September 2007 using data from seven GPS stations is conducted. The study employs the envelope, cross correlation and the VTEC variability index techniques. In the envelope analysis, the ionospheric anomalies are quantified by summing of the percentage of VTEC deviation in order to obtain the daily number of detections. In the two latter analyses, the correlation and variability index are performed between two station pairs and these parameters are compared with the referenced value. The correlation between the irregular VTEC variations and earthquake occurrence is then analyzed.

1.5 THESIS ORGANIZATION

The organization of this thesis follows the sequence of chapters. The thesis consists of seven chapters all together, which is organized as follows:

Chapter I provides a brief description of earthquake prediction and also explains the background, problem statement, objectives, scope of work and research methodology.

Chapter II contains the literature review of this study. The chapter begins with the basic components of seismo-ionospheric coupling and the types of ionospheric irregularities in the equatorial ionosphere. Following that, the chapter details the existing seismo-ionospheric coupling model to explain the physical processes involved before the occurrences of earthquake events as well as the types of pre-earthquake ionospheric perturbations at each atmospheric layer. Finally, the chapter discusses previous observations of the seismo-ionospheric perturbations before and during earthquake events.

Chapter III discusses the measurement systems and calculation methods. The chapter begins with the description of the GPS system constellation, signal structure, error sources as well as the ionospheric effects on the GPS measurements. The chapter also presents the calculations of GPS VTEC, GPS data processing techniques and ground-based GPS data sources. Following that, the chapter describes the calculation procedure of statistical analysis methods using GPS VTEC measurements, which are the envelope analysis, percentage of VTEC deviation, cross correlation coefficient and VTEC variability index techniques. The chapter also discusses the data sources from ground-base magnetometers and CHAMP satellite. Finally, the magnetic and solar conditions before and during earthquake periods are discussed.

Chapter IV investigates the ionospheric and geomagnetic responses during occurrences of strong Sumatra earthquakes using GPS and magnetometer measurements in the near zone of the epicentres. The chapter describes a method for correlating ionospheric and magnetic disturbances followed by results and discussion. In the results, both GPS VTEC obtained from all satellites and the VTEC along individual satellite passes during the earthquake events are presented followed by the results of the geomagnetic variations and pulsations obtained from ground-based magnetometer measurements. Finally, the chapter highlights the correlation between the ionospheric GPS VTEC and magnetic responses to the earthquake events.

Chapter V investigates the ionospheric perturbations before strong earthquake events in the Sumatra region during the period of 2004-2007 based on short-term analyses. The chapter introduces the geophysical locations of the earthquakes followed by the solar and magnetic conditions before, during and after the earthquake events. The results detail the daily VTEC variations and percentage of VTEC deviation obtained from GPS measurements in the near zone of the epicentres for the period between seven days and a day after the events. This is followed by the validation of the VTEC variations using measurements from a remote station. Following that, the earthquake precursor days are identified and the measurements of VTEC variations along individual satellite passes during these days are presented. These VTEC variations are further confirmed using the electron density measurements onboard CHAMP satellite. Finally, the chapter compares the variations of ground-based GPS VTEC and satellite-based electron density followed by discussion and conclusion.

Chapter VI presents the long-term analyses of the ionospheric perturbations using three statistical analysis methods for the period from July 2004 - June 2006 and the month of September 2007. Firstly, the chapter describes the proposed methods to identify long-term seismo-ionospheric perturbations followed by the analyses and results of the envelope, cross correlation and VTEC variability index techniques followed by summary.

Chapter VII contains the summary of the research contributions, conclusions and recommendations for future research.

CHAPTER II

LITERATURE REVIEW

This chapter gives a general description of how earthquakes occur, the Earth's ionosphere, atmospheric electric field coupling to the ionosphere and the earthquake preparation zone. Following that, the chapter details the types of ionospheric irregularities in the equatorial ionosphere. The existing theoretical model that explains all the possible physical processes during the seismo-ionospheric coupling is also discussed. This is followed by the review of ionospheric disturbances before and during earthquakes observed by different measurement techniques. The overview of the Global Positioning System (GPS) system is also described.

2.1 BASIC COMPONENTS OF SEISMO-IONOSPHERIC COUPLING

2.1.1 Earthquakes

Earthquakes are caused when stress is released from the rocks in the Earth's crust and upper mantle. This stress is due to friction between large plates floating on magma on the Earth's surface called plate tectonics. The location below the Earth's surface where the earthquake starts is called the hypocentre and the point at which the earthquake originates on the Earth's surface is called the epicentre. The Earth consists of four main layers: the inner core, outer core, mantle and crust. The crust is made up of hard rock, mainly granite and the mantle is mainly molten lava, on which the crust is floating. The crust and upper layer of the mantle form the lithosphere, which consists of huge and irregular shaped plates of different sizes called tectonic plates (Oreskes 2003).

The edges of the tectonic plates are called the plate boundaries, which is made up of many faults. Majority of the earthquakes and volcanoes occur on the fault lines. Figure 2.1 presents the global earthquake epicentres and continental tectonic plate boundaries. These tectonic plates are slowly moving around, sliding past each other, pulling apart, colliding or diving under one another. As the plates slide past each other, parts of the plates get stuck, while the rest of the plates keep moving subsequently building up stress and storing energy at the fault line. When the unstuck part of the plate has moved far enough, the force exerted pull the stuck regions apart and all the stored up energy is released and thus causing an earthquake (USGS 2009).

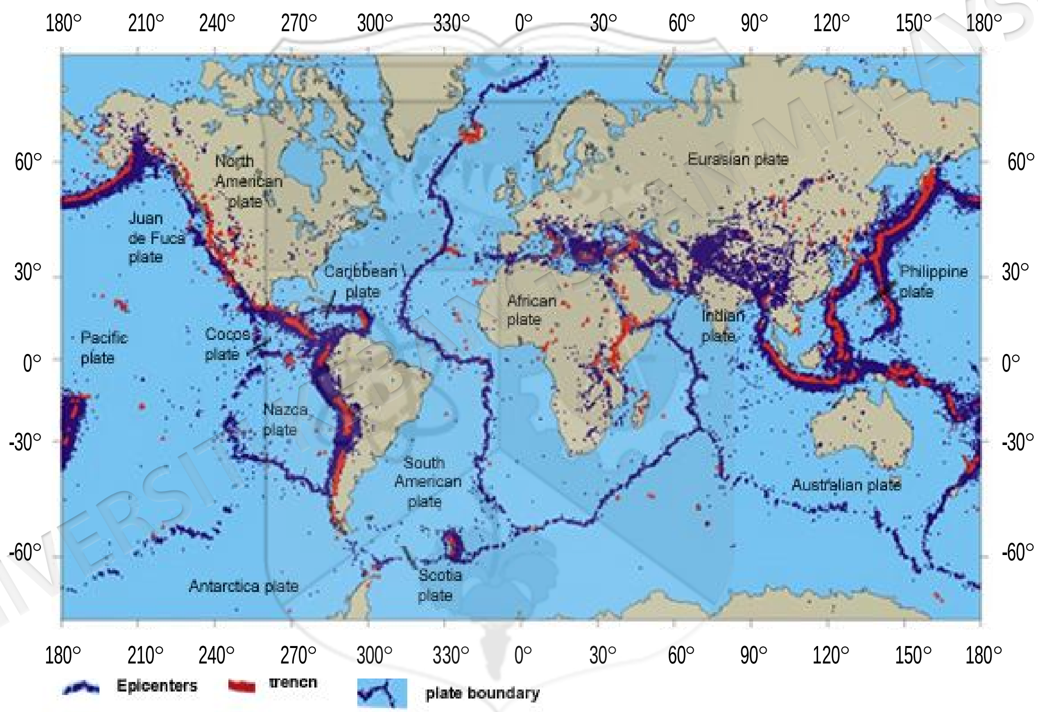

Figure 2.1 Global earthquake epicentres, continental tectonic plate boundaries and trenches.

Source: adapted from ScienceBlogs 2008

The occurrence of an earthquake is accompanied by the release of seismic waves that radiate from the earthquake source to all directions. These waves are recorded on seismographs as fluctuations of amplitude caused by the vibrations from earthquakes that travel through the Earth. Earthquakes produce different types of seismic waves with different velocities: the longitudinal P-waves (shock or pressure waves), S-waves (body waves) and surface waves (Rayleigh and Love waves). These seismic waves are used to determine different kinds of earthquake magnitude scales for the quantification of seismic energy released by an earthquake. The mainly used magnitude scales are the Richter or local magnitude (M_L), body wave magnitude (m_b), surface wave magnitude (M_s) and moment magnitude (M_w) (Pulinets and Boyarchuk 2004).

2.1.2 The Earth's Ionosphere

The Earth's atmosphere varies in density and composition as the altitude increases above the Earth's surface. The first 90 km of the atmosphere are basically neutral and consist of a homogeneous mixture of several gases with three primary layers; the troposphere of (0-15 km in altitude), the stratosphere (15-50 km in altitude) and the mesosphere (50-90 km in altitude). These atmospheric layers are generally well mixed by turbulence, which is primarily the result of thermal winds coupled with forces from the Earth's rotation (Hunt et al. 2000). During the daytime, weak ionization occurs in the mesosphere, which serves as a transition region to the ionosphere.

The ionosphere is the upper region of the Earth's atmosphere that extends from an altitude of 50 to 1000 km above the Earths' surface, which is strongly ionized. In this region, electrons are dislodged from atoms and molecules by solar radiation including the X-ray, ultraviolet and cosmic ray to produce ions. Figure 2.2 shows the altitude profile of electron density during day and night for various ionospheric layers. In the ionosphere, the ionized gases no longer tend to be uniformly mixed, whereby the gas molecules such as nitrogen (N_2) and oxygen (O_2) are found below 200 km, atomic oxygen (O) are found above 200 km, while the lighter gas molecules and atoms such as hydrogen (H) and Helium (He) are found above the altitude of 600 km. Free electrons and ions are present in nearly equal numbers in the ionosphere, which results in an overall neutral charge for the particle distribution. The mixture of positively and negatively charged ions, negative electrons and neutral gas is called plasma. The presence of these charged particles makes the ionosphere an electrical conductor, which supports electric currents as well as affects the propagation of radio waves and the corresponding radar measurements of objects within or above the ionosphere (Anderson & Fuller-Rowell 1999).

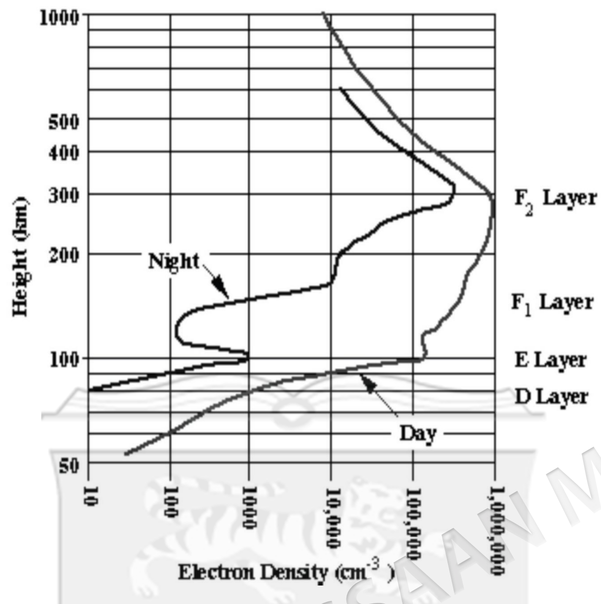

Figure 2.2 The altitude profile of the ionospheric electron density during the day and night for various ionospheric layers.

Source: (Moraes & Perella 2009)

The ionosphere is subdivided into layers or regions according to electron density, ion composition and their variability based on the Chapman electron density profile. These layers are the ionospheric D, E and F layers, which varies due to season, daily variation, solar production and the process of recombination of electrons (Moraes & Perella 2009). The D-layer represents the lower part of the ionosphere, which extends from 50 to 90 km in altitude and is only present during the daylight hours. The layer is formed by the ionization of molecular nitric oxide (NO) by hard X-rays and the Lyman series-alpha hydrogen radiation at a wavelength of 121.5 nanometer (nm) (Hunsucker & Hargreaves 2003). The maximum electron density in this layer is about 1.5×10^4 cm^{-3} during the daytime and layer disappears after sunset due to the recombination of electrons and ions (Chamberlain & Hunten 1987). Although the recombination rate of electrons and ions is high and the net ionization effect is low in the D-layer, the loss of wave energy is great due to frequent collisions of the electrons. As a result, high-frequency (HF) radio waves are not reflected by the

D layer but suffer loss of energy therein, therefore causes absorption of HF radio waves, particularly at 10 MHz and below.

The E-layer is the middle part of the ionosphere, which extends from 90 to 140 km above the Earth's surface. This layer consists of a normal E-layer and the sporadic E-layer (E_s). This layer is produced by the ionization is due to soft X-rays and far ultraviolet (UV) solar radiation of molecular oxygen (O_2). The main ionized components are the O_2 and N_2 and main ions O_2^+ and NO^+, which are formed from O_2^+ and N_2^+ as a result of ion-molecular reactions. The maximum electron density in the E-layer is $1.5x10^5$ cm^{-3} during the daytime, while it is about 10^4 cm^{-3} during night time (Chamberlain 1987). The normal E-layer can only reflect radio waves with frequencies lower than 10 MHz and absorb signals of higher frequencies. At night, both E-layers rapidly disappear because the primary source of ionization is no longer present. The normal E-layer in the auroral region and the sporadic E_s layer produce scintillation but their effects on the L-band GPS signals is minimal.

The F-region also consists of two layers, which are the F1 and F2 layers. The F1 layer extends from 140 to 200 km, while the F2-layer extends from 200 to 1000 km. These layers are formed through the ionization of O by Lyman continuum or by emission lines of He. The coronal X-rays also contribute to the ionization of O, O_2 and N_2. The F-layer contains a range of ions from NO^+ and O_2^+ in the F1 layer and H^+ and H_2^+ in the F2-layer. The maximum electron density in the F1-layer is about $2.5x10^5$ cm^{-3} at the nominal height of 200 km, while for F2-layer it varies from 10^5 to 10^6 cm^{-3} between the day and nighttime hours (Chamberlain & Hunten 1987). The peak electron density in the F-layer usually occurs in the F2-layer at an altitude of 350 km (Kelley 1989). The F2-layer has the highest electron density and has the most effect on GPS signals. At night, the F1-layer disappears due to dissociative recombination, while the F2-layer remains (Chamberlain & Hunten 1987).

2.1.3 Atmospheric Electric Field Coupling to the Ionosphere

The lower level atmospheric electric field is coupled to the ionosphere by the global electric circuit (GEC), which is a system of quasi-stationary electric currents between the ground and ionosphere driven by global thunderstorm activity (Pulinets 2009). Figure 2.3 presents the schematic diagram of the global electric circuit between the Earth and ionosphere. In the figure, R_{BL}, R_T, R_S, and R_i represent the vertical column resistances of the boundary layer, troposphere, stratosphere and internal resistance of the thunderstorm electric generator, respectively.

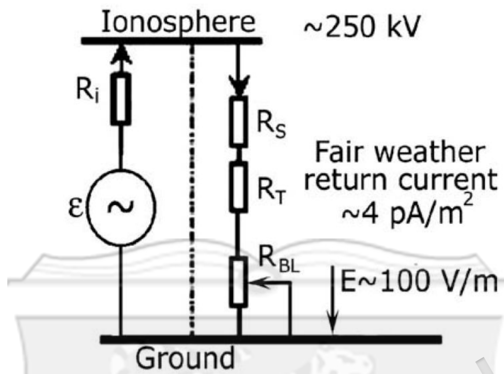

Figure 2.3 Schematic diagram of the global electric circuit between the Earth and ionosphere during fair weather.

Source: Pulinets 2009

The global electric circuit is considered the electric generator that provides the negative Earth potential in relation to the ionosphere and creating the potential difference (φ_i) of about 150-600 kV between the ground and ionosphere. According to the Ohm's law, the vertical electric current density is defined as

$$J_z = \sigma E_z \tag{2.1}$$

where σ is the conductivity determined by ionizing factor and E_z is the vertical electric field. During fair weather, the potential difference between the ground and ionosphere drives the vertical current density J_z of about 4 pAm^{-2} (Kobylinski & Michnowski 2007), which acts across the vertical column resistance R_T+R_S, defined as

$$R_{T,S} = \int_L^H \sigma(h)^{-1} dh \tag{2.2}$$

where L and H are the altitude of the lower and upper boundary of the troposphere or stratosphere, respectively and h is the altitude. These column resistances determine the total current between the ground and ionosphere. At any altitude the vertical current density can be written in the form of the potential difference between the ground and ionosphere as follows

$$J_z = \frac{\varphi_i}{R_T + R_S} \tag{2.3}$$

Tropical thunderstorms are known to generate on average an upward charging current (I_1) of about 1000-1500 A. An estimate of 1500-2000 thunderstorms occur at a time and the current produces by these thunderstorms is responsible for maintaining the potential difference between the ground and ionosphere (Kobylinski & Michnowski 2007). During fair weather conditions, the downward return current (I_2) closes the circuit and this current is normally positive (Roble and Tzur 1986). Both the ground and ionosphere are highly conducting with respect to the lower atmosphere and can be considered as almost equipotential except for the polar cap regions, where the ionospheric potential is strongly affected by intensive magnetospheric plasma convection induced by solar wind and geomagnetic field interaction.

The near ground atmospheric electric field is extremely sensitive to meteorological parameters. Therefore, the studies of lithospheric effects on the variations of the vertical electric field E_z can only be taken into account during fair weather conditions. The atmospheric electric field E_z near the ground level during fair weather conditions is normally about 100-250 V/m and is directed down. The downward electric field drives the positive ions downward and the negative ions upward creating an electrode effect at the near ground layer. The electrode layer at the near ground surface is very variable and depends on many factors such as geographic latitude, winds, emanation from the ground, surface irregularities of the observation location (Pulinets & Boyarchuk 2004).

2.1.4 The Earthquake Preparation Zone

Earlier studies have indicated that changes in the Earth's crust in the form of deformations, variations in seismic wave velocity, emanation of gases, changes in crustal electric conductivity are observed not only at the earthquake source but also in the zone exceeding the source by an order of a magnitude (Pulinets 2004). This leads to the development of the earthquake preparation zone conception, which is defined as the area on the ground surface where the pre-earthquake precursory phenomenon is expected to be observed. The concept was firstly introduced by Keylis-Borok and Malinovskaya (1964), who observed that the occurrence rate of moderate size earthquakes increases during several years prior to the occurrence of large earthquakes over a large area. The dimensions of the earthquake preparation zone was estimated by Dobrovolsky et al. (1979), which states that the size of the preparation area depends on the earthquake magnitude and can be presented in the following form:

$$R = 10^{0.43M} \tag{2.4}$$

where *R* is the radius of the earthquake preparation zone (km) from the hypocenter and *M* is the earthquake magnitude in Richter scale. The values of the earthquake preparation zone radius according to (2.4) are shown in Table 2.1.

Table 2.1 The values of the earthquake preparation zone radius versus the predicted earthquake magnitude.

Magnitude	3	4	5	6	7	8	9
Earthquake preparation zone radius, R (km)	19.5	52.5	141	380	1022	2754	7413

2.2 IONOSPHERIC IRREGULARITIES IN THE EQUATORIAL IONOSPHERE

The equatorial ionosphere is the region around the geomagnetic equator, which differs substantially from the geographic equator. It is difficult to extract the ionospheric variations that are associated with earthquakes particularly in the equatorial ionosphere, which is highly dynamic and unpredictable (Sharma et al. 2008). This is because the equatorial ionosphere is dominated by anomalies and irregularities such as the equatorial electrojet irregularities, equatorial ionospheric anomaly (EIA), equatorial spread-F plasma bubbles, regular and irregular variations of the ionosphere and other unknown parameters. The following sections discuss the main ionospheric phenomena that occur in the equatorial ionosphere.

2.2.1 Equatorial Ionospheric Anomaly (EIA)

The Equatorial Ionospheric Anomaly (EIA) is a regular phenomenon of the ionosphere, which is characterized as the occurrence of a trough in the ionization concentration near the magnetic equator and crests at about 15-20° north and south of the magnetic equator (Appleton 1946). The EIA, which is also known as the Appleton anomaly, usually occurs during quiet geomagnetic conditions from mid-morning to 16:00 to 18:00 LT and reaches its maximum development at 12:00 to 14:00 LT. However, the double crest structure gradually disappears in the evening and nighttime hours and the maximum electron concentration is restored at the magnetic equator (Zakharenkova et al. 2008; Yiyan et al. 2009). Figure 2.4 presents the global Vertical Electron Content (VTEC) map, which shows the maximum development of the EIA structure at 12:00 LT along the longitude 100°E during solar minimum. In this figure, the VTEC map is produced by the LEICA GNSS QC software, using the Ionosphere map Exchange (IONEX) data obtained from the Center for Orbit Determination in Europe (CODE) website.

The equatorial ionosphere is strongly affected by the north-south orientation of magnetic field lines (**B**) lying parallel to the surface of the earth at the equator. During the day, solar heating and tidal oscillations in the lower ionosphere move plasma across the magnetic field lines, which are horizontal at the magnetic equator. This set up a sheet of electric current in the ionospheric is about ±3° from the magnetic equator. The ionospheric current is known as the equatorial electrojet, which flows eastward during the day and westward at night (Hunt et al. 2000).

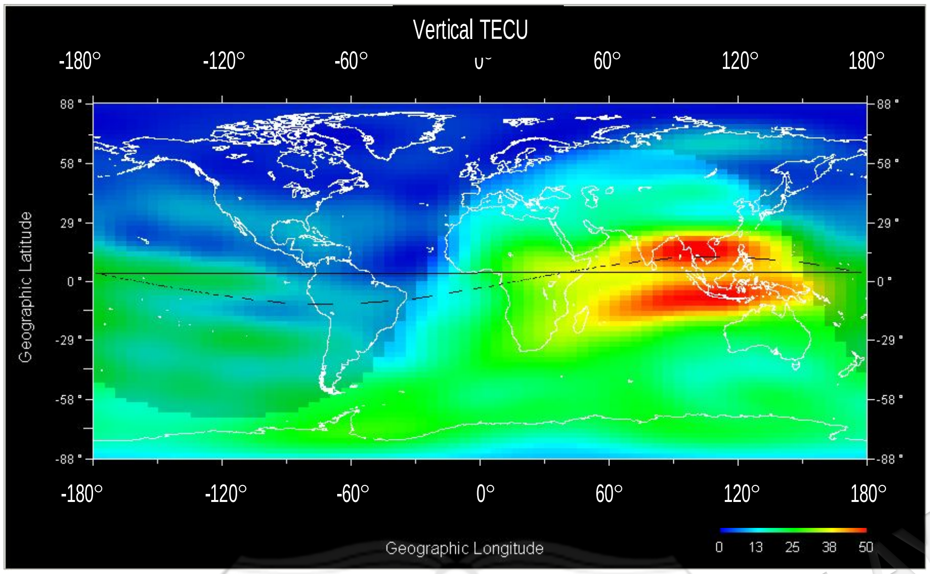

Figure 2.4 The global GPS VTEC map, which shows the maximum development of the EIA structure at 12:00 LT along the longitude 100°E during solar minimum.

Source: CODE 2010

Since the electric field (**E**) is established perpendicular to the magnetic field, an **ExB** drift moves the ionization vertically upwards during the day and downwards at night. The upward motion of ionization during the day is called the equatorial fountain, since ionization rises above the magnetic equator and then diffused along the magnetic field under the influence of gravity and pressure gradients (Moraes & Perrella 2009). The resulting enhancement of ionization at latitudes of ±15-20° and a trough in ionization concentration at the magnetic equator is termed the EIA. This phenomenon is also known as the fountain effect. Photo ionization caused by solar EUV radiation also plays an important role in the product ion of the EIA. Photo ionization can produce more electrons and therefore, enhance the background electron density. The day to day variability of the fountain effect and the neutral wind system may cause the crest of the EIA to move back and forth in latitudinal direction (Borah & Bhuyan 2005). As the EIA host the largest ionospheric electron densities, radio wave signals propagating in this region are most disturbed especially during the sunspot maximum period (Jursa 1985).

2.2.2 Equatorial Spread F Plasma Bubble

At post sunset hours, the ionospheric F-layer becomes unstable through a complex interaction between the electric field, neutral winds and the Earth's magnetic field (Rishbeth 1981). The **E** field increases as the neutral winds **V** increases and the **ExB** drift raises the F-layer. This process is known as the pre-reversal enhancement when the F-layer is forced against gravity, thus creating the Rayleigh-Taylor instability. As a result, bubbles form in the ionospheric plasma within an hour after sunset and rise upwards from a few hundred to over 1500 km at the magnetic equator (Sahai et al. 1994). These plasma bubbles extend along the geomagnetic field lines to the equatorial ionization anomaly crests. During the occurrences of these plasma bubbles, the ionosphere varies rapidly both in space and time, which give rise to strong radio frequency scintillations due to high ambient electron density particularly around the solar maximum period (Aarons & Basu 1994). The plasma bubbles normally peak around 20:00-21:00 LT and last up to four hours (Aarons et al. 1982; Basu et al. 1988). The occurrence of scintillation at the EIA crest region is proportional to solar activity (Aarons 1982).

2.2.3 Regular variations of the ionosphere

The ionosphere varies greatly due to the changes in the ionization from the Sun and also due to its response to the changes in the thermosphere. These ionospheric variations can be regular as well as irregular. The regular variations in the ionosphere include latitude dependence, diurnal, seasonal, 11-year, 27-day solar variations and the day-to-day ionospheric variability. The latitudinal dependence of ionospheric variations is mainly due to the change of solar zenith angle with latitude and also due to the change in the dip angle of the Earth's magnetic field. During the day, the solar radiation ionizes the ionosphere more obliquely with increasing latitude, therefore the intensity of the radiation and electron density production decreases with increasing latitude. There exists also a small longitudinal variation in the ionosphere due to the variation of the Earth's magnetic field with longitude along any given geographic latitude. The ionospheric electron density varies easily by an order of a magnitude from the polar to the equatorial regions (Papagianis 1972).

The diurnal variation of the ionosphere is a result of the 24-hour Earth rotation about its axis. The main feature of the diurnal variation is the day to night oscillation, whereby the electron density increases during the pre-morning hours, peaks in the afternoon and gradually decreases throughout the night. The amplitude of the diurnal variation varies with the solar and geomagnetic activity, season, latitude and longitude (Pulinets & Boyarchuk 2004).

The seasonal ionospheric variations result from the Earth revolving around the Sun, whereby the relative position of the Sun moves from one hemisphere to the other with changes in seasons. The noon ionospheric variation of the F2-layer generally peaks during the equinoxes (March and September) and minimum during summer. During the solar minimum, the noon ionospheric variations are greater in summer than those in winter but during the solar minimum, these ionospheric variations tend to be higher in winter as compared to summer (IPS 2008). The amplitude of the seasonal effect decreases with the declining solar activity. The seasonal effects are different in the northern and southern hemisphere, whereby the autumn equinox peak disappears in the southern hemisphere during the solar minimum. Meanwhile, the midnight seasonal behavior has an interesting feature for both hemispheres: the values during the solar maximum peak at spring, while the values during the solar minimum peak during the two equinoxes and are minimum during summer (Pulinets & Boyarchuk 2004).

The largest ionospheric variability is associated with the cycle of solar activity, which represents the fairly increase and decrease of the solar activity. The solar activity depends on the occurrence of the sunspot number (SSN), which is the appearance and disappearance of dark irregularly shaped areas on the surface of the Sun. The sunspot activity has a period of approximately 11.2 years (Papagianis 1972). The number of sunspots in existence at any time varies as some disappear and new ones appear. As the Sun rotates on its own axis, these sunspots are visible at 27-day intervals, which is the period required for the Sun to make one complete rotation. The 27-day sunspot cycle causes variation in the ionization density of the F2-layer on a day-to-day basis. Due to this reason, precise predictions of the day-to-day ionospheric variability in the F2-layer are not possible.

The day-to-day ionospheric variability is one of the most complex problems in modern ionospheric physics. This is due to the fact that it is impossible to determine the main cause of its effect. The sources that contribute to the day-to-day ionospheric variability can originate from above and below the ionosphere. The main source of the ionospheric variations from above is the solar variations, which effects include electromagnetic emissions and particle precipitation in the auroral regions. The sources from below the ionosphere are meteorological effects such as atmospheric tides and winds, acoustic gravity waves and other regular and irregular air movements (Kazimirovsky 2002). The ionospheric variability in the F2-layer has several characteristics: greater at night than during the day, greater in winter than in summer, higher during low solar activity periods, greater at the low and equatorial latitudes than at the mid latitude and dependent on geomagnetic activity (Aravindan & Iyer 1990; Jayachandran 1995; Rishbeth & Mendillo 2001; Ezquer et al. 2004; Somoye & Akala 2010). Most of these studies have used median, lower and upper quartiles to specify ionospheric variability due to their advantage of being less affected by large ionospheric deviations that can occur during magnetic storms (Ezquer 2004). During quiet geomagnetic periods, the value of the ionospheric day-to-day variability normally lies within the limits of 10-30% (Forbes et al. 2000; Rishbeth & Mendillo 2001; Bilitza et al. 2004).

2.2.4 Irregular variations of the ionosphere

Irregular ionospheric variations also have an important effect on radio wave propagation. Due to their irregular and unpredictable variations, communications capabilities can be drastically affected without any warning. The main irregular variations are such as the solar flares, sudden ionospheric disturbances and geomagnetic storms. Solar flares are large, sudden releases of energy on the sun that are indicated by relatively short-lived brightening of localized regions. The enhancement of X-ray and ultraviolet radiation intensity, which often accompany solar flares can affect the Earth's ionosphere and disrupt long-range radio communications. Direct radio emission at decimetric wavelengths may disturb operation of radars and other devices operating at these frequencies. The two main types of solar flare phenomena are the immediate effects and the delayed effects. The immediate effects occur simultaneously with the visible flare and consist of phenomena known as solar radio bursts and sudden ionospheric disturbances. The delayed effects occur 15 minutes to 72 hours after the flare and consist of ground-level events, polar cap absorption, geomagnetic disturbances, and aurora. Immediate effects are most pronounced with large flares, but important effects may also occur with subflares (FAS 2010).

Sudden ionospheric disturbances (SIDs) result from the interaction of solar flare radiations with constituents of the upper atmosphere (Liu et al. 2006c). The SID is the reaction of the ionospheric plasma to an impulsive ionization and has duration from a few minutes to several hours. These disturbances have important effects on radio communications and navigations over the entire radio spectrum (Davies 1990). The SID were generally recorded as the short wave fadeout, sudden phase anomaly, Doppler shifts, sudden cosmic noise absorption, sudden enhancement or decrease of atmospherics and sudden increase in total electron content (Davies 1990).

Geomagnetic storms are disturbances in the Earth's magnetosphere caused by a disturbance in space weather. These disturbances are associated with both solar flares and coronal mass ejections (CME). These geomagnetic storms result from the solar wind shock wave or cloud of magnetic field, which typically strikes the Earth's magnetosphere 3 days after the event. During geomagnetic storms, the interaction between the solar wind and the Earth’s magnetosphere produces intense the electric currents in the ionosphere, thus causing large variations in the ionosphere (Almomani 2007). Magnetic storms usually last 24 to 48 hours, but some may last for many days. The most prominent effects of ionospheric storms are a turbulent ionosphere and very erratic sky wave propagation.

2.3 THE EXISTING SEISMO-IONOSPHERIC COUPLING MODEL

The mechanism of seismo-ionospheric perturbations is not so well understood, although many articles have reported on the disturbances of the neutral and ionized upper atmosphere and their possible generation mechanisms. Among the hypotheses that have been proposed to explain the physical mechanisms of pre-earthquake electromagnetic and ionospheric perturbations are the piezomagnetism and turboelectric effects, activation of positive holes that reach the near-ground surface, dirty plasma diffusion, emissions of radioactive gas or metallic ions and the propagation of electromagnetic waves form the ground (Pulinets et al. 1994; Molchanov & Hayakawa 1998; Rapoport et al. 2004; Pulinets & Boyarchuk 2004; Freund 2006; Hayakawa 2006). The mechanism of emissions of radioactive gas or metallic ions changes the existing currents between the surface of the Earth and the lower ionosphere thus generating anomalous vertical electric field before earthquakes (Sorokin & Yaschenko 2000). Another mechanism is related to the atmospheric gravity waves which can be triggered by gas releases or thermal anomalies from the Earth's crust above the earthquake preparation area (Pulinets et al. 1994). The possibility of ionospheric heating by an electric current of seismic origin was shown by Sorokin and Chmyrev (1999). This current can be due to the convective transfer of charged soil aerosols, which are injected in the atmosphere. Freund (2006) proposed that mobile positive holes can be activated in the crust by microfractures during the dilatancy stage of the earthquake preparation. The outflow of these holes generates strong electric fields at the near ground surface giving rise to ionospheric perturbation observed by ELF, VLF and LF subionospheric measurements.

Among these hypotheses, the most promising physical model to explain the seismo-ionospheric anomalies is proposed by Pulinets and Boyarchuk (2004) in terms of upward propagation of vertical seismogenic electric field generated within the earthquake preparation zone into the ionosphere a few days before earthquakes. This seismogenic electric field will then influence the plasma density in the ionosphere. The model is divided into three parts: the generation of anomalous vertical electric field, penetration of seimogenic electric field into the ionosphere and seismo-ionospheric effects in the ionosphere, which are explained in the following sections.

2.3.1 Generation of Anomalous Electric Field

Earthquake epicentres are usually located near cracks in the Earth's crust, through which a significant amount of chemical substances such as radon, light gases and aerosols with a high metal content emanate from the Earth's crust to the near-ground layer (Pulinets & Boyarchuk 2004). Prior to an earthquake, processes such as mechanical transformation and active geochemical processes take place in the near-ground layer. Radon (^{222}Rn), which is a radioactive, colorless, odorless noble gas is one of the main ionization sources in the near-ground atmosphere because of its radiation properties. The ions in the near-ground atmosphere are ionized by radon creating main elementry tropospheric ions such as O^-, O_2^-, NO_2^-, NO_3^-, CO_3^-, NO^+ and H_3O^+. The large amount of water vapour molecules in the troposphere with density of about 10^{17} cm^{-3} an high dipole moment of p = 1.87 D, leads to ion-molecular reactions and formation of ion complexes such as $NO_3^-(H_2O)_n$, $NO_2^-(H_2O)_n$ and $O_2^+(H_2O)_n$. The average lifetime of these ions reaches 30-40 minutes or more (Smirnov 1992). The chemical reaction leads to the formation of heavy charged ion clusters of opposite signs. Due to the Coulumb attraction of positive and negative ion cluster, quasi-neutral clusters are formed. As a result, the near-ground layer of the earthquake preparation area is rich with neutral, stable and long lasting ion clusters (Pulinets et al. 2002). The difference between seismic areas and non-seismic areas is that the radon emanation is higher in seismic areas, which produces higher level of air ionization. Enhanced radon concentration has been reported during a few weeks before strong seismic events (King 1998; Sorokin & Yaschenko 2000).

Additional increase of ion content can be provided by intensive gas such as CO_2 discharged from the Earth's crust in seismic areas (Voitov & Dobrovolsky 1994). These gas releases generate air motion, which are strong enough to create instabilities to stimulate acoustic gravity wave generation. This intensive air movement decays the quasi-neutral ion clusters due to the weakness in the Coulumb reaction. As a result, the near ground atmosphere becomes rich in positive and negative ions with a concentration of 10^5-10^6 cm^{-3} within a short time (Pulinets et al. 2000). Due to the higher mobility of the negative ions, which are 1.3-1.4 times higher than the positive ones, a charge separation process is form at the ground surface with the negative ions at the top and the positive ones at the bottom. This leads to the generation of anomalously strong vertical electric field exceeding 1 kV m^{-1} with respect to the fair weather electric field of about 100-250 V m^{-1} in the near-ground atmosphere (Kim et al. 1994; Nikiforova and Michnowski 1995). The variation of this electric field can be both positive and negative (Nikiforova and Michnowski 1995; Hao et al. 2000).

2.3.2 Penetration of Seismogenic Electric Field into the Ionosphere

The penetration of anomalous vertical electric field of seismogenic origin into the ionosphere has been done experimentally by Kim et al. (1994) and Pulinets et al. (2000). Due to the equipotential geomagnetic field lines the altitude above 90 km, the E_z field penetrates to higher altitudes of the ionosphere. The electron temperature in the ionospheric F-layer is increased by Joule heating, giving rise to small-scale ionospheric irregularities by acoustic gravity waves (Hegai et al. 1997) and large-scale irregularities of the electron density in the ionospheric F2-layer (Pulinet & Lagen'ka 2003). Depending on the direction of the electric field (E_z) of either upward or downward, negative or positive deviations in the electron concentration may be created, respectively (Pulinets et al. 1998). Moreover, the shape of the area generating the electric field determines the shape of the irregularity in the ionosphere, i.e. circular or elongated (Pulinets and Boyarchuk 2004). These irregularities are observed by satellite and ground-based instruments. Due to the complex character of the particle drift ion the F-layer in crossed electric and magnetic fields (**ExB**), large scale anomalies cause by acoustic gravity wave propagation may not be only observed over the earthquake epicentre but also shifted in the equatorward direction (Pulinets 2004). However, the penetration efficiency of the seismogenic vertical electric field into the ionosphere is very low as the penetrated horizontal electric field in the ionosphere is only 0.7 mV/m during night time and much less during the daytime (Kim et al. 1994).

2.3.3 Anomalous Electric Field Effects in the Ionospheric F-layer

The final stage of the complex chain of events in seismo-ionospheric coupling is the anomalous electric field effects in the atmosphere, ionosphere and magnetosphere. Recent observations have reported the effects of the anomalous seismogenic vertical electric field in the ionospheric D-layer (Fux & Shubova, 1994), E-layer (Kim et al. 1994), F-layer (Pulinets et al, 1994) as well as effects in plasmasphere and magnetically conjugated points (Kim & Hegai, 1997; Pulinets et al, 1997) before the occurrence of earthquakes. The effects of the anomalous seismogenic electric field in the ionospheric F-layer have been modelled by Pulinets (2000). According to the model, the ionospheric plasma in the F-layer will move along the quasi-circular trajectories around the geomagnetic line force as a result of the **ExB** drift induced by the seismogenic electric field. The cross sections of the electron density distribution under the action of the seismogenic electric field at the altitude of 250 km and 500 km are presented in Figure 2.5. In this figure, the black dot represents the vertical projection of the epicentre at the ionospheric level. As shown in both figures, the ionospheric plasma in the F2-layer over the epicentre becomes nonuniform under the action of the seismogenic electric field. The characteristic size of the plasma concentration exceeds 400 km. The maximum variation in plasma concentration with respect to the unperturbed level at the altitude of 250 km and 500 km is about 30% and 20%, respectively (Pulinets 2000).

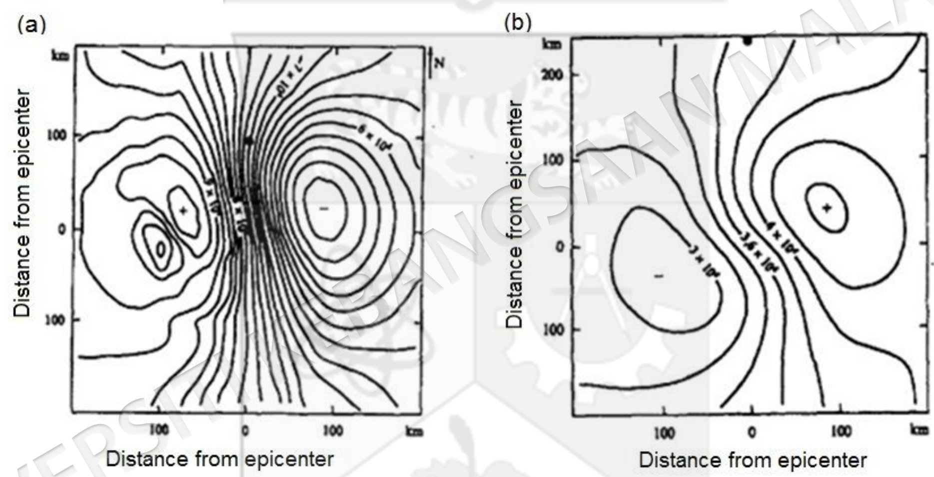

Figure 2.5 Contour of the electron density distribution under the action of the seismogenic electric field at the altitude of (a) 250 km and (b) 500 km. The black dot represents the vertical projection of the epicentre at the ionospheric level.

Source: Pulinets et al. 2000

As shown in Figure 2.5, the distribution of ionospheric plasma concentration in the F2-layer is characterized by both positive and negative electron density (N_e) perturbation. In the lower part of the ionospheric F2-layer, the ionospheric perturbation in the west and east of the earthquake epicentre are positive and negative, respectively. At the upper part of the F2-layer the situation is the opposite, whereby the ionospheric perturbation in the west of the epicentre is negative and positive in the east of the epicentre (Pulinets et al. 2000). Figure 2.6 summarizes all the physical mechanisms of the anomalous seismogenic electric field generation, its penetration from the near-ground level to the ionosphere and the magnetosphere as well as its effects at all levels of the atmosphere.

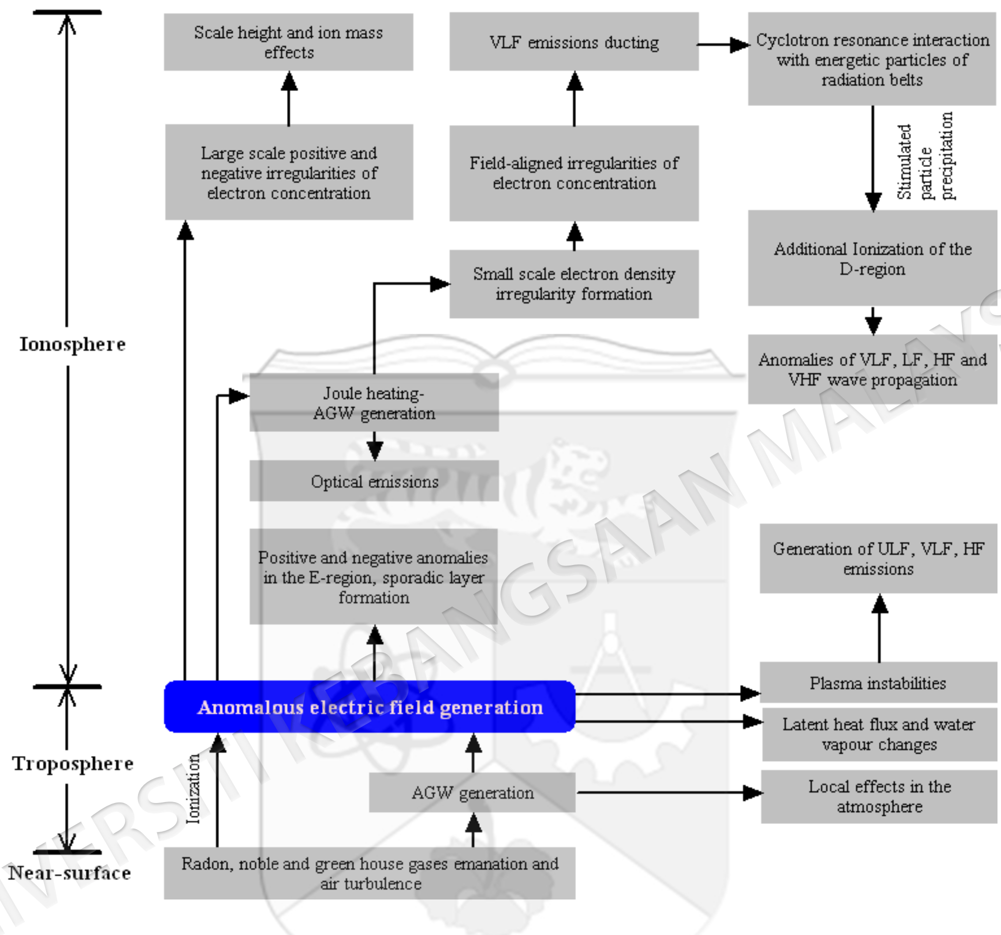

Figure 2.6 Block diagram of the seismo-ionospheric coupling model.

Source: Pulinets & Boyarchuk 2004

2.4 OBSERVATIONS OF PRE-EARTHQUAKE IONOSPHERIC PERTURBATIONS

The ionospheric variations prior to strong earthquakes have been studied for a long time. The earthquake-induced effects are very diverse and can be observed from the Earth's crust to thousands of kilometers from the Earth's surface (Devi et al. 2004). Different types of signals such as electric, magnetic, electromagnetic and luminous lights often observed before earthquakes, although seismic waves are the most obvious manifestation are often observed prior to large earthquakes (Bolt 1999). Recently, the seismo-electromagnetic and ionospheric variations are considered as the most promising tools for studying the ionospheric perturbations associated with earthquakes. Various ground-based and satellite measurement techniques have been employed to study the pre-earthquake ionospheric variations in search of short-term earthquake precursors. Figure 2.7 illustrates the possible types of electromagnetic and ionospheric earthquake precursors detected by ground-based and satellite measurement techniques.

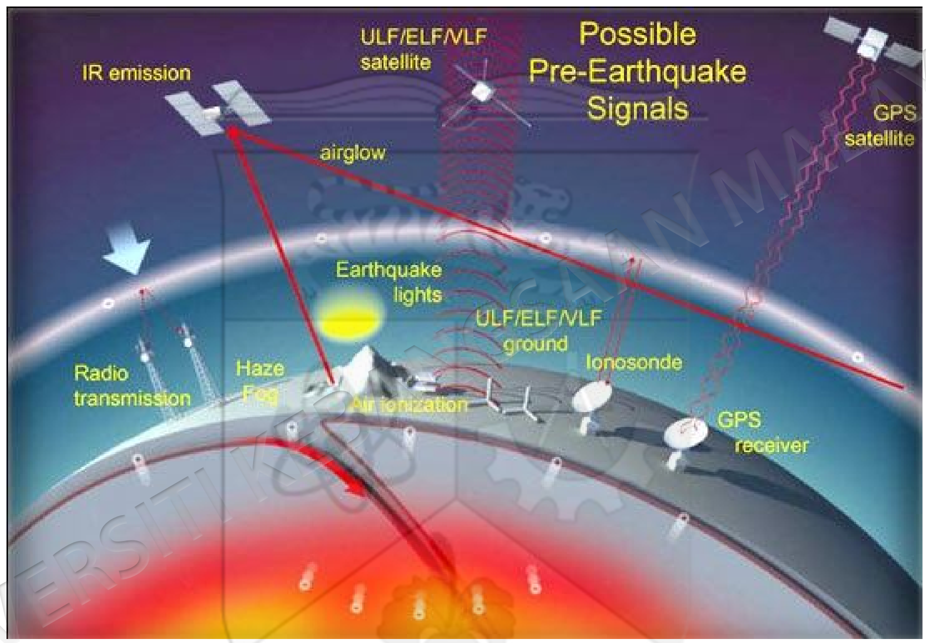

Figure 2.7 Possible types of electromagnetic and ionospheric earthquake precursors detected by ground and satellite based measurement techniques.

Source: Quakefinder 2010

The main ionospheric parameters, which have been extensively studied in the lower ionosphere before earthquake events are such as the amplitude of the ULF, ELF and VLF electromagnetic signals in the D-layer and the critical frequency of the sporadic E-layer (foEs). In the F2-layer, the ionospheric parameters are such as the critical frequency in the ionospheric F-layer (foF2), GPS TEC, electron and ion density and temperature as well as the modification of the equatorial ionization anomaly (EIA) prior to equatorial earthquakes. The observations of the pre-earthquake ionospheric variations in the F2-layer are discussed in the following sections:

2.4.1 Variations of critical frequencies (foEs and foF2)

The critical frequency (foF2), which is the plasma frequency at the peak of the ionospheric F2-layer is one of the most studied ionospheric parameters in vertical sounding. The first publications on pre-earthquake ionospheric perturbations using critical frequency measurements began since about four decades ago (Antsilevich 1971; Datchenko et al. 1972). Antsilevich (1971) observed a local increase in the ionospheric foE parameter above the epicentre zone before the 1966 Tashkent earthquake using ground-based ionosonde stations. One year later, Datchenko et al. (1972) observed anomalous ionospheric electron variations that occurred before the same earthquake and attributed them to the redistribution of electric charges within the Earth-atmosphere system. Since then, there have been many reports of anomalous variations in the ionospheric plasma foF2 using ground-based and satellite ionosondes (Pulinets et al. 1994, 1998a; Liu et al. 2000, 2004a, 2004b, 2008; Chou et al. 2001, 2002; Pulinets & Legen'ka 2003; Singh 2004; Hobara & Parrot 2005; Liperovskaya et al. 2006; Singh & Singh 2007).

Recently, Liu et al (2000, 2001), Chou et al. (2002) and Singh et al. (2004) conducted statistical investigations of the foF2 variations related to the strong earthquakes in Taiwan and India, and found significant decreases of up to in the during the local afternoon during 1-6 days before events. Singh and Singh (2007) examined the night time ionospheric foEs and foF2 measurements prior to some major earthquakes at the equatorial anomaly crest region in India using a ground-based ionosondes station located about 1000-2500 km from the epicentres. They observed anomalous decreases of up to 30% in the foF2 variations, while enhancements of about 100-155% were observed in the foEs variations during the pre-midnight and pre-morning hours from 4 days to a few hours before the main shocks. Pulinets et al. (1994) observed strong foF2 variations about 2 days before an earthquake in the Australian and New Guinea Islands region in 1980 using the topside ionospheric measurements onboard the Intercosmos-19 satellite. The ionospheric variations appeared in the form of foF2 depletion in the area near the epicentre and these variations are most pronounced during specific intervals of local time, i.e. before sunrise (4-5 LT) and in afternoon hours (14-18 LT). Pulinets and Legen'ka (2003) found large-scale ionospheric irregularities in the foF2 measurements from Intercosmos-19 and Alouette-1 satellites several hours or days before the 1964 Alaska and the 1980 Campania earthquakes. They also found that the region of these irregularities is not located directly above the earthquake epicentres but a little displaced from them. Pulinets and Boyarchuk 2004) indicated that the pre-earthquake foF2 variations measured by ground-based and satellite measurements could differ by sign, shape, lead time before an earthquake event, duration and amplitude due to their dependence on local time.

Although ionosondes have provided efficient means to study the seismo-ionospheric effects, the distribution of these instruments is still lacking in most parts of the world especially in seismically active regions. In the last years, the number of ground-based ionosondes stations has been significantly reduced as there are less than 60 stations worldwide that are routinely operational (Zakharenkova et al. 2008). In this respect, it is practically unfeasible to study the spatial modification of the ionosphere before and during earthquakes, which is a main disadvantage of this method.

2.4.2 Variations of the GPS Vertical Total Electron Content (VTEC)

The advent of GPS receiver technology provides a low cost solution to remote sensing the ionosphere on the global basis. Numerous regional networks of GPS receivers have been deployed to monitor the Earth's surface deformation. Owing to the utilization of two ultra high frequency waves, the same GPS receivers are used to simultaneously and continuously monitor the ionospheric vertical total electron content (VTEC) variations on a global scale (Otsuka et al. 2002). As the VTEC is very sensitive to the changes of the peak electron density in the ionospheric F2-layer, it is an ideal parameter to estimate the spatial sizes and temporal dynamics of seismo-ionospheric effects over the earthquake preparation area (Liu et al. 2001, 2004; Yiyan et al. 2009).

The ionospheric disturbances in the GPS TEC measurements were firstly reported by Calais and Minster (1995) using ground-based GPS receivers during the Northridge earthquake on 17 January 1994. Since then, many studies have reported pre-earthquake ionospheric anomalies using ground-based GPS stations (Liu et al. 2004a, 2008, 2009; Zakharenkova et al. 2006a; Dautermann et al. 2007; Saroso et al. 2008; Nishihashi et al. 2009; Yiyan et al. 2009; Kon et al. 2010). Some of these studies also highlighted that the disturbance area prior to large earthquakes extend over a distance of 1500 km in latitude and 4000 km in longitude. Liu et al. (2004) performed a statistical analysis on 20 M≥6.0 earthquakes in the Taiwan region using GPS TEC data and found that 80% of pre-earthquake ionospheric anomalies occurred at about 18:00-22:00 LT during 1-5 days before the events. More recently, Liu et al. (2008) examined the TEC obtained from of 8 GPS receivers scattered in Taiwan before the Pingtung earthquakes and found a reduction of about 7 TECU (30% from reference value) with a duration of 4.5 hours. Yiyan et al. (2009) reported increases and decreases of 40-70% in the TEC measurements during the afternoon hours of 13:00-18:00 LT about 3 days prior to the 2008, M7.9 Wenchuan earthquake in China. Using the GPS TEC map, they also found that these anomalies moved from the equatorial northern crest towards the equator a few days before the earthquake. Kon et al. (2010) conducted a statistical study on 12 years of GPS TEC measurements derived from global ionospheric maps (GIM) for large and destructive earthquakes in Japan during the period of May 1998 - May 2010. Their statistical results indicate the significance of positive TEC anomalies appearing 1-5 days before the earthquake events within 1000 km from the epicentre.

2.4.3 Variations of Plasma Parameter

The pre-earthquake plasma parameters such as the ion composition, electron density, temperature and energetic particles have been widely investigated using satellite-based measurements (Gokhberg et al. 1983; Boskova et al. 1993; Afonin et al. 1999; Hayakawa et al. 2000; Oyama et al. 2008; Akhoondzadeh et al. 2010). Gokhberg et al. (1983) found a local trough of 20% in the plasma density in both AE-C and ISI-2 satellite measurements above the epicentres of some mid-latitude earthquakes. Boskova et al. (1993) observed significant changes in the ion composition about 2 days before the 1990 Iranian earthquake using data onboard the Intercosmos-24 satellite. These changes are the increased concentration of light ions H^+ and He^+ along satellite passes close to the epicentre at altitudes of 2300-2500 km. More recently, Oyama et al. 2008 observed a systematic reduction in the ionospheric electron temperatures (Te) relative to the simulated model using HINOTORI satellite data during the afternoon hours within 5 days before and a day after the three strong earthquakes in the Philippines. The region of ionospheric disturbance extends to about 40° in longitude. Statistical studies by Akhoondzadeh et al. (2010) showed anomalous variations of electron and ion density and temperature observed by DEMETER satellite during 1-5 days before some strong earthquakes. These ionospheric anomalies, which are detected under quiet geomagnetic conditions, can be highly regarded as earthquake precursors (Akhoondzadeh et al. 2010).

2.4.4 The Modification of the Equatorial Ionization Anomaly

There has been great interest in the research of zonal electric field influence caused by the earthquake preparation processes on the equatorial ionosphere. It is well known that the equatorial ionization anomaly (EIA) is very sensitive to changes in the electric field (Zakharenkova et al. 2006). As mentioned in section 2.2.1, the EIA normally occurs in the mid-morning hours, reaches its maximum development in the afternoon and then gradually disappears in the evening and nighttime. At night, the EIA crests shift equatorward and the maximum electron concentration is restored at the geomagnetic equator. Recently, many research have been done to study the EIA modification structure prior to low-latitude and equatorial earthquakes (Liu et al. 2002; Pulinets & Lagen'ka 2002; Zakharenkova et al. 2006, 2008; Liu et al. 2010). Pulinets & Lagen'ka (2002) summarized the main features of the pre-earthquake EIA modification as follows; the daytime amplification of the crests (Pulinets & Lagen'ka 2002), disappearance of the crests (Pulinets & Boyarchuk 2004), and the nighttime double-crest structure with a trough near the epicentre (Zakharenkova et al. 2006, 2008). Liu et al. 2010 constructed daily latitude-time-TEC (LTT) plots to monitor the movement of the EIA crest prior to the 150M $\geq$ 5.0 earthquakes in Taiwan during 2001–2007 using measurements from a network of eight ground-based GPS receivers. They found that the EIA crest significantly moves equatorward and appears in an earlier or later time of the afternoon period a few days before the events along the Taiwan longitude.

2.5 COSEISMIC IONOSPHERIC DISTURBANCES (CID)

2.5.1 Acoustic Wave Disturbances

Coseismic ionospheric disturbances (CID) are ionospheric disturbances that are triggered by earthquakes (Heki & Ping 2005). Earlier research on ionospheric perturbations during earthquakes began since the 1960s (Bolt 1964; Davies & Baker 1965; Leonard & Barnes 1965; Row 1966; Yuen et al. 1969). Bolt (1964) observed air pressure waves excited by propagating seismic waves and by surface uplift in the earthquake source zone on barograms during the 1964 Alaskan earthquake. One year later, Davies and Baker (1965) and Leonard and Barnes (1965) observed ionospheric perturbation signature of the Rayleigh wave due to the Alaskan earthquake using ionospheric sounding networks. The waves occurred about 25-110 min after the earthquake at stations located far away from the epicentre. Row (1966) observed a long-period disturbance of about 90 min on high-frequency Doppler records and ionograms at Boulder, Colorado during the same earthquake and attributed it to acoustic-gravity pulse launched by the major ground displacement near the epicentre. Yuen et al. (1969) demonstrated a direct comparison between seismograms and Doppler shift records after the 1968 Hachinohe earthquake in Japan and found that the vertical oscillations in the ionospheric layer are caused by acoustic waves generated by the earthquake. Recently, Calais and Minster (1995, 1998) showed that ionospheric perturbations are produced by lithosphere-atmosphere-ionosphere coupling. During earthquakes, continuous vertical ground displacements generate atmospheric waves that propagate at infrasonic speeds in the atmosphere. The propagating surface seismic waves induce high-frequency acoustic wave as well as low-frequency gravity wave that propagate horizontally and upward, away from the source.

Lognonné et al. (2006) stated that the Rayleigh surface seismic waves produce the largest ground amplitude that propagate along the Earth’s surface, in the crust or upper mantle with velocities ranging from 3-4.5 km/s. This wave presents a combination of frequency and horizontal wavelength range, which is necessary for an efficient coupling with acoustic modes of the atmosphere (Artru et al. 2004). When the wave front propagation speed is much larger than the sound speed in the atmosphere, the generated atmospheric waves will propagate almost vertically from the surface location of the Rayleigh wave front. As the atmospheric density decreases exponentially with altitude, the wave amplitude increases exponentially as it propagates towards the ionosphere (Ducic 2003). The wave amplification can reach a factor of 10^5-10^6 (Jakowski et al. 2006). These waves manifest themselves as wave-like fluctuations of electron density due to collision interaction of the neutral atmosphere and charged particles (Afraimovich et al. 2005).

Calais and Minster (1995) firstly reported the detection of ionospheric disturbances due to acoustic gravity waves in the GPS TEC measurements after the Northridge earthquake on 17 January 1994. More recent studies have reported coseismic ionospheric disturbances (CIDs) using many GPS stations (Ducic 2003; Afraimovich et al. 2004; Heki & Ping 2005; Heki 2006; Artru et al. 2005). These studies have not only highlighted that atmospheric waves induced by earthquakes include different types of waves but have also discussed the source and the characteristics of the wave propagation. Heki et al. (2006) summarized the CID sources as follows; direct acoustic wave from the focal area with horizontal velocities of 700-1200 m/s and periods of 4-5 minutes (e.g. Heki & Ping 2005), gravity wave propagating obliquely upward from propagating Tsunami with horizontal velocities of 200-250 m/s and periods of 10-20 minutes (e.g. Artru et al. 2005), and secondary acoustic wave excited in far-field from the epicentre by Rayleigh surface wave with horizontal velocity of 3.5 km/s and a period of about 225 seconds (e.g. Ducic et al. 2003). Figure 2.8 illustrates these types of wave propagation and the sound speed profile with Earth's altitude.

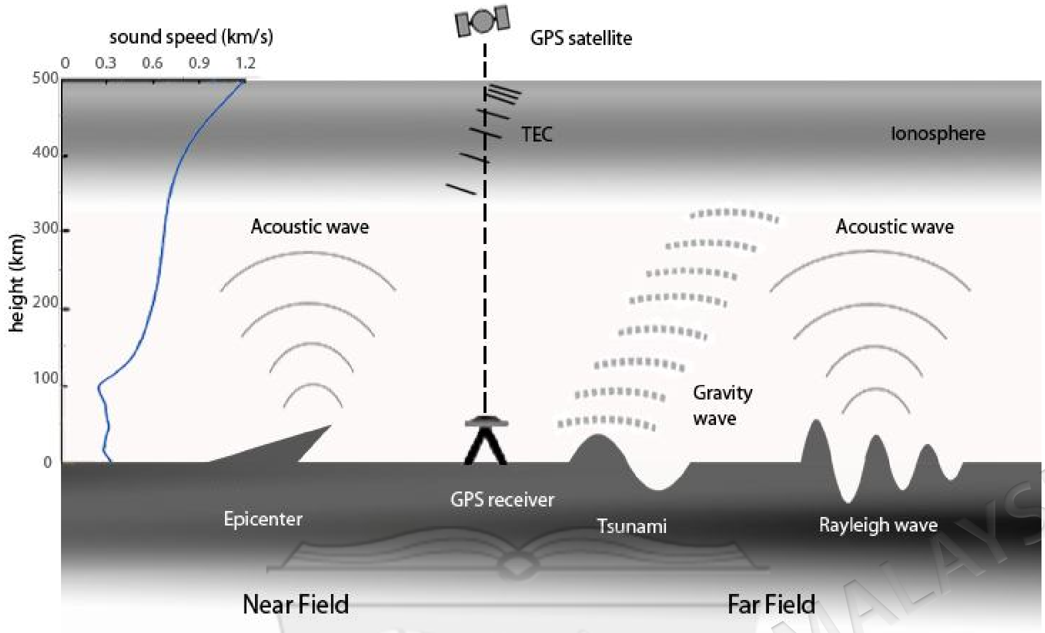

Figure 2.8 Types of atmospheric waves that cause ionosphere disturbances during earthquakes; i.e the direct acoustic wave from the focal area, gravity wave propagating obliquely upward from propagating tsunami and secondary acoustic wave excited in far fields by the Rayleigh surface wave. The sound speed profile with altitude in the Earth's atmosphere is also shown.

Source: adapted from Heki et al. 2006

2.5.2 Magnetic disturbances

Ground-based magnetic disturbances were also investigated during earthquakes (e.g. Ujihara et al. 2004; Iyemori et al. 2005; Kotsarenko et al. 2005). Ujihara et al. (2004) observed high-frequency fluctuations in the northward and eastward electric and magnetic field measurements that are similar to the seismogram readings during the aftershocks of the May 2003 earthquake in Japan using ground-based magnetotelluric equipment. Iyemori et al. (2005) observed two geomagnetic pulsations during the 26 December 2004 Sumatra earthquake using ground-based magnetometers of Phimai in Thailand and Tong Hai in China. The pulsations were of a Pc5 type with a period of 3.6 min at Phimai station and a Pc3 type with a period of 30 sec at Tong Hai station, detected about 12 min after the earthquake. Kotsarenko et al. (2005) performed fractal analysis on ten months of ULF magnetic data at magnetic stations in Japan and observed large enhancements of the fractal index in the H and Z components during the Izu earthquake swam and Miyakejima volcano eruptions in summer 2000.

2.6 GLOBAL POSITIONING SYSTEM (GPS)

The NAVSTAR Global Positioning System (GPS) is an all-weather, spaced based navigation system developed by the United States Department of Defense (DoD) and has been declared fully functional in April 1995. The system was deployed by military forces to accurately determine their position, time, velocity in a common reference system, anywhere or near the Earth on a continuous basis. Despite the main military goals of GPS, the system has attracted a broadband of users. Moreover, it has become an essential component of various applications such as surveying and mapping as well as precise time determination, vessel navigation and oceanography to international air traffic management (Parkinson 1994). The following sections only present a brief overview of the GPS system. Technical details about the system can be found in a large number of textbooks and reports.

2.6.1 GPS Components

GPS comprises of three basic segments: the space, control and user segments. The purpose of these segments is to provide continuous reliable positioning and timing services for GPS users.

a. Space Segment

The space segment comprises of the satellites in low earth orbit that provide the ranging signals and navigation data messages to the user equipment. The original GPS constellation on Block II/IIA consists of 24 operational satellites. As of 2007, there are 31 operational GPS satellites and additional of 3-4 decommissioned satellites that can be reactivated if needed (GPS.GOV 2011). The nominal GPS constellation consists of 24 satellites in 6 orbital planes of them with 4 satellites on each plane. The orbits are equally spaced around the Earth's equator at a 60° separation with an inclination angle of 55° relative to the equator. These GPS orbits are nearly circular and semi-synchronized and are located at an altitude of 20,200 km above the Earth's surface. Figure 2.9 presents the constellation of the GPS satellites. The orbital period of the GPS satellite is approximately 11 hours 58 minutes, so that each satellite makes two revolutions in one sidereal day. Therefore, in terms of a solar day (24 hours), each satellite is in the same position in the sky about four minutes earlier each day (Rizos 1999).

The GPS satellite orbit is designed to form a constellation, whereby at least four satellites are visible at anytime and anywhere (Spilker et al. 1996). Due to their high altitude, the GPS satellites can be viewed simultaneously over large portions of the Earth. These satellites are usually observed only above a certain vertical angle called the elevation angle. With full constellation, the space segment provides global coverage of four to eight satellites that are simultaneously observed above 15° elevation angle. If the elevation angle is reduced to 10°, occasionally up to 10 satellites will be visible and if the elevation angle is reduced to 5°, up to 12 satellites will be visible (Ya'acob 2010).

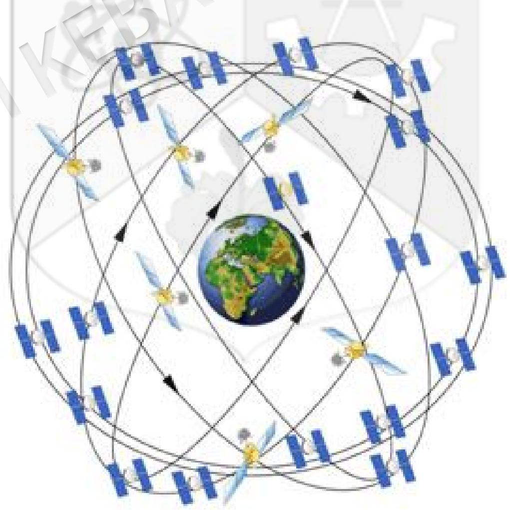

Figure 2.9 The GPS constellation

Source: GPS.GOV 2011

b. Control Segment

The control segment consists of three main components as shown in Figure 2.10. These are the master control station (MCS), ten monitor stations (MS) and upload stations. The MCS is located in at Shriever Air Force Base (AFB), Colorado Springs, USA. It is responsible for processing the tracking data in order to compute the satellite ephemerides and satellite clock corrections as well as other parameters essential to determining user position, velocity and time (PVT). It also initiates all operations of space segment, such as satellite maneuvering, signal encryption and satellite clock keeping (Rizos 1999). The monitor stations originally consisted of four ground stations, located in Hawaii, Ascension Islands, Diego Garcia and Kawajalein. However, six more stations of the National Geospatial-Intelligence (NGA) were added to the grid in 2005 to improve the accuracy (Komowa 2009). These monitor stations track the satellites and send the tracking data to the MCS. The upload stations, located at Ascension Islands, Diego Garcia and Kwajalein consist of ground antennas that uplinks navigation data up to the satellites and collect telemetry back for them (Rizos 1999).

Figure 2.10 The GPS control segment

Source: Kowoma 2009

c. User Segment

The user segment consists of the entire range of application equipments and computational techniques available to collect and process GPS data by both military and civilian users. It also contains infrastructure such as civilian reference stations for differential GPS (DGPS) in order to increase the system's positioning accuracy (Jannsen 1997). Although GPS was initially designed as a navigation system, nowadays a vast variety of applications such as surveying, geodesy, astronomical and telecommunications have been able to utilize GPS due to the advances in technology and processing procedures. These techniques make centimeter level accuracy possible at low cost.

GPS uses a reference coordinate system called the World Geodetic System 1984 (WGS-84). The user's coordinate are determined in this frame and can be transformed to other systems. GPS time is the atomic time scale implemented by a set of atomic clocks in the GPS ground control stations and the GPS satellites. GPS time is defined as the number of seconds elapsed from Saturday midnight of the present week. The GPS time was coincident with Universal Time Coordinated (UTC is maintained by the U.S. Naval Observatory USNO) at the GPS standard epoch of 6 January 1980. GPS time is synchronized with UTC at the microsecond level, within an integer number of seconds. The integer offset between GPS time and UTC arises because of the leap seconds periodically inserted for UTC (Hoffmann-Wellenhof et al. 1994). The fundamentals of the GPS signal structure, observables and error sources as well as the associated ionospheric effects on GPS are presented in the following sections.

2.6.2 GPS Signal Structure

Currently, GPS satellites broadcast ranging codes and navigation signals to Earth to determine location and synchronize time. At present, these signals are transmitted at two frequencies: L1 (1575.42 MHz), L2 (1227.60 MHz) and L5 (1176.45 MHz). The signal structure of the original and modernized GPS signals are described as follows:

a. Original GPS signals

The original GPS system contains two pseudorange (PRN) codes: the restricted precision P-code modulated on both L1 and L2 frequencies, usually reserved for military applications, and the coarse-acquisition (C/A) code, which is modulated only on the L1 frequency, intended primarily for civilian users. The precise P-code consists of a binary sequence 2.35×10^{14} bits in length that repeats itself every 266 days, and transmits a rate of 10.23 Mbps. The entire code is divided into 38 segments, whereby 32 of them are assigned to various satellites and the remaining 6 segments are reserved for other users. Each satellite transmits a unique 1-week segment of the P-code, which is initialized every Saturday midnight (Hofmann-Wellenhof et al. 1994; El-Rabbany 2002). The C/A code is a 1023 bit long binary sequence, transmitted at 1.023 Mbps and has a code wavelength of about 300 m. Hence, the entire C/A code repeats itself every millisecond (Hofmann-Wellenhof et al. 1994; Rizos 1999). Here, the Code Division Multiple Access (CDMA) technique is used, whereby each satellite transmits a unique PRN code, which allows the user's receiver to recognize multiple satellites on the same frequency (Kaplan 2006). In addition to the PRN ranging codes, the navigation message is modulated on both L-band frequencies at a rate of 50 bps. The navigation message consists of components such as the satellite date and time, status and health indication, ephemeris data and the satellite almanac (Hofmann-Wellenhof et al. 1994; Rizos 1999; El-Rabbany 2002).

b. Modernized GPS signals

Although GPS has performed extremely well, additional advances in technology and new demands on the existing system has led to the effort to modernize the GPS system. The GPS modernization program (GPS III) has been formed in 1998 and has an addition of three civilian signals and a new military signal to the new GPS satellites (McDonald 2002; Aerospace 2007). The modernized GPS signals are described as follows:

i. Civilian signal (L2C)

The L25 signal is an additional civilian-use signal other than the existing (C/A) signal. The task of the L2C signal is to improve the navigation accuracy, provide an easy-to-track signal and acting as a redundant signal in case of localized interference.

ii. Safety-of-Life (L5)

The L5 signal was fully broadcasted on the GPS IIR-20(M) satellite in May 2010 and is intended for safety-of-life applications such as civil aviation (GPS.GOV 2011).

iii. Military signal (M-code)

The new military (M-code) is broadcast on both L1 and L2 frequencies and spectrally separated from the GPS civil signals in those bands. The M-code was designed to further improve the anti-jamming, provide robust acquisition, increase accuracy and secure access of the military GPS signals (McDonald 2002; Kaplan 2006).

iv. Civilian signal (L1C)

The L1C is a civilian-use signal, which will be broadcasted on the same L1 frequency that currently contains the C/A signal used by all current GPS users. The task of this signal is to mitigate noise in the C/A code power, improve tracking and enable greater civil interoperability.

Table 2.2 summarizes the frequencies of the original and modernized GPS design.

Table 2.2: Frequencies of the original and modernized GPS signals

Band (Frequency)	Original GPS signal	Modernized GPS signal
L1 (1575.42 MHz)	Encrypted Precision P (Y) code	Encrypted Precision P(Y) code
	Coarse-Acquisition (C/A) code	Coarse-Acquisition (C/A) code and Military (M) code
L2 (1227.60 MHz)	Encrypted Precision (P) code	Encrypted precision P(Y) code
		L2 Civilian (L2C) code and Military (M) code
L5 (1176.45 MHz)		Safety-of-Life (SoL) Data Signal
		Safety-of-Life (SoL) Pilot Signal

2.6.3 GPS Observables

There are three basic GPS observables, which are the code pseudorange, carrier phase and Doppler measurements. The code pseudorange is the range measurement derived using the time delay between the received PRN code and the code replicated by the receiver multiplied by the speed of light. The pseudorange measurement would present the true geometric range between the satellite and the receiver antenna if satellite and receiver clocks were perfectly synchronized with each other, and all other error sources were negligible. However, in practice, there is always a bias between the satellite and receiver clocks, which means that the pseudorange measurement does not represent the true geometric range. Moreover, due to the fact that the GPS signal does not propagate through a vacuum medium, several atmospheric ranging errors exist in the GPS measurements.

The carrier phase measurement is phase difference between the satellite signal at the emission time and the receiver-generated carrier signal at the reception time. The carrier phase is measured in full cycles on both L1 and L2 frequencies and is made by differencing the receiver-generated phase with the incoming received phase. The accuracy of the phase measurement is 1-3 mm but the exact number of carrier cycles between the receiver and satellite is not known at the time of the first measurement (Dach et al. 2007). The unknown integer number of cycles is called initial phase ambiguity, which has the same value as long as the receiver keeps locked on to the phase transmitted by the satellite. Despite this ambiguity, the carrier phase measurement is more accurate than the pseudorange when the ambiguity is resolved, which method will be explained in Section 3.3.2.

The fundamental observation equations for both code and carrier phase observables on L1 and L2 frequencies and error sources are given as follows (Liu et al. 1996; Schaer 1999; Dach 2007):

$$P_{r,\,1}^{s} = \rho_r^s + c\left(\Delta t^s - \Delta t_r\right) + d_{r,\,ion1}^{s} + d_{r,\,trop}^{s} + c\left(b^{s,\,1} + b_{r,\,1}\right) + \varepsilon \tag{2.5}$$

$$P_{r,\,2}^{s} = \rho_r^s + c\left(\Delta t^s - \Delta t_r\right) + d_{r,\,ion2}^{s} + d_{r,\,trop}^{s} + c\left(b^{s,\,2} + b_{r,\,2}\right) + \varepsilon \tag{2.6}$$

$$L_{r,\,1}^{s} = \lambda \Phi_{r,\,1}^{s} = \rho_r^s + c\left(dt^s - dt_r\right) - d_{r,\,ion1}^{s} + d_{r,\,trop}^{s} + \lambda_1 N_{r,\,1}^{s} + \varepsilon \tag{2.7}$$

$$L_{r,\,2}^{s} = \lambda \Phi_{r,\,2}^{s} = \rho_r^s + c\left(dt^s - dt_r\right) - d_{r,\,ion2}^{s} + d_{r,\,trop}^{s} + \lambda_2 N_{r,\,2}^{s} + \varepsilon \tag{2.8}$$

where

$P_{r,\,1}^{s},\ P_{r,\,2}^{s}$: pseudorange code measurements between satellite and receiver on L1 and L2 frequencies, extracted from either the C/A code or the P-code (m)

$L_{r,\,1}^{s}, L_{r,\,2}^{s}$: carrier phase measurements between satellite and receiver on L1 and L2 frequencies (expressed in unit of distance) (m)

ρ_r^s : true geometric distance between satellite and receiver (m)

c : speed of light in free space (3×10^8 m/s)

dt^s, dt_r : satellite and receiver clock offsets relative to the GPS system time (s)

$d_{r,\,ion}^{s}$: ionospheric delay on both frequencies (m)

$d_{r,\,trop}^{s}$: tropospheric delay (m)

$b^s,\ b_r$: satellite and receiver biases (hardware delays) on both frequencies (s)

ε : random error due to multipath, receiver noise and etc (m)

$\Phi_{r,\,1}^{s},\ \Phi_{r,\,2}^{s}$: carrier phase between satellite and receiver on L1 and L2 frequencies

(cycles)

λ_1, λ_2 : carrier wavelength on L1 and L2 frequencies (m)

$N^s_{r,1}$, $N^s_{r,2}$: unknown integers number of cycles (or carrier phase ambiguity) between satellite and receiver on L1 and L2 frequencies (cycles)

From (2.5) to (2.8), the ionospheric delay $d^s_{r,\,ion}$, satellite and receiver biases b^s and b_r, the carrier wavelength λ and the carrier phase ambiguity N^s_r are dispersive (frequency-dependent) terms, while the remaining terms in these equations are non-dispersive (non-frequency) dependent. Therefore, the non-dispersive term that combines the true geometric distance between satellite and receiver ρ_r^s, the satellite and receiver clock offsets dt^s and dt_r, and the tropospheric delay $d^s_{r,\,trop}$ is expressed in the following formula (Schaer et al. 1999):

$$\rho'^s_r = \rho^s_r + c\left(dt^s - dt_r\right) + d^s_{r,\,trop} \tag{2.9}$$

The ionospheric delay $d^s_{r,\,ion}$ can also be substituted with the ionospheric refraction coefficient I^s_r, which represents the ionospheric delay related to the first frequency, f_1. Thus, (2.5) to (2.8) can be rewritten in a simplified, frequency-dependent notation expressed as follows (Schaer 1999):

$$P^s_{r,\,1} = \rho'^s_r + I^s_r + c\left(b^{s,\,1} + b_{r,\,1}\right) + \varepsilon \tag{2.10}$$

$$P^s_{r,\,2} = \rho'^s_r + \frac{f_1^2}{f_2^2} I^s_r + c\left(b^{s,\,2} + b_{r,\,2}\right) + \varepsilon \tag{2.11}$$

$$L^s_{r,\,1} = \lambda_1 \Phi^s_{r,\,1} = \rho'^s_r - I^s_r + \lambda_1 N^s_{r,\,1} + \varepsilon \tag{2.12}$$

$$L^s_{r,\,2} = \lambda_2 \Phi^s_{r,\,2} = \rho'^s_r - \frac{f_1^2}{f_2^2} I^s_r + \lambda_2 N^s_{r,\,2} + \varepsilon \tag{2.13}$$

where

I_r^s : L_1-related ionospheric delay coefficient, which is proportional to $1/f^2$ (m)

By comparing the code with the carrier phase observable from (2.10) - (2.13), it is notable that the sign of the ionospheric refraction for code measurement is positive but it is negative for phase measurement. This means that the ionospheric refraction delays the GPS code measurements and advances the carrier phases.

The Doppler frequency if the third observable that represents the rate of change of the carrier phase observable. It is a measure of the relative velocity between the satellite and receiver. The Doppler frequency measurement is not affected by cycle slips and does not have an integer ambiguity; therefore, it is used for cycle slip detection and velocity estimation. The observation equation can be expressed as follows (Wells 1987):

$$D = \dot{\Phi}_r^s = \dot{\rho}_r^s + c\left(\dot{dt}^s - \dot{dt}_r\right) + \dot{d}_{r,\,ion}^s + \dot{d}_{r,\,trop}^s + \dot{\varepsilon} \qquad (2.14)$$

where

$\dot{\Phi}_r^s$: Doppler (m/s)

$\cdot$: time derivative

2.6.4 GPS Error Sources

As mentioned in Section 2.6.3, the GPS measurements are affected by a number of error sources, which results in degradation of accuracy of GPS positioning. In general, the GPS errors and biases can be classified into three categories: satellite-dependent errors, receiver-dependent error and radio propagation errors. A huge quantity of literature related to GPS and its error sources can be found on websites and in textbooks (Hofmann-Wellenhof et al. 1994; Kaplan 1996). The main error sources are briefly discussed as follows:

a. Selective Availability and Anti-Spoofing

The selective availability (SA) is a method used by the US Department of Defense (DOD) to degrade the navigation accuracy of the GPS code pseudoranges and carrier phase observations. The SA can be implemented by two methods. The first method (δ-process) is achieved by dithering the fundamental frequency of the satellite clock. The second method (ε-process) is implemented by truncating the orbital information in the transmitted navigation message resulting in a degradation of the computed coordinates of the satellites. The GPS positioning accuracy under SA is degraded up to 100 m for horizontal position and up to 340 ns for timing. The SA has been turned off since 2 May 2000 and since then, the positioning accuracy has improved to 5 - 15 m (Liao 2000).

The anti-spoofing (AS) is another method to deny potential GPS spoofers, who generate an imitation GPS signal, which causes the receiver to track the wrong signal. The AS was implemented on 31 January 1994 to deny the dual frequency GPS civilian users the access to the military P-code (P1 or P2) through encrypting the P-code into the Y-code only to authorized users, while the unauthorized receiver becomes a single L1 frequency receiver. The broadcasted ionospheric model in the navigation message may be used to overcome the problem of absence of dual-frequencies, which are originally implemented to eliminate ionospheric effects. However, the ionospheric model is not as accurate as the method of using dual-frequencies data and thus degrading the positioning accuracy. The coarse-acquisition (C/A) may be used to replace the absence of the P-code (Xu 2007). The AS does not affect the C/A-code. The net of degradation of both SA and AS is 100 m for horizontal position and 167 ns for timing (Allan et al. 1990).

b. Tropospheric Delay Error

The troposphere is the lower part of the atmosphere, which is electrically neutral and nondispersive for GPS signal. Within the troposphere, the group and phase velocities of the GPS signal on both Ll and L2 frequencies are equal. The tropospheric delay is caused by the effects of neutral atoms and molecules in the troposphere on electromagnetic signals (Xu 2007). The magnitude of the tropospheric delay errors depends on atmospheric temperature, pressure and moisture content. The magnitude of the delay errors is highly correlated with the satellite elevation angles, where it increases significantly with lower elevation angles. For a low elevation satellite, the tropospheric delay will induce pseudorange and carrier-phase errors from about 2 m for a satellite at zenith to more than 20 metres (Spilker 1996). Therefore, the tropospheric effect is an important error source in precise GPS applications. The tropospheric range delay can be estimated using a number of models (e.g. Hopfield 1969; Saastamoinen 1973; Black & Eisner 1978).

c. Ionospheric Delay Error

As mentioned in Section 2.1.2, the ionosphere contains a significant number of ionized particles, which are the free ions and electrons. The ionosphere exerts severe influences on the propagation of radio waves, which are refracted, reflected and absorbed in various ways due to its dispersive properties. When a GPS signal propagates through the ionosphere, it is delayed or advanced significantly due to the presence of the free electrons in the region. The major ionospheric effects are such as the following (Klobuchar 1996): the group delay pseudorange; carrier phase advance; Doppler shift; Faraday rotation of all polarized signals; refraction or bending of the radio wave; distortion of pulse waveforms and amplitude and phase scintillation. Among these, the main ionospheric effects in geodetic observations are the group delay pseudorange and carrier phase advance. These effects are known as the ionospheric delay error, which is an indicator of the dispersive nature of the ionosphere (Suparta 2007). The ionospheric delay error is the second largest error source after SA and is a major concern for GPS applications because it corrupts the positioning and time transfer results. The ionospheric delay error of the GPS signal is normally from the range of a few meters to more 20 m within one day (Klobuchar 1996). It also varies according to several factors such as the user’s location, elevation angle, time of the day, time of the year and solar cycle. During periods of high solar activity, this delay can induce a vertical ranging error of about 15 m and a 50 ns timing error at the zenith direction (Klobuchar 1996).

CHAPTER III

METHODOLOGY

3.1 INTRODUCTION

This chapter describes the ionospheric effects on GPS applications, dual-frequency ground-based GPS measurement system and data processing technique to determine the ionospheric vertical total electron content (VTEC). A description of the GPS VTEC analysis using three statistical methods is also given. In addition to the GPS VTEC technique, a brief description on ground-based magnetometer and CHAMP satellite measurement techniques are also provided. Finally, the chapter ends with the magnetic and solar conditions before and during earthquake periods.

3.2 IONOSPHERIC EFFECTS ON GPS APPLICATIONS

3.2.1 Ionospheric Refraction Index

In order to examine the propagation effects of the radio signal propagating through the ionosphere, the refractive index must be specified. The refractive index is a function of frequency, which enables dual frequency GPS users to measure and correct the first order ionospheric range and range rate errors directly (Ya'akob 2010). A simplified form of the ionospheric refractive index η_{ion}, which has been derived from the Appleton-Hartree formula is expressed by the following equation (Brunner & Gu 1991):

$$\eta_{ion} = 1 - \frac{e^2}{2\left(4\pi\varepsilon_0 m_e\right)} \frac{N_e}{f^2} \tag{3.1}$$

where

N_e : electron density (electron/m^3)

e : charge of one electron (1.602x10^{-19} C)

ε_0 : permittivity in vacuum (8.854x10^{-12} C^{2}N^{-1})

m_e : mass of electrons (9.109x10^{-28}g)

By substituting values of constants e, m_e, and ε_0 in (3.1), the ionospheric refraction index can be expressed by:

$$\eta_{ion} = 1 \pm \frac{40.3\text{x}10^{16}}{f^2} N_e \tag{3.2}$$

Hence, the refractive index is proportional to the electron density N_e and inversely proportional to the signal frequency, f. The positive and negative sign represents the refractive index for pseudorange and phase measurements, respectively. By knowing the ionospheric refraction index, it is possible to derive the group delay and phase advance of the code and phase GPS signals, respectively.

3.2.2 Ionospheric Delay and Advance

The current GPS employs two carrier frequencies, which are L1 and L2 allowing the usage of dual-frequency receivers. The ionospheric effects on the GPS measurements are directly reflected in the form of group delay or carrier phase advance. The group delay results from the fact that the signal travels slower in the ionosphere than it does in free space. The phase signal however, travels faster in the ionosphere than in free space (Davies & Smith 2002). The ionospheric delay for single frequency can be obtained by integrating the refractive index in (3.2) along the GPS signal path from the satellite to receiver. The ionospheric delay I_r^s can be expressed in units of time delay by the following equation:

$$I_r^s = \int_r^s (n_{ion} - 1)\, dl = \pm \frac{40.3}{f^2} \int_r^s N_e dl \tag{3.3}$$

The positive and negative sign represents the group and phase delays, respectively. The integrated electron density along the line-of-sight represents the VTEC (in electrons/m^2) along the slant path of the GPS satellite and receiver. The slant VTEC and is expressed by (3.4):

$$STEC = \int_r^s N_e dl \tag{3.4}$$

Substituting (3.4) into (3.3), the ionospheric delay I_r^s for a single frequency receiver can be expressed in terms of VTEC as follows:

$$I_r^s = \pm \frac{40.3}{f^2} TEC \tag{3.5}$$

The ionospheric delay can also be expressed in units of distance by multiplying the right-hand term with the speed of light, *c*. The group delay for the dual-frequency receiver can be obtained by differencing the L2 from L1 frequency by assuming that both signals propagate along the same path through the ionosphere. Therefore, the group delay can be obtained from (3.5) as follows:

$$P_r^s = P_{r,\,1}^s - P_{r,\,2}^s = \pm 40.3TEC\left(\frac{1}{f_2^2} - \frac{1}{f_1^2}\right) \tag{3.6}$$

3.3 GPS VERTICAL TOTAL ELECTRON CONTENT (VTEC)

The main parameter that describes the ionospheric effects on GPS signals is the total electron content (VTEC), which is defined as the number of electrons in a vertical column that extends from the satellite to the receiver and having a cross section of 1-m^2 (in VTEC units: 1 VTECU = 10^{16} electron m^{-2}). The dispersive nature of the ionosphere allows the calculation of VTEC using dual-frequency GPS measurements.

3.3.1 Determination of the Vertical electron Content (VTEC)

There are two types of VTEC measurements, which are the slant VTEC (SVTEC) and the vertical VTEC (VTEC). The SVTEC is the VTEC measurement along the slant path between the satellite and receiver, which depends on the satellite elevation angle. For the absolute VTEC mapping using ground-based GPS data, the vertical VTEC (VTEC) is of main interest. In order to obtain the VTEC, the SVTEC measurements are converted to VTEC measurements using a suitable mapping function by employing the ionospheric single layer model (SLM) as shown in Figure 3.1. In this layer, it is assumed that all the free electrons are contained at the altitude of h_m. The altitude h_m is usually set to be 350, 400 or 450 km, which is approximately the altitude of the maximum electron density (Schaer 1999). The VTEC is determined at the ionospheric pierce point (IPP), which is the altitude of the intersection of the user line-of-sight to the tracked satellite with the center of the ionospheric slab. In this work, the IPP is set at the fixed altitude of 400 km above the Earth's surface.

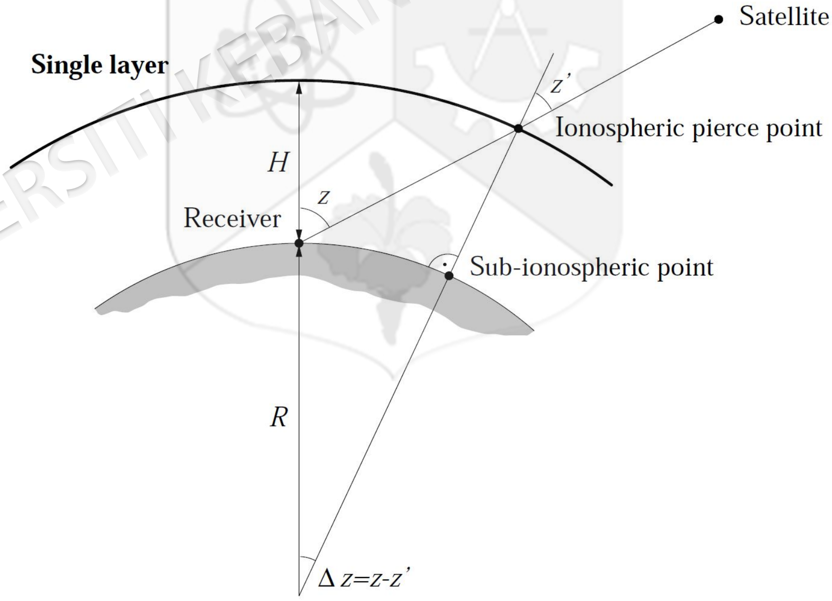

Figure 3.1 The ionospheric single layer model (SLM)

Source: Schaer (1999)

Referring to Figure 3.1, the SVTEC is converted to VTEC at a given IPP using the obliquity correction factor and is expressed in (3.7):

$$VTEC_r^s = STEC_r^s \cos z' \quad (3.7)$$

where

z’ : the zenith angle from the receiver to the IPP

In some literature, the ionospheric SLM mapping function is called the elevation-dependent mapping function, which is represented as follows (Schaer 1999):

$$F(z) = \frac{TEC(z)}{TEC(0)} = \frac{1}{\cos z'} = \frac{1}{\sqrt{1-\sin^2 z'}} \quad (3.8)$$

with

$$z' = \sin^{-1}\left(\frac{R_E}{R_E + h_m}\cos z\right) \quad \text{(degree)} \quad (3.9)$$

and

$$z = \frac{\pi}{2} - E \quad (3.10)$$

where

R_E : the mean radius of the Earth, which is ~6371 km

h_m : the height of the ionospheric SLM

E : the elevation angle to the tracked satellite (radian)

3.3.2 Determination of the Absolute VTEC

The absolute GPS VTEC measurements can be derived from both differential group delay (P1-P2) and differential phase advance (L1-L2). The GPS VTEC obtained from group delay measurements gives a level of absolute VTEC, but it is highly exposed to multipath effect with an error worse than 10^{15} m^{-2} when averaged on a 30 s interval (Plotkin 2003). On the other hand, the GPS VTEC obtained from phase measurements gives a high degree of accuracy corresponding to an error of at least 10^{14} m^{-2} when averaged on a 30 s interval, but level is unknown due to the ambiguity in the initial VTEC value (Afraimovich et al. 2001). Therefore, the VTEC level obtained from the differential phase advance measurements is adjusted to the VTEC derived from the corresponding code difference for each satellite-receiver pair (Otsuka et al. 2002).

The absolute GPS VTEC is estimated by assuming that the ionosphere is a spherical shell at fixed height of 400 km above the Earth's surface, which is approximately corresponding to the maximum electron density profile. The GPS observables are biased on instrumental delays; therefore the satellite and receiver biases are removed to obtain a precise measurement of VTEC (Sardon et al. 1994). The ambiguity term in the VTEC phase measurements is resolved by combining the code and phase measurements for each satellite path using the geometry free combination (GFC) method derived by Warnant and Pottiaux (2000). The following sections detail the calculation procedure of the absolute VTEC by using the geometry-free combination (GFC) of dual-frequency code and phase measurements.

a. Geometry Free Combination (GFC) Method

In this work, the GPS VTEC measurement of a dual-frequency GPS receiver is calculated using the geometry free combination (GFC) technique, which combines both pseudorange code and phase observables. This is done by subtracting the code or phase observable at L2 frequency ((2.10) or (2.11)) with the one at L1 frequency ((2.12) or (2.13)), by which the non-dispersive term, ρ'^{s}_{r} and random errors, ε are eliminated. The equations can be expressed as follows (Manucci et al. 1999; Schaer 1999; Warnant & Pottiaux 2000):

$$P_r^s = P_{r,1}^s - P_{r,2}^s = \left(\frac{f_2^{\,2} - f_1^{\,2}}{f_2^{\,2}}\right) I_r^s + c\left(\Delta b^s - \Delta b_r\right) \qquad (3.11)$$

$$L_r^s = L_{r,1}^s - L_{r,2}^s = -\left(\frac{f_2^{\,2} - f_1^{\,2}}{f_2^{\,2}}\right) I_r^s + \Delta N_r^s \qquad (3.12)$$

where

Δb_r, Δb^s : the receiver and satellite differential biases, respectively

N_r^s : the carrier phase ambiguity term

$\Delta b^s = b^{s,1} - b^{s,2}$, $\Delta b^r = b_{r,1} - b_{r,2}$

$\Delta N_r^s = \lambda_1 N_{r,1}^s - \lambda_2 N_{r,2}^s$ and

$\dfrac{f_2^2 - f_1^2}{f_2^2} \approx -0.647$

The term $c\left(\Delta b^s - \Delta b_r\right)$ in (3.11) is the differential group delay, which are satellite and receiver biases that are contained in code measurements due to the anti-spoofing effect. These biases are due to the fact that the L1 and L2 GPS frequencies undergo different propagation delays inside the receiver and satellite hardware (Warnant & Pottiaux 2000). As mentioned earlier, the dual-frequency P-code (P1 or P2) is encrypted into the Y-code (Y1 or Y2) under the anti-spoofing effect. For receivers, which report the C1-code instead of the P1-code, the C1-code is made compatible to the modern P1-code by adding the long term code bias (P1-C1) to the C1-code obtained from all the satellite passes (Almomani 2007). In this work, the term (P1-C1) for all satellite passes on a monthly basis obtained online from AIUB Data Center of Berne University, Switzerland (AIUB 2006). The mathematical expression to make the C1-code compatible with the modern P1-code is given as follows:

$$P_{r,1}^s = C_{r,1}^s + f(i) \qquad (3.13)$$

where *f(i)* is the empirically determined long-term average bias values of $(P1\text{-}C1)_i$ for all satellites *i*.

Substituting the ionospheric delay, I_r^s in (3.5) into (3.11) and (3.12), the geometry-free combination of code and phase measurements can be written as functions of VTEC as follows:

$$P_r^s = -\,0.105 VTEC_r^s + c\left(\Delta b_r - \Delta b^s\right) \quad \text{(m)} \qquad (3.14)$$

$$L_r^s = -0.552 VTEC_r^s + N_r^s \qquad \text{(cycle)} \qquad (3.15)$$

According to Warnant & Pottiaux (2000), the carrier phase ambiguity term N_r^s in the phase measurement can be resolved through a combination of both geometry code and phase measurements for each satellite and receiver pair. This is obtained by subtracting the code from the phase measurement and is expressed in (3.16):

$$P_r^s - L_r^s = \mathrm{c}\left(\Delta b_r - \Delta b^s\right) - N_r^s \qquad (3.16)$$

The GPS observables in (3.16) are biased on instrumental delays. Therefore, the GPS VTEC values are corrected from its satellite biases using the values provided by the AIUB Data Center of Berne University, Switzerland (AIUB 2006). Meanwhile, the VTEC values for the International GNSS Service (IGS) stations are corrected from its receiver biases by using values from the AIUB Data Center of Bern University, while values for SAMP and JUPEM stations are determined by using Bernese version 5.0.

3.3.3 The Coordinates of the Ionospheric Pierce point (IPP)

Assuming that the geographic latitude and longitude of the GPS receiver (ϕ_r, λ_r) are known, the coordinate of the ionospheric pierce point (IPP) can be obtained according to the observed azimuth and elevation angle to the tracked satellite and the single layer ionospheric model. The geographic latitude of the ionospheric pierce point (IPP) ϕ_{ipp} is given as follows:

$$\Phi_{pp} = \sin^{-1}\left(\sin\phi_r \cos\psi_{ipp} + \cos\phi_r \sin\psi_{ipp} \cos A\right) \qquad (3.17)$$

where

ϕ_r : latitude of the GPS receiver (radian)

ψ_{ipp} : angle subtended at the center of the Earth between the user position vector
and the Earth's projection of the pierce point (radian)

A : azimuth angle of the satellite at the user's position (radian)

From (3.17), the angle ψ_{ipp} is calculated as follows (Lin 2001):

$$\psi_{ipp} = z - z' = \frac{\pi}{2} - E - \sin^{-1}\left(\frac{R_E}{R_E + h_m} \sin z \right) \qquad (3.18)$$

Meanwhile, the geographic longitude of the ionospheric pierce point (IPP), λ_{ipp} is given as follows:

$$\lambda_{ipp} = \lambda_r + \sin^{-1}\left(\frac{\sin \psi_{ipp} \sin A}{\cos \phi_{ipp}} \right) \qquad (3.19)$$

Apart from the geographic coordinates, the geomagnetic coordinates (ϕ_m, λ_m) of the IPP are also calculated based on the geomagnetic coordinate system with its dipole axis intersecting the geographic sphere (Boreal pole) at approximately 78.7 °N in latitude and 290.1 °E in longitude (Biel 1990). The geomagnetic latitude ϕ_m and longitude λ_m are given in (3.20) and (3.21), respectively.

$$\phi_m = \sin^{-1}\left(\sin \phi_{ipp} \sin \phi_p + \cos \phi_{ipp} \cos \phi_p \cos\left(\lambda_{ipp} - \lambda_p \right) \right) \qquad (3.20)$$

$$\lambda_m = \frac{\sin^{-1}\left(\cos \lambda_{ipp} \sin(\lambda_p) \right)}{\cos \phi_m} \qquad (3.21)$$

where

ϕ_p, λ_p : the latitude and longitude of the Boreal pole (in radian), respectively.

In the GPS VTEC analysis, only the absolute VTEC measurements and the IPP coordinates that fall above the elevation mask angle of 30° are considered in order to minimize multipath effects.

3.4 GPS DATA PROCESSING

The signal processing to obtain the GPS VTEC was a multi-step operation. The raw binary data are taken from the receiver and converted into RINEX observation and navigation files using a Translate/Edit/Quality/Check (TEQC) routine developed by the University NAVSTAR Consortium (UNAVCO) (UNAVCO 2009). A Matlab program suite is then used to process, analyze and plot the data. Figure 3.2 gives an overall view of the data processing method.

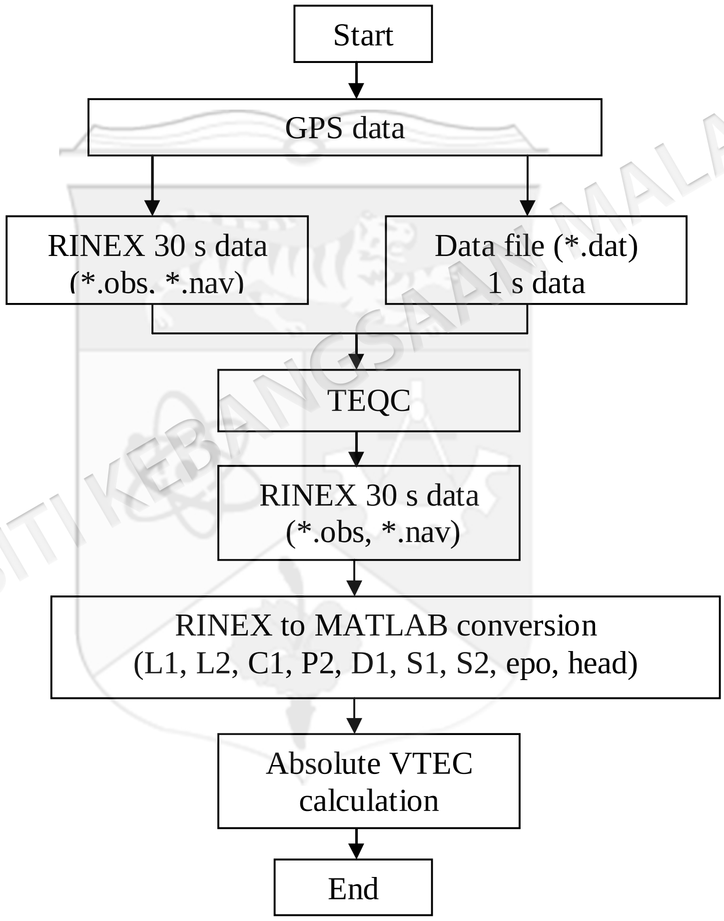

Figure 3.2 Flow chart of the data-processing method

3.4.1 Pre-processing

The GPS data are pre-processed prior to estimating the GPS VTEC. This is done because the position of the satellites and the ground position of the receiver must be precisely known in order to determine the GPS VTEC. The data pre-processing is conducted using the TEQC facility program and integrated into MATLAB programs developed by the Satellite Mobile Research Group (SMRG) at UKM (Almomani 2007). TEQC is a simple and unified approach to solving many pre-processing problems with GPS and GLONASS data and supports the data format of dual-frequency (L1 and L2) receivers such as Trimble, AshVTECh, AOA TurboBinary and Leica. In general, the main activities in pre-processing data involve ephemeris generation, transfer and decoding, screening and editing, database creation, reporting and quality control.

3.4.2 GPS Data Format

The measurable parameter of a GPS dual-frequency receiver produces five sets of binary format which are Dat, RINEX, SSF, Almanac and log files. However, the RINEX data and log files are mostly used in this work. The Receiver Independent Exchange (RINEX) file consists of observation (OBS), navigation (NAV) and meteorological (MET) data files. The data files are binary files that contain all the parameters required in the analysis while the log (*.log) files are used to record the status of logging activity. The OBS data file contains GPS measurements, the NAV data file contains ephemeris or orbit information and the MET data file contains pressure, temperature, relative humidity and etc. The OBS (*.o) and NAV (*.nav) are combined into one data file known as dat (*.dat). The observation file consists of observable types such as phase measurements on L1 and L2 (L1 and L2 in cycles), coarse-acquisition (C/A) - code pseudorange measurement on L1 (C1 in meters), precision (P code) pseudorange measurements on L1, L2 (P1 and P2 in meters), Doppler frequency measurements on L1 and L2 (D1 and D2 in Hz), and the signal-to-noise ratio (SNR) measurements (S1 and S2) of GPS L1 and L2 signals. In a normal operation, P1 is recorded but during observations collected under Anti-spoofing (AS), C1 is recorded instead.

The TEQC routine is used to translate the binary format (*.dat) into RINEX OBS and NAV files, to edit or correct, to cut or splice RINEX files as well as to check the quality of GPS data. These three main functions, which are translate, edit and quality check can be performed altogether, in pairs or separately. A standard data sampling rate of 30 s is executed in TEQC in order to reduce the processing time. To translate the binary format (*.dat) into an observation data set that consists of L1, L2, C1, P2, D1, S1 and S2 parameters and navigation data, a configuration command of TEQC in DOS mode can be implemented as follows:

teqc -O.int <a> -week <b> -O.dec <a> -O.obs L1+L2+C1+P2+D1+S1+S2 +nav test.06**n** 06030100.dat >test.06**o**

where

-	: to input or turn off an option
+	: to output or turn on an option
-O.int <a>	: sampling interval with <a> value, in seconds
-O.dec <a>	: modulo decimation of OBS epochs to # time (seconds by default); -O.dec 30s or -O.dec .5m results in epochs nominally at 00 and 30 seconds being output, millisecond jumps should be accounted for automatically.
<b>	: number of GPS week
-O.obs	: list of observables and the observables themselves in the data portion of the file
nav	: to put ephemeris information in 06030100.dat into the navigation file test.06n
06030100	: name of *.dat data for year 2006, month of March, day 01 and 00 hour

After the execution, two types of files will be formed, which are test.06o (observation file) and test.06n (navigation file). GPS observables can contain errors; therefore the erroneous observables for the particular hour are manually removed to obtain error free data. The MATLAB program (rinex2mat.m) is used to extract the GPS observables from both these files and arrange them into separate individual data files to ease processing. The extracted observables are further employed to determine GPS VTEC using MATLAB programs.

A spliced RINEX observation file normally contains post-header comment lines, in which the header information from observation files after the first one are also included. These comment lines must be removed before executing the MATLAB rinex2mat.m program. To remove the post-header comment lines, the **teqc** and LINUX **grep** commands in DOS and Cygwin modes, respectively are utilized as shown in the following:

```
teqc -phc test.06o >test1.06o
```

where

phc : post-header comments

test1.06**o** : new observation filename

However, the TEQC -phc option removes all the post-header comment lines except the comment lines shown in the following:

```
                    4  1
RINEX FILE SPLICE; other post-header comments skipped       COMMENT
```

To further remove these comment lines, a LINUX command from the Cygwin command prompt is implemented as follows:

```
grep –v "4  1" test1.06o | grep –v "RINEX FILE SPLICE" > test2.06o
```

a. RINEX Observation Data File

The RINEX observation data file contains a data record of a GPS station. The observation file consists of a header that contains all the auxiliary information of the receiver station needed for the post-processing of the data, and a data section that contains the observables. Table 3.1 shows the label and description of the observation data file header section.

Table 3.1 Label and description of the observation data file header section

Header Label	Description
RINEX VERSION / TYPE	- Format version (2.10) - File type (observation data) - Satellite system : G (GPS) R (GLONASS) S (Geostationary signal payload) T (NNSS Transit) M (Mixed)
PGM/ RUN BY/ DATE	- Name of program creating current file - Name of agency creating current file - Date of file creation
COMMENT	Comment line (s)
MARKER NAME	Name of antenna marker
MARKER NUMBER	Number of antenna marker
OBSERVER/ AGENCY	Name of observer/ agency
REC # / TYPE / VERS	Receiver number, type and version
ANT # / TYPE	Antenna number and type
APPROX POSITION XYZ	Approximate marker position (WGS84)
ANTENNA: DELTA H/E/N	- Antenna height: height of bottom surface of antenna above marker - Eccentricities of the antenna marker relative to marker to the east and north (in meters)
WAVELENGTH FACT L1/2	- Default wavelength factor for L1 and L2 1: Full cycle ambiguities 2: Half cycle ambiguities - zero or blank
# / TYPES OF OBSERV	- Number of different observation types stored in a file - Observation types
INTERVAL	Observation interval in seconds
TIME OF FIRST OBS	- Time of first observation record (4-digit-year, month, day, hour, min, sec) - Time system: GPS (=GPS time system)
END OF HEADER	Last record in the header section

Source: UNAVCO 2009

The data section of the observation data file has to following format:

```
06  03     1          0        0       0.0000000       0     10G16G   3G
    1G14G20G25G23G11G19G15
yy-mm-dd   hr-min-sec
--------------Epoch--------------   L  # PRN (G=GPS code)
```

where **L** is the event flag (usually zero) and **#** is the number of satellites in current epoch followed by the list of PRNs (satellite numbers with system identifier) observed in current epoch.

The layout of recorded observation data is given by the TYPES OF OBSERV as stated in the header. The data file allows 5 observation types to be recorded per line, so in the case of 7 types of observables as shown below, each data entry takes two lines for every satellite observed. The type and numbers of observables depend on the type and setting of the GPS receiver.

```
        7    L1    L2    C1    P2    D1    S1    S2            # / TYPES OF OBSERV
```

where

L1, L2 : phase measurements (cycles) with carrier frequencies L1 = $154f_0$ (1575.42 MHz) and L2 = $120f_0$ (1227.60 MHz) whereby f_0 is the fundamental L-band frequency, 10.23 MHz

C1 : pseudorange (meters) using C/A code on L1

P1, P2 : pseudorange using P-code on L1 and L2. In this data file, there are no P1 measurements available; therefore C1 is used as a substitute of P1

D1 : Doppler frequency (Hz)

S1, S2 : signal-to-noise ratio (SNR) for the L1 and L2 phase observations

```
Data record:
|-------L1------|   |-------L2------|   |-------C1-------|  |-------P2-------|    |----D1----|
404713.35444      231032.31845      23866602.2694      23866602.0334      -
268.0084
|------data-----LLIS   ------data-----LLIS   --------data------LLI   --------data------LLI    ----data---LLI
|--S1--|      |---S2--|
7.0004        7.0004
--data-LLI    --data-LLI|
```

where

LLI = loss of lock indicator, which has a range of 0-7, where

0 : OK	1 : cycle slip
4: anti-spoofing	Blank: unknown

S = signal strength, which has an interval of 1-9, where

1 : minimum possible signal strength

9 : maximum possible signal strength

0 or blank : blank or unknown

This data record is repeated for each satellite given in EPOCH/SAT record. An example of the RINEX observation file can be found in APPENDIX A1.

b. RINEX Navigation Data File

The navigation message consists of data bits that describe the GPS satellite orbits, clock corrections, ephemeris, almanac and other system parameters. The time-tagged data bits mark the time of transmission of each subframe at the time they are transmitted by the satellite vehicle (SV). The data entry for each satellite consists of 4 columns and 8 rows, which format is shown in Table 3.2.

Table 3.2 Data information of each satellite in the navigation message file

Row	Column 1	Column 2	Column 3	Column 4
1	PRN yy mm dd hh mm sec	svclk1	svclk2	svclk3
2	Iode	Crs	Delta n	M0
3	Cuc	Eccentricity	Cus	Sqrt (A)
4	Toe	Cic	OMEGA	CIS
5	Io	Crc	Omega	OMEGA DOT
6	IDOT	codeL2	gpswk#	L2Pflag
7	Svaccuracy	Svhealth	TGD	IODC
8	Transmission	Fitintv	Spare	spare

Table 3.3 gives the description of the parameters of the navigation file transmitted by each satellite.

Table 3.3 Description of the parameters in the navigation message file

Row	Parameter	Description
1	svclk1, svclk2, svclk3	Clock bias (sec), drift, (sec/sec), drift rate (sec/sec^2)
2	Iode	Age of data ephemeris (sec)
	Crs	Sine term for radius correction (meters)
	Delta n	Mean motion difference (rad/sec)
	M0	Mean anomaly (radians)
3	Cuc	Cosine term for radius correction (radians)
	e Eccentricity	Eccentricity
	Cus	Sine term for argument in latitude correction (radians)
	Sqrt (A)	Square root of semi-major axis (sqrt(m))
4	Toe	Time of ephemeris (sec in GPS week)
	Cic	Cosine term for inclination correction (radians)
	OMEGA	Nodes' longitude (radians)
	CIS	Sine term for inclination correction (radians)
5	Io	Inclination (radians)
	Crc	Cosine term for radius correction (meters)
	Omega	Argument of perigee (radians)
	OMEGA DOT	Rate of node's longitude (radians/sec)
6	IDOT	Rate of inclination (radians/sec)
	codeL2	Codes on L2 channel
	gpswk#	GPS week number
	L2Pflag	L2 P data flag
7	Svaccuracy	Satellite's accuracy and health (meters)
	Svhealth	Ionospheric group delay (sec)
	TGD	Age of data clock (sec)
	IODC	Issue of data, clock
8	Transmission	Transmission time of message (sec of GPS week)
	Fitintv	Fit interval (hours)
	Spare	Blank
	Spare	Blank

Source: UNAVCO 2009

3.4.3 Post-Processing

To calculate the GPS VTEC, the RINEX observation and navigation file for all the GPS observables are converted into ASCII files to make it readable in MATLAB. For this purpose, a MATLAB program called rinex2mat.m, which combines together the rinex_O.exe and rinex_N.exe (16 bit program) with Borland C++ version 3.1. This procedure separates all the observables to ease processing and classification as well as to identify and reduce cycle slips. These observables are then used to calculate the absolute VTEC measurements using MATLAB programs developed at the Satellite Mobile Research Group (SMRG) in UKM (Almomani 2007). The VTEC measurements are obtained at 30 s sampling rate, 30° elevation mask and at 400 km by using (3.7). By averaging the original absolute VTEC measurements obtained from all satellites at 30 s sampling rate over a period of 15 minutes, the high frequency ripples in the original VTEC is reduced, hence a more smoothed absolute VTEC measurement is obtained (Almomani 2007).

3.5 GPS DATA AND VALIDATION

In this work, the GPS VTEC measurements are determined using data from the Malaysia Department of Surveying and Mapping (JUPEM), International GNSS Service (IGS) and GPS Array (SUGAR) networks. The VTEC measurements using the method described in Section 3.3.2 are validated with those obtained from the Global Ionospheric Map (GIM). The sections are discussed as follows:

3.5.1 Data sets

GPS data obtained from 12 sets of dual-frequency permanent GPS receiver stations surrounding the earthquake epicenters are collected to examine the ionospheric disturbances before and during the 2004-2007 earthquake events in Sumatra. Table 3.4 provides the geographic and geomagnetic coordinates and instrument setup of these receivers. Among these, only BAKO, COCO, NTUS and SAMP stations belong to the International GNSS Service (IGS), BSAT and PSKI are stations of the Sumatran GPS Array (SUGAR) network, while the remaining six stations belong to the Malaysian Mapping and Surveying Department (JUPEM) network. The GPS data at stations belonging to the IGS and SUGAR networks are obtained online from the SOPAC data archive (SOPAC 2009), in which the RINEX observation files use the Hatanaka (d-file) compression format and were processed with 30 seconds interval. Meanwhile, the GPS raw data of the JUPEM network stations were supported by JUPEM and were processed into RINEX files with 30 seconds interval.

Table 3.4 The geographic and geomagnetic coordinates and instrument setup of the GPS receivers

Station and Country	ID	Coordinate		Receiver and year of installation	Antenna and year of installation
		Geographic	Geomagnetic[a]		
Arau (Malaysia)	ARAU	6.50°N, 100.28°E	2.14°S, 171.79°E	TRIMBLE 4000SSI (1998-2006) TRIMBLE NETR5 (2007)	TRM29659.00 (1998-2006) TRM55971.00 (2007)
Bakosurtanal (Indonesia)	BAKO	6.49°S, 106.85°E	16.07°S, 178.17°E	TRIMBLE 4000SSE (1998)	TRM14532.00 (1998)
Bulasat (Indonesia)	BSAT	3.08°S, 100.28°E	12.58°S, 171.61°E	ASHVTECH MICROZ (2002)	ASH701945B_ M SCIT (2002)
Cocos Island (Australia)	COCO	12.19°S, 96.85°E	22.82°S, 167.50°E	ASHVTECH UZ-12 (1996)	AOAD/M_T (1996)
Geting (Malaysia)	GETI	6.22°N, 102.11°E	2.33°S, 173.59°E	TRIMBLE 4000SSI (1998-2006) TRIMBLE NETR5 (2007)	TRM22020.00+ GP (1998-2006) TRM55971.00 (2007)
Kement. Tanah Pemb. & Kooperasi (Malaysia)	KTPK	3.16°N, 101.72°E	5.67°S, 173.18°E	TRIMBLE 4000SSI (1998-2006)	TRM29659.00 (1998-2006)
Langkawi (Malaysia)	LGKW	6.33°N, 99.85°E	2.29°S, 171.36°E	TRIMBLE 5700 (2005)	TRM41249.00 (2005)
Nanyang VTECh. Uni. of Singapore (Singapore)	NTUS	1.36°N, 103.69°E	7.56°S, 175.12°E	AOA SNR-12 ACT (1997-2006) LEICA CRS1000 (2007)	AOAD/M_T (1997-2006) LEIAT504 (2007)
Pulau Sikuai (Indonesia)	PSKI	1.12°S, 100.35°E	10.41°S, 171.72°E	ASHVTECH MICROZ (2002)	ASH701945B_ M SCIT (2002)
Sampali (Indonesia)	SAMP	3.62°N, 98.70°E	5.28°S, 170.18°E	ASHVTECH Z-XII3 (2000-2006) ASHVTECH UZ-12 (2007)	ASH700936 (2000)
Univ. Sains Malaysia Penang (Malaysia)	USMP	5.36°N, 100.30°E	3.34°S, 171.80°E	TRIMBLE 4000SSI (1998-2006)	DORNE MARGOLIN TRIM (1998-2006)
Univ. Teknologi Malaysia (Malaysia)	UTMJ	1.56°N, 103.64°E	7.34°S, 175.07°E	TRIMBLE 4000SSI (1998-2006)	TR GEOD L1/L2 GP (1998-2006)

[a] The geographic-geomagnetic coordinate conversion tool obtained from the UK solar system data center (http://www.wdc.rl.ac.uk/cgi-bin/wdcc1/coordcnv.pl), based on the Altitude Adjusted Corrected Geomagnetic Coordinate System (AACGM)
Source: http://sopac.ucsd.edu

3.5.2 Validation of VTEC Measurements

The GPS VTEC measurements determined with the method described by Warnant and Pottiaux (2000) is validated with the measurements of the Global Ionospheric Maps (GIM) in IONEX format. The GIM VTEC is determined using the IONEX data, which is obtained online from the CODE database (CODE 2010). It is generated by the IGS community with resolution of 5° in longitude and 2.5° in latitude and time interval of 2 hours. The GIM VTEC provides the possibility to monitor the ionospheric changes of different origins continuously and globally with high accuracy and reliability. The VTEC over the reference station is extracted from the interpolation for every 2 hour interval. Figure 3.3 presents the comparison between the VTEC measurement at NTUS station and the GIM VTEC obtained from CODE over the coordinate of NTUS station between 20 and 26 December 2004 and the regression plot of both VTEC measurements. As shown in Figure 3.3(b), both VTEC measurements calculated using different techniques show a good correlation of 92% with 95% confidence level.

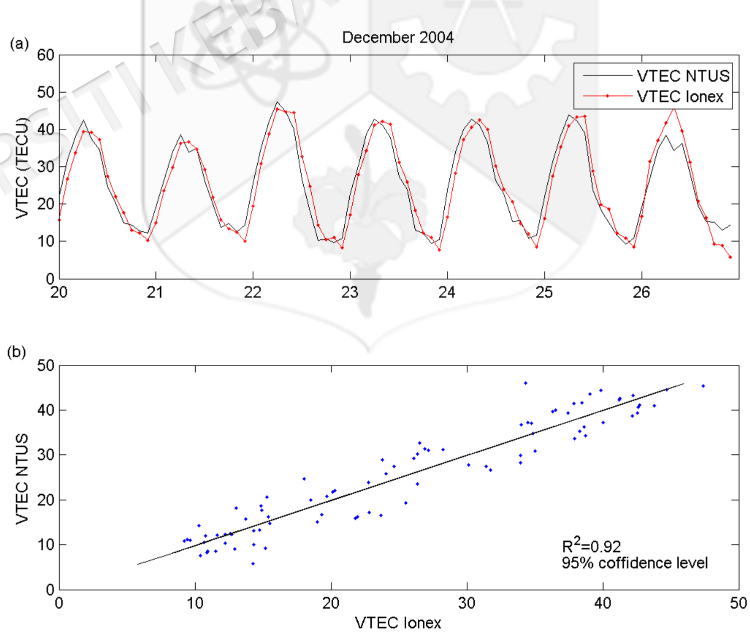

Figure 3.5 (a) GPS VTEC determined by Warnant and Pottiaux (2000) and CODE GIM VTEC measurements between 21 and 26 December 2004 over the coordinate of NTUS station and (b) regression plot of both VTEC measurements.

3.6 STATISTICAL ANALYSIS TECHNIQUES USING GPS VTEC

3.6.1 Envelope Method

To identify the ionospheric response to earthquake preparation using the envelope method, the median of the GPS VTEC for the previous 15 days and the associated standard deviation, σ are utilized to construct the upper and lower bounds of the inter-quartile range (IQR). These bounds are computed during the earthquake periods to better separate seismic anomalies from natural and seasonal variations (Liu et al. 2004). Under the assumption of a normal distribution, the IQR is 1.34σ. The upper and lower bounds can be determined using the following formulae:

$$IQR_{UB} = VTEC_{median} + 1.34\sigma \tag{3.22}$$

$$IQR_{LB} = VTEC_{median} - 1.34\sigma \tag{3.23}$$

where

$VTEC_{median}$: the 15-day running median and

σ : the associated standard deviation.

If an observed VTEC exceeds either the associated upper or lower bound, a positive or negative anomaly is detected, respectively with a confidence level of 80-85% (Liu et al. 2004).

3.6.2 Percentage of VTEC deviation (ΔVTEC%)

In the analysis of Chapters V and VI, the percentage of VTEC deviation (ΔVTEC%) with respect to both lower and upper bounds defined in (3.22) and (3.23) is computed during the months of the earthquake events. This index gives information about the positive and negative phases that occur during the earthquake period and can be obtained using the following equations (Dabas et al. 2007; Sharma et al. 2008):

$$\Delta TEC\%\ (\text{positive}) = \frac{\text{TEC - IQR}_{\text{UB}}}{\text{IQR}_{\text{UB}}} \times 100 \tag{3.24}$$

If VTEC $\leq$ IQR_{UB}, then ΔVTEC% (positive) = 0

$$\Delta TEC\%\ (\text{negative}) = \frac{\text{TEC - IQR}_{\text{LB}}}{\text{IQR}_{\text{LB}}} \times 100 \tag{3.25}$$

If VTEC $\geq$ IQR_{LB}, then ΔVTEC% (negative) = 0

In this analysis, the ΔVTEC% is computed based on a 15-minute average VTEC in order to reduce computation time. In this work, the geomagnetic and solar data, obtained from the WDC and NOAA databases, respectively were examined during the months of earthquakes. To rule-out the possibility of an irregular VTEC detection during moderate geomagnetic and high solar activity, the hourly ΔVTEC% values for $|Dst|>15$ nT, $Kp>4$ and $F10.7>150$ are filtered out from the analysis. For more accurate detection, ΔVTEC% values during days with moderate geomagnetic activity ($Dst<-50$ nT) are also removed from the analysis.

To obtain the number of the irregular VTEC detections for the entire study period, which is from July 2004 - June 2006 and September 2007, the envelope method is applied to the ΔVTEC% time series at ARAU, USMP, UTMJ, NTUS, PSKI, BSAT and COCO stations. The detection is defined as the sum of weighted detections in (3.26):

$$N_{weighted}(t) = \sum_{1}^{k} N_{station}(t) \tag{3.26}$$

where

$N_{weighted}(t)$: the total number of weighted ΔVTEC% detections per day

k : number of stations

$N_{station}(t)$: the number of detections of ΔVTEC% per station per day

3.6.3 Correlation Analysis Technique

This correlation analysis technique is built on the concept of the earthquake preparation zone, which is described earlier in Chapter II. The idea of this technique is based on the fact that geomagnetic storms have global effects, whereas seismic-ionospheric coupling variations are characterized by their local behavior in that they appear only inside the earthquake preparation area. Thus, the ionospheric behavior between the two ionospheric stations is expected to be the same during geomagnetic storms, hence the correlation coefficient will be high during this time. However, the correlation coefficient is expected to drop in the presence of precursory signals at the location where the epicenter is closer to one of the two stations. The two ionospheric stations should be very close in latitude to ensure the similarity of their reaction to geomagnetic storms and they should not differ too much in longitude due to the Local Time (LT) dependence of ionospheric variability (Pulinets et al. 2004). Figure 3.4 presents a diagram of two receiver stations' position and earthquake preparation area according to the correlation analysis technique.

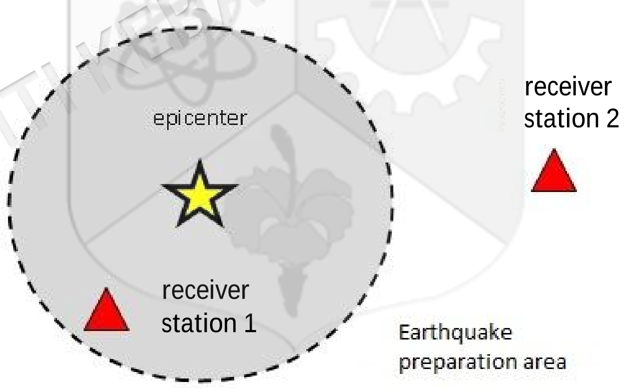

Figure 3.4 Diagram of the receiver station position and earthquake preparation area according to the correlation analysis technique.

Source: Pulinets et al. (2004)

In this technique, the GPS VTEC measurements between two stations, in which the one located inside the earthquake preparation area is cross correlated with the other station located outside it. In order to eliminate the diurnal variation of VTEC, the VTEC measurements are normalized by using the following equation:

$$\text{TEC}_{\text{norm}} = \frac{\text{TEC-TEC}_{\text{monthly median}}}{\text{TEC}_{\text{monthly median}}} \quad (3.27)$$

The normalized VTEC measurements are then cross correlated between two stations to obtain the correlation coefficient variability during the entire observation period. The calculation of daily correlation coefficient is calculated as follows (Pulinets et al. 2004):

$$\rho = \frac{\sum_{i=0,k} \left(TEC_{1,i} - \overline{TEC_1} \right) \left(TEC_{2,i} - \overline{TEC_2} \right)}{k\left(\sigma_1 \sigma_2\right)} \quad (3.28)$$

whereby

$VTEC_1$, $VTEC_2$: VTEC measurements corresponding to the first and second ionospheric stations, respectively.

$\overline{TEC}_1$, $\overline{TEC}_2$: the daily VTEC mean of each station.

σ_1, σ_2 : the daily standard deviation of each station

k : the number of records for each day.

The daily mean and standard deviation are given in (3.29) and (3.30):

$$\overline{TEC} = \frac{\sum_{i=0,k} TEC_i}{k+1} \quad (3.29)$$

$$\sigma^2 = \frac{\sum_{i=0,k} \left(TEC_i - \overline{TEC_i} \right)^2}{k} \quad (3.30)$$

3.6.4 Regional Ionospheric Variability Index

The ionospheric variability index method is based on the concept of the earthquake preparation zone. This parameter is useful for estimating the spatial ionospheric variability by describing the VTEC variability over a region. The variability index is calculated by taking the difference of maximum and minimum of VTEC hourly values of any two stations considered in this study (Pulinets et al. 2007). The maximum and minimum differences of VTEC hourly values are given in (3.31) and (3.32), respectively:

$$\Delta TEC_{\max} = \max\left\{TEC_{1,i} - TEC_{2,i}\right\}_{i=0,k} \tag{3.31}$$

$$\Delta TEC_{\min} = \min\left\{TEC_{1,i} - TEC_{2,i}\right\}_{i=0,k} \tag{3.32}$$

whereby the index *i* corresponds to the hour of the day. For all the mentioned statistical methods, only the VTEC hourly values that fall under quiet geomagnetic conditions with |Dst|>15 nT, Kp>4 and F10.7>150 are considered in the analyses.

3.7 MAGNETOMETER MEASUREMENTS

Magnetometers measure the local strength and direction of the geomagnetic field, as well as the electric currents in the upper atmosphere and in near-Earth space (Almomani 2007). Magnetometers are generally categorized into two parts that are classed by their methods of calibration; the absolute and relative. Absolute magnetometers measure the magnitude of the magnetic field or its component in absolute physical units, while relative magnetometers measure the deviation from a reference to a determined, absolute magnetic field measurement (Jankowski & Sucksdorff 1996). The geomagnetic field observed all over the globe is a vector field. Three components of the total field intensity vector, ***F*** are needed to describe the field, which are the *X*, *Y* and *Z* components as shown in Figure 3.5.

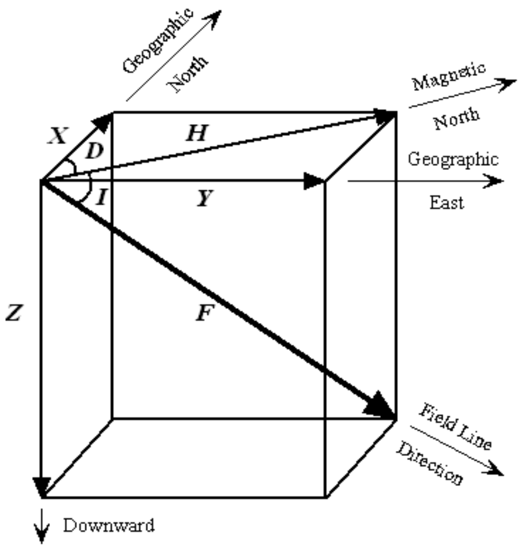

Figure 3.5 Diagram of geomagnetic field components

Source: Jankowski & Sucksdorff 1996

Geomagnetic field measurements are normally represented either in *HDZ* or *XYZ* coordinates. The elements of the *XYZ* representation include the north-south component (*X*), east-west component (*Y*) and vertical component (*Z*). In the case of the *HDZ* representation, *H* is the horizontal component of the local magnetic meridian (positive direction towards the magnetic north), *D* is the magnetic declination or the angle between the geographic north direction and the magnetic meridian and *Z* is the vertical component. The relations between the components are expressed by the following formulae (Jankowski & Sucksdorff 1996):

The total field intensity, *F*:

$$F = \sqrt{X^2 + Y^2 + Z^2} = \sqrt{H^2 + Z^2} \tag{3.33}$$

whereby the *X*, *Y* and *Z* components are expressed by (3.34):

$$X = H\cos D, \qquad Y = H\sin D \qquad , Z = F\sin I = H\tan I \tag{3.34}$$

and the horizontal component, *H* the declination, *D* are defined in (3.35) and (3.36):

$$H = \sqrt{X^2 + Y^2} \tag{3.35}$$

$$D = \tan^{-1}\left(\frac{Y}{X}\right) \tag{3.36}$$

The angle that the total field intensity, F makes with the horizontal plane, H is called the inclination, I or the dip angle (Campbell 2003):

$$I = \tan^{-1}(Z / H) \tag{3.37}$$

There are many types of magnetometers used for continuous magnetic field measurements namely overhauser, fluxgate, induction type, proton precession, torsion and optical pumped magnetometers (IRF 2009). Fluxgate magnetometers are the most popular magnetic instruments at modern digital observatories due to their robust construction, reliable electronics and precision level (Jankowski & Sucksdorff. 1996). In this work, the ground-based magnetometer data from Kototabang (KTB), Phu Thuy (PHU), Zhaoqing (GZH), Kakadu (KDU) and Lanzhou (LZH) stations are employed. Table 3.5 provides the geographic and geomagnetic coordinates, types of measurement and instrument setup at these stations. The 1 second data from KTB station are supported by the Solar-Terrestrial Environment Laboratory, Nagoya University, Japan while the 1 minute corrected data from the remaining stations are obtained online from the INTERMAGNET database (http://www.intermagnet.org). The 1 second data from KTB station are pre-processed to remove outliers that are considered as irregular signals. To identify these outliers, the difference of the geomagnetic field values for each second is computed followed by setting a threshold of ±0.5 nT. Only the geomagnetic field values that lie within the threshold are regarded as usable data, while the rest are filtered out.

Table 3.5 The geographic and geomagnetic coordinates, type of measurement and instrument setup of the magnetometer stations.

Station (Country)	ID	Coordinate		Measurement	Instrument (year of installation)
		Geographic	Geomagnetic[a]		
Kototabang (Indonesia)	KTB	0.20°S, 100.32°E	10.63ºS, 171.93°E	*HDZ*	Fluxgate magnetometer (2003)
Kakadu (Australia)	KDU	12.60°S, 132.50°E	22.09 ºS, 204.47 ºE	*XYZ*	Fluxgate and Proton Precession magnetometers (2000)
Lanzhou (China)	LZH	36.10°N, 103.80°E	30.21°N, 175.87°E	*XYZ*	DI-fluxgate and Overhauser effect proton scalar magnetometers (2002)
Phu Thuy (Vietnam)	PHU	21.03°N, 105.96 °E	13.85°N, 177.52°E	*XYZ*	DI-fluxgate and Overhauser effect proton scalar magnetometers (1996)
Zhaoqing (China)	GZH	23.00°N, 112.50°E	16.01°N, 184.05°E	*HDZ*	DI-fluxgate and Overhauser proton precession magnetometers (2003)

[a] The geographic-geomagnetic coordinate conversion tool obtained from the UK solar system data center (http://www.wdc.rl.ac.uk/cgi-bin/wdcc1/coordcnv.pl), based on the Altitude Adjusted Corrected Geomagnetic Coordinate System (AACGM)

3.8 CHAMP SATELITE DATA

The CHAllenging Mini-satellite Payload (CHAMP) is a German small satellite mission for geoscientific and atmospheric research and applications, managed by the GFZ German Research Centre for Geosciences (GFZ 2010). CHAMP satellite is in almost circular and near polar orbit with an altitude of about 450 km. The satellite moves in the meridional direction almost at the height of the ionospheric electron concentration maximum. In addition to the ground-based GPS VTEC measurements, the satellite-based electron density (N_e) data obtained by a planar Langmuir probe onboard the CHAMP satellite are also used to study the pre-earthquake ionospheric perturbations in Chapter V. In the analysis, the corrected electron density variations with 15 seconds sampling values along the longitude range of 90-120°E during a few days before the earthquakes are examined.

3.9 MAGNETIC AND SOLAR CONDITIONS BEFORE AND DURING EARTHQUAKE PERIODS

It is difficult to detect the disturbances coming from the Earth's surface at ionospheric level under strong solar and magnetic activity. The measurements of ionospheric disturbances induce by earthquakes can be corrupted by strong solar and magnetic activities. Therefore, it is necessary to examine whether the earthquakes occurred during low or strong geomagnetic and solar conditions. The geomagnetic and solar data as well as the interplanetary magnetic field of the Bz component, which are obtained from the WDC, NOAA and CDAWeb databases, respectively were analyzed for the period between ten days and a day after the Sumatran earthquake events of 26 December 2004, 26 February 2005, 28 March 2005, 24 July 2005 and the 12 September 2007.

3.9.1 The December 2004 Earthquake

Figure 3.6 presents the disturbance storm time (Dst) index, auroral electrojet (AE), interplanetary magnetic field of the z-component (IMF Bz), geomagnetic Ap and Kp, and solar indices, F10.7 and SSN for the period between 16 and 27 December 2004. The vertical dashed line in the figure marks the time of the 26 December 2004 earthquake, which is at 00:58 UT. The horizontal dashed line shows the threshold value of the Dst, AE, Bz, Kp, Ap, F10.7 and SSN indices defined for this study, which are ±15 nT, 100 nT, -5 nT, 4, 7, 150 and 150, respectively (Dabas et al. 2007; Consolini et al. 2002; Kumar et al. 2005; WDC 2006; Davies et al. 1999). As shown in this figure, the AE index from 16 to 18 December shows increased intensification of up to 400 nT, while strong fluctuations were observed in the IMF Bz. During this period, Dst gradually decreased and exceeded the threshold value, simultaneous with the enhancements in the Kp and Ap indices. The geomagnetic levels during the days of 19 and 20 December were quiet. The period from 21-22 December showed moderate geomagnetic activity due to coronal hole wind streams (IPS 2008). On 21 December, a sudden enhancement of Dst (24 nT) was seen at 7:00 UT followed by a sudden decrease to -21 nT at 10:00 UT. Significant intensifications in the AE index, fluctuations in the Dst and enhancements in the Kp and Ap were also observed during this day almost simultaneously and this condition persisted until the following day. The direction of the interplanetary magnetic field, IMF B_z on 21 and 22 December 2004 turn from northward to southward (Bz<0) for a short time period and with a minimum value of -7 nT. On 23 December, the Dst value gradually increased to its normal level until the day before the earthquake. The geomagnetic level on the day prior to the event (25 December) was classified as "quiet to unsettled" by IPS, as fluctuations were seen in the IMF Bz and slight enhancements were found in the AE and Kp indices. Meanwhile, the period prior to the event, i.e. between 16 and 25 December 2005 were classified as very low solar activity as reported by IPS. The readings of solar indices, 10.7 cm solar flux (F10.7) and sun spot number (SSN) for the days between 16 and 25 December 2004 range from 92-101 and 11-47, respectively.

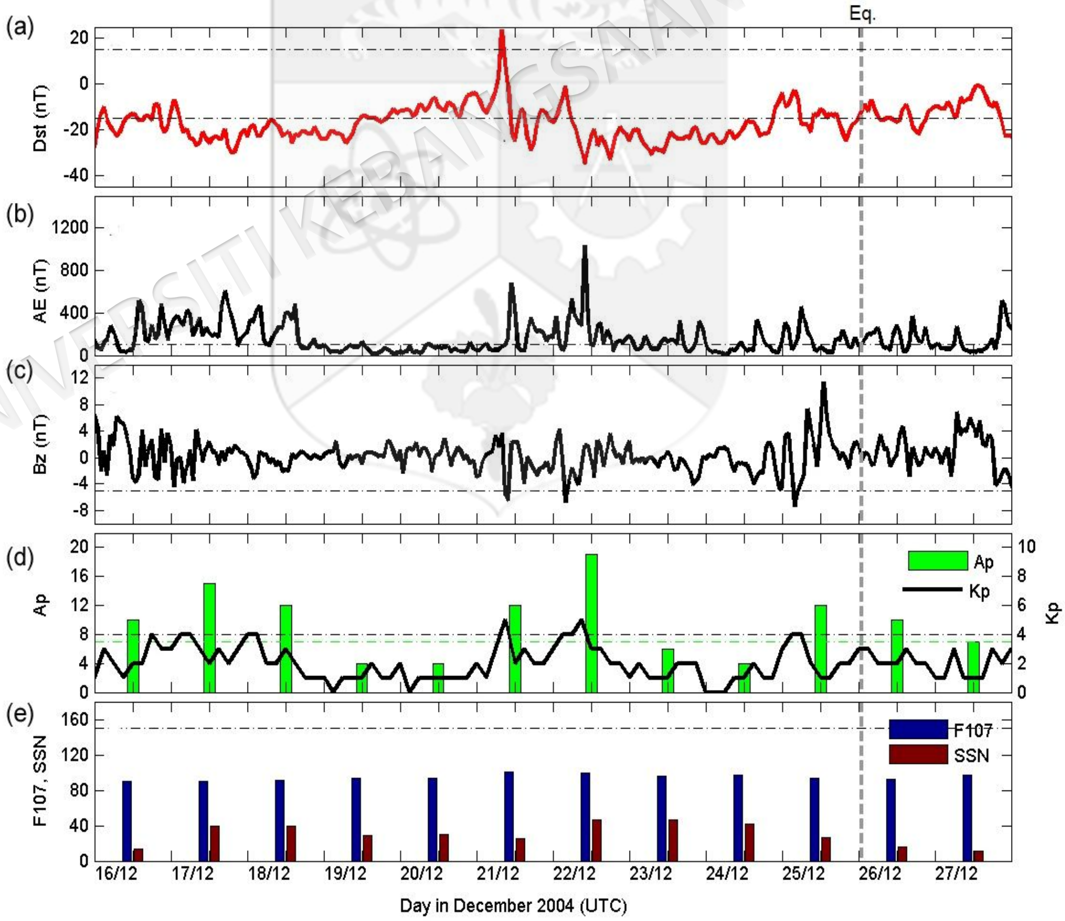

Figure 3.6 The Dst, AE, IMF Bz, Ap, Kp, F10.7 and SSN indices between 16 and 27 December 2004. The vertical dashed line shows the time of the earthquake.

The geomagnetic conditions for both days on 26 and 27 December 2004 were classified as “quiet to unsettled” (IPS 2008). During the time of the earthquake, the geomagnetic indices Dst, Kp and Ap record values of -12 nT, 3 and 10, respectively. The interplanetary magnetic field, IMF B_z during this time records a value of -0.58 nT, and reach a daily minimum of -2.80 nT. The period from 26 to 27 December 2004 was characterized by very low solar activity as reported by IPS. The readings of solar indices, 10.7 cm solar flux and sun spot number (F10.7/SSN) for the day during and after the event are 92/16 and 97/11, respectively.

3.9.2 The February 2005 Earthquake period

Figure 3.7 shows the plots of geomagnetic and solar indices of Dst, AE, IMF Bz, Ap, Kp, F10.7 and SSN between 16 and 27 February 2005. The 26 February 2005 earthquake occurred at 12:56 UT, as marked in figure. As shown in the figure, the geomagnetic levels during the period between 16 and 21 February were characterized as disturbed. During this period, a series of sudden decreases in the Dst index, which largely exceeded the threshold value was observed. The decreases in Dst coincide with the large enhancements in the AE index, the southward turning of the IMF Bz and enhancements in the Kp and Ap values. Meanwhile, the geomagnetic conditions during days of 22 and 23 February were characterized as quiet, as the Dst values did not exceed the threshold value and no significant enhancements were observed in the geomagnetic indices. Following this day, the AE started to intensify again, simultaneous with the fluctuation in the IMF Bz and this condition persisted until the day prior to the event. In contrast with geomagnetic conditions, the solar activity during the period prior to the earthquake is characterized as low (IPS 2008). The values of F10.7 and SSN for the days between 16 and 25 February 2005 range from 76-113 and 12-60, respectively.

During the 26 February 2005 earthquake, the geomagnetic indices Dst, Kp and Ap record values of -9 nT, 3 and 9, respectively, while the IMF Bz and AE record values of -1.54 nT and 146 nT, respectively. The period from 26 to 27 February 2005 was classified as very low solar activity and the observed geomagnetic field levels on both days were classified as “quiet to unsettled”. The solar indices F10.7 and SSN for the day of the earthquake and the following day were 77/27 and 76/12, respectively.

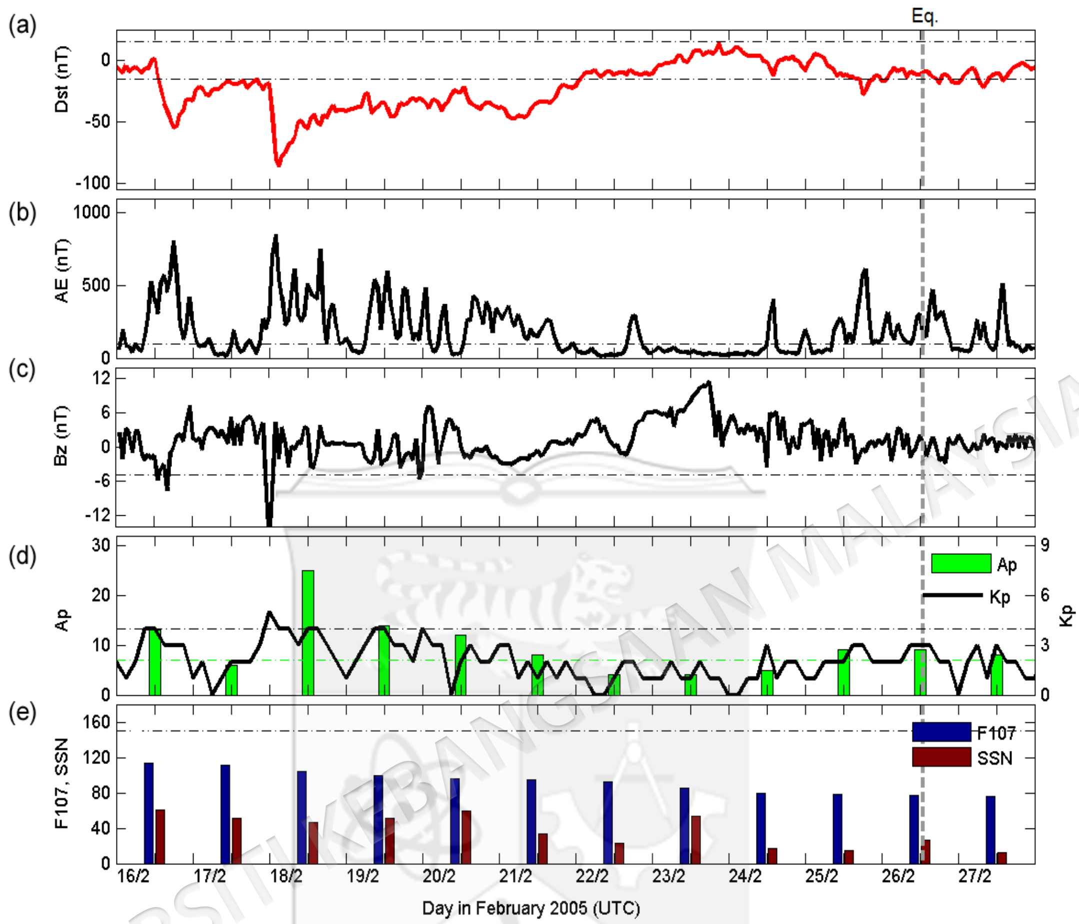

Figure 3.7 The Dst, AE, IMF Bz, Ap, Kp, F10.7 and SSN indices between 16 and 27 February 2005.

3.9.3 The March 2005 Earthquake period (21-29 March 2005)

The period from 18 to 29 March 2005 was characterized by very low solar activity as reported by IPS. Figure 3.8 shows the plot of Dst, IMF Bz, Ap, Kp, F10.7 and SSN indices for 10 days before, during and a day after the earthquake. In this figure, the time of the earthquake is marked by the vertical dashed line, which is at 16:09 UT. As shown in the figure, the period between 18 and 21 March 2005 was geomagnetically disturbed as the Dst values fall below the threshold value, simultaneously with the southward turning of IMF Bz (-6 nT) and enhancements in the AE, Kp and Ap indices. However, the geomagnetic condition from 22 to 24 March was observed to be very quiet, followed by a sudden decrease in the Dst and IMF Bz, intensifications in the AE and enhancements in the AE and Kp values from 25-27 March. Following this time, the geomagnetic level returns to its normal state about a few hours prior to the event. The values of F10.7 and SSN for the days between 18 and 27 March 2005 range from 78-96 and 35-65, respectively.

At the time of the earthquake, the geomagnetic indices Dst, Kp and Ap record values of -17 nT, 1 and 4, respectively. The observed geomagnetic field levels for this period as classified by IPS were "quiet" on 28 and 29 March 2005, respectively. The IMF Bz and AE indices record values of 1.56 nT and 53 nT, respectively at the time of the earthquake. The readings of solar indices (F10.7/SSN) for the day of the earthquake and the following day were 80/15 and 79/15, respectively.

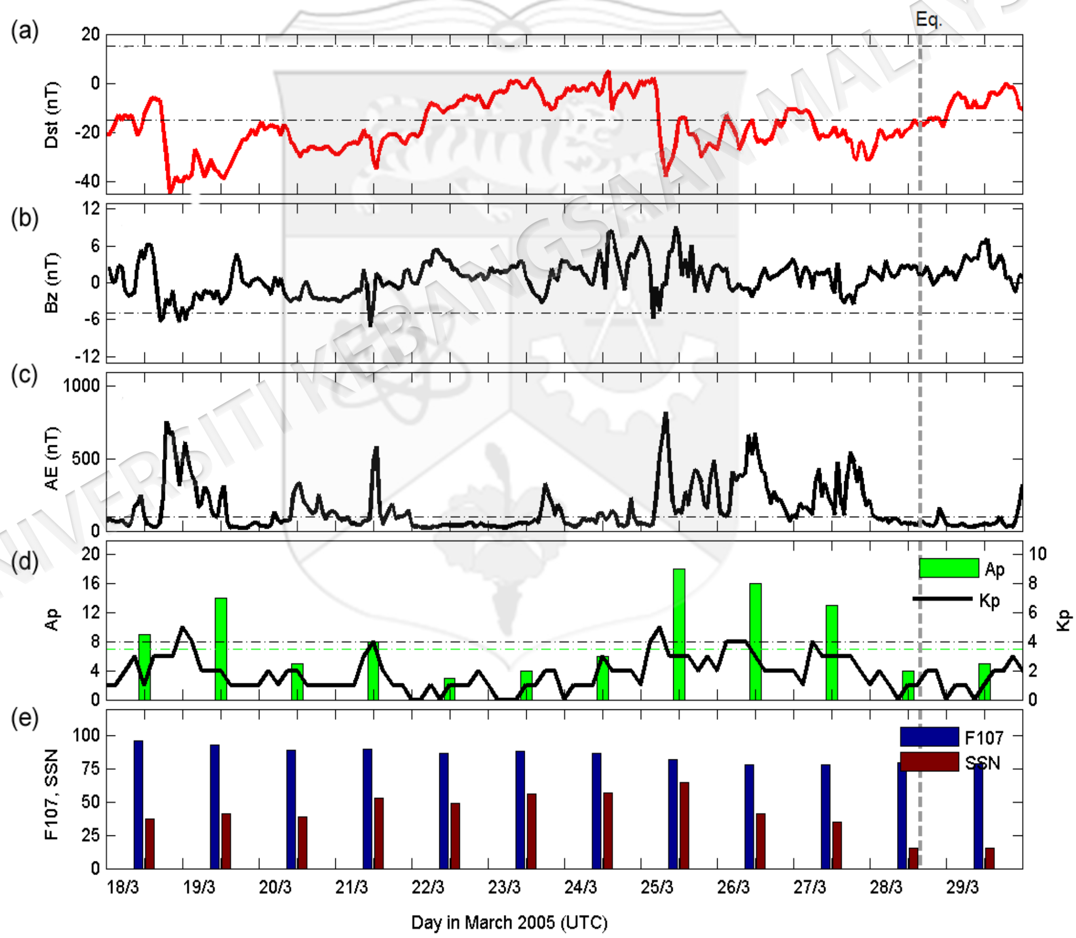

Figure 3.8 The Dst, AE, IMF Bz, Ap, Kp, F10.7 and SSN indices between 18 and 29 March 2005.

3.9.4 The July 2005 Earthquake period

Figure 3.9 presents the geomagnetic and solar indices for the period from 14 to 25 July 2005. The 24 July 2005 earthquake occurred in Nicobar Island, India at 15:42 UT with a magnitude of 7.2, as marked in the figure by the vertical dashed line. The period prior to the event was classified as very low solar activity except for days of 14 July, whereby the solar activity was classified as high by IPS. A minor storm occurred on 18 July with a Dst minimum of -76 nT and Kp and Ap values of 6 and 34, respectively (WDC 2007). During this time, the AE index shows large enhancements of up to 1000 nT, while the IMF Bz fluctuated strongly between negative and positive values of about 3-15 nT, indicating a disturbed geomagnetic period. This condition continues until about a day prior to the earthquake, when the geomagnetic indices gradually return to their normal values. During the period between 14 and 23 July 2005, the solar indices F10.7 and SSN values range from 71-90 and 0-16, respectively.

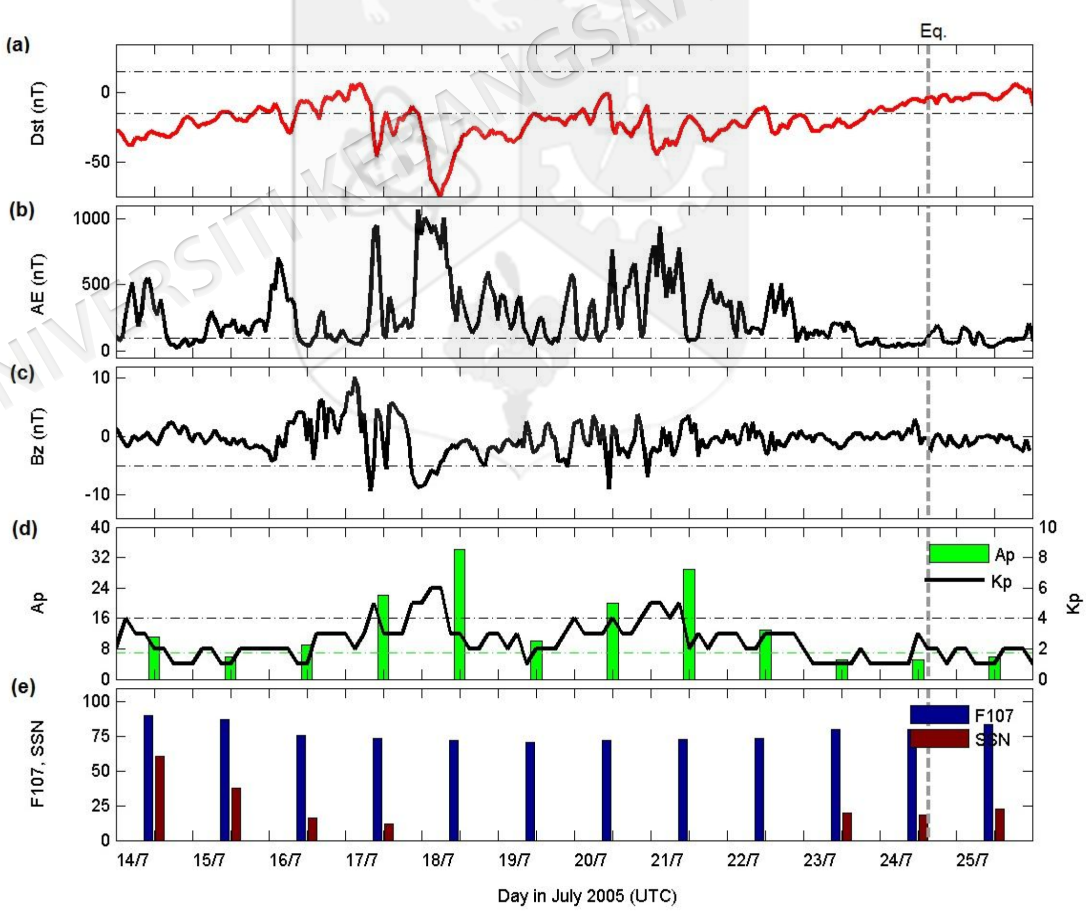

Figure 3.9 The Dst, IMF Bz, Ap, Kp, F10.7 and SSN indices between 14 and 25 July 2005.

During the time of the 24 July 2005 earthquake, the Dst, Kp and Ap indices record values of -4 nT, 2 and 5, respectively, while the IMF Bz and AE at the time of the event are -0.36 nT and 94 nT. Meanwhile, the solar indices (F10.7/SSN) on 24 and 25 July 2005 record values of 80/18 and 84/23, respectively.

3.9.5 The September 2007 Earthquake period

Figure 3.10 presents the geomagnetic and solar indices for the period from 2 to 13 September 2007. As shown in this figure, two earthquakes occurred on 12 September 2007, which are the M8.5 earthquake at 11:10 UT and the M7.9 earthquake at 23:49 UT. The period between 6 and 11 September 2007 were characterized by very low solar activity as reported by IPS.

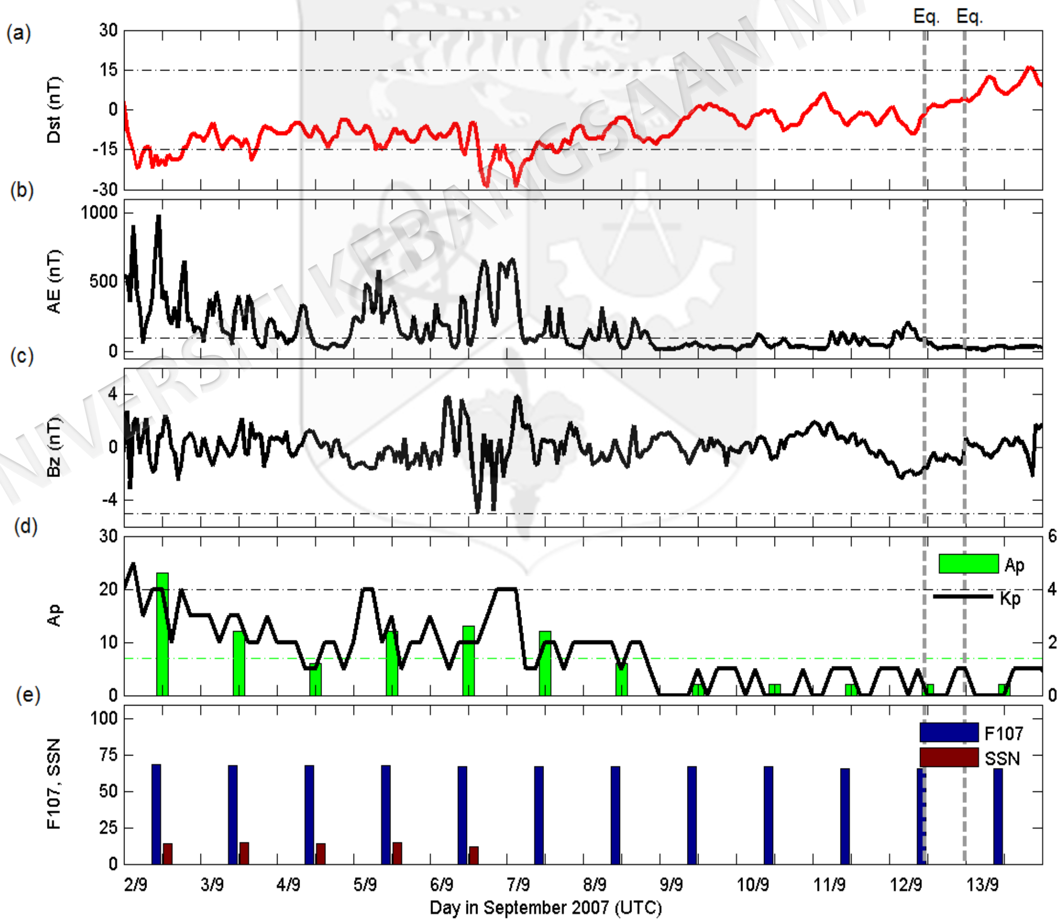

Figure 3.10 The Dst, AE, IMF Bz, Ap, Kp, F10.7 and SSN indices between 2 and 13 September 2007.

As shown in Figure 3.10, the geomagnetic levels during the period between 2 and 8 September 2007 were disturbed with significant intensifications in the AE index. On 6 September 2007, a sudden storm commencement (SSC) was observed in the Dst and IMF Bz indices, followed by a sudden decrease reaching -29 and -5 nT, respectively. During this time, the Dst and Kp indices exceeded their threshold values and significant intensifications in the AE index were also seen. However, the geomagnetic condition from 3 days to a few hours before the 12 September earthquake events was characterized as quiet as no pronounced geomagnetic activity was found. Meanwhile, the F10.7 and SSN values for the period between 6 and 11 September 2007 range from 66-67 and 0-12, respectively.

During both the M8.5 and M7.9 earthquakes on 12 September 2007, the readings of Dst, Kp and Ap indices are -2 nT/1/2 and 4 nT/1/2, respectively. The IMF Bz and AE values during the time of these events are -1.48/95 nT and -0.93/29 nT, respectively. It was observed that the geomagnetic level on the day of the two events was characterized as quiet, as also classified by IPS. Meanwhile, the solar indices (F10.7/SSN) on 12 and 13 September 2007 both record values of 66/0.

3.10 SUMMARY

An overview of the GPS measurement system, including its pseudorange and carrier phase observables and their main error sources were presented in this chapter. This chapter also presented the methodology of the total electron content calculation using ground-based GPS measurement technique, data processing method as well as the employment of three statistical analysis methods using GPS VTEC measurements. Additional measurements such as the ground-based magnetometer and CHAMP satellite techniques were also described. The magnetic and solar conditions during periods of large earthquake events will be used to interpret the coseismic and pre-earthquake GPS VTEC disturbances, which will be investigated in the Chapters IV and V.

CHAPTER IV

INVESTIGATION OF IONOSPHERIC AND MAGNETIC DISTURBANCES DURING EARTHQUAKES

This chapter investigates the ionospheric and geomagnetic responses during the 26 December 2004, 28 March 2005, 14 May 2005 and 12 September 2007 Sumatra earthquakes using GPS and magnetometer measurements in the near zone of the epicenters. It also attempts to correlate the ionospheric and magnetic disturbances using filtering techniques. Firstly, a method for correlating ionospheric and magnetic disturbances is introduced. Both GPS VTEC obtained from all satellites and the VTEC along individual satellite passes during the earthquake events are analyzed. Following that, the geomagnetic variations and pulsations obtained from ground-based magnetometer measurements are analyzed. The correlation between the ionospheric GPS VTEC and magnetic responses to the earthquake events is also presented. Finally, the chapter ends with discussion and conclusion.

4.1 PROPOSED METHOD FOR CORRELATING IONOSPHERIC AND MAGNETIC DISTURBANCES

To investigate the ionospheric and geomagnetic responses during the earthquake events, the filtration technique is used on both GPS VTEC and magnetic field measurements. In the analysis of the VTEC along individual satellite passes, the moving-mean filter is employed using a method derived by Afraimovich et al. (2001). In this method, the VTEC time series during the earthquake observation periods is smoothed by averaging over a sliding window of 5 minutes and filtered in the range of 2-10 minutes. The purpose of this procedure is to eliminate effects of the regular ionosphere, such as temporal variations and trends introduced by the orbital motion of the satellite (Afraimovich et al. 2001). This will result in a single-pulse, N-wave, which is caused by shock waves traveling in air (Kanamori et al. 1991). With respect to the filtration period used in this analysis, only GPS measurements with 30-second sampling intervals are considered.

In the magnetic field analysis, the variations of the geomagnetic horizontal (H), declination (D) and vertical (Z) components and the geomagnetic pulsation are examined. In the geomagnetic pulsation analysis, the same type of pulsations observed by Iyemori et al. (2005), which the short period Pc3 and the long period Pc5 pulsation have been selected. The Pc3 pulsation is in the frequency range between 22.22 and 100 mHz, while the range of Pc5 pulsation is between 1.67 and 4.67 mHz. To obtain these pulsations, the values of the geomagnetic measurements are filtered using a band-pass filter of Butterworth type for a period range of 10-45 seconds (Pc3) and 2.5-10 minutes (Pc5). The period range for the Pc5 pulsation corresponds with the one selected for the GPS VTEC analysis along individual satellite passes. The Pc5 pulsation is also used in the correlation analysis with the filtered GPS VTEC.

4.2 GEOGRAPHICAL LOCATION OF EARTHQUAKES

In the both studies of ionospheric and magnetic responses during earthquakes, and the short-term pre-earthquake ionospheric perturbation (Chapter V), several strong earthquakes with magnitude of M > 6.5 that took place surrounding the Sumatra region during the period of 2004-2007 are selected. These earthquakes ruptured along a 1200 km boundary between the Indian Plate and the Burma Microplate, which is considered part of the Eurasian Plate (Shapiro et al. 2008). Figure 4.1 presents the locations of the earthquake epicenters (star and circle) and GPS receiver stations (triangle), in geographic coordinates. As shown in the figure, the epicenters of these earthquakes are located along the subduction zone extending from the Andaman Trench in the northwest to the Sunda Trench in the southeast. The occurrence time, geographic coordinates, depth and magnitude of these events are presented in Table 4.1. The depths of the epicenter vary from 10 to 34 km. The analysis of co-seismic disturbances for events 1, 3, 4 and 6 will be presented in this chapter, while the analysis of pre-earthquake ionospheric perturbations for events 1, 2, 3, 5, 6 and 7 will be presented in Chapter V.

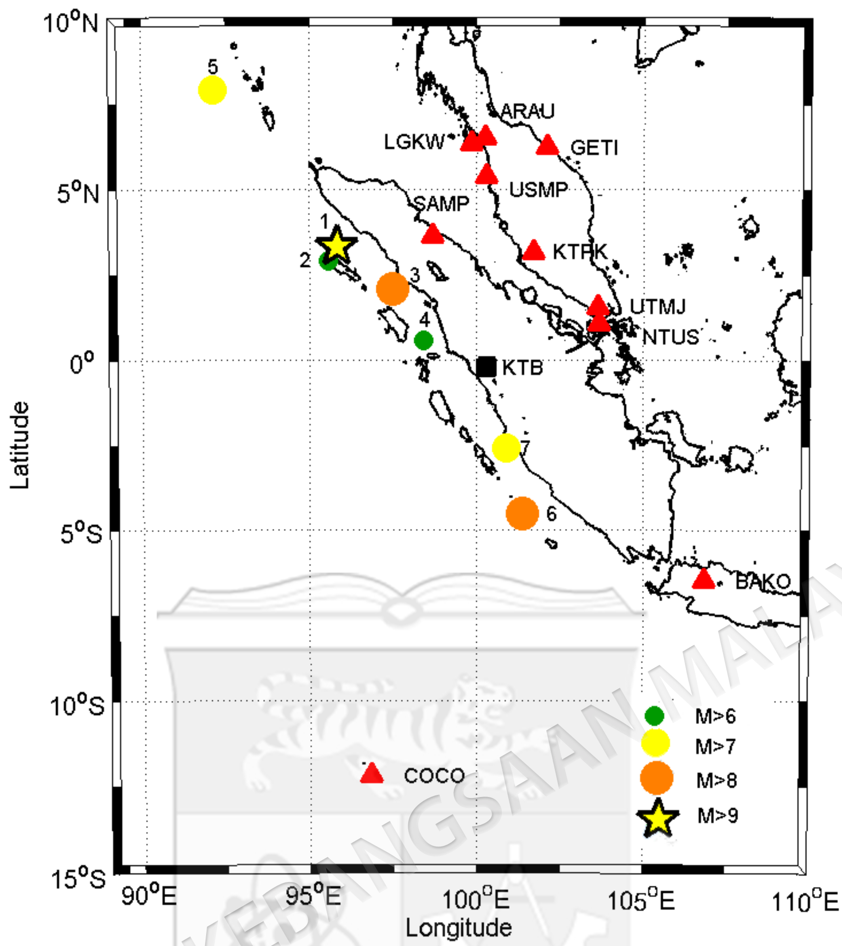

Figure 4.1 Geographic locations of the earthquake epicenters during the period of 2004-2007 (star and circle) and GPS receiver stations (triangle).

Table 4.1 The occurrence time, geographic coordinates, depth, magnitude and earthquake preparation radius of selected earthquake events during 2004-2007 (USGS 2009).

Event	Date	Time of earthquake (UT)	Place	Geographic Lat. (°)	Geographic Lon. (°)	Depth (km)	M
1	26.12.2004	00:58	North Sumatra	3.32°N	95.85°E	30	9.3
2	26.2.2005	12:56	Simuele	2.93°N	95.56°E	27	6.8
3	28.3.2005	16:09	North Sumatra	2.08°N	97.01°E	30	8.6
4	14.5.2005	5:05	Nias Region	0.59°N	98.40°E	34	6.8
5	24.7.2005	15:42	Nicobar Islands, India	7.91°N	92.14°E	16	7.2
6	12.9.2007	11:10	South Sumatra	4.52°S	101.37°E	34	8.5
7	12.9.2007	23:49	Kepulauan Mentawai	2.51°S	100.91°E	30	7.9

In this chapter, GPS data obtained from ten sets of dual frequency permanent GPS receiver stations and magnetometer station in the near zone of the earthquake epicenters are collected to examine the ionospheric disturbances during strong earthquake events over Sumatra. These GPS stations are SAMP, ARAU, USMP, LGKW, GETI, KTPK, NTUS, UTMJ, BAKO and COCO, while the magnetometer station is KTB. Table 4.2 presents the geographic and geomagnetic coordinates of the GPS and magnetometer stations and their distances from the epicenters.

Table 4.2 The geographic and geomagnetic coordinates of the considered GPS stations and their distances from the epicenters

GPS station	GG Coordinate	GM Coordinate[a]	Event 1	Event 2	Event 3	Event 4
			Distance from epicenter (km)			
SAMP	3.62°N, 98.70°E	5.28°S, 170.18°E	318	247	339	952
ARAU	4.50°N, 100.28°E	2.14°S, 171.79°E	606	602	690	-
USMP	5.36°N, 100.30°E	3.33°S, 171.80°E	543	-	-	1105
LGKW	4.33°N, 99.85°E	2.29°S, 171.36°E	555	568	659	-
GETI	4.22°N, 102.11°E	2.33°S, 173.59°E	764	656	750	1197
KTPK	3.16°N, 101.72°E	5.67°S, 173.18°E	-	537	-	-
NTUS	1.36°N, 103.69°E	7.56°S, 175.12°E	-	-	-	703
UTMJ	1.56°N, 103.64°E	7.34°S, 175.07°E	887	-	593	-
BAKO	4.49°S, 104.85°E	14.07°S, 178.17°E	-	1442	1144	-
COCO	12.19°S, 94.85°E	22.82°S, 167.50°E	1725	1698	1302	986
KTB[b]	0.20°S, 100.32°E	10.63ºS, 171.93°E	560	447	235	495

[a] UK solar system data center (http://www.wdc.rl.ac.uk/cgi-bin/wdcc1/coordcnv.pl)
[b] Magnetometer station

4.3 ANALYSIS OF IONOSPHERIC AND MAGNETIC VARIATIONS DURING EARTHQUAKES

This section investigates the GPS ionospheric disturbances in the near zone of the epicenters during the 26 December 2004, 28 March 2005, 14 May 2005 and 12 September 2007 earthquake events. In these analyses, both GPS VTEC obtained from all satellites and the VTEC along individual satellite passes during these events are analyzed. In this work, the GPS VTEC measurements for the day before and after the events are also examined to determine whether the ionospheric disturbance is caused by earthquake or due to other sources such as solar-terrestrial phenomena. Additionally, the geomagnetic measurements as well as the magnetic pulsations of Pc3 and Pc5 type in the H, D and Z components obtained from 1-second ground-based magnetometer measurements at KTB station during the earthquake events are also analyzed. The analyses are discussed as follows:

4.3.1 The 26 December 2004 Earthquake

a. Observations of ionospheric VTEC variations

The VTEC variations during the earthquake event on 26 December 2004 at seven GPS stations are presented in Figure 4.2. The vertical dashed line in the figure marks the time of event. As shown in the figure, the GPS VTEC obtained from all satellites show no clear coseismic ionospheric disturbances (CID) at all the seven stations. However, previous studies have reported occurrences of CID during the same event at stations in the near zone of the epicenter. Hence, it is also necessary to examine the VTEC along individual satellite passes during the event, which gives a better insight on the effect and possible locations of the ionospheric disturbances.

Figure 4.3 presents the sub-ionospheric tracks for all visible satellites at SAMP station during the period of two hours, which is between 0:48 and 2:48 UT on the day of the 26 December 2004 earthquake. The solid and open circles on the satellite trajectories denote the start and end time of the observation period, respectively. In this figure, about 8 satellites were observed at 5° elevation angle mask during the observation period of the earthquake event.

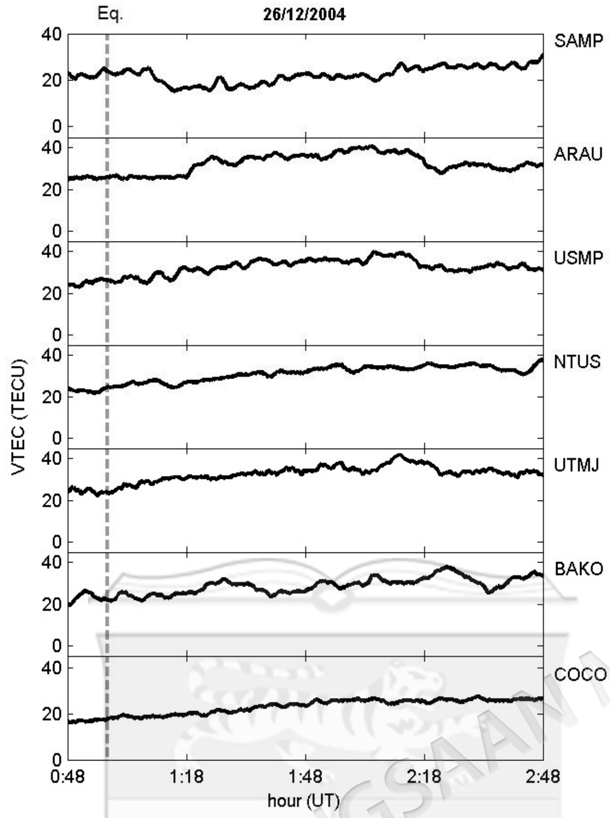

Figure 4.2 VTEC variations between 00:48 and 2:48 UT during the 26 December 2004 earthquake at seven GPS stations

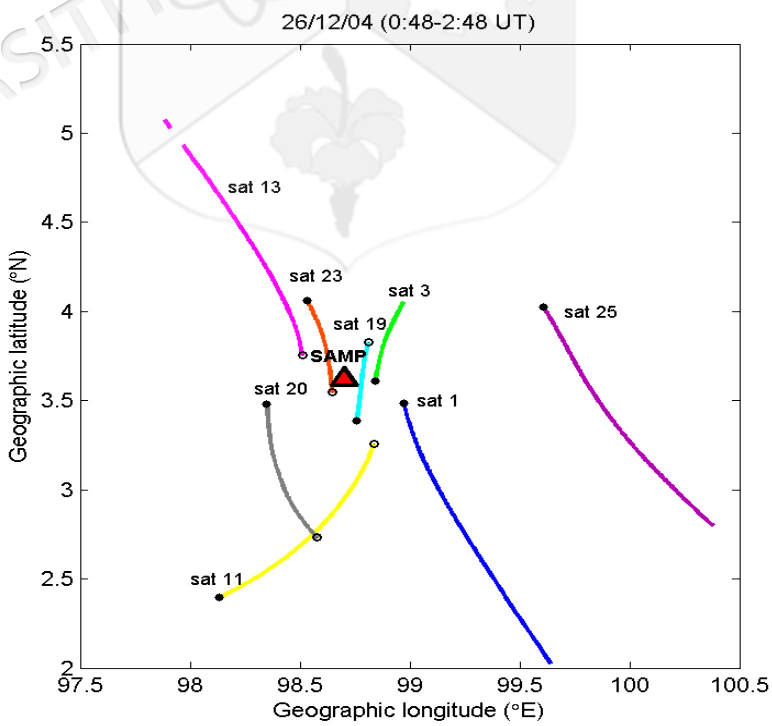

Figure 4.3 The visible GPS satellites at SAMP station for the period of 0:48-2:48 UT on 26 December 2004.

The temporal and spatial variations of the VTEC irregularities during the event are examined using measurements from individual satellites. As mentioned earlier, 8 GPS satellites were observed at SAMP during the earthquake period. However, only satellite 23 was affected by the earthquake. Figures 4.4(a)-(c) present the VTEC variations between 0:48 and 2:00 UT on 26 December 2004 for satellite 23 at SAMP, ARAU and USMP stations. In these figures, the cross line shows the satellite track at IPP in geographic coordinates. Figure 4.4(d) illustrates the epicenter and the satellite trajectories of these satellites above their respective GPS stations on 26 December 2004. It should be noted that the observation period in this analysis was characterized by quiet geomagnetic and very low solar activity, as mentioned in Section 3.9.1. As shown in Figure 4.4(a), a VTEC variation with 4 oscillations and with duration of 40 minutes was observed from 00:58 to 1:42 UT during the earthquake day. During this time, the VTEC fluctuates between 2 to 7 TECU with minimum and maximum values of 16 and 23 TECU, respectively. Following this time, the VTEC gradually returns to its normal level. In Figure 4.4(b), the VTEC variation at ARAU station show 3 oscillations observed from the time of the event until 24 minutes later. The VTEC fluctuates between 1 and 4 TECU between 00:58 and 1:22 UT. About 15 minutes later, another increase in VTEC was seen from 1:37 to 1:44 UT. As shown in Figure 4.4(c), the VTEC measurement at USMP station did not show any significant variation until about 16 minutes after the event with 3 oscillations between 1:14 and 1:40 UT. The duration of these oscillations is about 26 minutes and its peak-to-peak value is 3 TECU. Following this event, the VTEC gradually increases to its normal level.

These long-term periods VTEC disturbance that is observed following the earthquake may not reflect the CID occurrence but could be due to the variations of the solar zenith angle and satellite elevations. Therefore, it is necessary to filter the VTEC variations to obtain short-term disturbances that may be caused by earthquakes. Figure 4.5 presents the VTEC variations and filtered VTEC for satellite 23 during the period between 0:48 and 2:00 UT on 25, 26 and 27 December 2004 at SAMP, ARAU and USMP stations, respectively. In the bottom panels of Figures 4.5(a)-(c), the solid line represents the mean value of the filtered VTEC and the dashed line is threshold value of $\pm 2\sigma$ during the 1.2 hour interval whereby σ is the standard deviation of the filtered VTEC. If an observed filtered VTEC exceeds its corresponding threshold value, a significant disturbance is detected. The red dot marks the peak amplitude of the oscillation.

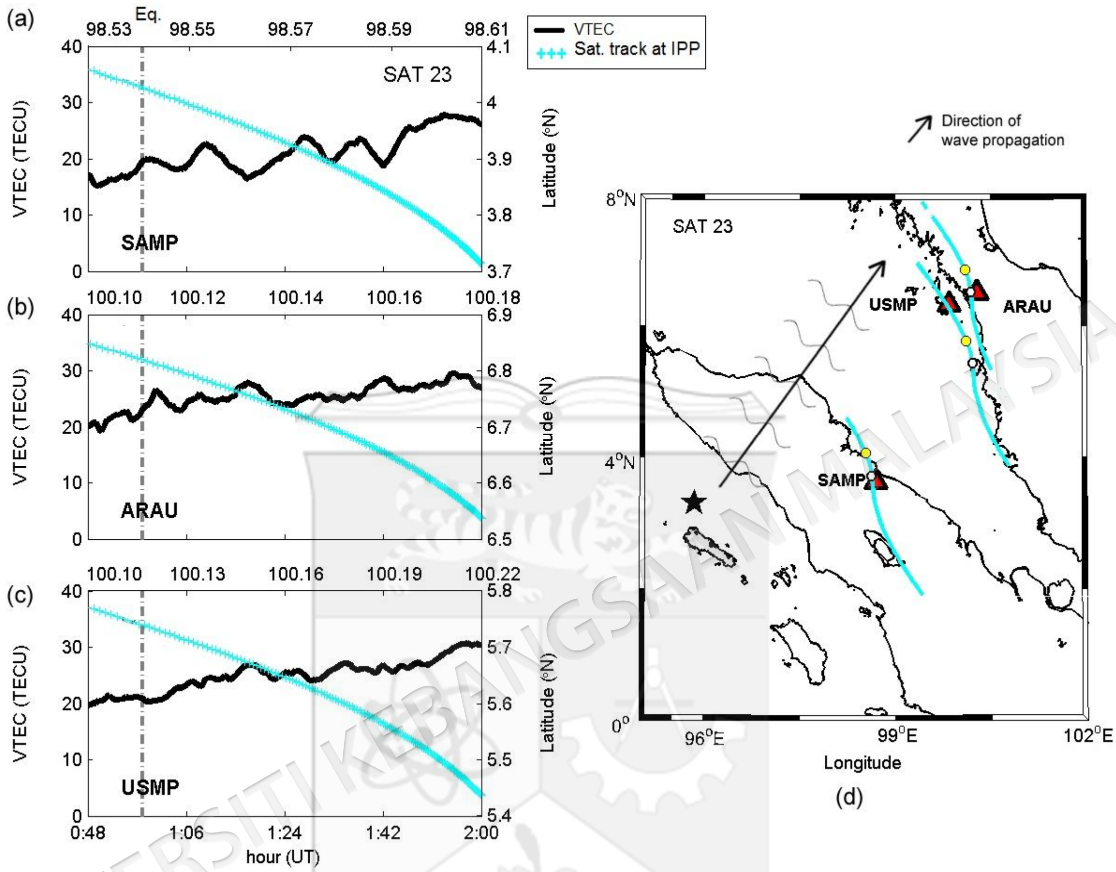

Figure 4.4 Temporal and spatial VTEC variations observed for satellite 23 between 0:48 and 2:00 UT on 26 December 2004 at (a) SAMP, (b) ARAU and (c) USMP stations. (d) Satellite trajectories on 26 December 2004. The solid and open circles denote time marks for 0:48 and 2:00 UT, respectively. The arrow shows the direction of the wave propagation.

As shown in Figure 4.5(a), a sinusoidal wave, which consists of 4 oscillations was detected at SAMP station. These oscillations have periods of about 7 minutes and peak amplitude of about 1.0 TECU at 1:10 UT. As shown in Figure 4.5(b), 3 oscillations were observed at ARAU station with the peak disturbance amplitude detected about 16 minutes after the event. The period of these oscillations is about 8 minutes and the peak amplitude was observed at 1:14 UT with a value of 0.75 TECU. In Figure 4.5(c), rapid VTEC oscillations with short periods were observed about 4-15 minutes after the event at USMP station. Following this time, 3 oscillations with periods varying between 8.4 and 9 minutes were detected. The peak amplitude of this disturbance was detected at 1:14 UT with a value of 0.85 TECU. It is also shown that the disturbance peak amplitude in the filtered VTEC during the earthquake day exceeds the threshold reference value and is an order magnitude larger than the VTEC fluctuation intensity observed on the day before the earthquake. During the same earthquake, significant GPS-CID were observed by Heki et al. (2006) and Otsuka et al. (2006) by satellites 13, 20 and 23. Among these satellites, the most prominent disturbance was observed by satellite 13 with peak-to-peak amplitude of about 11 TECU, followed by satellites 23 and 20. The results do not show any GPS-CID from satellite 13 and 23 as the GPS VTEC from both these satellites were filtered by the cut-off elevation angle of 30°. However, the peak-to-peak amplitude and period of the GPS-CID observed by satellite 23 in this results is consistent with the ones observed by Heki et al. (2006) and Otsuka et al. (2006).

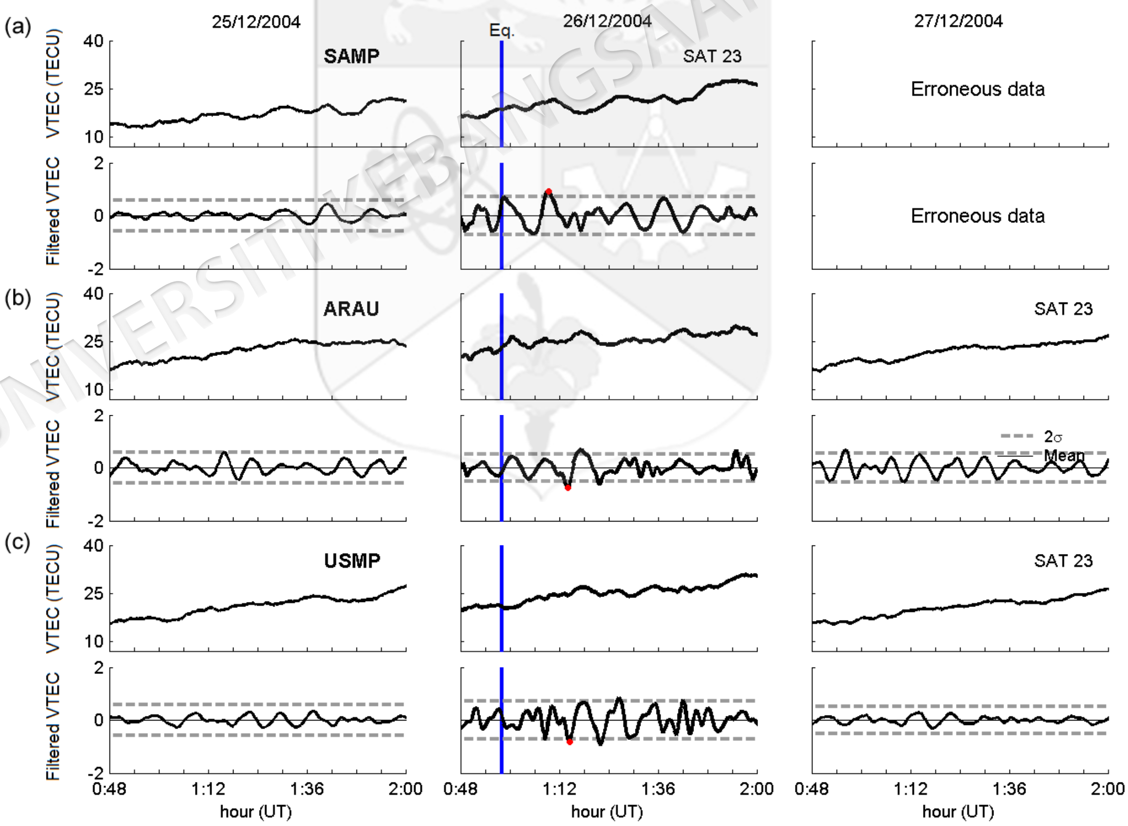

Figure 4.5 VTEC variations and filtered VTEC for satellite 23 at (a) SAMP, (b) ARAU and (c) USMP stations between 00:48 and 2:00 UT on 25, 26 and 27 December 2004.

The horizontal propagation velocity of the near zone ionospheric disturbances during the earthquake event is estimated. The calculation takes into account the distance and time lag of the disturbance peak arrivals between the sub-ionospheric points (SAT 23) at SAMP and at ARAU and USMP stations. The time lag of the disturbance peak arrivals are 4 minutes (between SAMP and ARAU) and (between SAMP and USMP), while the distances between the satellites are 353 km and 257 km, respectively. Therefore, the estimated horizontal propagation velocities (distance/time lag) of the observed ionospheric disturbances are 1471 m/s and 1071 m/s. The average velocity of these disturbances is 1271 m/s, which is coincident with the typical sound velocity at ionospheric height (Lognonné 2006).

b. Observation of Geomagnetic variations

Figure 4.6 presents the 1-second geomagnetic variations and the filtered geomagnetic H, D and Z measurements in the Pc3 and Pc5 bands from 0:48 to 2:00 UT on 26 December 2004 at KTB station, located about 560 km from the epicenter. As shown in Figure 4.6(a), rapid fluctuations were observed in the Z-component about 5 minutes after the earthquake. During this time, the magnetic field fluctuates from 0.1 to 0.3 nT with periods of about 14-16 seconds. Shortly after that, a sudden increase and decrease in the H-component (8 nT), a sudden decrease and increase in the D-component (6 nT) and a sudden decrease in the Z-component (0.6 nT) that represent a shock wave were observed simultaneously at 1:06 UT. About 12 minutes after this event, an increase and decrease of about 1-3 nT were seen almost simultaneously in all the magnetic field components between 1:15 and 1:30 UT. About 25 minutes later, the geomagnetic field starts to return to its normal level.

As shown in Figure 4.6(b), a significant Pc3 pulsation was observed simultaneously in the H, D and Z components at 1:06 UT, which is about 8 minutes after the earthquake. The Pc3 pulsation has a peak amplitude of about 3 nT for both H and D components and 0.2 nT in the Z-component. The pulsation has a period of about 22 seconds and was coincident with the shock wave observed in the geomagnetic field variations in Figure 4.6(a). In Figure 4.6(c), a Pc5 pulsation, which time interval is highlighted in the grey colored area, was observed at about 8 minutes after the event. The pulsation was detected simultaneously in the H, D and Z components with magnitudes of 0.6, 0.5 and 0.1 nT, respectively and with period of about 4.2 minutes. About 14 minutes after this pulsation, a second Pc5 oscillation was detected in all the geomagnetic components. However, this oscillation is probably due to the recovery phase of the geomagnetic field enhancement and depletion induced by the earthquake.

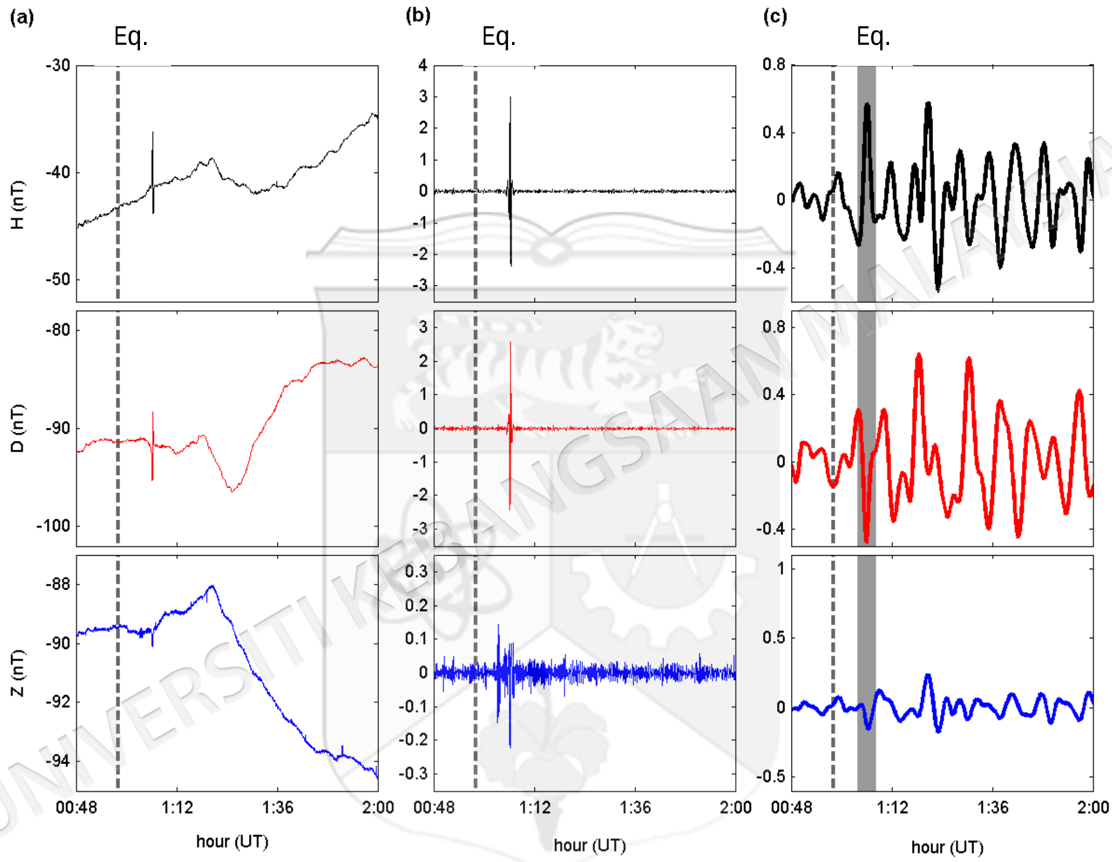

Figure 4.6 (a) Geomagnetic field variations and the filtered geomagnetic H, D and Z components between 0:48 and 2:00 UT on 26 December 2004 in the (b) Pc3 and (c) Pc5 bands

In middle or low latitudes, magnetic Pc5 pulsations are normally observed in much wider area both in latitude and longitude and on a global scale. If it is a normal Pc5 pulsation generated by external sources, the amplitude is normally larger at higher latitudes. In order to validate the Pc5 pulsation observed at KTB station, 1-min measurements are compared with higher latitude INTERMAGNET stations such as Phu Thuy, PHU (GMlat.: 13.84°N), Zhaoqing, GZH (GMlat.: 14.01°N), Kakadu, KDU (GMlat.: 22.09°S) and Lanzhou, LZH (GMlat.: 30.21°N). Although not shown in the result, no Pc5 pulsation of a similar period was observed at 1:06 UT at those stations. Therefore, it is believed that the oscillation detected 8 minutes after the event at KTB station has a local character and might be related to the earthquake. On the other hand, the second Pc5 oscillation, which was detected 14 minutes after the first one was also observed at all the four higher latitude stations, showing a global character and therefore, cannot be due to the earthquake.

c. Correlation between the ionospheric and magnetic disturbances

The results of GPS VTEC and magnetic analyses show a relation between the magnetic Pc5 pulsation at KTB station and the CID observed earlier in the VTEC measurements at SAMP station. Therefore, both the ionospheric VTEC and geomagnetic responses to the 26 December 2004 earthquake at GPS (SAMP) and magnetometer (KTB) stations are combined as shown in Figure 4.7. In this figure, the power of the filtered VTEC at SAMP station (i.e $|TEC|^2$) for satellite 23 and the filtered geomagnetic H and D components at KTB station ($|H|^2$ or $|D|^2$) during the event are presented. The time of the oscillation peak of both ionospheric and geomagnetic responses is also shown in the figure.

As shown in the figure, the peak arrivals of both ionospheric and geomagnetic disturbances were observed about 8-12 minutes after the earthquake at SAMP and KTB stations. The results show a close approximation in the time lag of the ionospheric and magnetic disturbances observed at both stations during the earthquake. It is believed that the earlier magnetic field response to the earthquake is due to the shorter time required by the acoustic waves to propagate upward to the E-layer at 100-120 km altitude than the time required for them to propagate upward to the F-layer at about 400 km altitude measured by GPS observables.

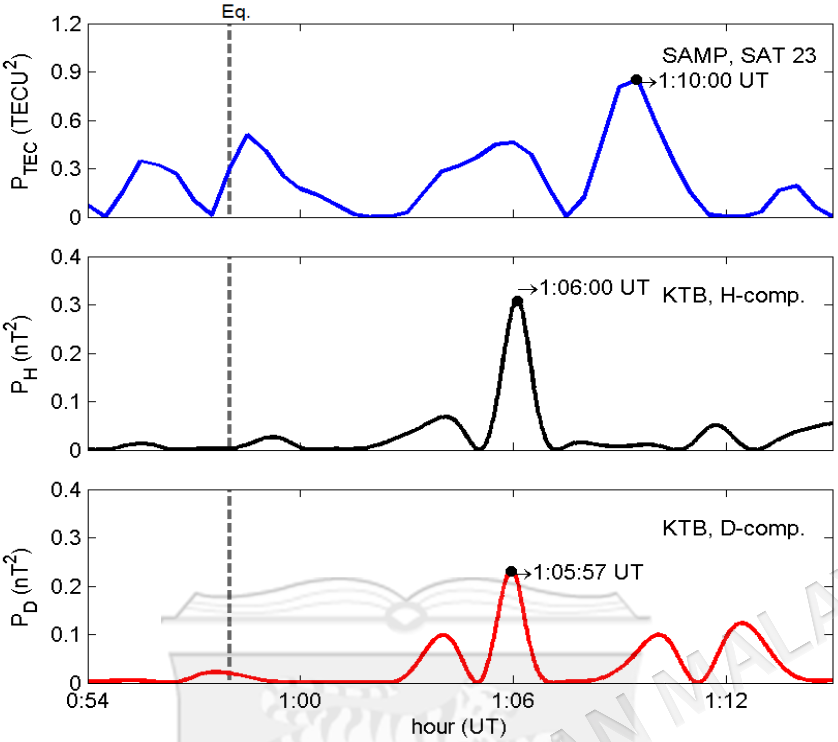

Figure 4.7 The time series of the power of filtered GPS VTEC at SAMP station and filtered geomagnetic H and D components at KTB station during the earthquake event. The time of the oscillation peak is shown.

4.3.2 The 28 March 2005 Earthquake

a. Observations of ionospheric VTEC variations

Figure 4.8 presents the VTEC variations during the earthquake event on 28 March 2005 observed at seven GPS stations surrounding the earthquake epicenter. As shown in the figure, wave-like ionospheric disturbances were clearly seen at SAMP (247 km) and ARAU (602 km) stations a few minutes after the earthquake but no significant ionospheric signatures were observed at the remaining GPS stations. The two GPS stations where effects of the earthquake were observed are located northeast of the epicenter, while the other GPS stations where VTEC variations were not seen after the earthquake are located relatively east and south of the epicenter. This observation shows directivity of the VTEC variations with respect to the azimuth of the epicenter, as will be discussed later in the chapter. With respect to this observation, the following analysis will focus on the ionospheric disturbances observed at SAMP and ARAU stations only.

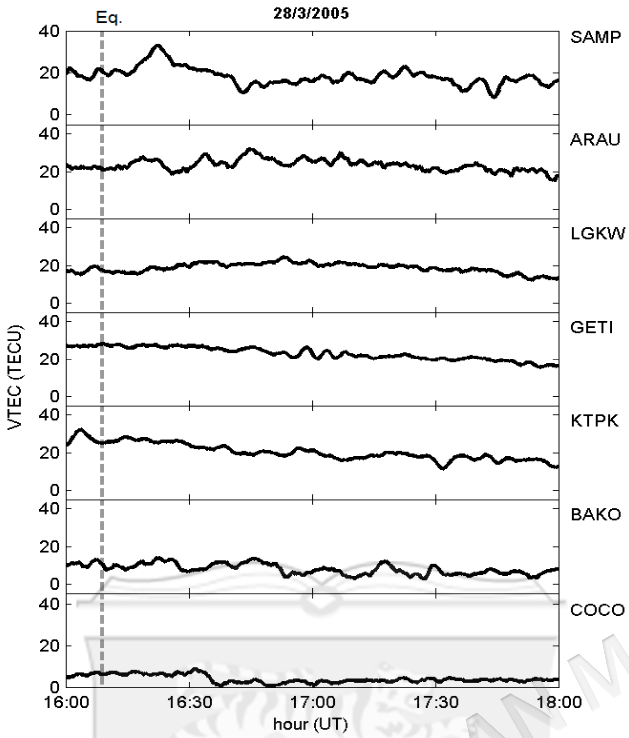

Figure 4.8 VTEC variations between 16:00 and 18:00 UT during the 28 March 2005 earthquake at seven GPS stations.

Figure 4.9 shows the VTEC variations between 16:00 and 18:00 UT on 27, 28 and 29 March 2005 at SAMP and ARAU stations. It should be noted that the observation period in this analysis was characterized by quiet geomagnetic and very low solar activity, as mentioned in Section 3.9.3. As shown in Figure 4.9(a), episodes of VTEC enhancement-depletion were observed from the time of the earthquake until about 2 hours after the event during the earthquake day. At the time of the event, an increase of about 1 TECU was observed for about 4 minutes; followed by sudden VTEC increase of about 11 TECU between 16:12 and 16:23 UT. The VTEC reaches a peak of about 30 TECU at 16:23 UT, and then gradually decreases until it reaches its minimum value of 13 TECU at 16:46 UT. Following this time, the VTEC starts to recover to its normal level for about 20 minutes to complete a one-wave cycle. The duration of this sinusoidal wave is about 54 minutes and its peak-to-peak value is 17 TECU. Shortly after this time, a similar sinusoidal wave was observed between 17:12 and 17:50 UT but appears smaller in amplitude. This wave oscillates for a length of 38 minutes and has a peak-to-peak value of 8 TECU.

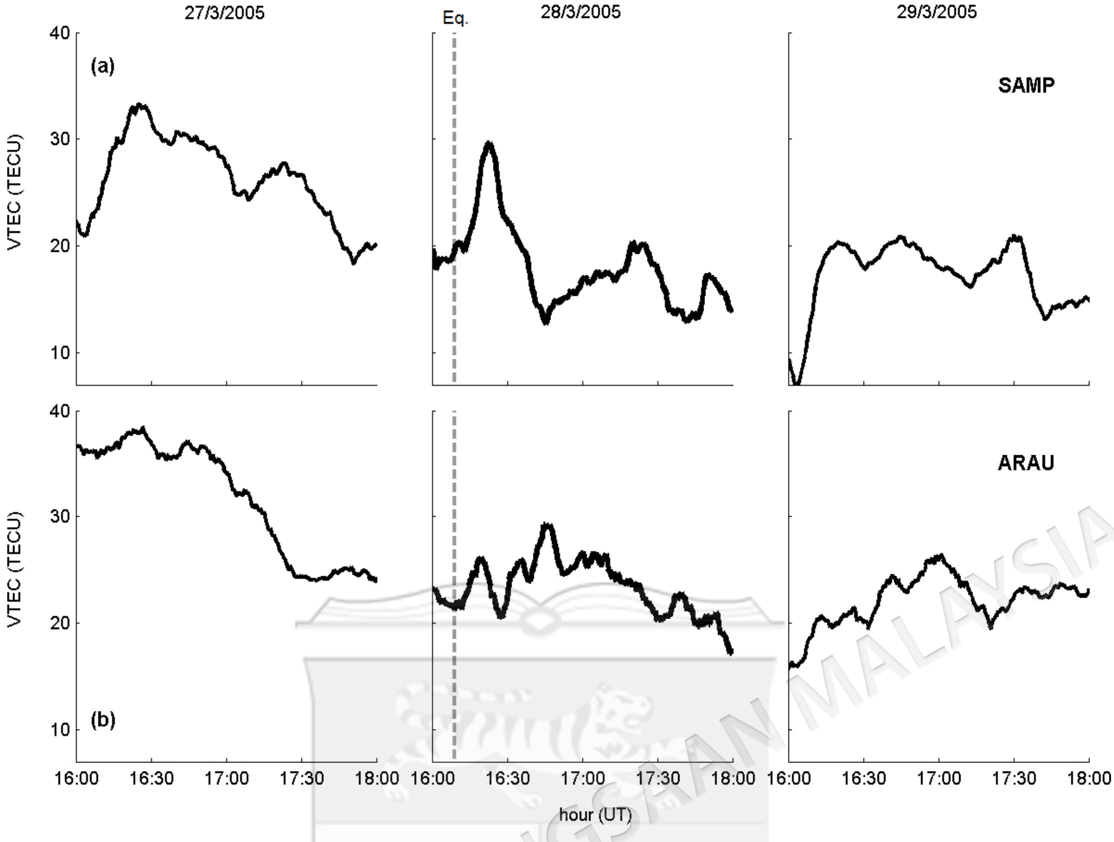

Figure 4.9 VTEC variations between 16:00 and 18:00 UT on 27, 28 and 29 March 2005 at (a) SAMP and (b) ARAU stations.

As shown in Figure 4.9(b), a VTEC variation with 3 oscillations and with duration of about 43 minutes was observed from 16:13 to 16:56 UT during the earthquake day. The VTEC during this time fluctuates between 2 and 6 TECU with minimum and maximum value of 21 and 27 TECU, respectively. Following this event, the VTEC gradually decreases for about 27 minutes before another VTEC variation with 2 oscillations was detected between 17:18 and 17:54 UT. The VTEC during this time fluctuates between 2 and 3 TECU for duration of 36 minutes. Following that, VTEC gradually decreases to its normal level. It was observed that such VTEC oscillations were not detected on the day before and after the earthquake at both SAMP and ARAU stations.

Figure 4.10 presents the sub-ionospheric tracks for all visible satellites at SAMP station during the period between 16:00 and 18:00 UT on the day of the 28 March 2005 earthquake. As shown in this figure, about 9 satellites were observed at 5° elevation angle mask during the observation period of the earthquake event.

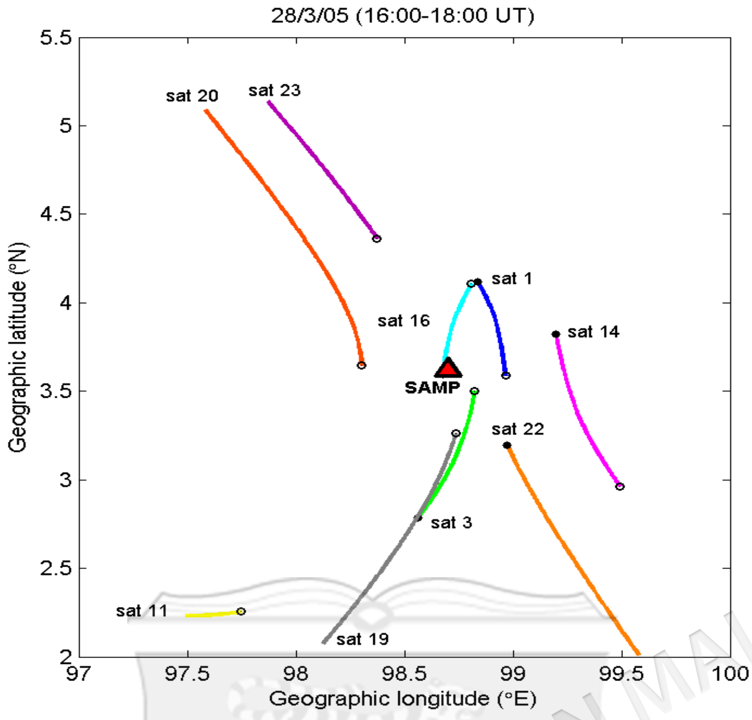

Figure 4.10 The visible GPS satellites at SAMP station for the period of 16:00-18:00 UT on 28 March 2005.

As shown in Figure 4.10, 9 GPS satellites were observed at SAMP during the earthquake period. However, only satellite 16 at SAMP and ARAU stations and satellite 1 at LGKW station were affected by the earthquake. The VTEC variations, the satellite tracks at IPP and the satellite trajectories observed for satellite 16 at SAMP and ARAU stations and satellite 1 for LGKW station between 16:00 and 17:12 UT on 28 March 2005 are presented in Figure 4.11. It is shown in the figure that the direction of the wave propagation is towards the northeast from the epicenter.

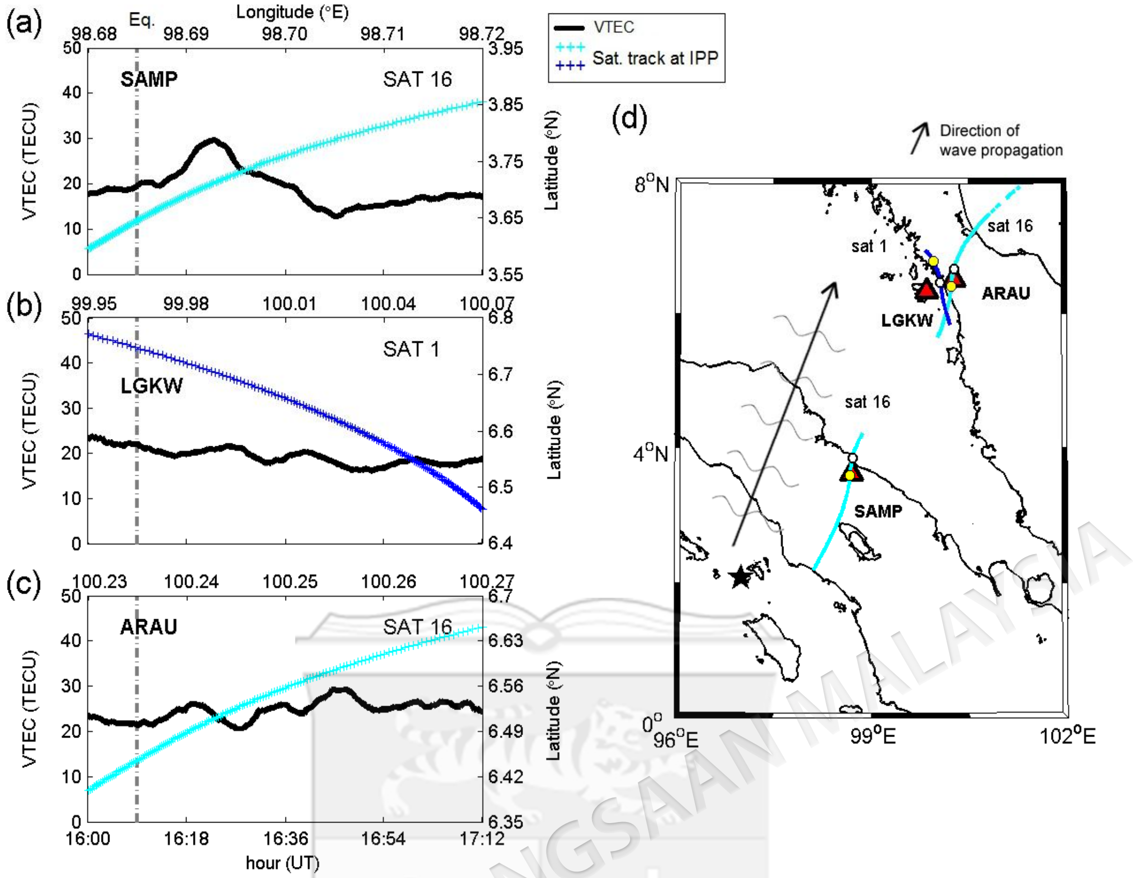

Figure 4.11 Temporal and spatial VTEC variations observed between 16:00 and 17:12 UT on 28 March 2005 at (a) SAMP, (b) LGKW and (c) ARAU stations. (d) Satellite trajectories on 28 March 2005.

Figure 4.12 presents the VTEC variations and filtered VTEC during the period between 16:00 and 17:12 UT on 27, 28 and 29 March 2005 at SAMP, LGKW and ARAU stations, respectively. As shown in Figure 4.12(a), a non-periodic oscillation which resembles a shock wave was observed about 13 minutes after the earthquake at SAMP station. The peak of the oscillation corresponds to the peak of VTEC at 16:22 UT. The period of this oscillation is about 4.8 minutes and its peak amplitude is about 4 TECU. As shown in Figure 4.12(b), an oscillation was detected at LGKW station about 18 minutes after the event. This oscillation has a period of about 7.5 minutes and a peak amplitude of about 1.0 TECU at 16:27 UT. Meanwhile, Figure 4.12(c) shows rapid VTEC oscillations of short periods observed starting from the time of the earthquake to about 15 minutes after the event at ARAU station. Following this time, a sinusoidal wave which consists of 3 oscillations was detected. These oscillations have periods varying between 8.4 and 10 minutes and peak amplitude of about 1.5 TECU at 16:33 UT. It is also shown in each figure that the disturbance peak amplitude in the filtered VTEC during the earthquake day exceeds the threshold reference value and is an order magnitude larger than the VTEC fluctuation intensity observed on the day before the earthquake.

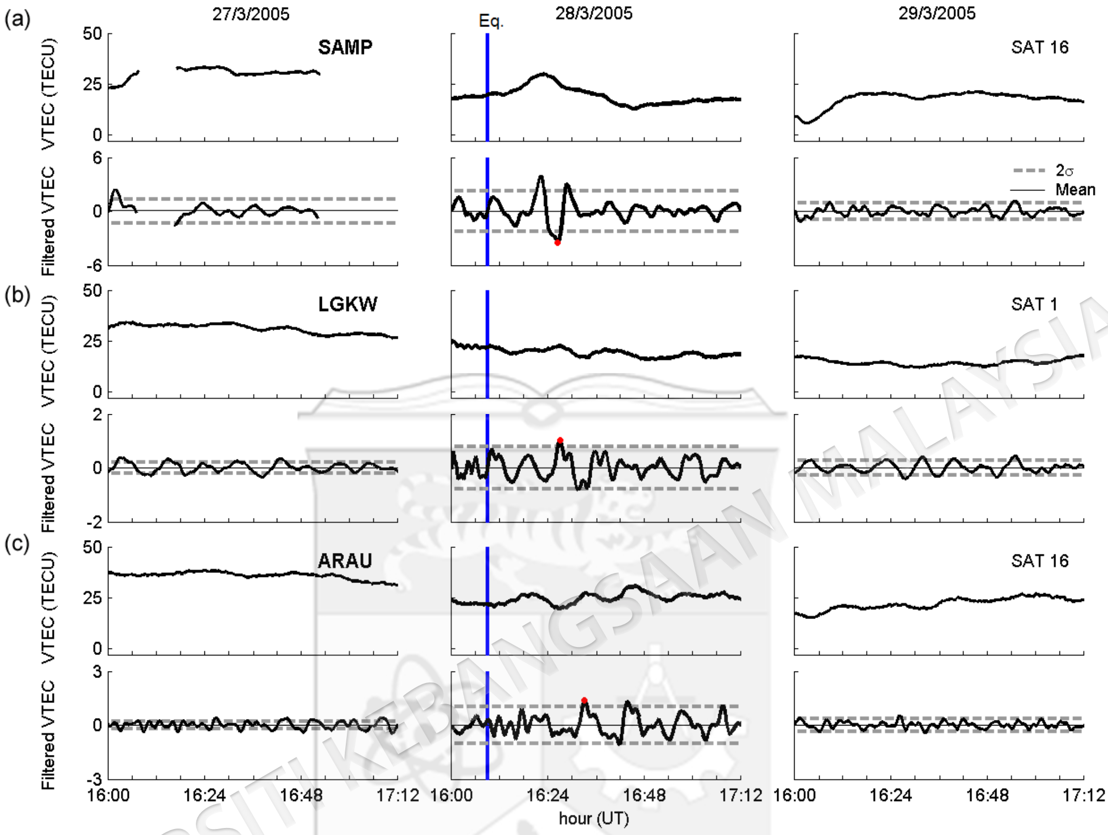

Figure 4.12 VTEC variations and filtered VTEC for satellite 16 at SAMP and ARAU stations and satellite 1 at LGKW station between 16:00 and 17:12 UT on 27, 28 and 29 March 2005

Figure 4.13 shows the filtered VTEC and period-time diagrams obtained by wavelet analyses using Mexican hat mother function for satellite 16 at SAMP and ARAU stations and satellite 1 at LGKW station between 16:00 and 17:12 UT on 28 March 2005. It can be seen that the periods of the CID signal detected following the earthquake is 4-5 minutes at SAMP station but becomes longer at LGKW (6-7 minutes) and at ARAU (8-10 minutes) stations.

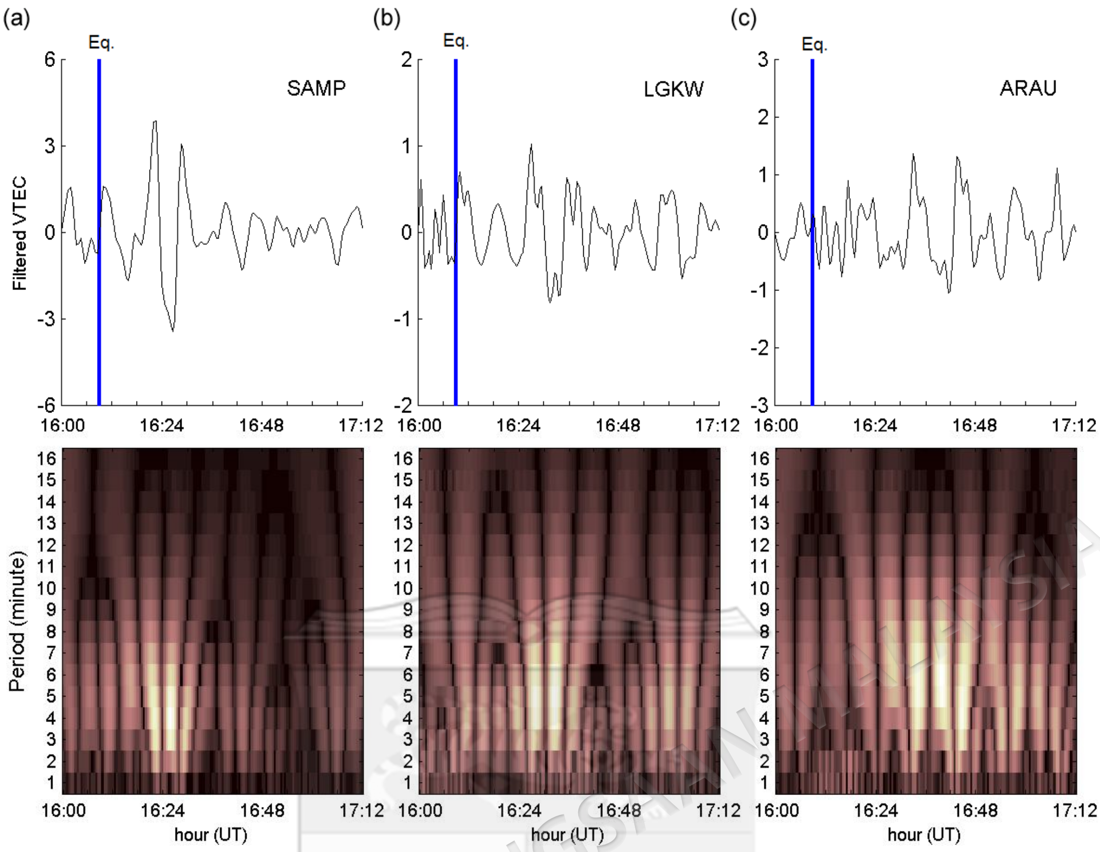

Figure 4.13 Filtered VTEC and period-time diagrams obtained by wavelet analyses using Mexican hat mother function for satellite 16 at (a) SAMP and (b) ARAU stations and satellite 1 at (c) LGKW station between 16:00 and 17:12 UT on 28 March 2005.

In this case, the horizontal propagation velocity takes into account the distance and time lag of the disturbance peak arrivals between the sub-ionospheric points at SAMP (SAT 16) and at LGKW (SAT 1) and ARAU (SAT 16) stations. The time lag of the disturbance peak arrivals are 4.6 minutes (between SAMP and LGKW) and 10.5 minutes (between SAMP and ARAU), while the distances between the satellites are 343 km and 325 km, respectively. Therefore, the estimated horizontal propagation velocities of the observed ionospheric disturbances are 1243 m/s and 517 m/s. The average velocity of these disturbances is 880 m/s, which is coincident with the typical sound velocity at ionospheric height.

b. Observation of Geomagnetic variations

Figure 4.14 presents the geomagnetic variations, the filtered geomagnetic H, D and Z measurements in the Pc3 and Pc5 bands from 16:00 to 17:12 UT on 28 March 2005 at KTB station, located about 447 km from the epicenter. As shown in Figure 4.13(a), high frequency variations in the geomagnetic field H, D and Z components were simultaneously observed about 2 minutes after the earthquake. During this time, the magnetic field of the three components fluctuates between 0.2 and 0.9 nT with periods of about 4-5 seconds. These fluctuations occur 1 minute later than the theoretical arrival time of the seismic P-wave determined by USGS National Earthquake Information Center (http://neic.usgs.gov/neis/eq_depot/2005/eq_050328). Shortly after this event, a sudden decrease in the H-component (2 nT), a gradual increase in the D-component (1 nT) and sudden decrease in the Z-component (0.5 nT) were observed almost simultaneously between 16:18 and 16:23 UT. About 25 minutes after the earthquake, the geomagnetic field components start to increase to their normal level.

Referring to Figure 4.14(b), significant fluctuations in the Pc3 band were observed simultaneously in the H, D and Z components shortly after the time of earthquake. These fluctuations have periods of about 18-22 seconds and duration of about 2 minutes. After this time, no pronounced fluctuations in the Pc3 band were seen as the one found during the 26 December 2004 event. As shown in Figure 4.14(c), a Pc5 pulsation was clearly seen in the magnetic H, D and D components at 16:20 UT, which is about 11 minutes after the earthquake. This pulsation was coincident with the decrease in the H-component and increase in the D-component and has a period of 4.8 minutes. No Pc5 pulsation of such a period was observed during this time at PHU, GZH, KDU and LZH stations. Therefore, it is believed that the Pc5 pulsation detected at 16:20 UT at KTB station has a local character and might be related to the earthquake. It is also shown in the figure that a second Pc5 oscillation was detected in the geomagnetic H and Z components about 15 minutes after the arrival of the first one. However, this oscillation was also detected at all the four higher latitude stations, showing a global character and therefore cannot be due to the earthquake.

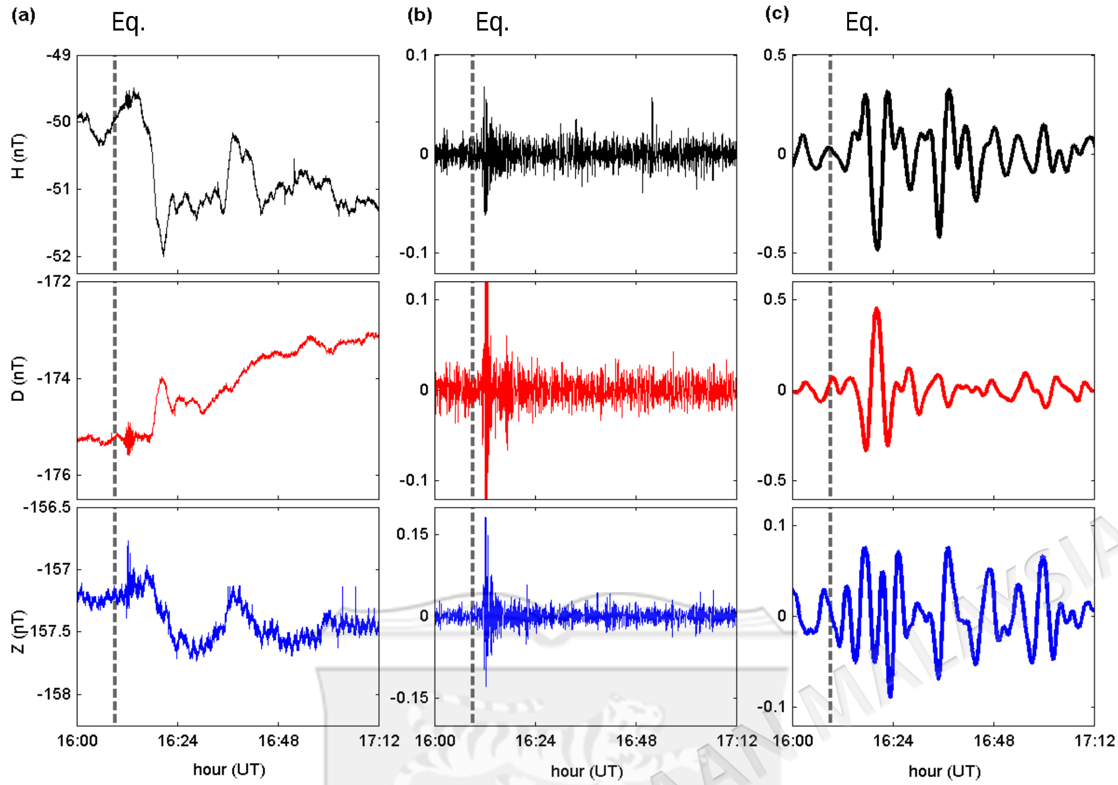

Figure 4.14 (a) Geomagnetic field variations and the filtered geomagnetic H, D and Z components between 16:00 and 17:12 UT on 28 March 2005 in the (b) Pc3 and (c) Pc5 bands

c. Correlation between the ionospheric and magnetic disturbances

The results of both the ionospheric VTEC and geomagnetic responses to the 28 March 2005 earthquake at GPS (SAMP) and magnetometer (KTB) stations are combined as shown in Figure 4.15. In this figure, the power of the filtered VTEC at SAMP station (i.e$|TEC|^2$) for satellite 16 and the filtered geomagnetic H and D components at KTB station ($|H|^2$ or $|D|^2$) during the event are presented. The time of the oscillation peak of both ionospheric and geomagnetic responses is also shown in the figure. As shown in the figure, the peak arrivals of both ionospheric and geomagnetic disturbances were observed about 11-13 min after the earthquake at SAMP and KTB stations. Similar to the 26 December 2004 earthquake event, the results during the 28 March 2005 earthquake also shows a consistency in the time lag of the ionospheric and magnetic disturbances observed at both stations during the event.

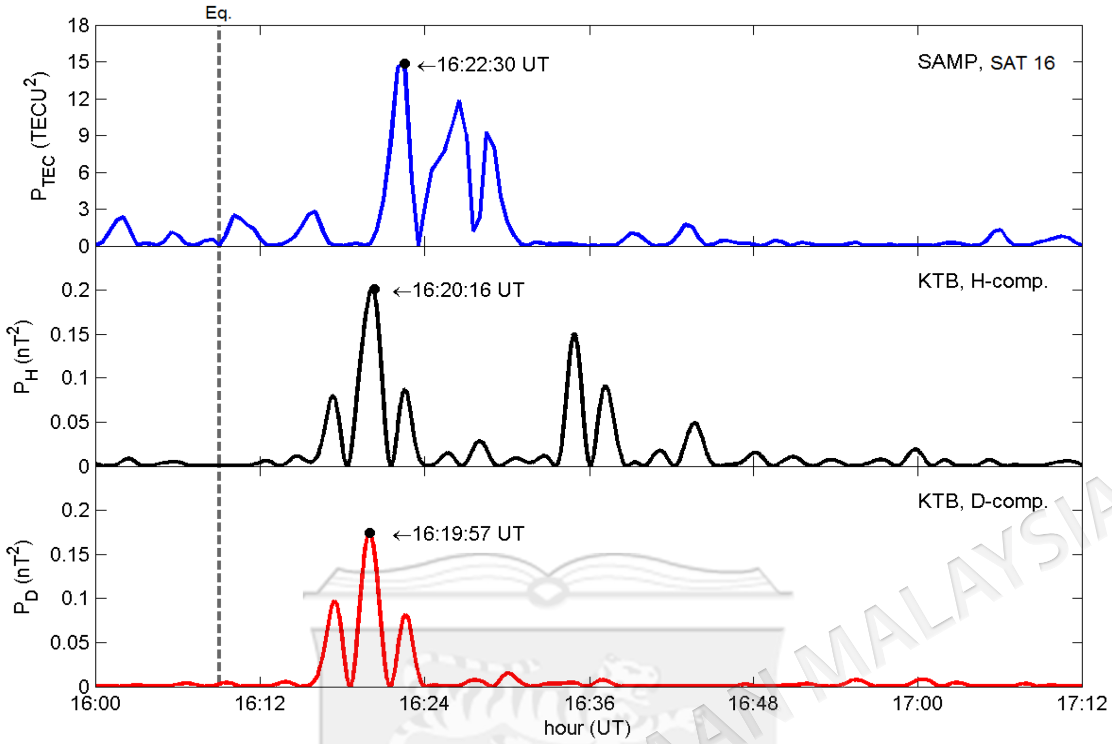

Figure 4.15 The time series of the power of filtered GPS VTEC at SAMP station and filtered geomagnetic H and D components at KTB station during the earthquake event. The time of the oscillation peak is shown.

4.3.3 The 14 May 2005 Earthquake

a. Observations of ionospheric VTEC variations

The same VTEC analysis presented earlier was repeated during the 14 May 2005 earthquake, whereby VTEC variations from seven GPS stations surrounding the epicenter are examined as shown in Figure 4.16. As highlighted in the figure, a sudden decrease in VTEC was observed about 10 minutes after the event at SAMP station, located about 339 km from the epicenter but no significant ionospheric signatures were observed at the remaining GPS stations at the same time. Sudden depletions of VTEC are seen at both UTMJ and BAKO stations shortly after the event but these VTEC depletions could not have caused by the earthquake. This is due to the fact that ionospheric response to the 14 May 2005 earthquake event should be observed first at the station located nearest to the epicenter (SAMP) and not at stations located farther from the epicenter. Similar to the previous event, the effect of the earthquake was observed only in the northeast direction of the epicenter. The observation period in this analysis was characterized by quiet geomagnetic and very low solar activity by IPS (IPS 2008) with Dst, Kp, Ap, F10.7 and SSN values of -39 nT, 3, 8, 100 and 91, respectively (WDC 2007; NOAA 2007).

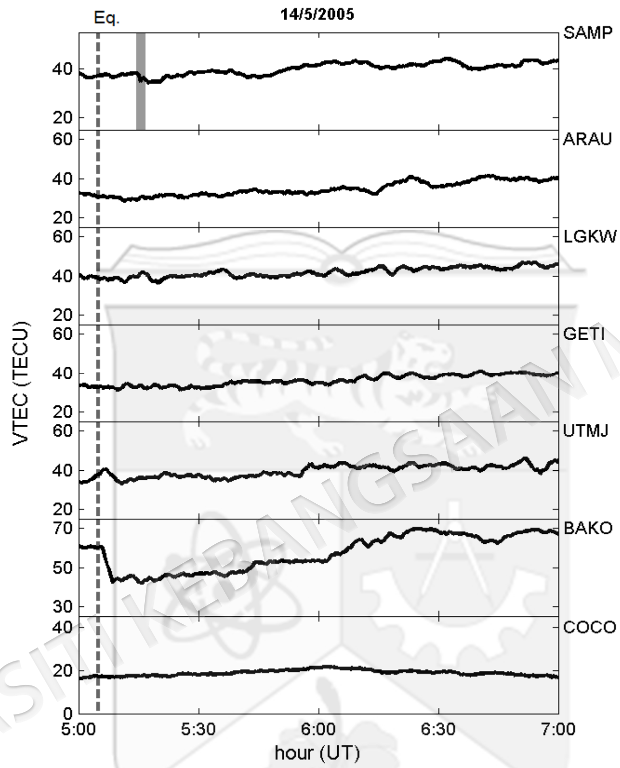

Figure 4.16 VTEC variations between 5:00 and 7:00 UT during the 14 May 2005 earthquake at seven GPS stations.

The sub-ionospheric tracks for all visible satellites at SAMP station during the period between 5:00 and 7:00 UT on the day of the 14 May 2005 earthquake is shown in Figure 4.17. As shown in this figure, about 9 satellites were observed at 5° elevation angle mask during the observation period of the earthquake event.

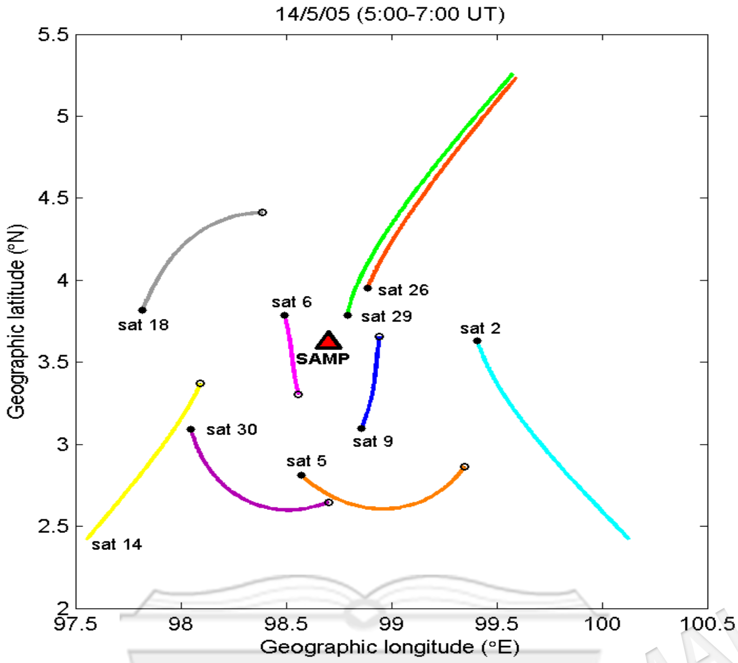

Figure 4.17 The visible GPS satellites at SAMP station for the period of 5:00-7:00 UT on 14 May 2005.

Figure 4.18 presents the VTEC variation from 5:00 to 7:00 UT during the event at SAMP station. The area in grey shows the time interval of the observed VTEC disturbance. As shown in the figure, a VTEC depletion of about 3 TECU was observed about 10 minutes after the earthquake. The VTEC then increases slightly and decreases again for a length of about 1 minute between 5:16 and 5:17 UT. Following that, the VTEC starts to increase to its normal level.

Although 9 GPS satellites were visible during the earthquake period but only satellites 6, 9, 26 and 29 show pronounced ionospheric disturbances as shown in Figure 4.19. In this figure, the VTEC variations along individual satellites, the satellite tracks at IPP and the satellite trajectories observed for satellites 6, 26 and 29 at SAMP and satellite 9 at ARAU, respectively between 5:00 and 6:12 UT on 14 May 2005 are presented. As shown in Figures 4.19(a)-(d), a VTEC depletion of about 2-3 TECU was observed for duration of 1 minute for both SAT 6 and 26 respectively, while a VTEC enhancement of about 3 TECU followed by a VTEC dip was observed from 5:16 to 5:20 UT for SAT 29 at SAMP station. At ARAU station, a VTEC variation which consists of a sudden decrease followed by an increase, both of about 4 TECU was observed between 5:15 and 5:20 UT for SAT 9.

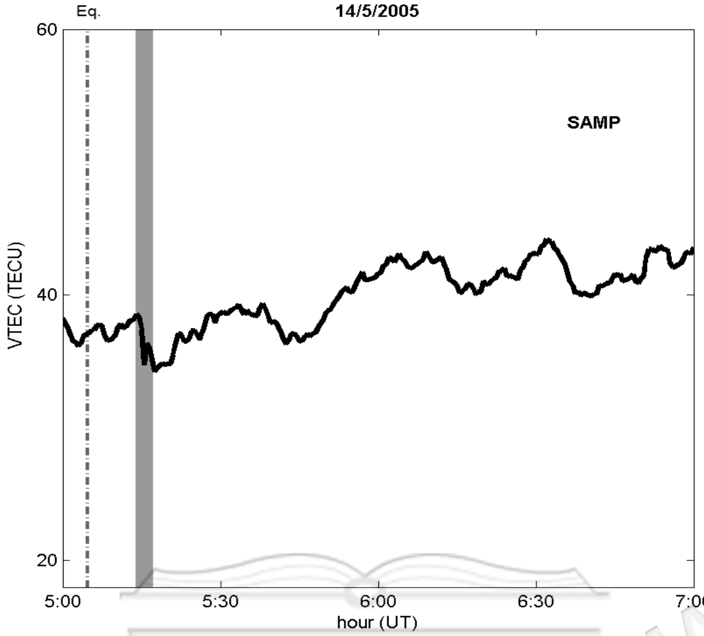

Figure 4.18 VTEC variation between 5:00 and 7:00 UT during the 14 May 2005 earthquake at SAMP station. The area in grey highlights the time interval of the VTEC depletion.

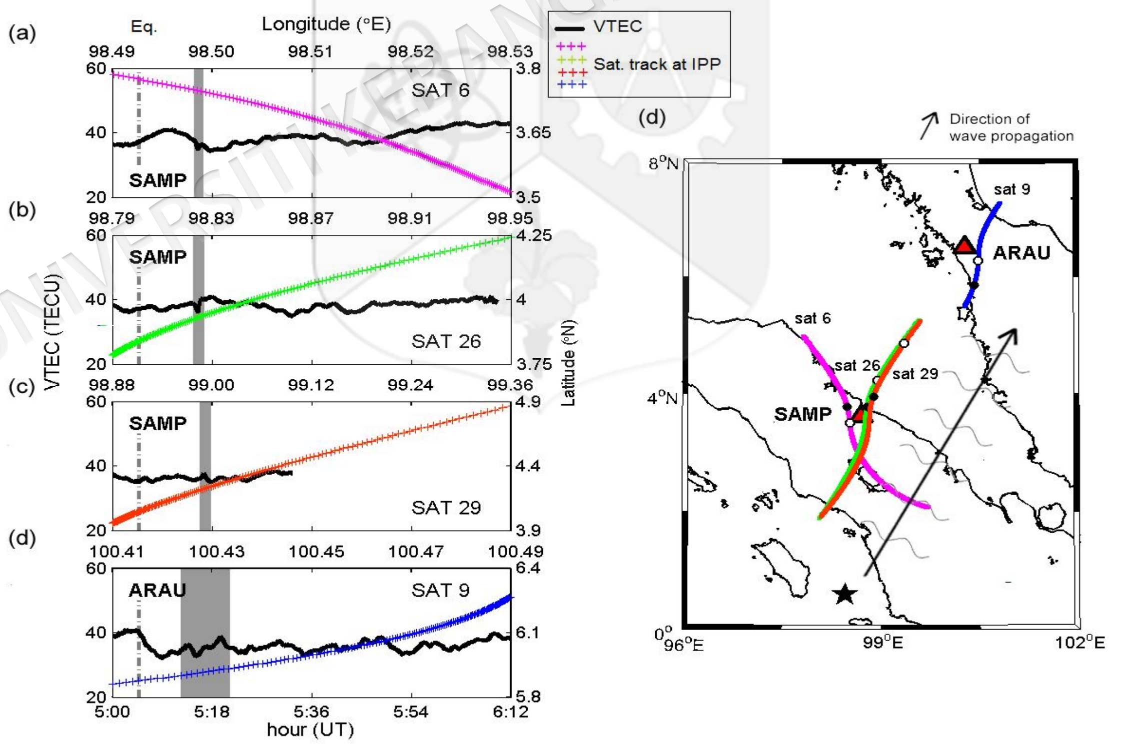

Figure 4.19 Temporal and spatial VTEC variations for satellites (a) 6, (b) 26, (c) 29 at SAMP station and (d) satellite 9 at ARAU station between 5:00 and 6:12 UT on 14 May 2005. (e) Satellite trajectories on 14 May 2005. The solid and open circles denote time marks for 5:00 UT and 6:12 UT respectively.

Figure 4.20 presents the VTEC variations and the filtered VTEC observed for satellites 6, 26 and 29 at SAMP and satellite 9 at ARAU respectively between 5:00 to 6:12 UT on 13 and 14 May 2005. It is noted that the day of 15 May 2005 was characterized by disturbed geomagnetic activity, therefore was not included in this analysis. As shown in Figures 4.20(a)-(c), pronounced N-shaped oscillations in the filtered VTEC were coincident with the sudden VTEC variations at 5:15 UT for SAT 6, 26 and 29 on 14 May 2005 at SAMP station. These oscillations were observed simultaneously at about 10 minutes after the earthquake and have a common disturbance period of about 504 seconds. The peak amplitude of the oscillation varies between 8.6 and 9.6 TECU, which far exceeds the specified reference value and is at least a five order magnitude larger than the VTEC fluctuation intensity observed on the day before the event. In Figure 4.20(d), the negative and positive pulses in the filtered VTEC were coincident with the sudden VTEC decrease and increase observed between 5:15 and 5:20 UT for SAT 9 at ARAU station. In this case, the time lag of the observed oscillation peak at 5:20 UT with respect to the time of the earthquake is about 14 minutes, and the disturbance period is about 396 seconds. During this time, the amplitude varies between 2.2 and 2.4 TECU and slightly exceeds the reference value. Such a disturbance was not observed a day prior to the event.

In these analyses, it is found that although the moving-mean filter is a useful method to detect VTEC disturbances during earthquakes, it also has a weakness of displaying high jumps when the VTEC measurements are discontinuous. This could lead to false detection of ionospheric VTEC disturbances as shown in Figure 4.12a (27 March 2005) and in Figures 4.20b-d (13 May 2005). Therefore, this method would work more efficiently if VTEC measurements were always continuous.

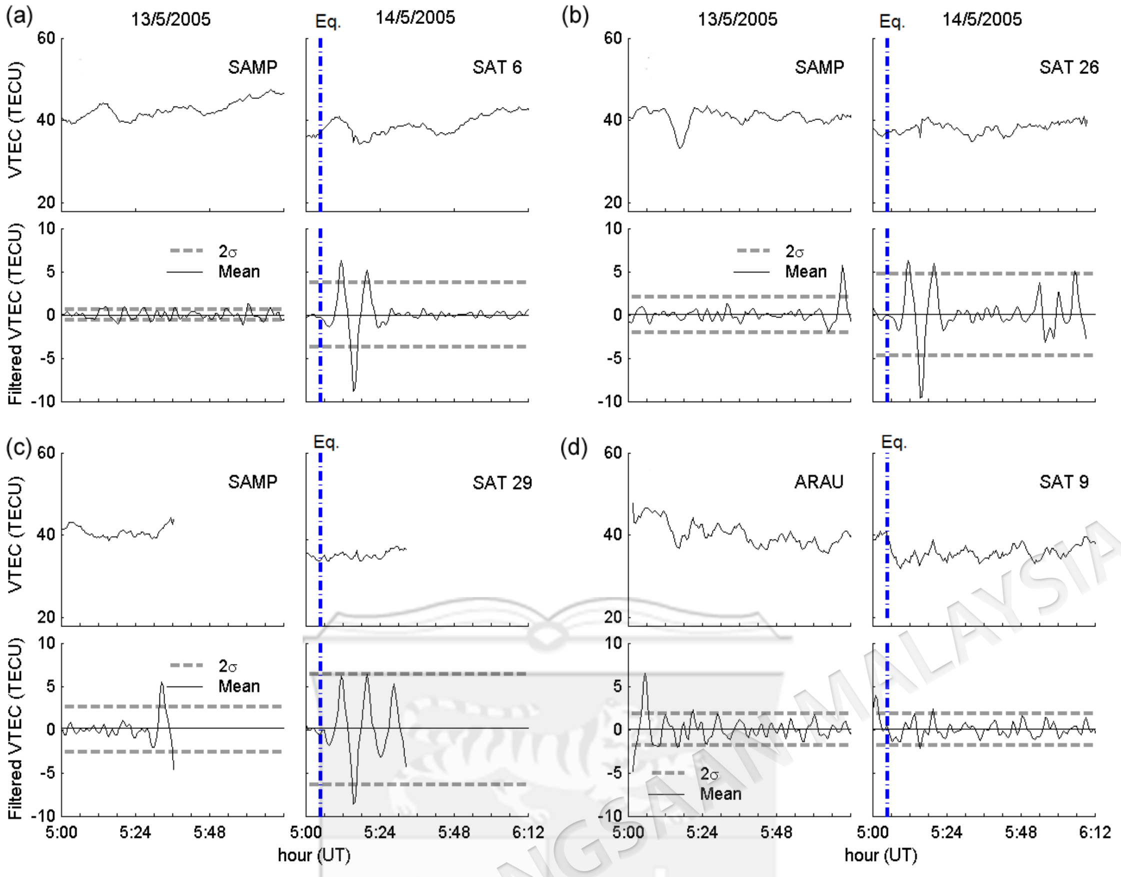

Figure 4.20 VTEC variations and the filtered VTEC for satellites 6, 26 and 29 at SAMP station and satellite 9 at ARAU station respectively for the period between 5:00 and 6:12 UT on 13 and 14 May 2005.

In this event, the horizontal propagation velocity is approximated by taking the distance and time lag of the disturbance peak arrivals between the satellites at SAMP (SAT 6, 26 and 29) and at ARAU (SAT 9). The time lag of the disturbance peak arrivals is 4 minutes while the distances between the satellites are 332 km (between SAT 6 and SAT 9), 300 km (between SAT 26 and SAT 9) and 274 km (between SAT 29 and SAT 9). Hence, the estimated horizontal propagation velocities of the observed ionospheric disturbances are 1384 m/s, 1250 m/s and 1143 m/s, with an average velocity of 1259 m/s. Similar to previous events, this average velocity also coincides with the typical sound velocity at ionospheric height, which indicates that these shock waves are the CID of direct acoustic waves from the epicenter as mentioned in Chapter 2. The results also show that the CID observed at both SAMP and ARAU stations during the 14 May 2005 earthquake are similar to the characteristics of shock acoustic wave (SAW) propagation (Afraimovich et al. 2001, 2005). The geomagnetic field measurements during the 14 May 2005 earthquake are also examined but no significant magnetic disturbances were found during the earthquake period.

4.3.4 The 12 September 2007, M8.5 Earthquake

a. Observation of ionospheric VTEC variations

Figure 4.21 presents the VTEC variations from five GPS stations surrounding the epicenter of the 12 September 2007, M8.5 earthquake. As shown in the figure, a pronounced VTEC variation was found about 20 minutes after the event at SAMP station, which is located about 953 km from the epicenter but no significant ionospheric signatures were observed at the remaining GPS stations. Similar to the previous event, the effect of the earthquake was observed only in the northeast direction of the epicenter. As mentioned earlier in Section 3.9.5, the observation period during the event was characterized by quiet geomagnetic and very low solar activity.

Figure 4.22 presents the sub-ionospheric tracks for all visible satellites at SAMP station during the period of two hours, which is between 11:00 and 13:00 UT on the day of the 12 September 2007 earthquake. As shown in this figure, about 9 satellites were observed during the observation period of the earthquake event but only satellites 4 and 8 at SAMP and satellites 4 and 27 at USMP stations observe pronounced disturbances. The VTEC variations along individual satellites, the satellite tracks at IPP and the satellite trajectories observed for these satellites between 11:00 and 12:12 UT on 12 September 2007 are presented.

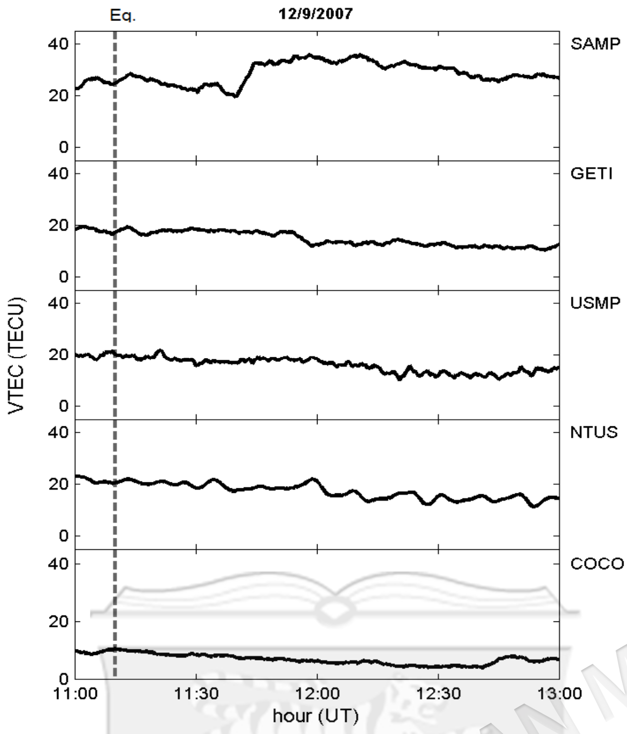

Figure 4.21 VTEC variations between (a) 11:00 and 13:00 UT and (b) 23:30 and 1:30 UT during the 12 September 2007 earthquakes of M8.5 at five GPS stations.

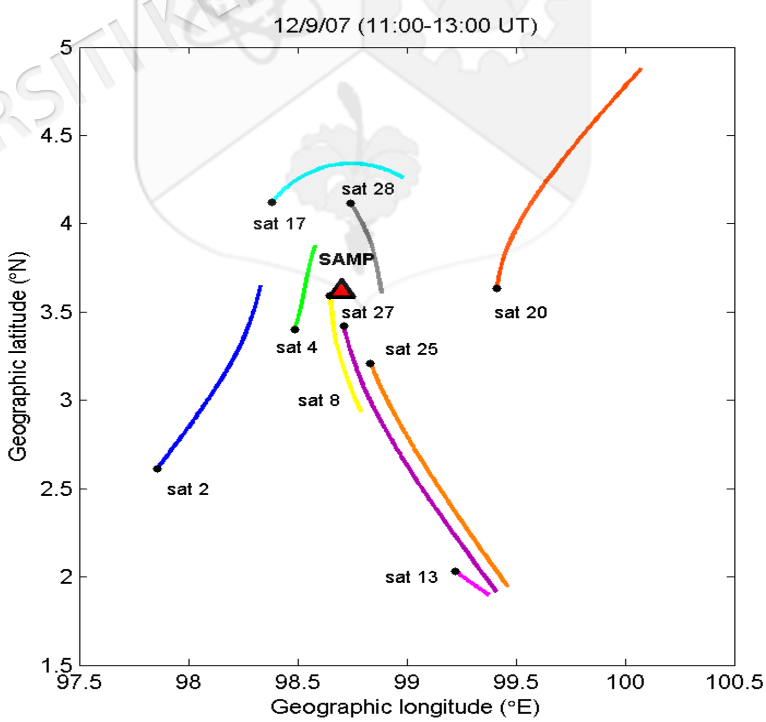

Figure 4.22 The visible GPS satellites at SAMP station for the period of 11:00-13:00 UT on 12 September 2007.

Referring to Figure 4.23(a), a sinusoidal wave, which consists of a depletion-enhancement of about 4-8 TECU was seen between 11:15 and 11:45 UT at SAMP station (SAT 4). In Figure 4.23(b), the VTEC variation for SAMP (SAT 8) show 3 oscillations with peak-to-peak value of about 7 TECU and duration of 35 minutes was observed from 11:25 to 12:00 UT. As shown in Figures 4.23(c)-(d), a VTEC enhancement of about 4 TECU was observed for satellite 4, while a VTEC enhancement and depletion was seen for satellite 27 between 11:33 and 11:45 UT at USMP.

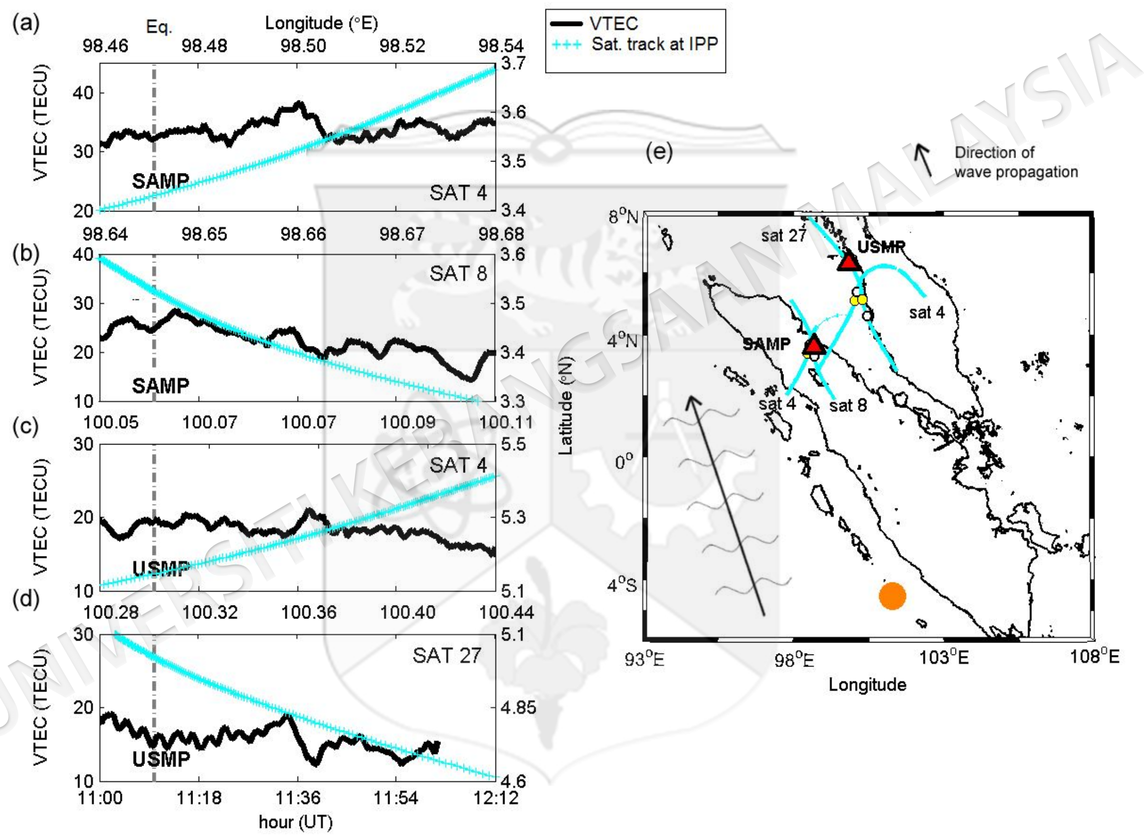

Figure 4.23 Temporal and spatial VTEC variations observed between 11:00 and 12:12 UT on 12 September 2007 at (a)-(b) SAMP and (c)-(d) USMP stations. (e) Satellite trajectories on 12 September 2007.

Although not shown in the result, VTEC oscillations were also observed at GETI station but its amplitude is largely attenuated. The two GPS stations (SAMP and USMP) where effects of the earthquake were observed are located northwest of the epicenter, while no VTEC variations were seen after the earthquake at COCO station, which is located south of the epicenter. Similar to the previous earthquake events, this observation shows directivity of the VTEC variations with respect to the azimuth of the epicenter.

Figure 4.24 presents the VTEC variations and the filtered VTEC for satellites 4 and 8 at SAMP station and satellites 4 and 27 at USMP station for the period between 11:00 and 12:12 UT on 11, 12 and 13 September 2007. As shown in Figure 4.24(a), short period VTEC fluctuations were observed starting from 8 minutes following the event until about 39 minutes after by SAT 4 at SAMP station. The oscillation reached its peak at 11:31 UT with amplitude of 1.2 TECU and duration of about 5.4 minutes. In Figure 4.24(b), the peak oscillation observed by satellite 8 was detected at about 20 minutes after the event (11:30 UT) with a longer period of about 7.5 minutes. As shown in Figures 4.24(c)-(d), non-periodic oscillations were detected by both satellites 4 and 27 at about 24 and 27 minutes after the earthquake, respectively. The oscillations observed by SAT 4 and 27 correspond to the associated VTEC peak and have periods of about 4.9 and 7.2 minutes, respectively and peak amplitudes of 1.1 and 1.4 TECU, respectively. It is also shown in the figure that no significant VTEC oscillations were detected on the day before and after the earthquake day during the observation period.

The horizontal propagation velocity in this event is approximated by taking the distance and time lag of the disturbance peak arrivals between the satellites at SAMP (SAT 4 and 8) and at USMP (SAT 4 and 27). The time lags of the disturbance peak arrivals are 4.5 minutes (between SAT 4), 7.5 minutes (between SAT 4 and 27), 3 minutes (between SAT 8 and SAT 4) and 4 minutes (between SAT 8 and SAT 27). The distances between these satellites in the same order are 261 km, 255 km, 256 km and 247 km. Thus, the estimated horizontal propagation velocities of the observed ionospheric disturbances are 666 m/s, 570 m/s, 1386 m/s and 1025 m/s, with an average velocity of 912 m/s. The result shows consistent propagation velocity with those observed in previous events, although the GPS CID during this event were detected at GPS stations located about 1000 km away from the epicenter.

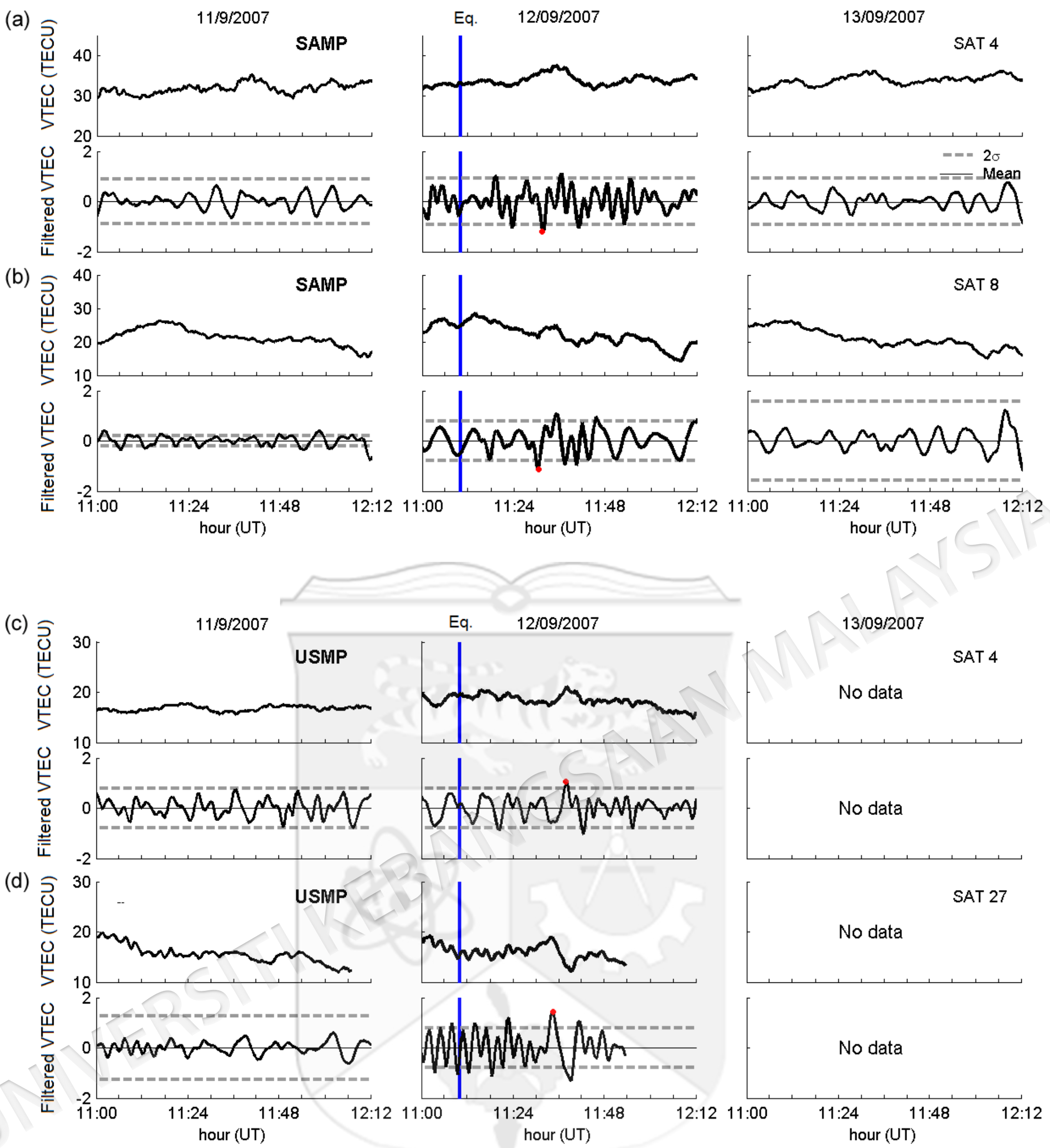

Figure 4.24 VTEC variations and the filtered VTEC for satellites (a) 4 and (b) 8 at SAMP station and satellites (c) 4 and (d) 27 at USMP station for the period between 11:00 and 12:12 UT on 11, 12 and 13 September 2007

b. Observation of Geomagnetic variations

Figure 4.25 presents the geomagnetic field variations and the filtered geomagnetic H, D and Z components during the M8.5 earthquake event that occurred at 11:10 UT on 12 September 2007 event at KTB station. The KTB station is located about 495 km from the epicenters of the earthquake events, respectively. As shown in Figure

4.25(a), rapid fluctuations in the H and D components and a sudden decrease of 0.3 nT in the Z-component were seen about 2 minutes after the event. During this time, the H and D components fluctuate between 0.3 and 0.6 nT with periods of 4-6 seconds. Following that time, a sudden decrease in the H, D and Z components were observed almost simultaneously at about 11:21 UT. About 35 minutes after, the geomagnetic field components start to recover to their normal levels.

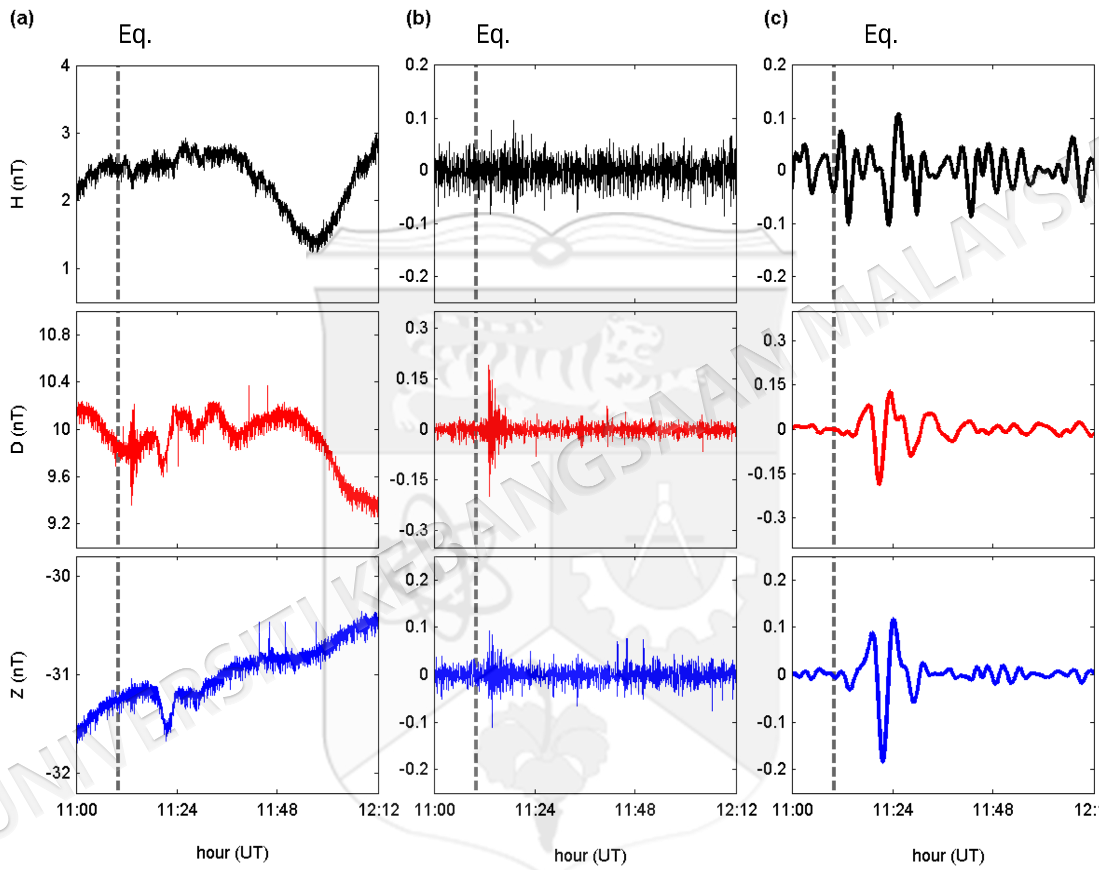

Figure 4.25 (a) Geomagnetic field variations and the filtered geomagnetic H, D and Z components between 11:00 and 12:12 UT on 12 September 2007 in the (b) Pc3 and (c) Pc5 bands.

As shown in Figures 4.25(b), strong fluctuations in the Pc3 band with periods of about 14-18 seconds were found shortly after the earthquake. These fluctuations correspond with the high frequency variations in Figure 4.25(a). However, no significant fluctuations in the Pc3 band were found after this period. As shown in Figure 4.25(c), a Pc5 pulsation was detected in all the geomagnetic components about 11 minutes after the event. The Pc5 pulsation corresponds to the decrease in the H, D and Z variations and has a period of about 4.8 minutes. The measurements at higher latitude stations such as at PHU, GZH, KDU and LZH stations also showed no such Pc5 pulsation, indicating that the pulsation observed at KTB station might be generated by the earthquake.

4.4 DISCUSSION

Table 4.3 summarizes the parameters of the ionospheric disturbances during the 26 December 2004, 28 March 2005, 14 May 2005 and 12 September 2007 earthquake events. In this table, the time of the oscillation peak (UT) (obtained from filtered GPS VTEC in Figures 4.5, 4.12, 4.20 and 4.24), coordinates of the ionospheric disturbances at sub-ionospheric points (degree), time lag of the disturbance with respect to the earthquake (δt), maximum amplitude (A_{max}), disturbance period (ΔT) and velocity of the ionospheric disturbances (m/s). The table shows that the time lag, period and average horizontal propagation velocity of the ionospheric disturbances during all the events are 10-27 minutes, 5-8 minutes and 912-1271 m/s, respectively.

It is shown that the average horizontal propagation velocities of the ionospheric disturbances for events 2 and 4 are slightly lower than the one in event 3 despite their larger magnitudes. However, the relationship between the earthquake magnitude and the horizontal propagation velocity has not been reported before. Previous observations made by Afraimovich et al. (2001, 2005) during several earthquake events show independent relation between the horizontal propagation velocity and the earthquake magnitude. Therefore, it is believed that the velocity of the CID varies from one event to another and is most probably connected with the earthquake morphology and occurrence time. It is worth mentioning here that both events 2 and 4 occurred during nighttime, at about 23:09 LT and 18:10 LT, respectively, while the event 3 occurred during midday, at about 12:05 LT, which may be the reason for the variation in the velocity of the CID between the two events.

Table 4.3 The parameters of the ionospheric disturbances during four Sumatra earthquake events.

Event	Station	Sat.	t_{peak} (UT)	Lat. (°N)	Lon. (°E)	δt (s)	$\|A\|_{max}$ (TECU)	ΔT (s)	Vel. (m/s)	Ave. Vel. (m/s)
1	26 December 2004, t = 00:58:53 UT									
	SAMP	23	1:10:00	3.95	98.57	667	1.0	420		
	ARAU	23	1:14:00	4.71	100.14	907	0.75	480	1471	1271
	USMP	23	1:14:00	5.62	100.17	907	0.85	504	1071	
2	28 March 2005, t = 16:09:36 UT									
	SAMP	16	16:22:30	3.67	98.69	774	3.9	288		
	LGKW	1	16:27:00	4.65	100.01	1050	1.0	450	1243	922
	ARAU	16	16:33:00	4.51	100.24	1404	1.4	504	600	
3	14 May 2005, t = 5:05:18 UT									
	SAMP	6	5:15:30	3.72	98.50	612	8.8	504	1384	
		26	5:15:30	3.85	98.80	612	9.6	504	1250	1259
		29	5:15:30	4.05	98.92	612	8.6	504	1143	
	ARAU	9	5:19:30	5.99	100.45	852	2.4	396		
4	12 September 2007, t = 11:10:26 UT									
	SAMP	4	11:31:26	3.54	98.51	1260	1.2	324		
		8	11:30:29	3.48	98.65	1203	1.2	450		
	USMP	4	11:37:58	5.28	100.09	1652	1.1	414	666	912
									570	
		27	11:34:30	4.95	100.32	1444	1.4	432	1386	
									1025	

As mentioned earlier, the GPS VTEC variations during all the events show directivity with respect to the azimuth of the epicenters in the northwest and northeast direction. The directivity of CID has been reported by Calais and Minster (1995) and Heki and Ping (2005) in the mid-latitude region and by Astafyeva and Afraimovich (2006), Otsuka et al. (2006) and Shinagawa et al. (2007) over the equatorial region. In this study, CID was observed over the equatorial region where the geomagnetic lines are nearly horizontal. Otsuka et al. (2006) and Shinagawa et al. (2007) found larger VTEC enhancements to the north of the epicenter compared to the south, while no VTEC enhancements were seen east of the epicenter during the 26 December 2004 Sumatran earthquake. The observations were attributed to the directivity of the response of the electron density variation to the acoustic waves in the neutral atmosphere. Similar to these observations, it is found that VTEC variations occurred northwest and northeast of the epicenters, while no VTEC variations were observed in the south and east of the epicenters.

This directivity is due to the fact that the geomagnetic field is nearly horizontal in the north of the epicenter and oblique in the south. As acoustic waves propagate to ionospheric heights, neutral particles oscillate through the ion-neutral collision and move the ions parallel to the geomagnetic lines but restrict the ion motion in the oblique geomagnetic field lines. The absence of the VTEC variations in the south of the epicenters (e.g. BAKO and COCO stations) is most probably due to their large distances from the epicenters, while in the east of the epicenters, the ion mobility is not affected by the neutral wind perpendicular to the geomagnetic field lines.

The observations during the 26 December 2004, 28 March 2005 and 14 May 2005 events show that only the nearest stations to the epicenters detected disturbances, which are SAMP, ARAU, USMP and LKGW but no VTEC disturbances were observed at UTMJ, KTPK and GETI even though they are located about 500-900 km northeast of the epicenters. Previous observation made by Astafyeva and Afraimovich (2006) during the December 2004 earthquake however, showed secondary CID in the form of wave packets in both northeast and northwest of the epicenter up to a distance of 5000 km. The absence of the VTEC disturbances at UTMJ, KTPK and GETI stations could be due to the difference of the angle between the line-of-sight and the acoustic wavefront (Heki, 2006a, 2006b). The CID function consists of positive and negative parts, which partly cancel each other when the line-of-sight is not parallel with the acoustic wavefront. Heki (2006b) used the ray tracing method on acoustic waves and found that shallower incidence angles cause larger disturbances than deeper angles as the positive and negative parts cancel less of each other. The results coupled the fact that the absence of the N-wave signal at UTMJ, KTPK and GETI stations might be partly due to their deep incidence angle.

The geomagnetic field measurements show the occurrences of high frequency fluctuations of periods 4-16 seconds in the geomagnetic H, D and Z components shortly after the earthquakes. This phenomenon is probably due to the vibration of the magnetometer sensor by the earthquake. If the P/S wave reaches KTB station, the sensor also vibrates. This is because the seismic waves cause the Earth's crust to conduct. When the ground vibrates with velocity $\boldsymbol{v}$ in the Earth's magnetic field $\boldsymbol{B}$ during the earthquake, the electromotive force $\boldsymbol{v}\times\boldsymbol{B}$ is generated in the Earth, resulting in the flow of electric currents in the conducting crust. These currents give a rise to magnetic fields at the observation stations on the Earth's surface (Honkura et al. 2000; Ujihara et al. 2004). As the Earth's magnetic field intensity is more than 30,000 nT, even a small motion of the magnetic sensor in the background magnetic field will result in large magnetic field variations measured by the sensor. Since the magnitudes of the considered earthquakes are large (M>7) and KTB station is located only 230-560 km from the epicenters, the magnetometer sensor should suffer the oscillation of the seismic waves by the earthquake.

As for the Pc5 pulsations of 4.2-4.8 minutes that occurred at about 11 minutes after the earthquake, Iyemori et al. (2005) proposed an ionospheric dynamo mechanism in the ionospheric E-layer at an altitude of 100-120 km over the epicenter. This mechanism is generated by the vertical wind oscillation caused by the atmospheric duct resonance set up by the earthquake. During the earthquake, vertical ground motions cause atmospheric waves to propagate upward to the ionosphere, and then part of the wave energy is reflected back to the ionospheric E-layer to form a duct resonance (Tahira 1995). The result is a vertical oscillation in the atmosphere with a resonance period of 4.8 minutes in the ionospheric E-layer, which is generated by the dynamo current. Since the geomagnetic latitudes of the epicenters and KTB station are almost the same, about 10±4° South of the geomagnetic equator, the electric field produced by the dynamo current in the east-west direction over the epicenter is mapped along the geomagnetic field lines above KTB station. The electric field then generates the ionospheric currents, which consist of the Pederson in the north-south and Hall in the east-west direction. These ionospheric currents are observed over KTB station as the magnetic Pc5 pulsation in the horizontal (H) and declination (D) components. The time lag of the observed Pc5 pulsation is consistent with the time required for acoustic waves to travel from ground to the ionosphere, as also observed by Iyemori et al. (2005).

The pulsation periods of about 4.2-4.8 minutes are consistent with the resonant period of the atmospheric oscillation observed by Shinagawa et al. (2007) during the 26 December 2004 Sumatran earthquake. By modeling the sea surface perturbation, they have reproduced an atmospheric oscillation with periods of 3-5 minutes at an altitude of about 100-120 km above the epicenter. Acoustic waves with periods of about 3-5 minutes are considered to be trapped between the ground and the lower thermosphere and these waves have a standing wave character directly over the earthquake region (Walterscheid et al. 2003; Shinagawa et al. 2007). The results coupled the fact that the acoustic waves in neutral motion induced near the epicenter drives the oscillatory electric field in the ionosphere, as proposed by Iyemori et al. (2005).

The occurrence of the magnetic Pc3 pulsation of 18-22 seconds at about 8 minutes after the 26 December 2004 event can be explained as the generation of magnetohydrodynamic (MHD) waves by the dynamo current and electric field in the ionosphere (Pokhotelov et al. 1995). These waves propagate in the upper ionosphere to the magnetosphere as a magnetosonic wave that could cause field-line resonance (FLR) if resonance conditions are met. The Pc3 type pulsation observed at KTB station could be explained as the result of FLR. The possible mechanisms of the Pc3 and Pc5 geomagnetic pulsations are illustrated in the schematic drawing as shown in Figure 4.26.

As shown earlier, the correlation between the ionospheric and geomagnetic responses shows a good agreement during two of the events studied, which are events 1 and 3. The results are compared with those in previous observations. Otsuka et al. (2006) modeled the ray paths of the acoustic waves using the altitude profile of the sound velocity. In this model, the calculated time lag for these waves to reach the ionospheric F-layer at a horizontal distance of about 250 km from the epicenter is about 15 minutes. This time lag is close to the one observed at SAMP station. However, the calculated result in the model represents that acoustic waves take about 20 minutes to reach the E-layer at a horizontal distance of about 450 km from the epicenter, whereas the Pc5 pulsation at KTB station was detected 11 minutes after the earthquake. The discrepancy between the calculated and observational results is probably due to the assumption in the model that acoustic waves are generated from a point source at the epicenter. It is likely that acoustic waves are generated at multiple point sources, which move to the north from the epicenter (Otsuka et al. 2006).

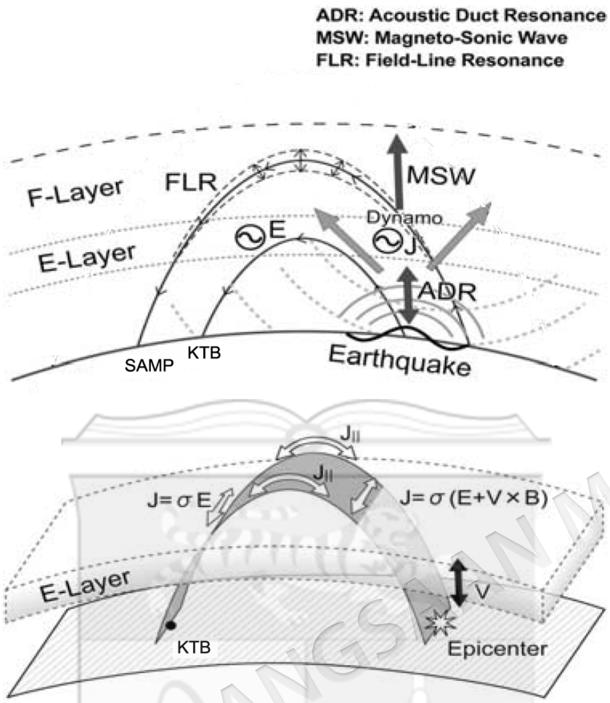

Figure 4.26 A schematic drawing of the possible generation mechanism of geomagnetic pulsations caused by an earthquake.

Source: Adapted from Iyemori et al. (2005)

It is also observed that the period of both GPS VTEC and magnetic oscillations are similar. Francis (1975) analyzed the properties of acoustic-gravity modes using a realistic dissipative atmosphere with viscosity and thermal conductivity. They found that ducted acoustic waves propagate in the thermosphere and carry significant energy at ionospheric F region heights. Based on this hypothesis, it is believed that the acoustic waves with a period of about 5 minutes are trapped between the ground and the E-layer. However, some of the wave energy leaks into the thermosphere, producing oscillations with similar periods in the ionospheric F region as seen in the VTEC variation at SAMP station.

4.5 CONCLUSION

The investigation of ionospheric and geomagnetic responses during the 26 December 2004, 28 March 2005, 14 May 2005 and 12 September 2007 Sumatran earthquakes have been conducted using GPS and magnetometer stations located in the near zone of the epicenters. These earthquake events occurred during very low solar and geomagnetic activity. The GPS VTEC results show directivity in the VTEC variations in the northeast direction of the epicenters only. This phenomenon could be due to the ion mobility that is largest when acoustic wave propagation is parallel to the geomagnetic field lines, which in this case is in the northeast of the epicenters. VTEC variations were not observed in the east of the epicenters, as the ion mobility is not affected by the neutral wind perpendicular to the geomagnetic field lines. During the four events, VTEC oscillations with periods of 5-8 minutes were observed about 10-27 minutes after the events and have horizontal propagation velocities of 912-1271 m/s. The geomagnetic field measurements at KTB station show high frequency fluctuations shortly after the earthquake, followed by a long period Pc5 pulsation occurring at about 11 minutes after the event. In addition to these disturbances, a Pc3 pulsation was also observed at about 8 minutes after the 26 December 2004 earthquake. It is concluded that the rapid fluctuations are due to the vibration of the magnetometer sensor, while the Pc5 pulsation is caused by the ionospheric dynamo mechanism set up by the upward propagating acoustic wave to the ionosphere. The Pc3 pulsation is most likely attributed to the magnetic field line resonance with a magnetosonic wave generated from the electric and magnetic fields of the dynamo current caused by the earthquake. The results of correlation between the filtered GPS VTEC and Pc5 pulsation were in good agreement, suggesting that the acoustic pulse generated near the epicenter propagates upwards to ionospheric heights and induce disturbances in the ionospheric E and F regions.

CHAPTER V

SHORT-TERM ANALYSIS OF IONOSPHERIC PERTURBATIONS BEFORE EARTHQUAKES

This chapter investigates the occurrence of ionospheric perturbations prior to the strong earthquake events surrounding the Sumatra region that occurred during the period of 2004-2007 primarily using the GPS technique. The investigation based on short-term analysis was done for six strong earthquake events with magnitude greater than 6.5 using VTEC measurements at seven GPS stations located surrounding the earthquake epicentres. The chapter also compares the results of VTEC variations with electron density measurements obtained from CHAMP satellite. This chapter is structured in the following manner: the geographical location of the earthquakes, the magnetic and solar conditions during each earthquake event, followed by the results, discussion and conclusion. In the analyses, the diurnal variations of the GPS VTEC measurements and the percentage of VTEC deviation for several days before, during and a day after each event are presented alongside the magnetic and solar data. The VTEC measurements along individual satellite passes are also presented in this chapter. Finally, the chapter investigates the electron density data obtained from CHAMP satellite over the earthquake epicentres during each earthquake observation period.

5.1 GEOGRAPHICAL LOCATION OF THE EARTHQUAKES

As mentioned in Section 4.2, the short-term pre-earthquake ionospheric perturbation analysis for six strong earthquakes with magnitude of $M > 6.5$ that took place surrounding the Sumatra region during the period of 2004 - 2007 are selected for this study. Table 5.1 presents the occurrence time, geographic coordinates, depth, magnitude and the radius of the earthquake preparation zone of these events. In this work, the radius of the earthquake preparation zone for each earthquake is estimated using the Dobrovolsky formula in (2.4):

Table 5.1 The occurrence time, geographic coordinates, depth, magnitude and earthquake preparation radius of selected earthquake events during 2004-2007 (USGS 2009).

Event	Date	Time of earthquake (UT)	Place	Geographic Lat. (°)	Geographic Lon. (°)	Depth (km)	M	Earthquake preparation radius, R (km)
1	26.12.2004	00:58	North Sumatra	3.32°N	95.85°	30	9.3	9977
2	26.2.2005	12:56	Simuele	2.93°N	95.56°	27	6.8	839
3	28.3.2005	16:09	North Sumatra	2.08°N	97.01°	30	8.6	4988
5	24.7.2005	15:42	Nicobar Islands, India	7.91°N	92.14°	16	7.2	1247
6	12.9.2007	11:10	South Sumatra	4.52°S	101.37°	34	8.5	4518
7	12.9.2007	23:49	Kepulauan Mentawai	2.51°S	100.91°	30	7.9	2495

In this analysis, GPS measurements obtained from ARAU, USMP, UTMJ, NTUS, PSKI, BSAT and COCO receiver stations surrounding the earthquake epicentres are collected to examine the ionospheric perturbations prior to large earthquake events over Sumatra. Table 5.2 presents the geographic coordinates of the GPS receiver stations and their distances from the epicentres. In the table, the highlighted box in grey indicates that the station is located outside the boundary of the earthquake preparation radius, which is calculated using (2.4). In the analysis, GPS VTEC anomalies associated with earthquakes located within distances between 90 and 2300 km are investigated.

Table 5.2 The geographic coordinates of GPS stations and their distances from the epicentres.

GPS station	GG Coordinate	Country	Distance from epicentre (km) Event 1	2	3	5	6	7
ARAU	6.50°N, 100.28°E	Malaysia	606	654	602	912	1231	1004
USMP	5.36°N, 100.30°E	Malaysia	543	-	-	945	1105	878
UTMJ	1.56°N, 103.64°E	Malaysia	887	-	-	1456	722	-
NTUS	1.36°N, 103.69°E	Singapore	897	-	-	-	703	530
PSKI	1.13°S, 100.35°E	Indonesia	703	698	515	1352	394	-
BSAT	3.08°S, 100.28°E	Indonesia	493	845	679	1519	201	94
COCO	12.19°S, 96.85°E	Australia	1725	1687	1698	2295	986	1164

- indicates 'No data' period

5.2 ANALYSIS OF IONOSPHERIC VARIATIONS BEFORE EARTHQUAKES

The ionospheric perturbations before the six earthquake events over Sumatra are investigated. In these analyses, both GPS VTEC obtained from all satellites and the VTEC along individual satellite passes prior to these events are analyzed. In this work, the diurnal VTEC variations as well as the percentage of VTEC deviation for the period between seven days before and a day after the events are presented. Based on the solar and magnetic conditions presented in Chapter 3, the seismo-ionospheric anomalies are identified and characterized. The GIM VTEC and CHAMP satellite electron density measurements are also examined to confirm the observations of the GPS VTEC variations. The ionospheric variability at equatorial latitudes and the behavior of the equatorial ionization anomaly (EIA) structure before the occurrences of strong earthquakes in the Sumatra region is also investigated. The six events are discussed in the following sections:

5.2.1 The 26 December 2004 Sumatra-Andaman Earthquake

a. GPS VTEC variations

The Sumatra-Andaman earthquake of 26 December 2004 is the fourth largest earthquake in the world since 1900 and is the largest since the 1964 Prince William Sound, Alaskan earthquake. The earthquake occurred off the west coast of Northern Sumatra near Banda Aceh, Indonesia at 00:58 UT with a magnitude M9.3 and depth of 30 km as shown in Table 5.1. Figure 5.1 presents the geomagnetic indices Dst, AE, Kp and Ap, and the VTEC variations and the associated upper and lower bounds for the observation period between 16 and 27 December 2004 observed at six GPS stations. The vertical dashed line in the figure marks the time of the earthquake. The horizontal dashed lines in Figures 5.1(a)-(b) show the threshold values of the Dst and Kp indices, which are 15 nT and 4, respectively. The crosses in Figures 5.1(c)-(h) show detections of VTEC values, which exceed the upper and lower bounds using the method discussed in Section 3.6.1. In these figures, detections were seen between the period of 10 days and a few hours before the event at all the 6 stations. The detections were also observed a day after the event but they are due to the aftershocks of the earthquake.

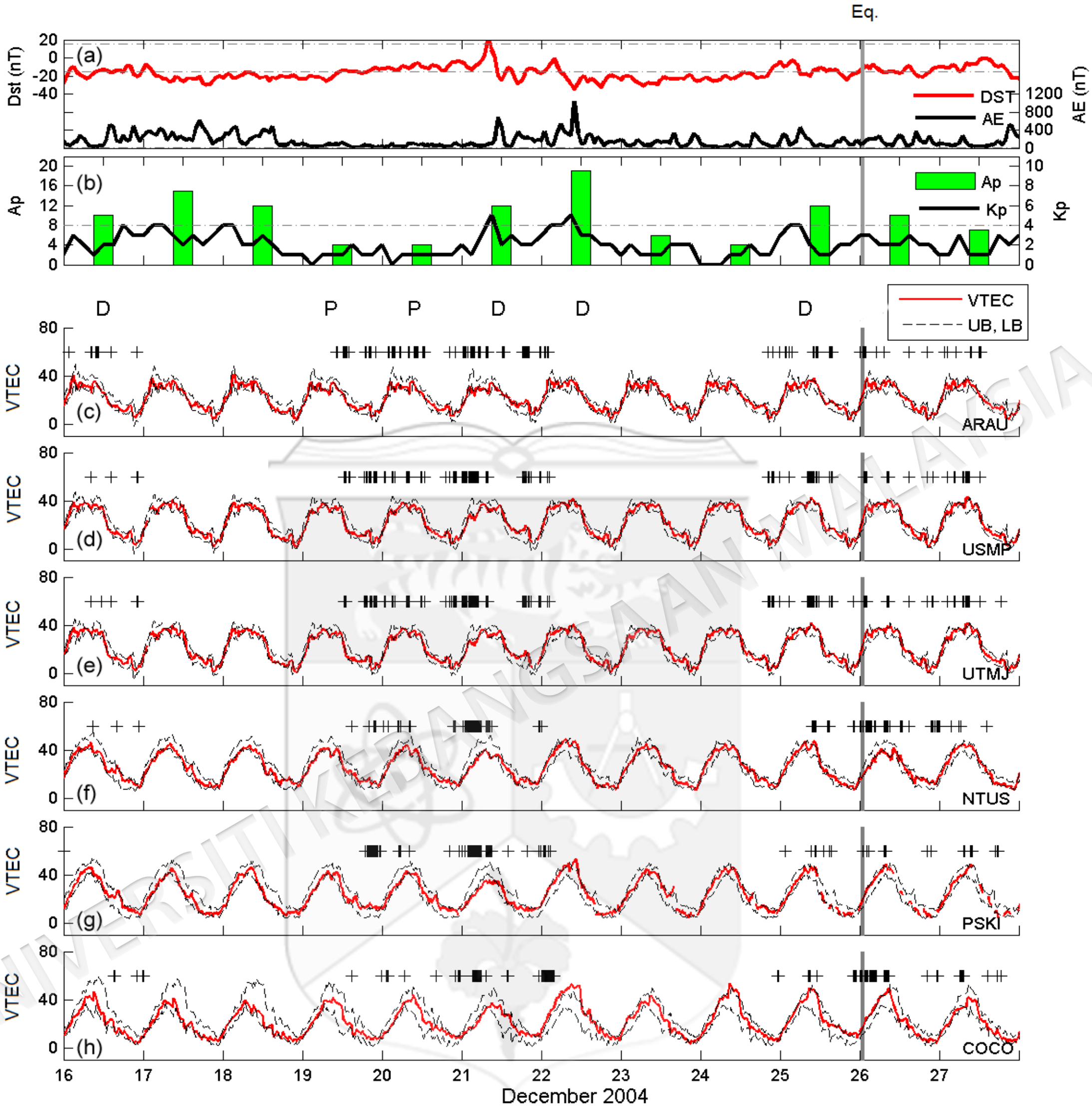

Figure 5.1 The geomagnetic indices (a) Dst and AE, (b) Ap and Kp, and the (c-h) VTEC variations (red solid line) and their associated lower and upper bounds (grey dashed lines) between 19 and 27 December 2004 at six GPS stations. The crosses show detections of VTEC anomalies.

As indicated by the Dst, AE, Kp and Ap indices in Figure 5.1(a)-(b), the geomagnetic conditions during the days of 16, 21, 22 and 25 December were disturbed, while the geomagnetic levels on 19 and 20 December were characterized as quiet. Akhoondzadeh et al. (2010) stated that ionospheric anomalies that are detected during quiet geomagnetic conditions can be regarded as earthquake precursors. Based on this statement, only VTEC anomalies observed on 19 and 20 December are considered as possible pre-earthquake ionospheric anomalies, hence they are highlighted by the P character and the ones seen on disturbed days are highlighted by the D character.

Figure 5.2 presents the percentage of VTEC deviation, calculated using (3.34)-(3.35) for the same observation period presented in Figure 5.1 at six GPS stations. In this figure, the positive and negative values of the filtered ΔVTEC% show the variation with respect to the upper and lower bound, respectively.

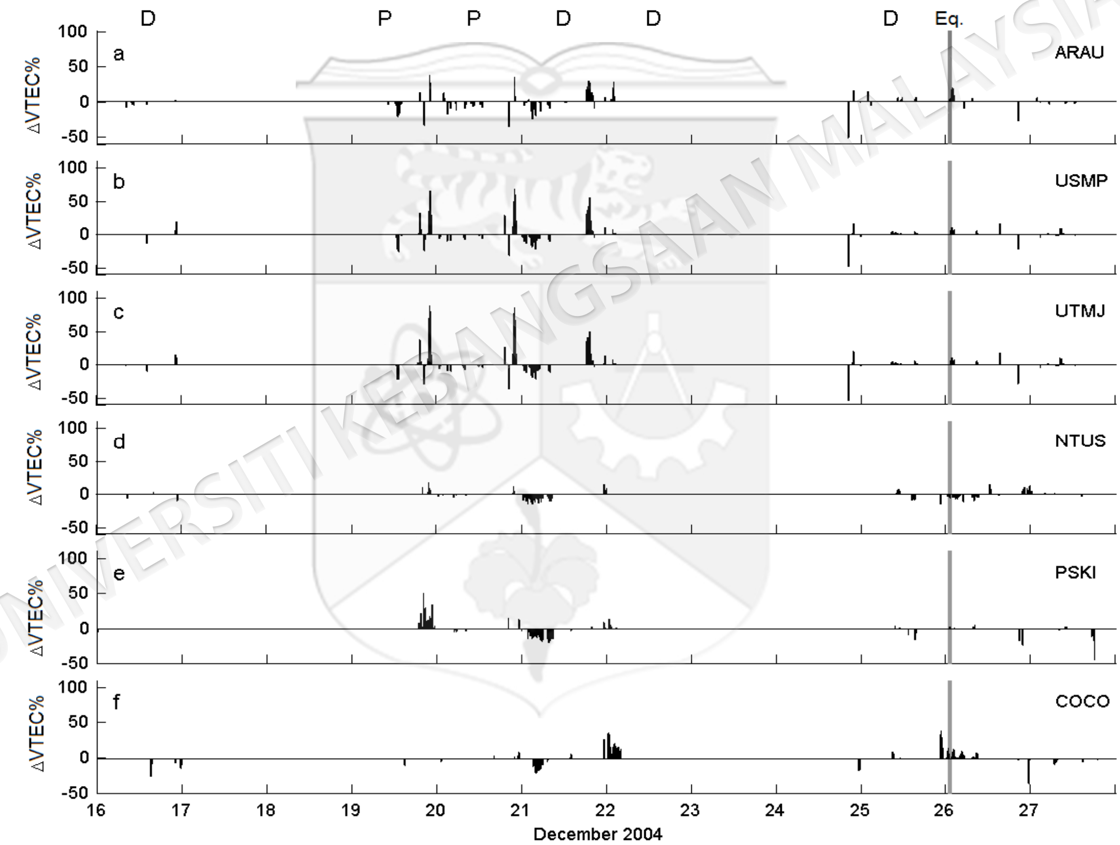

Figure 5.2 The percentage of VTEC deviation between 16 and 27 December 2004 at six GPS stations. The positive and negative values show the ΔVTEC% with respect to their upper and lower bound, respectively.

Referring to the days highlighted in Figure 5.2, significant increases in ΔVTEC% of about 17-87% were observed simultaneously from 18:00-23:00 UT on 19 and 20 December 2004 at ARAU, USMP, UTMJ, NTUS and PSKI stations but were not observed at COCO station. The precursory effects of the great Sumatra-

Andaman earthquake have already been reported by Dabas et al. (2007) and Saroso et al. (2008) using ground-based measurements obtained from a single station at New Delhi and Indonesia, respectively. However, it is again been examined in this result for the comparison between ground and satellite based ionospheric measurements.

As shown earlier in Figure 5.2, significant increases and decreases were found during 6-7 days before the 26 December 2004 earthquake. These anomalies occurred during very quiet geomagnetic conditions. However, Kazimirovski (2002) stated that the VTEC also generates significant day-to-day variations during magnetically quiet periods due to the thermospheric dynamics caused by different types of atmospheric disturbances from the lower atmosphere. Earlier observations have confirmed that the day-to-day VTEC variability caused by thermospheric dynamics in the equatorial latitudes does not usually exceed 20% (Forbes et al., 2000; Rishbeth and Mendillo, 2001; Bilitza et al., 2004). The result shows that the maximum values of the daytime positive anomalies observed during 6-7 days before the event mostly exceeded 20%. Dabas et al. (2007) also found such anomalies in the foF2 measurements about 1, 4 and 7 days before the same earthquake but they appear to be much weaker than the ones observed in this result. Saroso et al. (2008) also observed VTEC anomalies on 21 December 2004 (5 days before the same earthquake) using measurements at Sampali station in Indonesia. However, the ionospheric anomalies considered as earthquake precursors by Dabas et al. (2007) and Saroso et al. (2008) fall on disturbed days, which are 21, 22 and 25 December and thus cannot be regarded as earthquake related signals.

In order to test the locality of the observations in Figures 5.1-5.2, the VTEC variations and the percentage of VTEC deviation analyses are repeated by examining the measurements from a CORS GPS station at Bar Habour (BARH), USA (44.39°N, 68.22°W) as shown in Figure 5.3. BARH station is a remote station, which is located about 14490 km away from the earthquake epicentre. As shown in the top panel of the figure, detections of VTEC anomalies were also found from 19 and 20 December 2004 during very quiet geomagnetic conditions at BARH station. In the bottom panel of the figure, it was observed that the ΔVTEC% values on these days range from about -23 to 23% but they appear insignificant and different from the ones observed at stations closer to the epicentre.

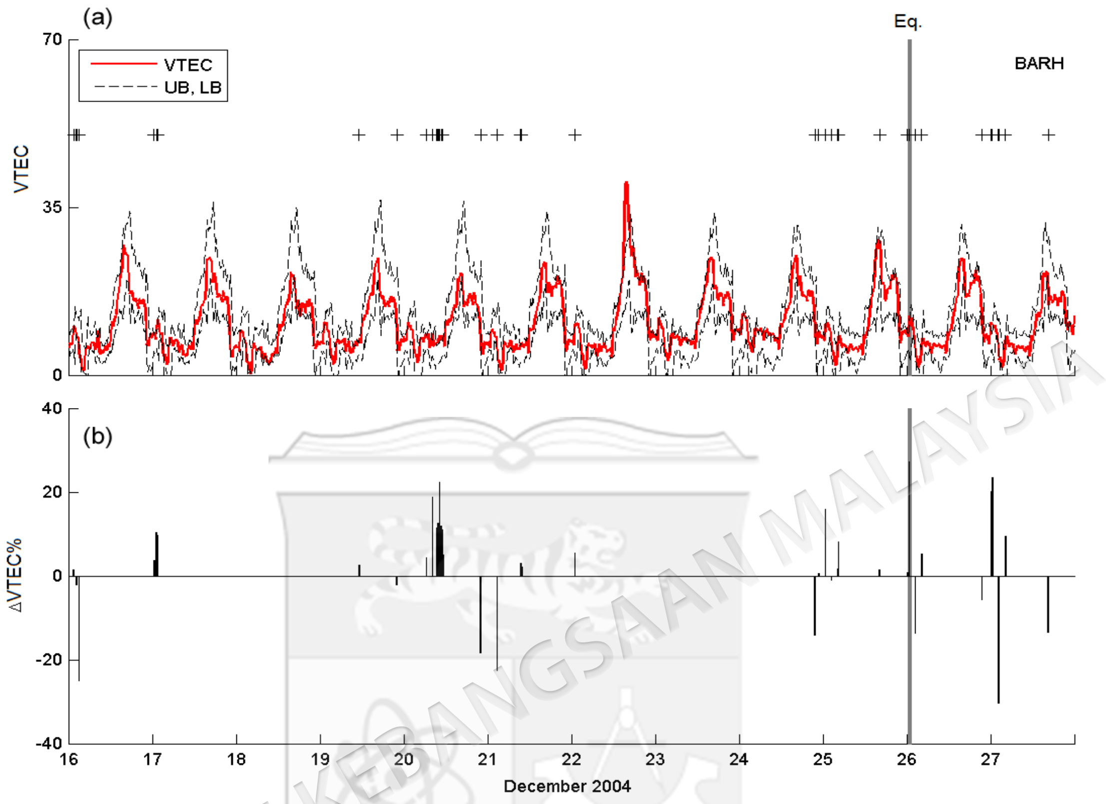

Figure 5.3 Validation of VTEC variations and percentage of VTEC deviation between 16 and 27 December 2004 at BARH station, which is located 14490 km away from the epicentre.

To investigate the temporal and spatial variations of the VTEC anomalies before the event, measurements from individual satellites are examined. This analysis gives a better insight on the effect and possible locations of the ionospheric anomalies. As shown earlier in Figures 5.1-5.2, VTEC anomalies were detected simultaneously on 19 and 20 December 2004 at six stations. Based on these detections, VTEC variations are zoomed in during the period from 17:00-22:00 UT on 19 and 20 December for satellite 15 and the upper bound of 19 December at 6 GPS stations as shown in Figure 5.4. The arrow in the figures indicates increase or decrease in VTEC with respect to the upper bound. The right panel of the figure illustrates the epicentre and the satellite trajectories above the respective GPS stations on 19 December 2004. Although it is not shown in the result, 12 satellites were observed during the period of

17:00-22:00 UT on 19 December 2004 at PSKI station but only satellite 15 was significantly affected by the earthquake preparation process.

As shown in Figure 5.4(a)-(f), the VTEC measurements on 19 and 20 December 2004 show variability from one station to another. During both days, VTEC increases of about 2-5 TECU with respect to the upper bound were generally observed from 18:00-22:00 UT almost simultaneously at ARAU, USMP and UTMJ stations. The VTEC at both NTUS and PSKI stations on 19 December only start to increase from 19:00-22:00 UT, while the VTEC on the following day did not show any significant variation. Meanwhile, no increase in VTEC was observed on both days at COCO station. It is worth to mention that the VTEC variations, which fall below the upper bound level are not considered as positive anomalies, as formulated in (3.34). It was observed that the VTEC increases detected by satellite 15 correlate well with the increases found in the ΔVTEC% shown in Figure 5.2. These positive anomalies were observed within the boundary of the earthquake preparation zone at distances ranging from 500-1700 km from the epicentre, which are within the radius of the earthquake preparation zone of the 26 December 2004 earthquake as mentioned in Table 5.1.

In order to further confirm the GPS VTEC anomalies on 19 and 20 December, the CHAMP electron density measurements during these days were obtained from GFZ (http://isdc.gfz-potsdam.de). Unfortunately, the N_e measurements during the observation time of the VTEC anomalies could not be examined due to data unavailability.

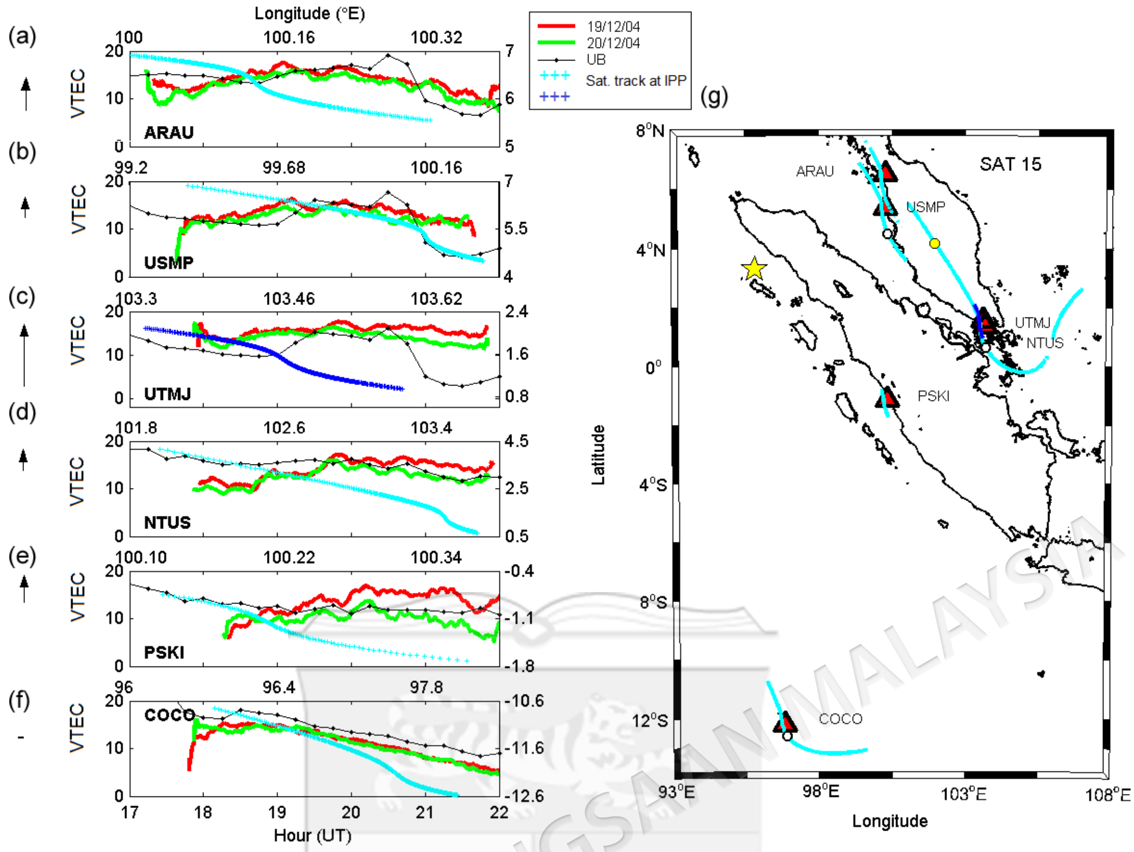

Figure 5.4 (a)-(f) Temporal and spatial VTEC variations as well as the associated upper bound at 6 GPS stations for satellite 15 observed during 17-22 UT on 19 and 20 December 2004. (g) The satellite trajectories on 19 December. The solid and open circles denote time marks for the start and end of the observation period, respectively.

5.2.2 The 26 February 2005 Earthquake

a. GPS VTEC variations

The 26 February 2005 earthquake occurred on Simuele Island in Northern Sumatra at 12:56 UT with a magnitude M6.8 and depth of 27 km. The same analysis presented in the previous event is repeated, whereby the geomagnetic indices as well as the VTEC variations and the associated upper and lower bounds as well as the percentage of VTEC deviation between 16 and 27 February 2005 at four GPS stations are shown Figures 5.5 and 5.6, respectively. As mentioned in Section 3.10.2, only days of 22 and 23 February were characterized by both very quiet and very low geomagnetic and solar activity, respectively. As shown in Figure 5.5(c)-(f), detections of pre-earthquake

VTEC anomalies were found about from 4 days to a few hours before the event at all the four stations but only the anomalies on 22 and 23 February were detected during quiet geomagnetic conditions.

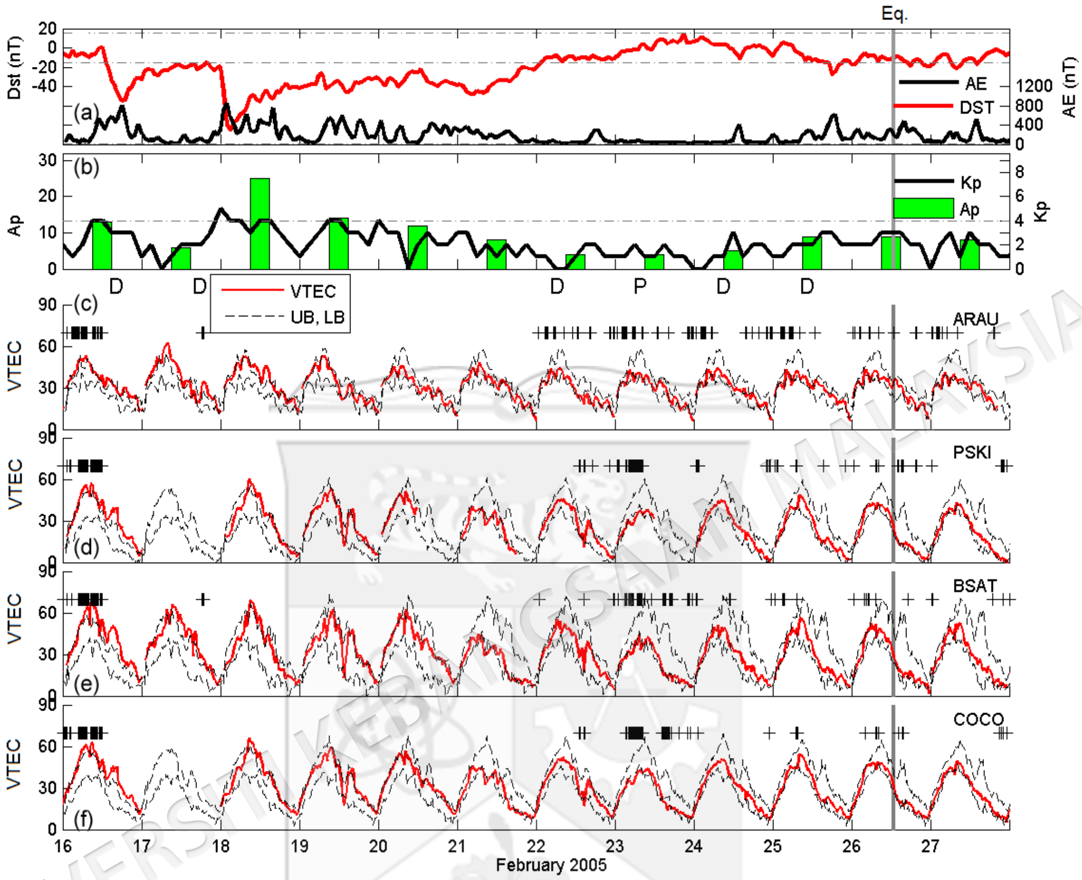

Figure 5.5 The geomagnetic indices (a) Dst and AE, (b) Kp and Ap and (c)-(f) VTEC variations and the associated upper and lower bounds between 16 and 27 February 2005 at four GPS stations.

Referring to marked days in Figure 5.6, decreases in the ΔVTEC% were prominently observed on 22 and 23 February, which is 3-4 days before the event. On 22 February 2005, significant decreases with short periods were observed almost simultaneously at about 16-28% from 13:00-15:00 UT at ARAU, PSKI and COCO stations but they were not apparently seen at BSAT station. However, the quick plot of the rate of VTEC index (ROTI) at Chumphon, Thailand station of the SEIALION network (http://wdc.nict.go.jp) during the same time shows medium scintillation activity in the nighttime period. Therefore, the anomaly detected on 22 February is most likely due to the equatorial plasma depletions and cannot be regarded as earthquake precursors. During 23 February 2005, VTEC decreases during two periods were observed; the first was observed during 4:00-8:00 UT with values of about 10-18% at all the four stations, while the second occurred during 14:00-17:00 UT and observed only at BSAT and COCO stations. These negative anomalies were seen with duration of about 3-4 hours.

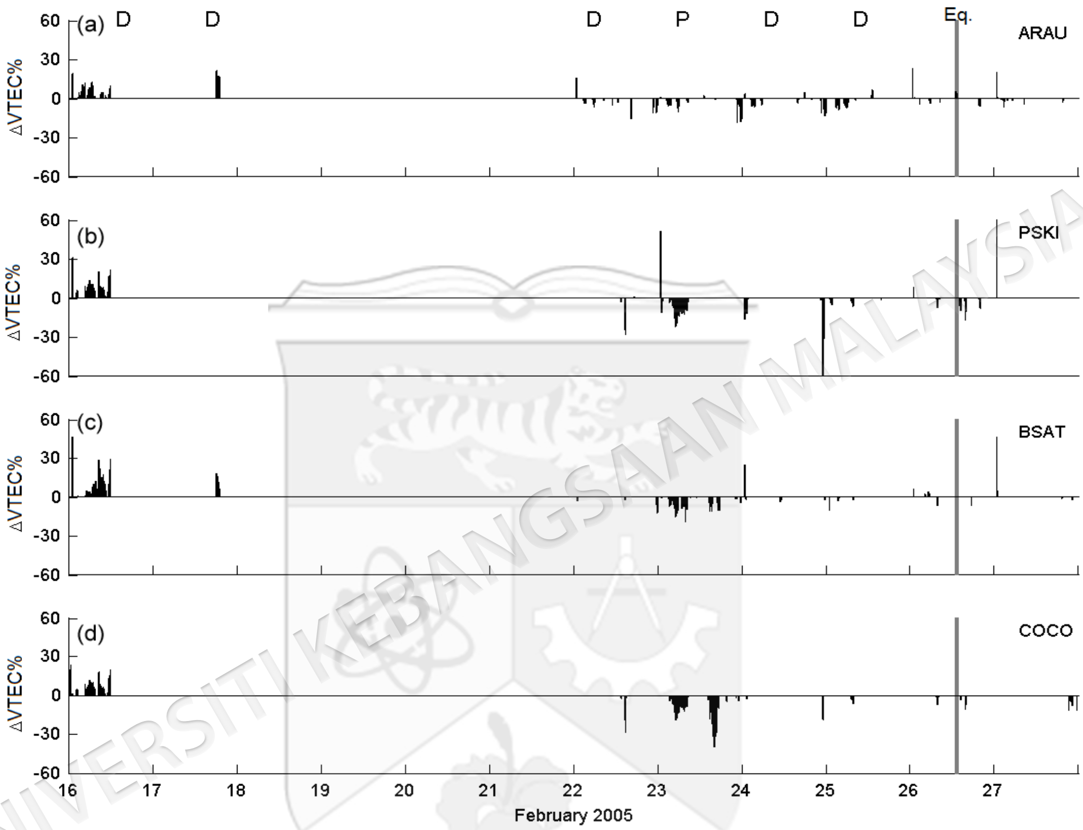

Figure 5.6 The percentage of VTEC deviation between 16 and 27 February 2005 at four GPS stations.

To validate the observations of VTEC variations and the percentage of VTEC deviation, the same analysis is repeated by examining the measurements at Hyderabad (HYDE) station (17.42°N, 78.55°E), which is located about 2458 km away from the earthquake epicentre as shown in Figure 5.7. As shown in Figures 5.7(a), detections were also found during the period before and after the event. From Figure 5.7(b), it was observed that the ΔVTEC% decreases on 23 February 2005 observed during the local night and early morning hours of 12:00-23:00 UT at BSAT and COCO stations in Figure 5.6(c)-(d) were also clearly seen at HYDE station with stronger VTEC variations. The fact that the nighttime negative anomalies on this day was also observed far away from the source indicates a global phenomena, hence are less likely associated with the earthquake. However, the daytime negative VTEC anomalies observed during the same day at all the four GPS stations near the epicentre were not detected at HYDE station. Therefore, the daytime anomalies on 23 February detected from 4:00-8:00 UT during very quiet geomagnetic condition could be associated to the earthquake and are further confirmed using CHAMP electron density measurements.

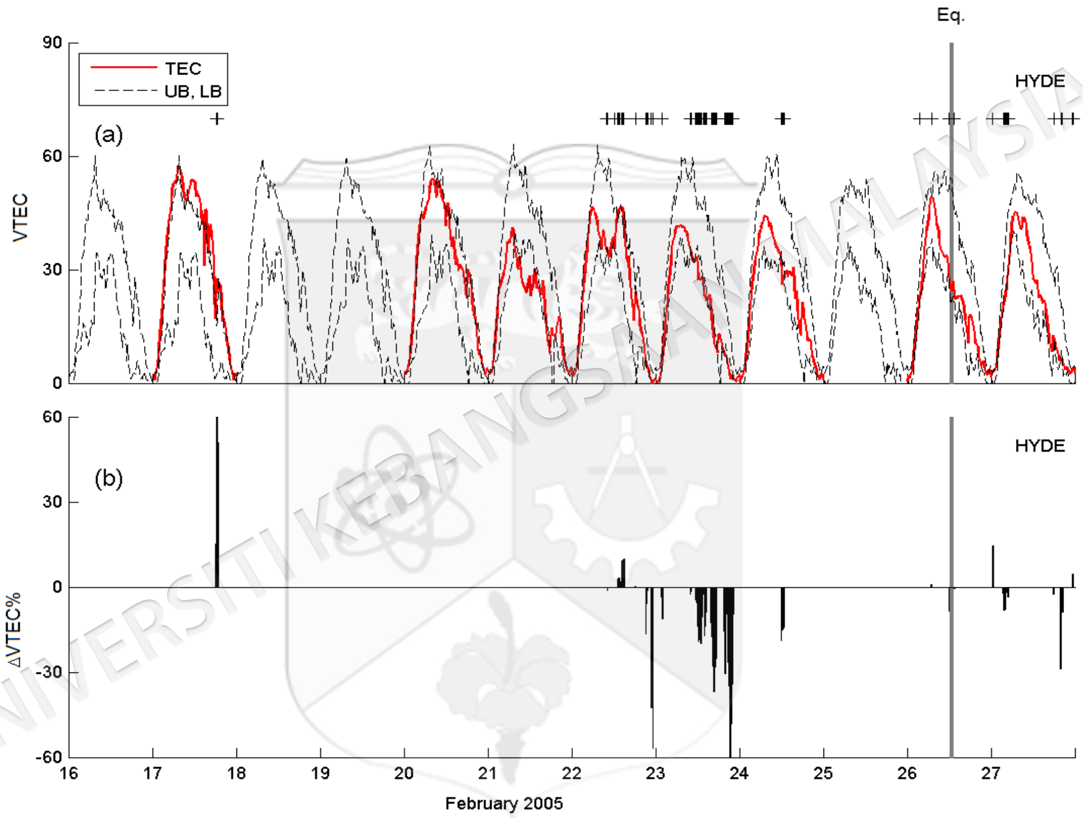

Figure 5.7 Validation of VTEC variations and percentage of VTEC deviation between 16 and 27 February 2005 at HYDE station, which is located 2458 km away from the epicentre.

During the observation of VTEC anomaly on 23 February 2005, 12 satellites were visible during the period of 4:00-8:00 UT at ARAU station but only satellites 2, 10 and 28 show pronounced negative anomaly. With respect to this observation, an example of the VTEC variations, associated lower bounds, satellite tracks at IPP and satellite trajectories for satellite 10 on 23 February 2005 are presented in Figure 5.8 during the period of 4:00-8:00 UT at four GPS stations.

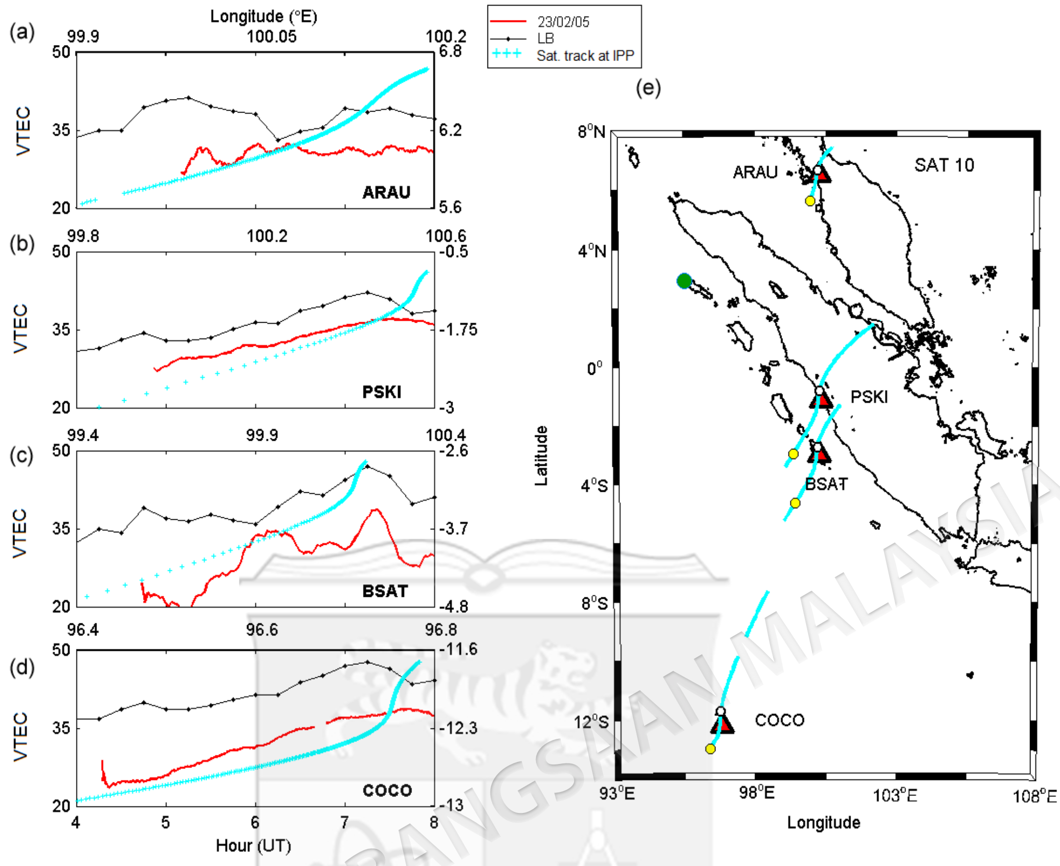

Figure 5.8 (a)-(d) Temporal and spatial VTEC variations, the associated lower bounds and (e) the satellite trajectories for satellite 10 during 4:00-8:00 UT on 23 February 2005 at four GPS stations.

As shown in Figures 5.8(a)-(d), VTEC decreases were observed at all the four stations with respect to their associated lower bounds on 23 February 2005. During this day, the values and durations of the VTEC decreases observed at these four stations vary from 6-15 TECU and 2.8-3.7 hours, respectively. It is interesting to observe that the pre-earthquake VTEC anomalies associated with the 26 February 2005 event extend to about 1700 km away from the epicentre. This scale is larger than that expected from the Dobrovolsky et al. (1979) formula (2.4) as shown in Table 5.2.

b. CHAMP electron density variations

In order to confirm the GPS VTEC anomalies on 23 February 2005, the electron density measurements obtained from CHAMP satellite were examined. Prior to the 26

February 2005 earthquake, CHAMP was flying along the longitude sector of about 70-110°E during the local evening hours (LT=UT+8). Figure 5.9(a) presents the electron density variation of 23 February and the median value of 6-15 February observed during the daytime hours of 9:00-10:00 UT (17:00-18:00 LT) along the longitude sector of about 90°E. In the figure, the vertical lines mark the latitude positions of the COCO, BSAT, PSKI and ARAU stations, arranged in the order of ascending latitude (from left to right). As shown by the median value, the usual latitudinal distribution of electron density during the evening hours also takes shape in the form of a double-crest curve with a trough over the magnetic equator. It is shown that an EIA transformation in terms of crests disappearance and crest displacement over the epicentre was observed 3 days before the event (23 February). In contrast with the GPS VTEC variations shown in Figures 5.13(a)-(d), the N_e variations at the latitude positions of ARAU, PSKI and BSAT stations show significant enhancements with respect to the median value instead of depletions, while the no apparent enhancement was observed at the latitude position of COCO. A plausible explanation of such discrepancy is the time difference of these observations, whereby the daytime VTEC anomalies on 23 February were seen during 4:00-8:00 UT, whereas the N_e measurements were only available during 9:00-10:00 UT.

Figures 5.9(b)-(c) show the geographical projections of three satellite passes along the longitudes of 70, 100 and 110°E on 23 February and their N_e measurements, respectively. The temporal shift of each satellite is about 1.5 hours. In Figure 5.9(c), it is evident that the EIA amplification observed near the epicentre was not found far away from the source. Therefore, it is believed that the EIA modification during the daytime detected from 3 days before the event has a local character and most likely due to the earthquake preparation of the 26 February 2005 event.

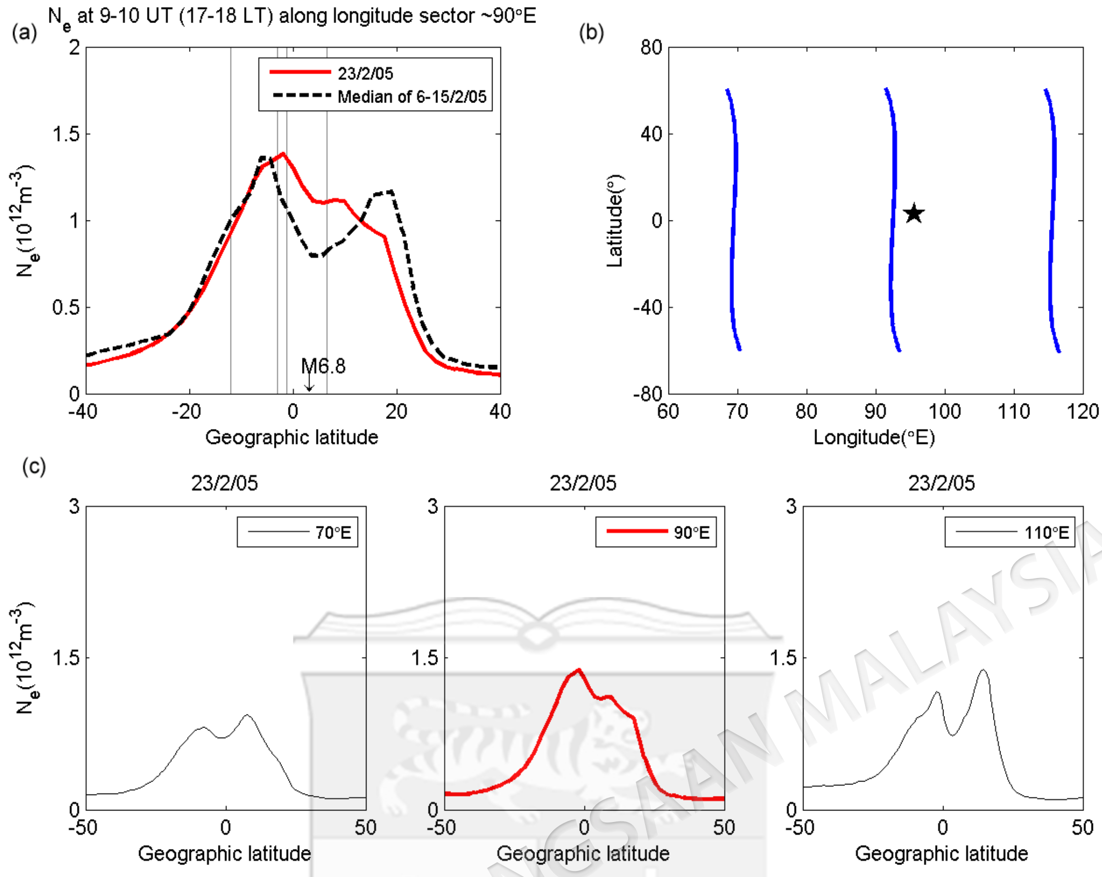

Figure 5.9 (a) The CHAMP N_e variations observed from 9:00-10:00 UT on 23 February 2005 and the median for 16-15 February along the longitude of about 90°E. The vertical lines mark the latitude positions of the GPS stations. (b) The geographical projection of the satellite passes and (c) N_e measurements along the longitudes of 70°E, 90°E and 110°E on 23 February.

5.2.3 The 28 March 2005 Earthquake

a. GPS VTEC variations

The 28 March 2005 earthquake is the second largest event in Sumatra during the period of 2004-2007. The earthquake occurred in Northern Sumatra at 16:05 UT with a magnitude of 8.6 and a depth of 30 km. Figure 5.10 presents the VTEC variations and their associated upper and lower bounds, while Figure 5.11 presents the ΔVTEC% variations between 21 and 29 March 2005 at four GPS stations. As shown in Figure 5.10, sudden decreases in VTEC were observed during 14:00-16:00 UT, particularly on 22, 23 and 28 March. To check for F-region plasma depletion, the half-orbit of level 2 electron density (N_e) data measured by the Langmuir Probe instrument (ISL) onboard DEMETER satellite (http://demeter.cnrs-orleans.fr) are examined throughout the observation period prior to the event. Plasma depletions were found during the hours of 14:00-16:00 UT near the magnetic equator by satellite orbits 03826_1, 03827_1, 03826_1 (22 March), 03840_1, 03841_1, 03842_1 (23 March) and 03915_1 (28 March) at longitudes 85-135°E. As the stations considered in this study are located near the magnetic equator, the sudden decreases in the local VTEC are most likely due to equatorial plasma depletion, which normally occurs at night even during geomagnetically quiet periods (Sahai et al., 1999). Therefore, detections of VTEC anomalies and ΔVTEC% values for temporal intervals of 14:00-16:00 UT on the affected days are removed from the analysis. In the figure, detections were found mostly from 22-26 March but only days of 22-24 March are most likely related to the earthquake event as the period coincides with geomagnetic quiet days. The anomalies detected on 25 and 26 March cannot be convincingly regarded as earthquake related signals as they occurred on geomagnetically disturbed days.

As shown in Figures 5.11, both positive and negative ionospheric anomalies were clearly observed at all four stations during 4-6 days before the event, and these anomalies even persisted a day after. During 22 March 2005, it was observed that the sign of the ΔVTEC% observed during 3:00-12:00 UT varies from one station to another. Only ΔVTEC% decreases were seen at ARAU station, whereas both increases and decreases were detected at PSKI and BSAT. The ΔVTEC% at COCO station on the other hand, detected only increases. The anomaly during this day is most intense at COCO station, which is located at the southern crest of the EIA with a maximum increase of about 67%. Such an enhancement was also reported by Dabas et al. (2007) on 22 March 2005 at the ionosonde station located in the northern crest of the EIA. During 23 and 24 March, decreases of about 20% were found at ARAU, PSKI and BSAT stations, while no data are available at COCO during these days.

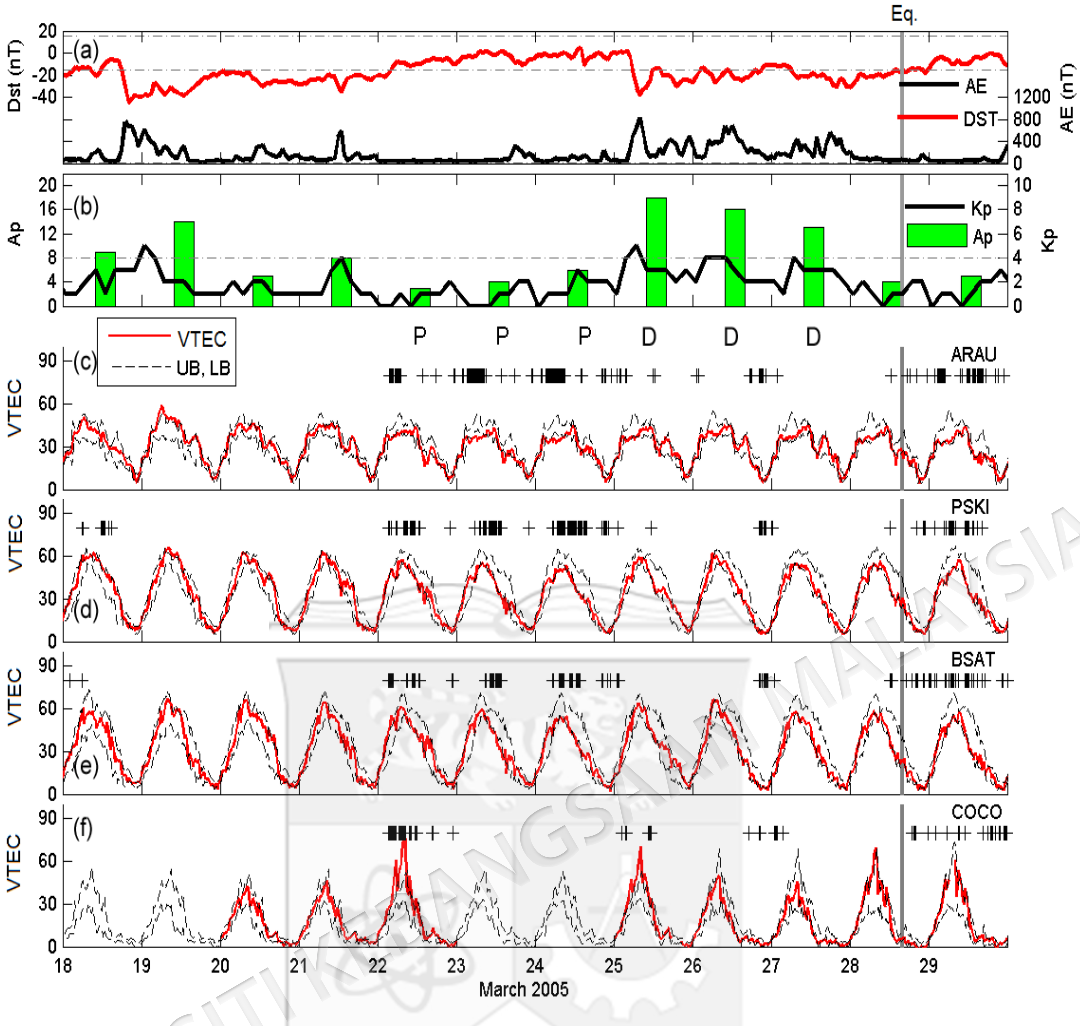

Figure 5.10 The geomagnetic indices (a) Dst and AE, (b) Ap and Kp, and the (c)-(f) VTEC variations and the associated upper and lower bounds between 18 and 29 March 2005 at four GPS stations.

Figure 5.12 presents the validation of the VTEC variation and percentage of VTEC deviation in Figures 5.10-5.11 at BARH station. As shown in Figure 5.12(a), detections of VTEC anomalies were also observed about 4-6 days before the event. In Figure 5.12(b), the ΔVTEC% values prior to the event range from about -35 to 50%. Although these positive and negative anomalies are significant, they do not exhibit the same character with those observed at stations nearer to the epicentre. Hence, it is most likely that the VTEC anomalies observed earlier at the four GPS stations in Figures 5.10-5.11 have a local character and are effects of the 28 March 2005 earthquake preparation process.

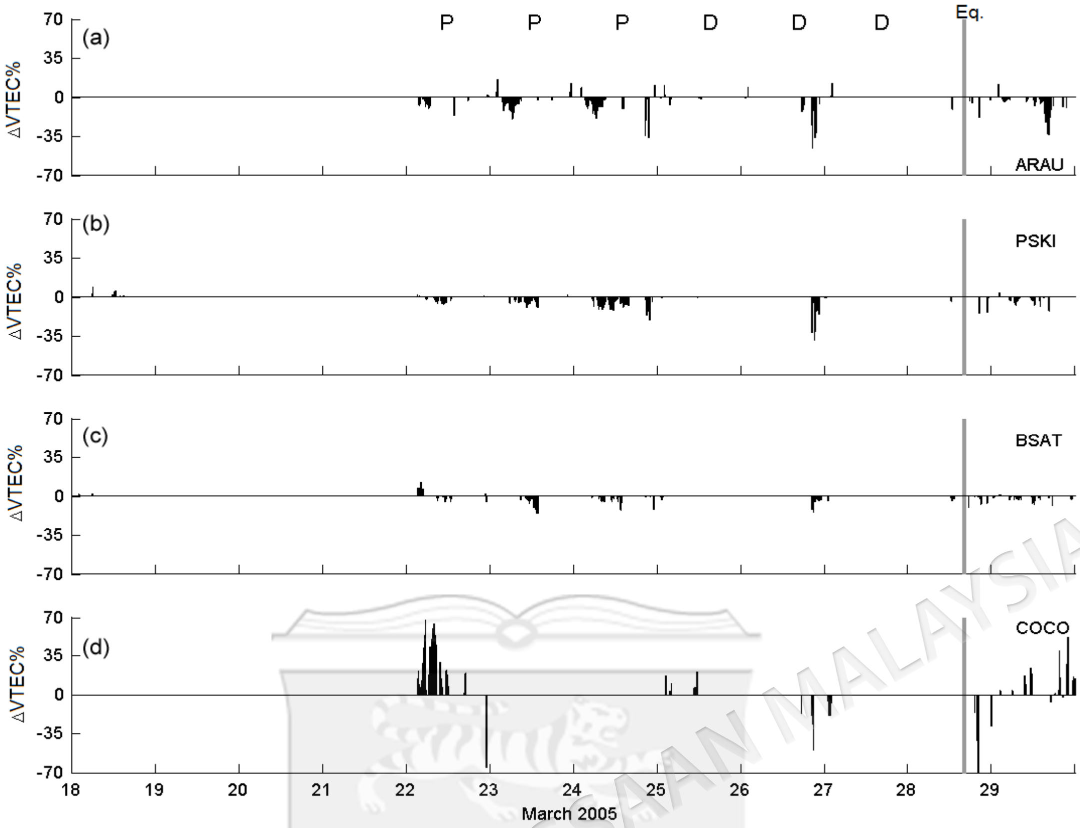

Figure 5.11 The percentage of VTEC deviation between 18 and 29 March 2005 at four GPS stations.

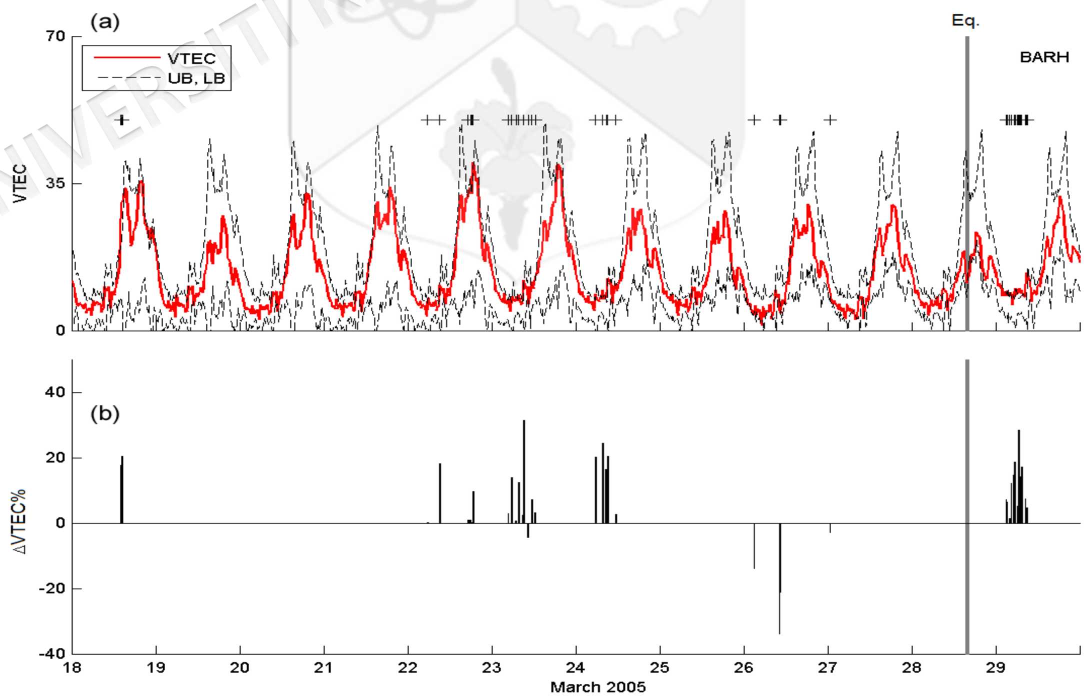

Figure 5.12 Validation of VTEC variations and percentage of VTEC deviation from 18 to 29 March 2005 at BARH station, which is located 14650 km away from the earthquake epicentre.

During the observation of VTEC anomalies on 22, 23 and 24 March 2005, 16 satellites were visible during the periods of 3:00-7:00 UT, 10:00-15:00 UT and 18:00-23:00 UT at PSKI station. However, only satellite 7 (3:00-7:00 UT), and satellites 29, 30 and 21 (10:00-15:00 UT) show negative and positive ionospheric anomalies. Figures 5.13 shows the VTEC variations along individual satellites and the associated lower and upper bounds, the satellite tracks at IPP and their trajectories on 22, 23 and 24 March 2005 at four stations. As shown in Figure 5.13(i), both decreases and increases in VTEC were observed at the four stations with respect to the lower and upper bounds, respectively during 3:00-7:00 UT on 22 March 2005. At ARAU station, a VTEC decrease of about 8 TECU was observed for duration of about 2.7 hours, while the VTEC decrease at PSKI was detected with a value of only about 0.6 TECU for 5 minutes. On the other hand, VTEC increases were simultaneously observed at both BSAT and COCO stations with values of about 7 TECU and duration of 1 hour.

Figure 5.13(ii) shows the VTEC variations and the upper and lower bounds on 22 March 2005 observed for satellite 29 at ARAU station from 5:00-11:00 UT, satellite 30 at both PSKI and BSAT and satellite 21 at COCO from 11:00-15:00 UT on 22, 23 and 24 March 2005. As shown in the figure, VTEC decreases at ARAU station during all the three days were observed with values of 6-9 TECU from 5:30-9:00 UT. The duration of the decreases is between 1.2 and 3 hours. About an hour after this event, VTEC decreases were detected at PSKI and BSAT stations with values of about 14 and 10 TECU, respectively and durations of 4.3 and 3 hours, respectively during the three days. A VTEC positive variation was observed at COCO station with an increase of 12 TECU and duration of 1 hour on 22 March 2005. However, the VTEC variations on 23 and 24 March 2005 at COCO station could be analyzed due to data unavailability. From these observations, it was clearly shown that the ionosphere in the region surrounding the earthquake epicentre does not only exhibit positive and negative anomalies but also show some variability during a few days before the great March 2005 earthquake.

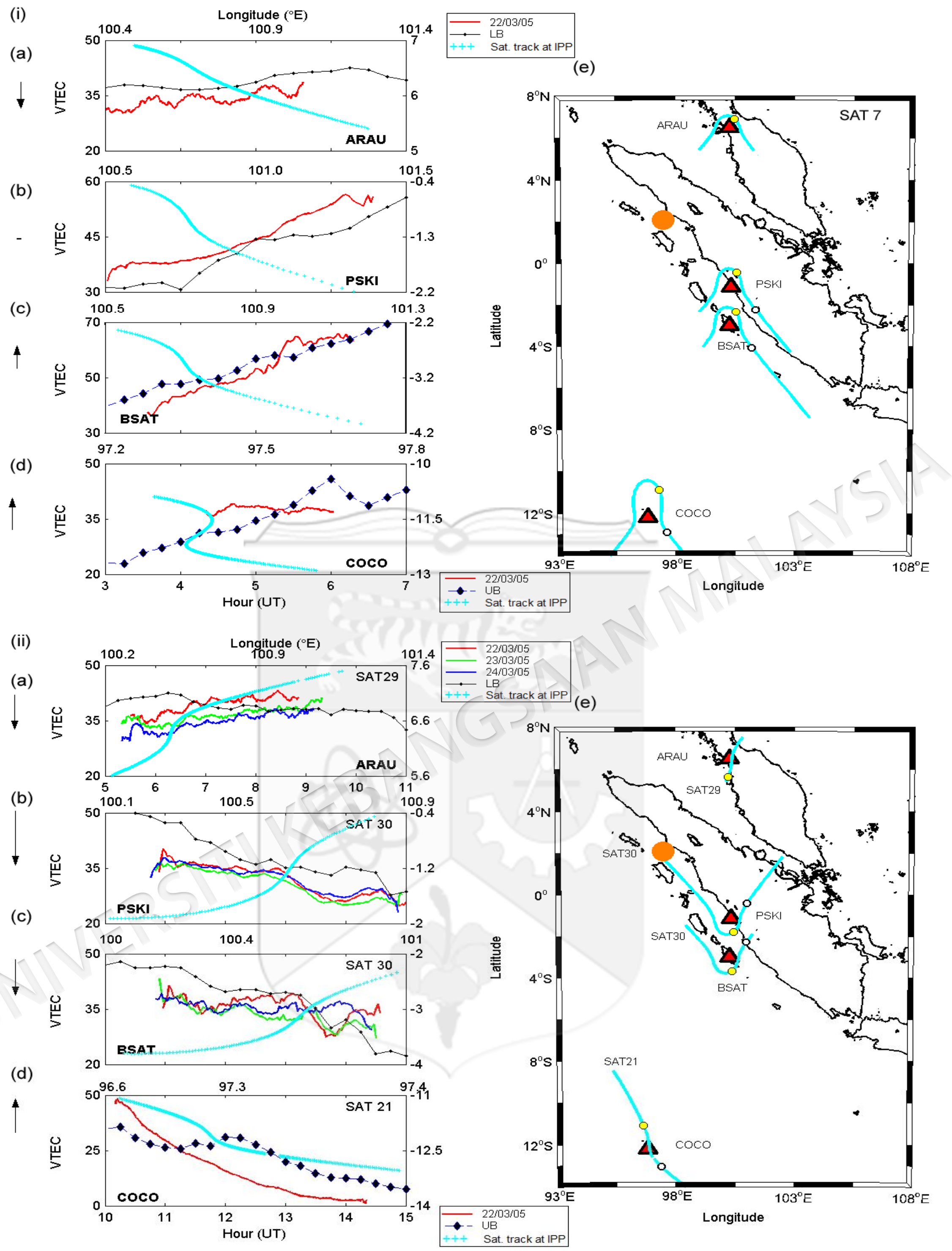

Figure 5.13 Temporal VTEC variations and the associated lower and upper bounds (i) for satellite 7 during 3:00-7:00 UT and (ii) satellite 29 from 5:00-11:00 UT and satellites 30 and 21 during 10:00-15:00 UT on 22, 23 and 24 March 2005 at four stations. Also shown on the right panel of each figure are the satellite trajectories.

b. CHAMP electron density variation

In order to confirm the GPS VTEC anomalies, the electron density measurements obtained from CHAMP satellite were examined. Prior to the 28 March 2005 earthquake, CHAMP was flying along the longitude sector of about 75-125°E during the local afternoon hours (LT=UT+8). Figure 5.14(a) presents the N_e variations during 6:00-8:00 UT (14:00-16:00 LT) on 22, 23 and 24 March 2005 and the median of 11-20 March 2005 near the longitude sector of the epicentre (~100°E). In this figure, the vertical lines mark the latitude positions of the COCO, BSAT, PSKI and ARAU stations, arranged in the order of ascending latitude (from left to right). Figures 5.14(b)-(c) show the geographical projections of three satellite passes along the longitudes of 75, 100 and 125°E on 23 March and their N_e measurements, respectively. The temporal shift of each satellite is about 1.5 hour.

As shown by the median value in Figure 5.14(a), the usual EIA in the afternoon appears in the form of a double-crest structure with a trough over the magnetic equator. However, the EIA modification in the form of crest amplification and trough deepening in the near-epicentral region with respect to the median value was observed between 4 and 6 days prior to the event. During these days, the electron concentration at the crest and trough increases and decreases by about 40 and 20%, respectively relative to the median value. This phenomenon was also reported a few hours before 20 March 1979 earthquake, whereby Pulinets and Lagen'ka (2002) observed significant EIA trough deepening and the crest amplification in the afternoon using the topside foF2 measurements onboard the Intercosmos-19 satellite. In Figure 5.14(c), it is evident that the EIA amplification that took place particularly in the southern crest was clearly seen near the epicentre region but was not observed along the longitude of 75°E on 23 March. The crest amplification also occurred at longitude 125°E but its amplitude is not as pronounced as the one near the epicentre. Hence, it is believed that the EIA amplification that occurred during 4-6 days before the earthquake has a local character and might be due to the earthquake preparation.

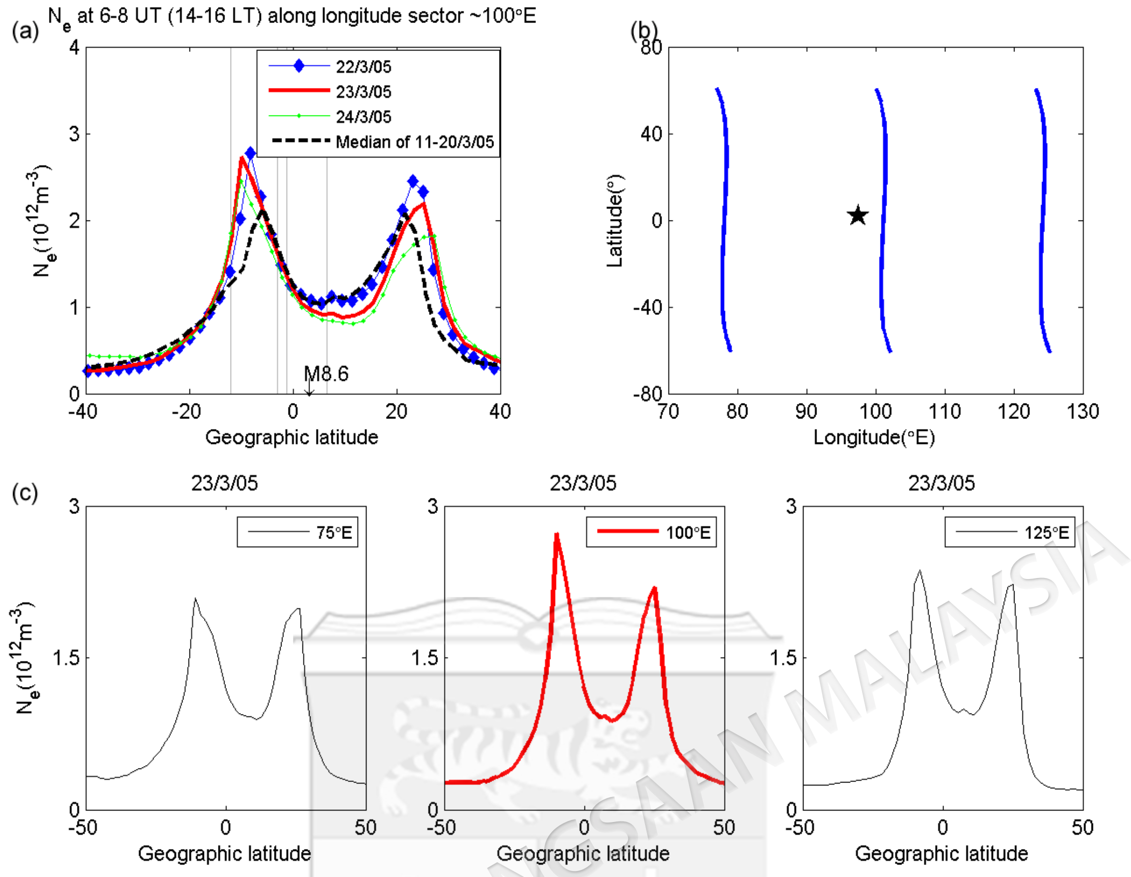

Figure 5.14 (a) The CHAMP N_e variations observed from 6:00-8:00 UT on 22, 23 and 24 March 2005 and the median for 11-20 March along the longitude of about 100°E. The vertical lines mark the latitude positions of the GPS stations. (b) The geographical projection of the satellite passes and (c) N_e measurements along the longitudes of 75°E, 100°E and 125°E on 23 March.

5.2.4 The 24 July 2005 Nicobar Island Earthquake

Figures 5.15 and 5.16 show the VTEC and the ΔVTEC% variations, respectively during the observation period of the 24 July 2005 earthquake in Nicobar Islands in India, which is between 14 and 25 July 2005 at six GPS stations. As presented in both of these figures, VTEC anomalies were observed from 10 days to a few hours before the earthquake, and even persisted the day after at all the six stations. In Figures 5.16(c)-(h), these anomalies were observed as significant decreases with respect to the lower bound. VTEC decreases of up to 21% were seen during 1:00-6:00 UT on 17 July 2005 at all six stations but these occurred during the recovery phase of a minor magnetic storm that occurred on 11 July 2005 (IPS 2008). Hence, these decreases of

VTEC cannot be associated with seismic effects. On 20 July 2005, significant decreases of 30-44% were observed simultaneously from 5:00-8:00 UT (13:00-16:00 LT) at both PSKI and BSAT stations but were not apparently seen at the remaining four stations. The fact that these significant decreases of VTEC were observed outside (PSKI and BSAT) and not inside the earthquake preparation radius (ARAU and USMP) indicates global effect, thus cannot be due to the earthquake.

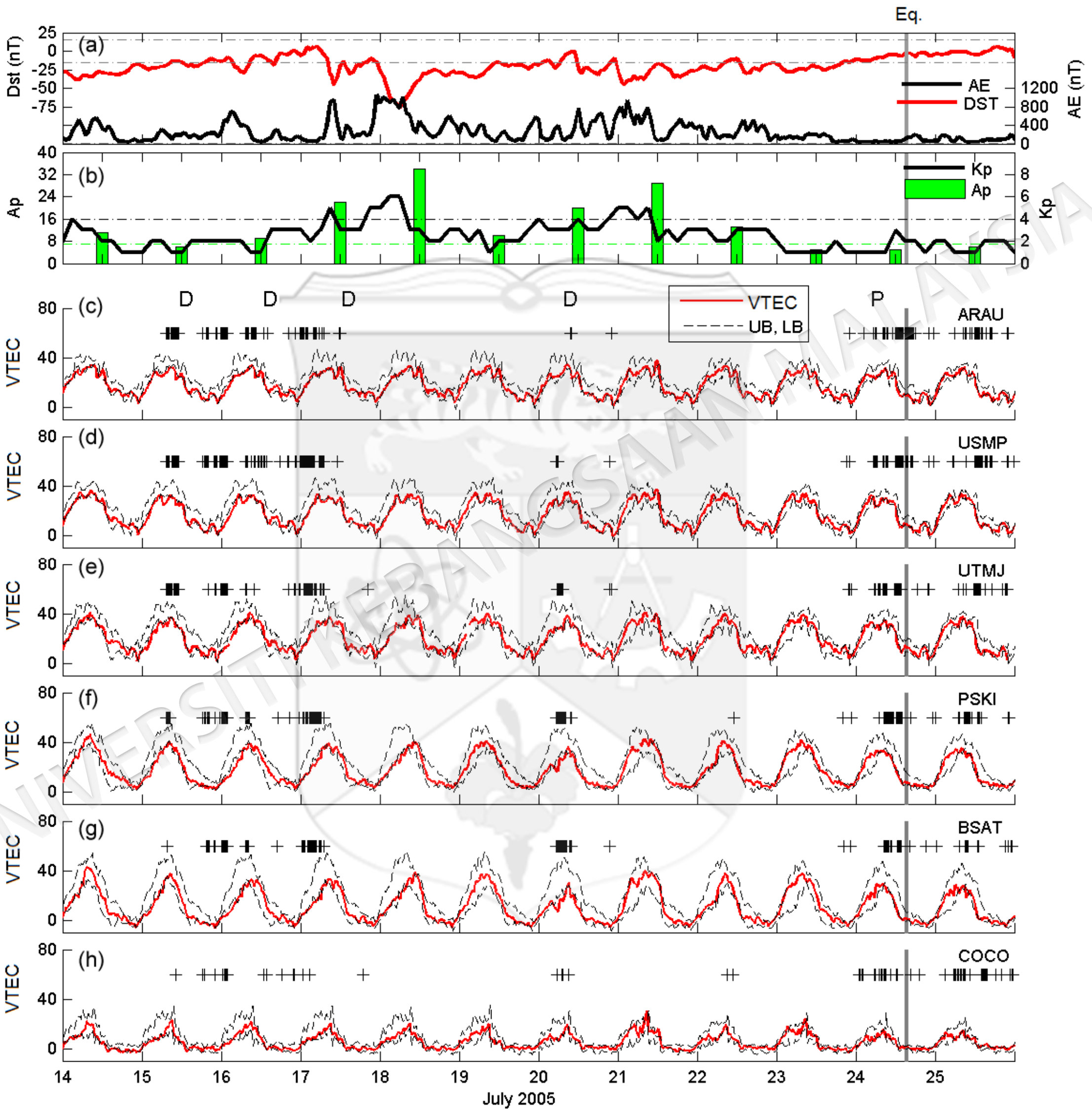

Figure 5.15 The geomagnetic indices (a) Dst and AE, (b) Ap and Kp, and the (c)-(h) VTEC variations and their associated lower and upper bounds between 14 and 25 July 2005 at six GPS stations.

About a few hours before the earthquake, significant decreases of 15-41% were observed at all the stations. During this time, the anomaly was most intense at the station nearest to the epicentre, which is ARAU (912 km) with a decrease of 41%

and become less intense with increasing distance. The VTEC anomalies on 20 and 24 July 2005, which occurred during very low geomagnetic and solar activity, are further confirmed using CHAMP data as shown in Figure 5.17.

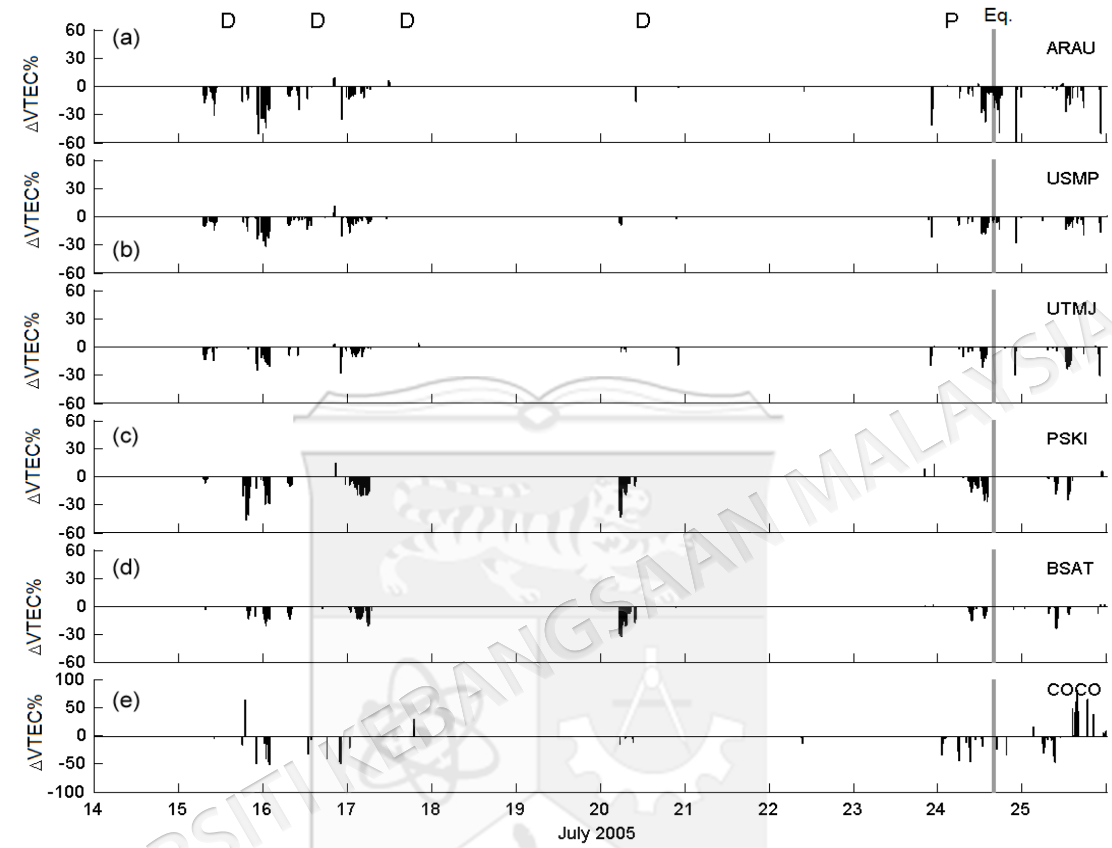

Figure 5.16 The percentage of VTEC deviation between 14 and 25 July 2005 at six GPS stations.

To validate the anomalies observed a few hours before the earthquake, the same analysis is repeated by using measurements at a remote station in Tehran (TEHN) (35.69°N, 51.33°E), which is located 5163 km away from the epicentre as shown in Figure 5.17. As shown in Figure 5.17(a), detections of VTEC anomalies were also observed between 7 days and a few hours before the event. In Figure 5.17(b), the ΔVTEC% values prior to the event were observed within a range from about -6 to +2%, which is very insignificant as compared to those observed at stations nearer to the epicentre. Hence, it is most likely that the VTEC anomalies observed at the six GPS stations near the epicentre in Figures 5.15-5.16 are the effects of the 24 July 2005 earthquake preparation process.

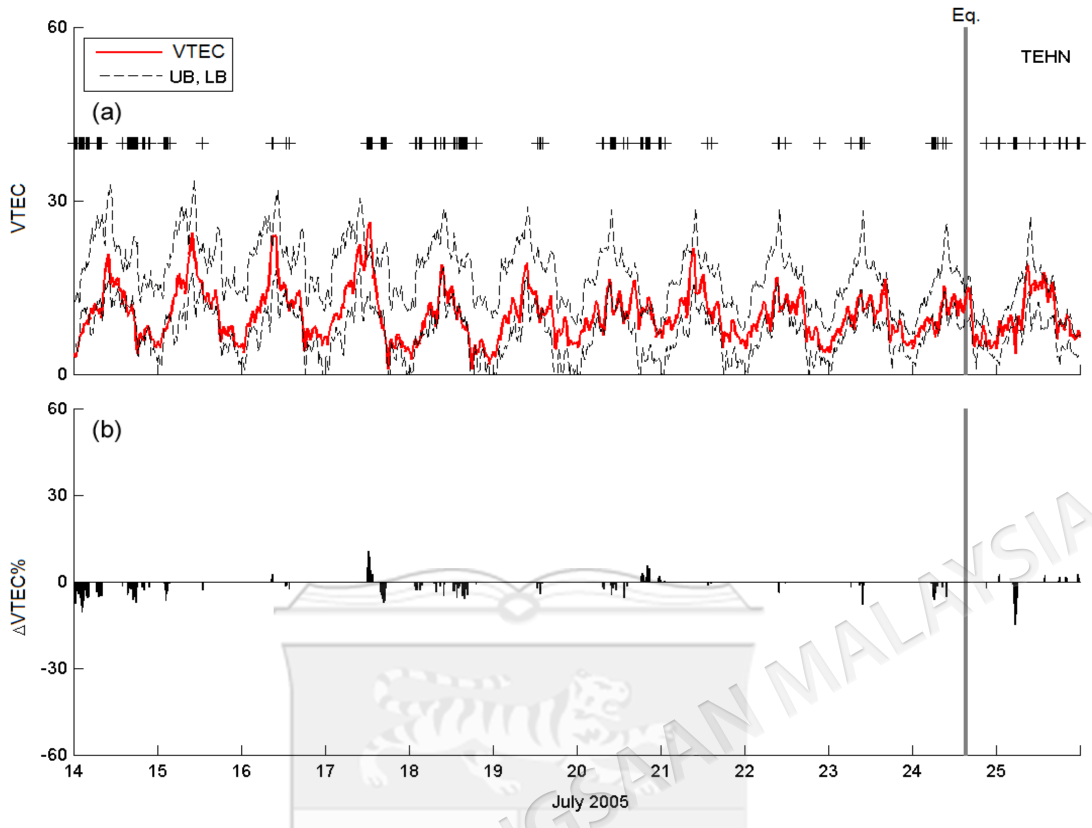

Figure 5.17 Validation of VTEC variations and percentage of VTEC deviation between 14 and 25 July 2005 at TEHN station, which is located 5163 km away from the epicentre.

During the observation of VTEC anomaly on 24 July 2005, 16 satellites were visible during the period of 11:00-15:00 UT at PSKI station but only satellites 11, 13, 16 and 23 show pronounced negative anomaly. Figure 5.18 presents an example of the VTEC variations, the associated lower bounds, satellite tracks at IPP and satellite trajectories for satellite 13 on 24 July 2005 during the period of 11:00-15:00 UT at five GPS stations. As shown in Figures 5.18(a)-(e), the decrease of VTEC were observed at all the five stations with respect to their associated lower bounds on 24 July with values of about 5-11 TECU and durations of about 2.5-3.5 hours. Similar to the 26 February 2005 event, it was observed that the possible precursory VTEC anomalies associated with the 24 July 2005 earthquake extended to about 1500 km but with decreased values of 11-25 VTECU. This scale is larger than that expected from the empirical formula of earthquake preparation radius by Dobrovolsky et al. (1979) as shown in Table 5.2.

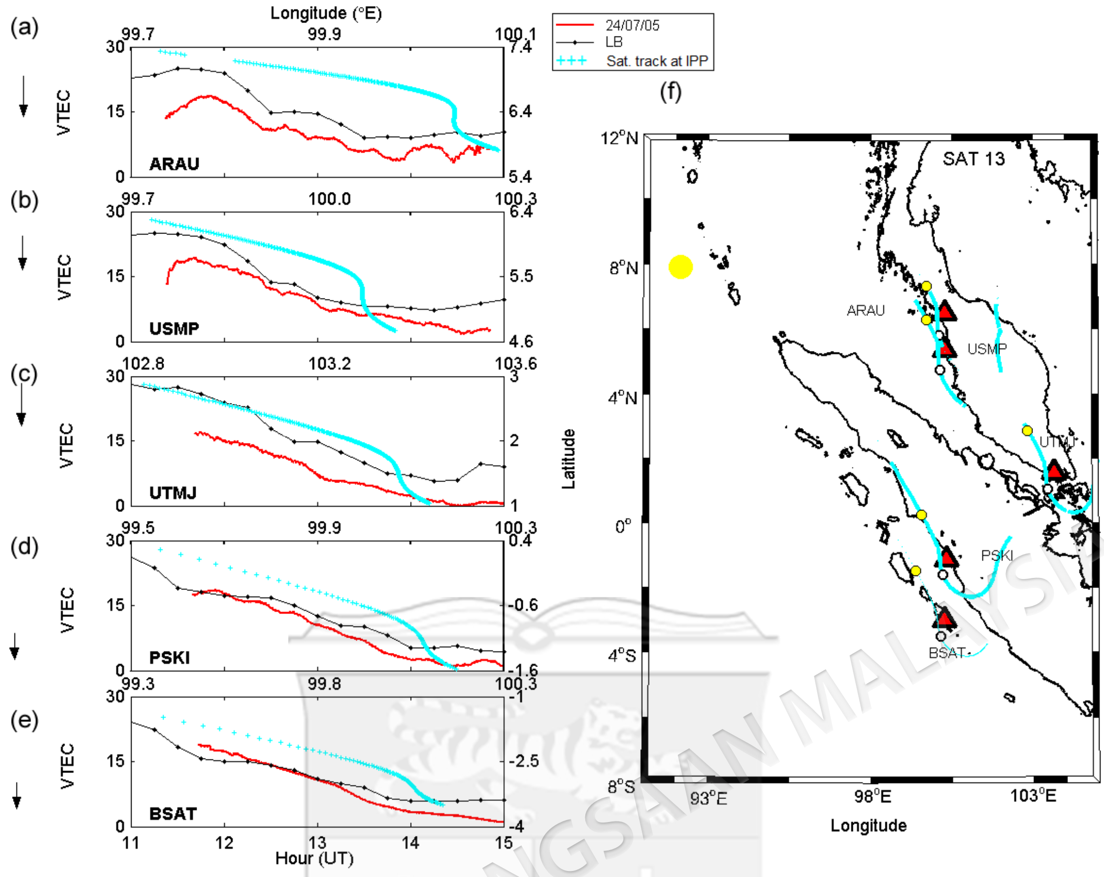

Figure 5.18 Temporal VTEC variations and the associated lower bound for satellite 13 during 11:00-15:00 UT on 24 July 2005 at five GPS stations. Also shown on the right panel of each figure are the satellite trajectories.

b. CHAMP electron density variations

Figure 5.19(a) presents the N_e variations on 24 July 2005 and the median value of 6-15 July 2005 during the period from 8:00-10:00 UT (16:00-18:00 LT), as well as the latitude positions of the COCO, BSAT, PSKI, NTUS, UTMJ, USMP and ARAU stations. As shown in this figure, no EIA modification was observed on 24 July 2005 but a significant decrease in relative to the median value was seen at all the latitude positions of the GPS stations. The decrease of N_e was observed about 6 hours before the earthquake at all the latitude positions of the six GPS stations with values of about 16-44%. The N_e variations are in close approximation with those observed in the ΔVTEC% at the six GPS stations in Figures 5.16(a)-(f).

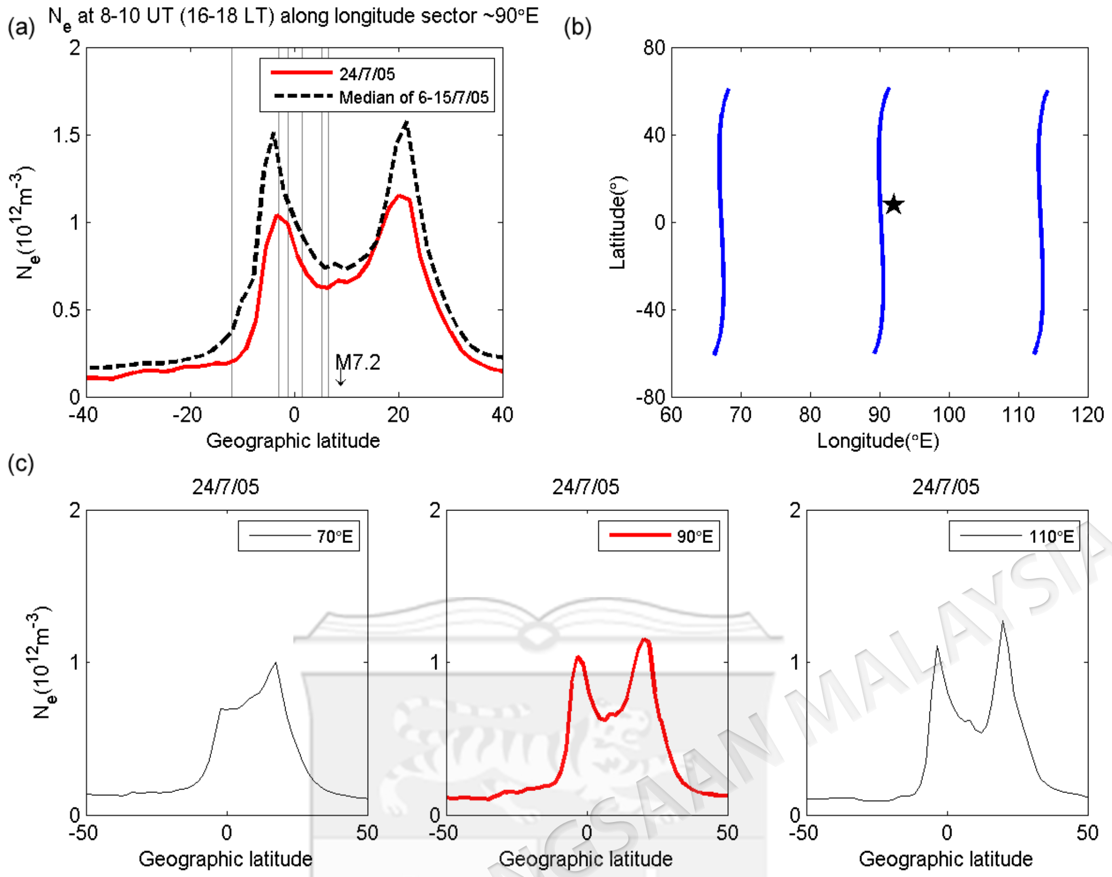

Figure 5.19 (a) The CHAMP N_e variations observed from 8:00-10:00 UT on 24 July 2005 and the median for 6-15 March along the longitude of about 90°E, (b) The geographical projection of the satellite passes and (c) N_e measurements along the longitudes of 70°E, 90°E and 110°E on 24 July.

In Figure 5.19(c), it is shown that the usual afternoon EIA structure about 20° west of the epicentre was not observed but the two peak structure was clearly seen near the epicentre with a significant reduction relative to the median value in Figure 5.19(a). The same EIA structure was found 20° east of the epicentre but its decrease is not as apparent as the one near the epicentre. Therefore, the decrease in the EIA structure near the epicentral area could be a possible effect of the 24 July 2005 earthquake.

5.2.5 The 12 September 2007 South Sumatra Earthquakes

a. GPS VTEC variations

Two large earthquakes occurred in South Sumatra on 12 September 2007 with magnitudes of M8.5 and M7.9 at 11:10 UT and 23:49 UT, respectively. The results of VTEC and ∆VTEC% variations at NTUS, BSAT and COCO stations for the period between 6 and 13 September 2007 are presented in Figures 5.20 and 5.21, respectively. As shown in Figure 5.20, detections were found from 8 to 12 September, but the detection on 8 September is probably due to the time delay effects of the sudden storm commencement on 6 September. Based on this observation, only the VTEC anomalies from 9-12 September are considered as possible earthquake related anomalies, as they were detected during very quiet geomagnetic conditions. In Figure 5.21, ∆VTEC% increases and decreases were observed almost simultaneously at all three GPs stations between 3 days and a few hours before the events. The ∆VTEC% increases of about 16-55% were observed during 13:00-20:00 UT on 9, 11 and 12 September, while the decreases of about 17-40% were seen during 5:00-9:00 UT on 9, 10 and 11 September. It was observed that the ∆VTEC% variations were more prominent at BSAT and COCO stations than that at NTUS, although NTUS is located about 300-600 km nearer to the earthquake epicentres than COCO. During a few hours before second event (M7.9), increases in ∆VTEC% of about 20% were observed at all the 3 stations but the most intense anomaly was seen at BSAT station, which is closest to the epicentre (94 km).

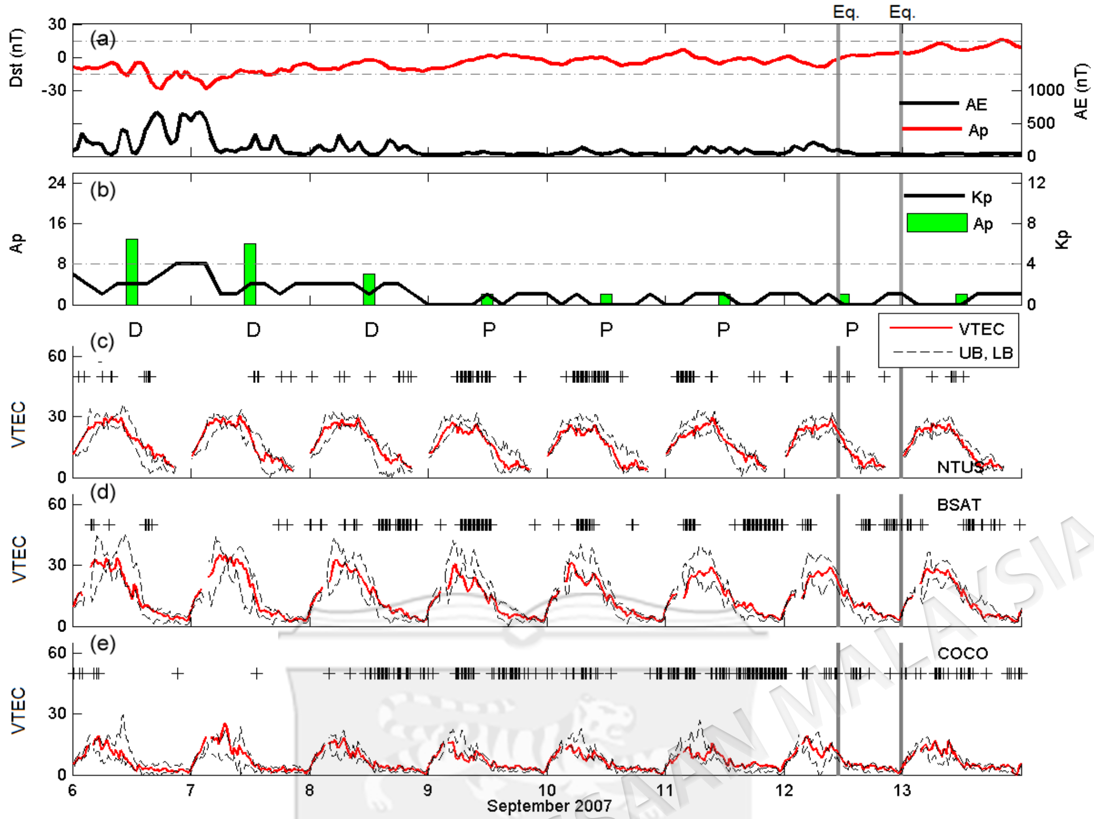

Figure 5.20 The geomagnetic indices (a) Dst and AE, (b) Ap and Kp, and the (c)-(e) VTEC variations and the associated upper and lower bounds between 6 and 13 September 2007 at 3 GPS stations.

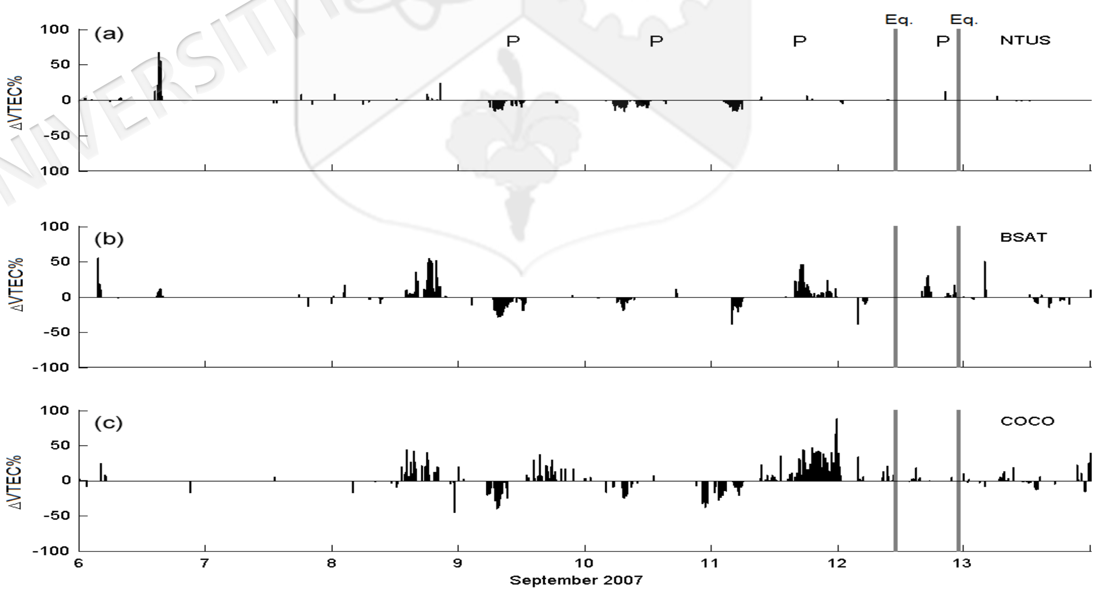

Figure 5.21 The percentage of VTEC deviation between 6 and 13 September 2007 at three GPS stations.

The VTEC variations and the percentage of VTEC deviation are compared with the measurements at an IGS station in Malindi (MALI), Kenya (2.99°S, 40.19°E) as shown in Figure 5.22. MALI is located about 6700 km away from the earthquake epicentres. In Figure 5.22(a), it is shown that detections of VTEC anomalies were found throughout the observation period of the analysis at MALI station. As shown in Figure 5.22(b), the ΔVTEC% values during the days of the observation period are mostly less than the normal day-to-day ionospheric variability except for the one on 7 September 2007. During 7 September 2007, continuous detection of positive VTEC anomalies, which lasted for many hours were seen with a maximum ΔVTEC% value of about 33%. However, these significant anomalies cannot be caused by the 12 September 2007 Sumatran earthquakes because these anomalies were observed far away from the epicentres (6700 km). Furthermore, the significant VTEC anomalies detected between 3 days and a few hours before the events at stations near the epicentres shown earlier in Figures 5.27 and 4.28 were not observed at all at MALI station, suggesting that these ionospheric anomalies have a local character and are most likely related to the 12 September 2007 earthquakes.

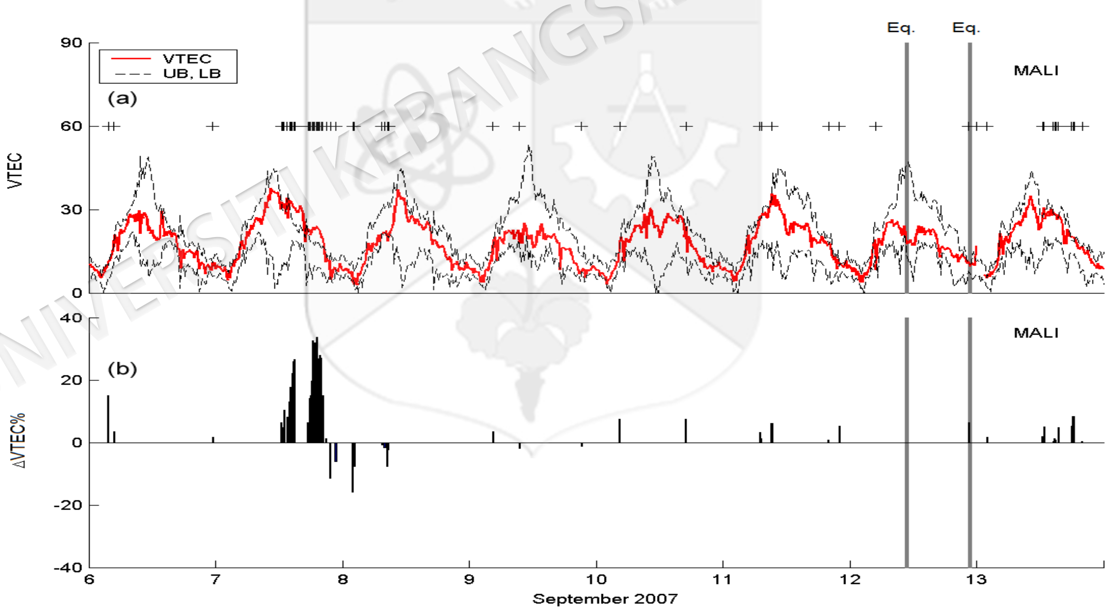

Figure 5.22 Validation of VTEC variations and percentage of VTEC deviation between 6 and 13 September 2007 at MALI station, which is located about 6700 km away from the epicentres.

During the observation of VTEC anomalies, 13 satellites were visible during periods of 6:00-10:00 UT and 16:00-20:00 UT. However, only satellites 13 and 20 (6:00-10:00 UT) and satellites 26 (16:00-20:00 UT) show pronounced negative and positive ionospheric anomalies, respectively as shown in Figures 5.23(i)-(ii), respectively. In Figure 5.23(i), the VTEC variations along individual satellites and the lower bound for 9 September 2007, the satellite tracks at IPP and the satellite trajectories observed for satellite 13 at NTUS and BSAT stations and satellite 20 at COCO between 6:00 and 10:00 UT on 9, 10, and 11 September 2007 are presented. Figure 5.23(ii) shows the same plots for satellite 26 on 9 and 11 September 2007 and the upper bound for 9 September 2007 between 16:00 and 20:00 UT at all the three stations.

As shown in Figures 5.23(i), similar VTEC variations were observed on 9 and 10 September 2007 at both NTUS and BSAT stations. During the period between 6:10 and 7:30 UT, VTEC decreases of about 4-7 TECU with respect to their lower bounds were observed. Following this time, the VTEC return to their normal values from 7:30 to 7:50 UT and decrease for about 2 hours. The VTEC variations on both days reach their maximum at 10:00 UT with decreases of about 6-12 TECU. The total duration of these decreases is about 3.3 hours. On 11 September, the VTEC decreases are similar to those observed during the two previous days but with a shorter duration of about 2 hours. Meanwhile, the VTEC variation at COCO station shows simultaneously decreases of about 4 TECU between 6:30 and 8:10 UT on 9, 10 and 11 September at COCO station. After this time, VTEC on 9 and 10 September continue to decrease from 8:10 to 9:00 UT, while no VTEC decrease was detected during this time on 11 September. The duration of the VTEC anomaly detected on both 9 and 10 September at COCO station is about 2.5 hours, whereas the one observed on 11 September is about 1.7 hours.

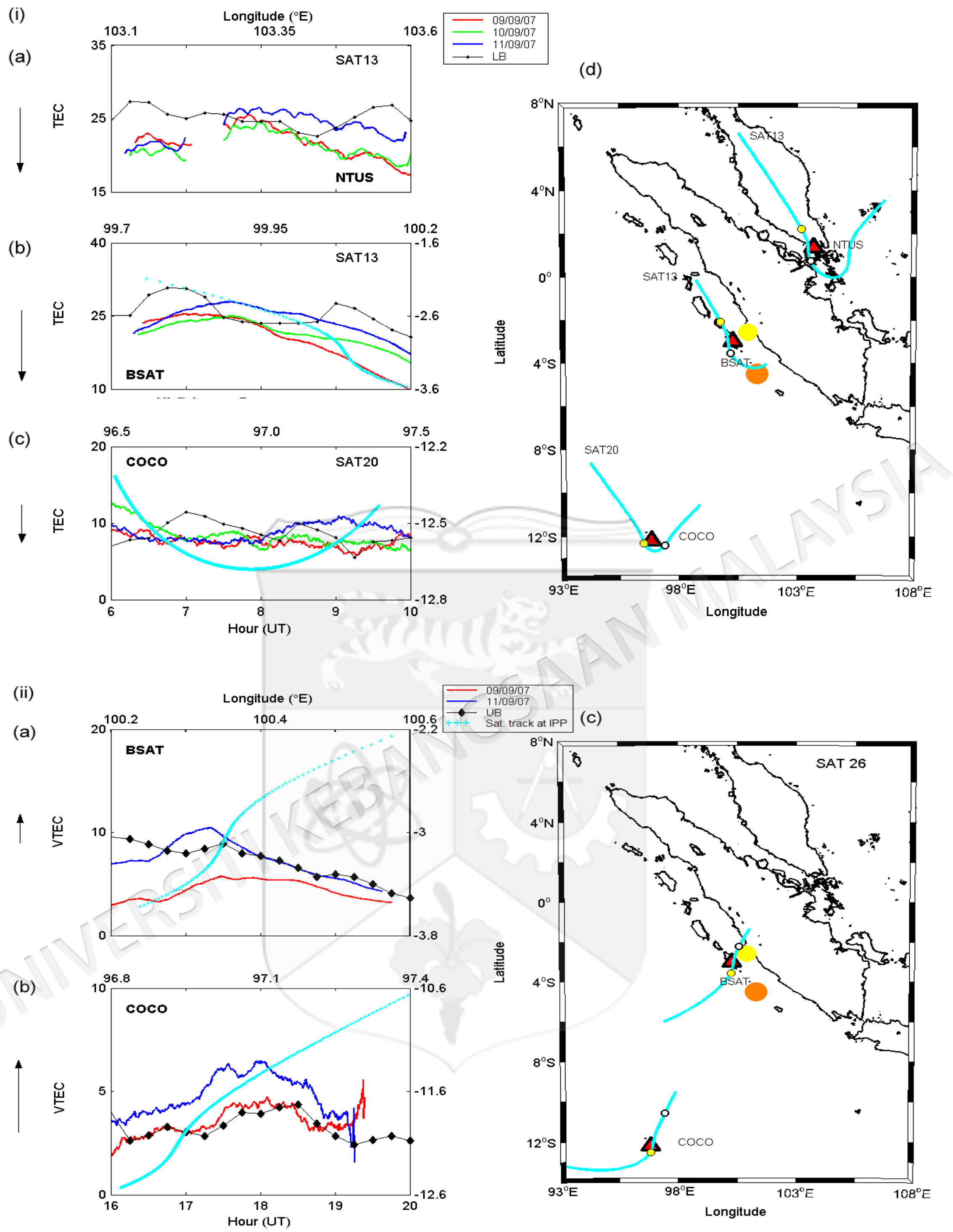

Figure 5.23 Temporal VTEC variations and the associated (i) lower bound for satellites 13 and 20 during 6:00-10:00 UT on 9, 10, and 11 September 2007 and (ii) upper bound for satellite 26 during 16:00-20:00 UT on 9 and 11 September 2007 at NTUS, BSAT and COCO stations.

As shown in Figure 5.23(ii), no VTEC increase was observed on 9 September as the values fall below the upper bound, while a VTEC increase with respect to the upper bound of about 2.5 TECU was observed on 11 September from 16:05-19:05 UT and lasted for about 3 hours. Meanwhile, VTEC increases of about 0.8-2.5 TECU were seen almost simultaneously from 16:00-19:20 UT at COCO station on 9 and 11 September.

b. CHAMP electron density variations

Figure 5.24 presents the N_e variations during 7-9 UT (15-17 LT) between 9 and 12 September 2007 and the median of 1-5 September near the longitude sector of the epicentre (~110°E). The vertical lines in the figure mark the latitude positions of COCO, BSAT and NTUS stations. The geographical projections of three satellite passes along the longitudes of 85, 110 and 135°E on 9 September and their N_e measurements, respectively are shown in Figures 5.24(b)-(c). As shown in Figure 5.24(a), an EIA modification in terms of crests disappearance and crest displacement over the magnetic equator was observed on 9 September 2007. No EIA modification was seen on 10, 11 and 12 September but the N_e measurements mostly show decreases at the latitude positions of NTUS, BSAT and COCO stations. Similar to the observation of ΔVTEC% variation in Figure 5.21, it is also shown that larger N_e variations were observed at the positions of BSAT and COCO stations than the one observed at the position of NTUS station. In Figure 5.24(c), the comparison between the N_e measurements at longitudes 85, 110 and 135°E shows that the daytime EIA modification on 9 September did not take place at 85°E but was observed near the two earthquake epicentres. However, the fact that the same modification was found along the longitudes ranging from 135-170°E and even 2 weeks after the event (not shown in the result), suggests seasonal effects on the EIA behaviour and no link with the 12 September 2007 earthquakes.

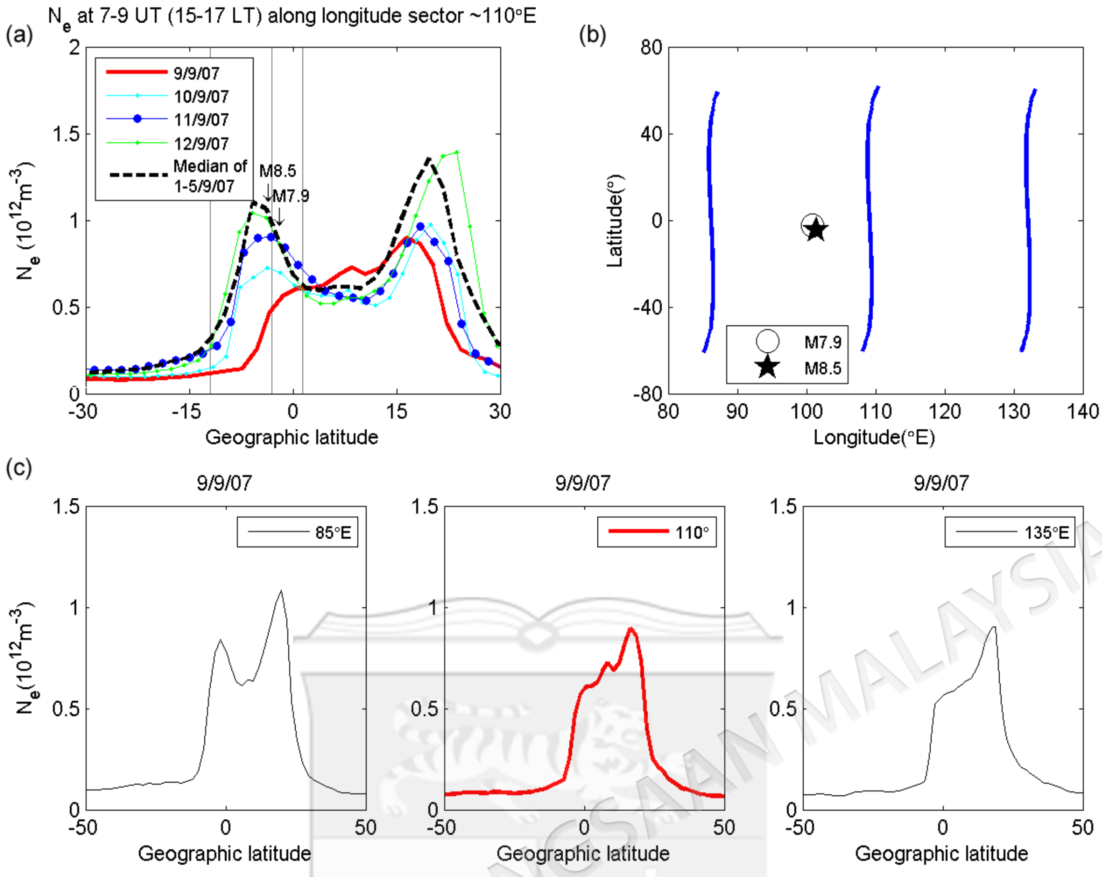

Figure 5.24 The CHAMP N_e variations observed from 7:00-9:00 UT between 9 and 12 September 2007 and the median of 1-5 September. The latitude positions of COCO, BSAT and NTUS stations are also shown. (b) Satellite passes on 9 September and (c) N_e measurements along the longitudes of 85°E, 110°E and 135°E.

5.3 DISCUSSION

Table 5.3 summarizes the results of the ionospheric anomalies in the GPS VTEC and electron density measurements detected before the seven large earthquakes. In this table, the day prior to the event, time (LT=UT+8), the average of the maximum ΔVTEC% (ΔVTEC%$_{max}$) and ΔN_e% and the latitude positions of the detected anomaly in the EIA region are shown. As mentioned earlier, the ionosphere near the epicentres of the Sumatra earthquakes reacts differently relative to its location in the EIA structure. In this respect, the table also indicates the position of each detected anomaly either in the trough or crest region of the EIA. The average ΔVTEC%$_{max}$ at the trough is determined by averaging the maximum ΔVTEC% values at ARAU, UMSP, UTMJ, NTUS, BSAT and PSKI stations, while the value at the crest is obtained by taking the maximum ΔVTEC% at COCO station. Meanwhile, the average ΔN_e% is obtained by averaging the values at the latitude positions of the considered GPS stations in the trough and crest regions.

Table 5.3 The ionospheric anomalies detected before six large earthquake events. The day is relative to the earthquake day.

Event	GPS VTEC				CHAMP Electron density (N_e)			
	Day	Time (LT)	Average of $\Delta VTEC\%_{max}$	Position in EIA region	Day	Time (LT)	Average of ΔN_e%	Position in EIA region
1	26 December 2004, t = 00:58 UT (8:58 LT)							
	6	4:00	+40	Trough				
2	26 February 2005, t = 12:09 UT (12:56 LT)							
	3	13:00	-17	Trough	3	18:30	+20	Trough
		13:00	-19	Crest	3	18:30	-23	Crest
3	28 March 2005, t = 16:09 UT (00:09 LT on 29 March 2005)							
	4	17:30	-15	Trough	4	15:50	-15	Trough
	5	17:30	-15	Trough	5	15:20	-7	Trough
	6	11:00	+1	Trough				
	6	11:00	+67	Crest				
	6	17:00	-9	Trough	6	14:50	-3	Trough
	6	17:00	+63	Crest	6	14:50	+13	Crest
5	24 July 2005, t = 15:42 UT (23:42 LT on 25 July 2005)							
	0	13:00	-24	Trough	0	16:50	-19	Trough
	0	13:00	-45	Crest	0	16:50	-43	Crest
6 & 7	12 September 2007, t = 11:10 UT (19:10 LT) *23:49 UT (7:49 LT on 13 September 2007)							
	0*	1:00	+30	Trough				
	0*	23:00	+18	Crest				
	0	1:00	+46	Trough	0	15:20	-4	Trough
	0	7:00	+88	Crest	0	15:20	-13	Crest
	1	12:00	-28	Trough	1	16:30	+6	Trough
	1	12:00	-28	Crest	1	16:30	-20	Crest
	2	15:00	-19	Trough	2	16:10	-17	Trough
	2	15:00	-25	Crest	2	16:10	-52	Crest
	3	15:00	-23	Trough				
	3	15:00	-40	Crest				

The results show that the ionospheric GPS VTEC anomalies were observed between 6 days and a few hours before the six large earthquakes. The VTEC variations show both positive and negative anomalies with respect to the background value. The table shows that both positive and negative ionospheric anomalies were detected in the GPS VTEC between 6 days and a few hours before the seven large earthquakes surrounding Sumatra. These anomalies were confirmed by using CHAMP electron density measurements. It is shown that most of the significant variations observed in the VTEC and N_e have similar signs. As shown in Table 5.4, the maximum variation of these anomalies mostly occurs during daytime between 4:00 and 17:00 LT prior most of the events. On average, these anomalies have the same amplitude as the day-to-day variability, which is about ±20% but the VTEC variations can be more pronounced with decreases and increases of up to 45% and 88%, respectively at certain moments of local time. The duration of the anomaly of a given sign was observed between 1 and 5 hours, which is very short as compared to magnetic storm effects that normally take days to recover to the normal state. The comparison between GPS VTEC anomalies and CHAMP electron density measurements show that most of the variations observed in the VTEC and N_e have similar tendencies in the sign despite some discrepancies in the ground and satellite-based measurements.

The results are compared with those of previous observations. Hobara and Parrot (2005) demonstrated the daily ΔfoF2 variation between -80 and +45 days around the 1968 Hachinohe earthquake in Japan as a function of different local times (LT). In this work, it is found that the anomalies exceeded their background values between 4:00 and 17:00 LT during 4-9 days before the earthquake. The results show that the daytime VTEC anomalies are in close approximation with their observation as well as with those reported by Liu et al. (2000; 2002; 2004), Sharma et al. (2008) and Yiyan et al. (2009).

As shown in Table 5.3, the observations prior to the earthquake events 3, 5, 6 and 7 show that the magnitude of the local VTEC anomalies does not only depend by their distances from the epicentre but also by their latitude positions in the EIA. In the result, the magnitude of the anomalies detected during the daytime is larger at the station located in the crest region (COCO) as compared to those located in the trough region. Previous observation made by Sharma et al. (2008) during the 1967 Koyna earthquake showed that the ionospheric anomalies detected in the EIA trough region during nighttime were of higher magnitudes than those in the northern crest region although these anomalies are located further from the epicentre. The observation by Sharma et al. (2008) was attributed to the migration of ionospheric anomalies to the direction of the equatorward meriodional winds and the **ExB** drift during the nighttime. In contrast to their observation, the VTEC anomalies in this result were mostly observed in the daytime, during which the direction of meridional winds is toward the crests. Therefore, it is possible that the anomalies generated within the earthquake preparation zone follow the same direction and appear to be more pronounced in the near crest region as shown in Figures 5.17d and 4.26c. The upward **ExB** drift due to the eastward electric fields in the afternoon can also play a significant role for directing these anomalies towards the crest from the equator.

In the analysis of electron density variations, the daytime EIA modification in terms of crests disappearance and crest amplification occurred during a few days before the earthquakes on 26 February 2005 and 28 March 2005. Pulinets and Boyarchuk (2004) stated that the eastward electric field is responsible for the EIA development in the afternoon. If the earthquake preparation area lies between the crests of the EIA and close to the magnetic equator, the anomalous upward electric field from the epicentre will interact with the eastward electric field, which will result in the EIA shape distortions. Sorokin and Chmyrev (1999) and Pulinets and Boyarchuk (2004) explained the upward seismogenic electric field in relation with the vertical turbulent transportation of injected aerosols and radioactive particles. The increase of atmospheric radioactivity level during the earthquake preparation leads to increases in ionization and electric conductivity at the near-ground atmosphere. The joint action of these processes subsequently leads to the intensification of the electric field in the atmosphere and ionosphere. The anomalous vertical electric field has been reported to have peak-to-peak variations of up to 1.5 kV/m during a few hours before earthquakes in Russia and China (Vershinin, 1999; Hao et al., 2000). Only the electric field, which is perpendicular to the geomagnetic field lines, penetrates into the ionosphere causing electron density irregularities (Kim and Hegai, 1997).

To explain the EIA modification of the first type, the results are compared with those of previous observations. Pulinets and Lagen'ka (2002) reported the EIA modifications prior to some strong earthquakes at equatorial latitudes by analyzing the electron density onboard the Intercosmos-19 satellite over the regions of the epicentres. In this work, it is found that about 2 hours before the July 1979 earthquake, the local daytime F2-ionospheric layer descended from 600 to 400 km and the electron concentration over the epicentre increased by about 70%. This phenomenon was also observed by Liu et al. (2002; 2008) and Yiyan et al. (2009) before some strong earthquakes in Taiwan and China, whereby abnormal ionospheric decreases were seen in the northern crest in the afternoon during a few days before the events. They also showed the movement of these anomalies from the crest towards the equator. Liu et al. (2002) concluded that the upward electric field near the epicentre and the equatorial-ward neutral wind in the ionosphere stimulated the equator-ward motions and significant decreases in the EIA crest. Similar to these observations, it is found that the crests disappearance and crest displacement over the magnetic equator occurred 3-5 days before the 26 December 2004 and 12 September 2007 earthquakes.

As for the daytime crest amplification that occurred during a few days before the 28 March 2005 earthquake, Pulinets and Lagen’ka (2002) and Ruzhin et al. (1998) reported the trough deepening and crest amplification using upper ionospheric data from INTERCOSMOS-19 and ALOUETTE satellites, respectively before some strong earthquakes at equatorial latitudes. Ruzhin et al. (1998) suggested that the generation of anomalous eastward electric field at the epicentre of future earthquakes together with Earth’s magnetic field at ionospheric level may cause the intensification of the fountain effect. Namgaladze et al. (2007) proposed the vertical drift of the F2-region ionospheric plasma under the influence of zonal electric field of seismogenic origin. To check this hypothesis, model calculations were carried out by using the Upper Atmosphere Model (UAM), which is a global numerical model of the Earth’s upper atmosphere. In this model, the ionospheric response to the action of zonal electric fields of seismogenic sources at low latitude was investigated by switching on the electric field sources in the UAM electric potential equation. It was shown that the action of the near-equatorial source intensifies the EIA in the near-epicentral area of the ionosphere by deepening the minimum of foF2 over the magnetic equator and displacing the crests from equator to the middle latitudes. The results in the form of daytime EIA amplification before the 26 February and 28 March 2005 earthquakes are found to be in good agreement with results of previous observations and numerical calculations. Based on previous observations and hypotheses, the results in this chapter couple the fact that the anomalous upward electric field generated near the epicentre region interacts with the eastward electric field, hence inducing the ionospheric anomalies in the near epicentre region and equatorial anomaly shape distortions.

5.4 CONCLUSION

This chapter investigates the short-term ionospheric perturbations before six M > 6.5 earthquakes that occurred during the period of 2004-2007 in the Sumatran region using GPS stations surrounding the epicentres and CHAMP satellite data. The behaviour of the near-equatorial ionosphere before these events was also investigated. This study has shown the efficiency to observe pre-earthquake anomalies in the ground-based GPS VTEC and also satellite-based electron density near large earthquake epicentres. The results showed that positive as well as negative anomalies were observed mostly during the daytime from a few hours to 6 days before these events and with duration of about 1-5 hours. These anomalies were detected during very quiet and low magnetic and solar conditions, respectively. Prior to the earthquakes, the GPS VTEC and electron density measurements show similar tendencies but both show variability in the trough and crest regions. This variability is probably due to the direction of meriodional winds and eastward electric fields towards the crests during the daytime as well as the EIA modifications that occurred a few days before the earthquakes. The EIA modification appears in the form of crest amplification during the daytime. It is concluded that the EIA amplification is caused by the vertical drift of the F2-region ionospheric plasma under the influence of zonal electric field of seismogenic origin. The results of the GPS VTEC and electron density anomalies were in good agreement, suggesting that the anomalous upward seismogenic electric field interacts with the eastward electric field and induce the ionospheric anomalies in the near epicentre region as well as equatorial anomaly shape distortions.

Despite the consideration of many factors in the detection of pre-earthquake ionospheric anomalies such as the solar and geomagnetic activity, ionospheric day-to-day variability, equatorial plasma depletion and locality, these anomalies should be further studied before regarding them as earthquake precursors. This is due to the complicated nature of earthquakes and the equatorial ionosphere, which are highly dynamic and unpredictable. Nevertheless, the study of pre-earthquake ionospheric anomalies by joint ground and space-based techniques might improve the understanding of the physical processes during the earthquake preparation process that is not completely understood. The other challenge in this research is to statistically demonstrate the relation between an anomalous signal and a given earthquake and to quantify the background variability of the ionosphere in the absence of earthquakes. Therefore, the next chapter discusses the ionospheric VTEC variations during both earthquake and non-earthquake periods based on long-term data basis using several statistical analysis methods.

CHAPTER VI

LONG-TERM ANALYSIS OF IONOSPHERIC PERTURBATIONS

The short term analysis of pre-earthquake ionospheric perturbation has been investigated in Chapter V. In this chapter, the long-term statistical analysis of temporal correlation is performed between irregular VTEC and earthquake occurrence using three statistical analysis techniques, which are the envelope, correlation and the VTEC variability index. The study is based on continuous GPS VTEC measurements during the periods of July 2004 - June 2006 and September 2007 at stations surrounding the earthquake epicentres in Sumatra, which are ARAU, USMP, UTMJ, NTUS, PSKI, BSAT and COCO stations. The correlation between the irregular VTEC and 57 earthquake events with magnitudes greater than 6.0 Richter scale that took place within the latitudes 7°S to 7°N and longitudes from 90° to 100°E (NEIC 2010) is analyzed using the three statistical methods. The analysis of each statistical method takes into account the filtration of GPS VTEC measurements during periods of high geomagnetic and solar activity. With this respect, the pattern of the ionospheric VTEC variability during quiet and low geomagnetic and solar activity for each method is presented. Finally, results between the statistical analysis techniques are cross compared and summarized.

6.1 ENVELOPE ANALYSIS TECHNIQUE

The long-term statistical analysis of temporal correlation between the irregular ionospheric VTEC and occurrences of 57 strong earthquake events surrounding the Sumatra region is investigated during the periods of July 2004 - June 2006 and September 2007. The map of the earthquake epicentres and GPS receiver stations used in this study is available in APPENDIX B. The time, latitude, longitude and depth of these earthquake events are detailed in APPENDIX C. In this work, the time series of the percentage of VTEC deviation using the envelope analysis technique is firstly presented to quantify the VTEC variations. To obtain the temporal pattern of the irregular VTEC, the average of the percentage of VTEC deviation and the total number of ΔVTEC% detections are analyzed alongside the geomagnetic and solar indices. This is to determine whether the irregular VTEC is caused by the earthquake preparation or due to other sources such as solar-terrestrial phenomena. The analyses are presented as follows:

a. Time series of ΔVTEC%

Figure 6.1 presents the time series of the Dst index and the percentage of VTEC deviation (ΔVTEC%) between July and December 2004 at seven GPS stations. In the figure, the vertical lines mark the time of 10 earthquake events with magnitudes of 6, 7, 8 and 9 during the six month period. As mentioned previous chapter, the ΔVTEC% in this analysis is filtered out during days of moderate and high geomagnetic and solar activity, respectively, whereby |Dst|<-50 nT, Kp>4 and F10.7>150. As shown in the Figure 6.1, strong positive and negative ΔVTEC% variations of up to 50% and 100%, respectively were observed during 3 weeks before the M7.3, 25 July 2004 event followed by strong positive ΔVTEC% of nearly 100% about 2 weeks before the event at ARAU, USMP, UTMJ, NTUS and COCO stations. It is shown that the magnitude of the positive ΔVTEC% detected 2 weeks before the July event was much stronger at stations located closer to the epicentre (ARAU, USMP, UTMJ, NTUS) and becomes weaker with distance. However, strong ΔVTEC% variations were also found even during non-earthquake periods, which is between August and early November 2004 at all seven stations. During this period, larger positive ΔVTEC% variations with values reaching 100% with respect to the upper bound were observed at PSKI and COCO stations. This observation is most probably due to seasonal VTEC variation, whereby VTEC variability is normally higher during the equinoctial months of September and October (Bagiya et al. 2009). Meanwhile, strong ΔVTEC% variations were also found within 7 days before the M9.3, 26 December 2004 event and the subsequent aftershocks at all seven stations, which the analysis for the large earthquake has been presented in detail in Chapter 5. It was also observed that the large VTEC variations also exceed the normal day-to-day variability, which is typically about 30% at the equatorial latitudes (Bilitza et al. 2004).

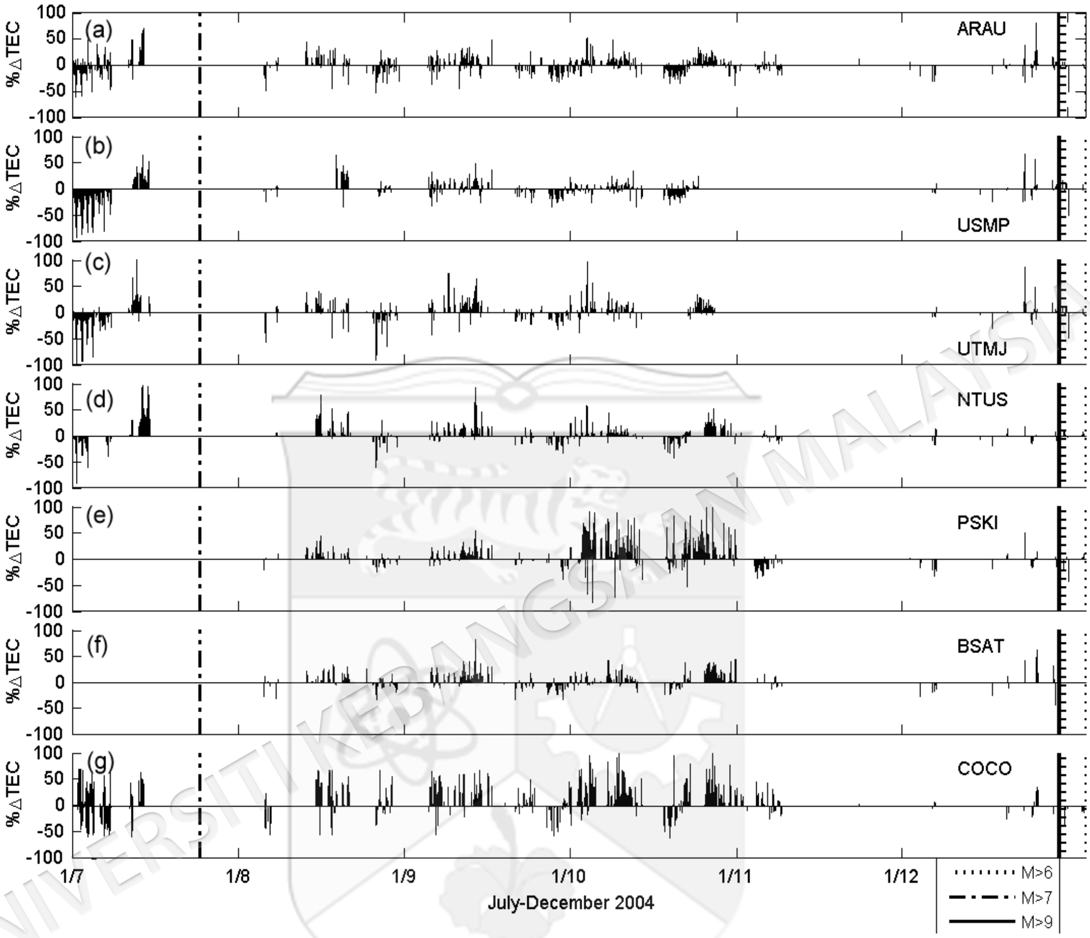

Figure 6.1 The percentage of VTEC deviation between July and December 2004 at seven GPS stations.

The same analysis in Figure 6.1 is repeated during the year 2005, whereby ΔVTEC% at six GPS stations are examined during the period between January and June and July and December 2005 as presented in Figures 6.2 and 6.3, respectively. In Figure 6.2, about 26 strong earthquakes took place during the first half of 2005. As shown in the figure, no pronounced ΔVTEC% was observed prior to the events in January 2005 at all the six stations as majority of these values are filtered out due to moderate geomagnetic activity during this month. After this period, pronounced ΔVTEC% variations were seen a few days before and even after the events at all the six stations and this trend follow until June 2005. It was shown that starting from April 2005 onwards; the ΔVTEC% at COCO station is largely varied with both positive and negative variations of up 100% and this condition persisted until October 2005.

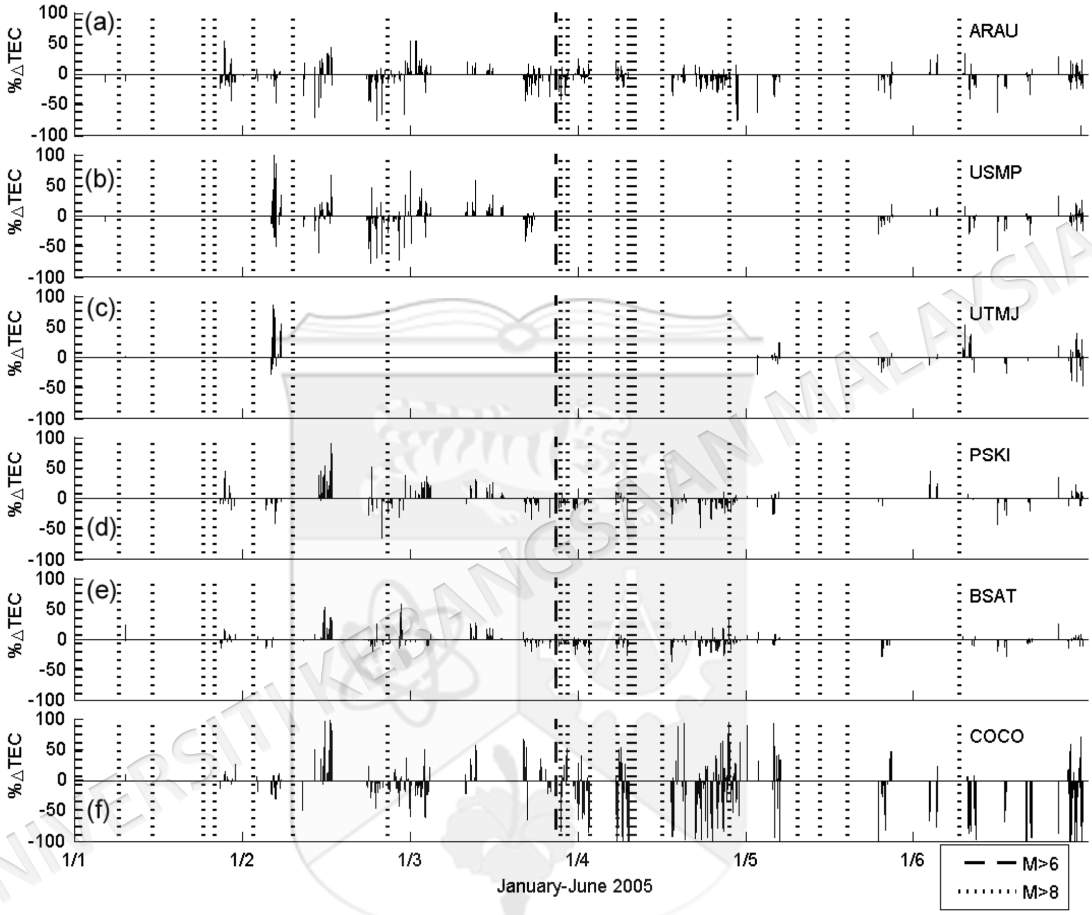

Figure 6.2 The percentage of VTEC deviation between January and June 2005 at six GPS stations.

As shown in Figure 6.3, ΔVTEC% variations were observed during a few days before the 3 earthquake events but larger ΔVTEC% variations were seen during the non-earthquake period, which is between August and November 2005 at all the six stations. During the non-earthquake period, the same trend was observed at all the six stations with the largest ΔVTEC% variation found at the equatorial anomaly crest station, COCO.

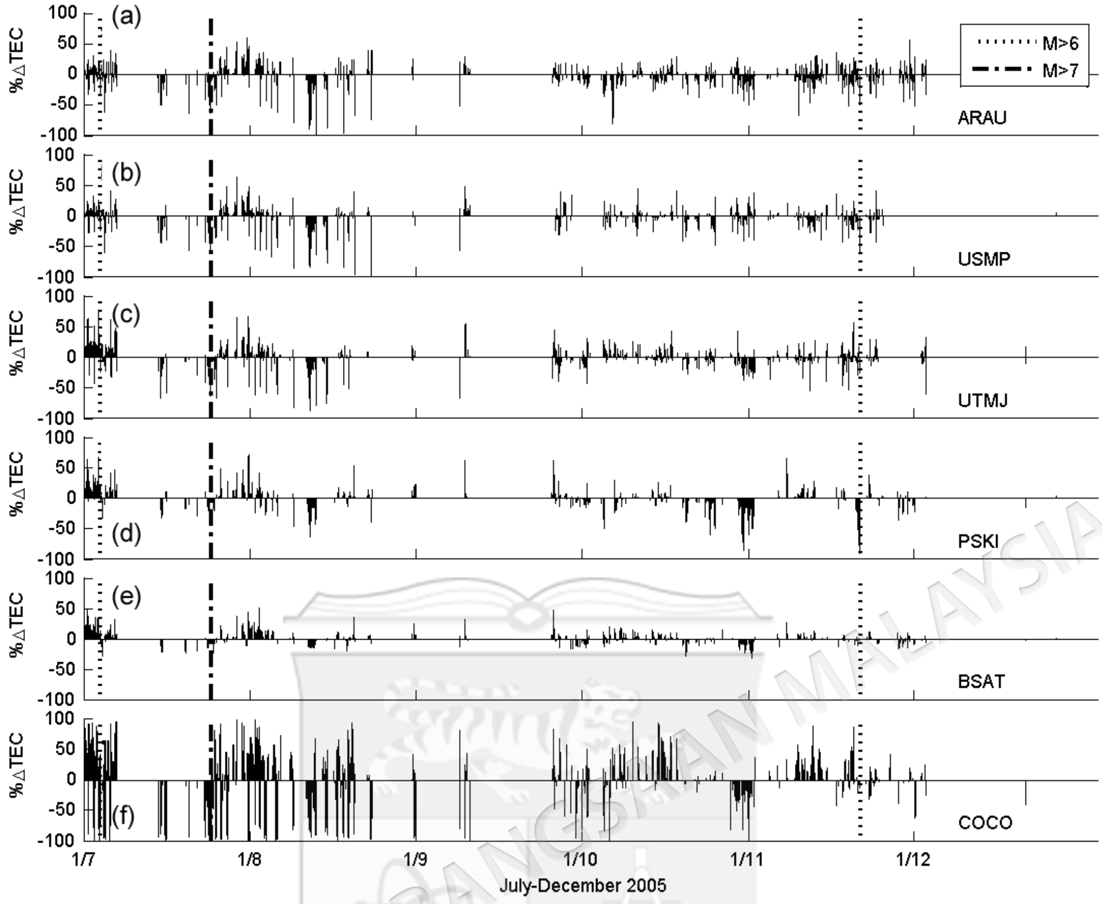

Figure 6.3 The percentage of VTEC deviation between June and December 2005 at six GPS stations.

Figure 6.4 presents the ΔVTEC% between January and June 2006 at six GPS stations. As shown in the figure, most of the ΔVTEC% variations observed at all the six stations during this observation period were found in the months of March and June 2006, which do not coincide with any earthquake event. The largest ΔVTEC% variation during the equinoctial and summer months was observed at COCO station.

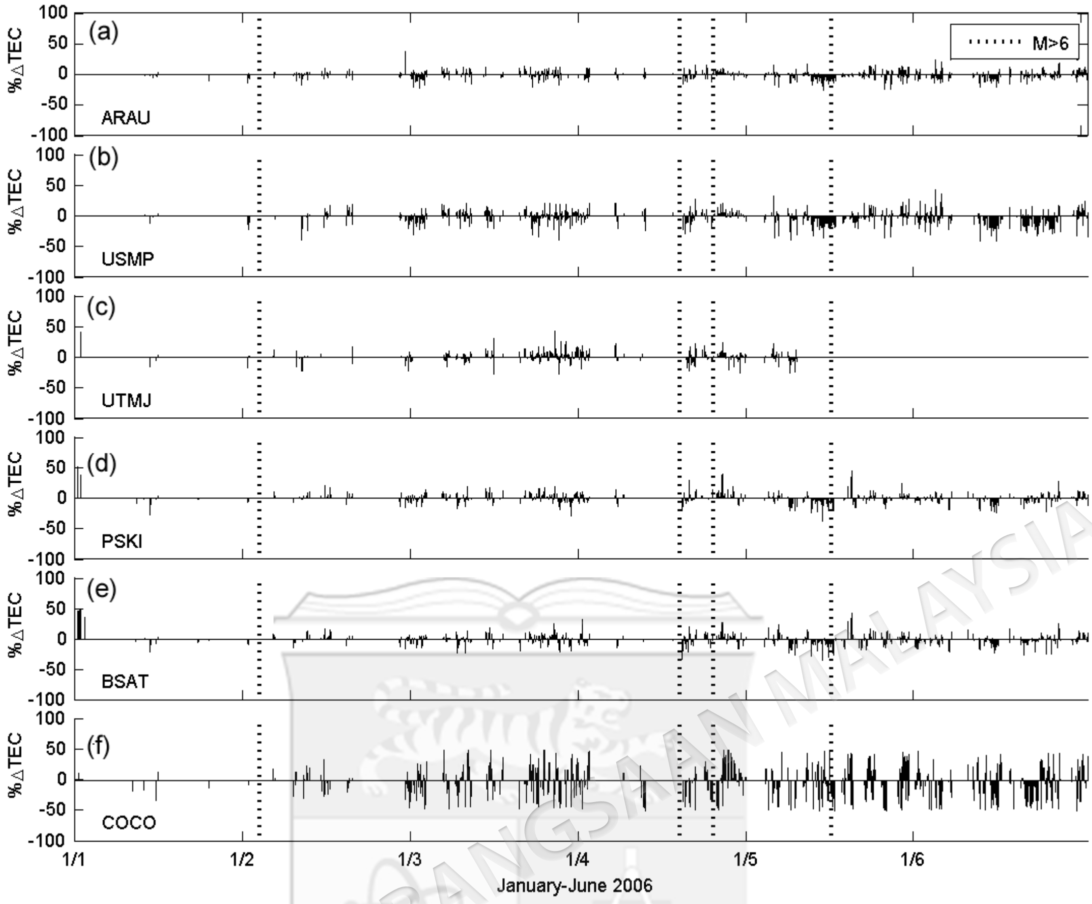

Figure 6.4 The percentage of VTEC deviation between January and June 2006 at six GPS stations.

As for the month of September 2007, the geomagnetic Dst index and the percentage of VTEC deviation between 6 and 30 September 2007 at three GPS stations are presented in Figure 6.5. As shown in the figure, strong ΔVTEC% variations were found within a week before the 10 strong earthquake events throughout the month of September 2007 at all the three stations.

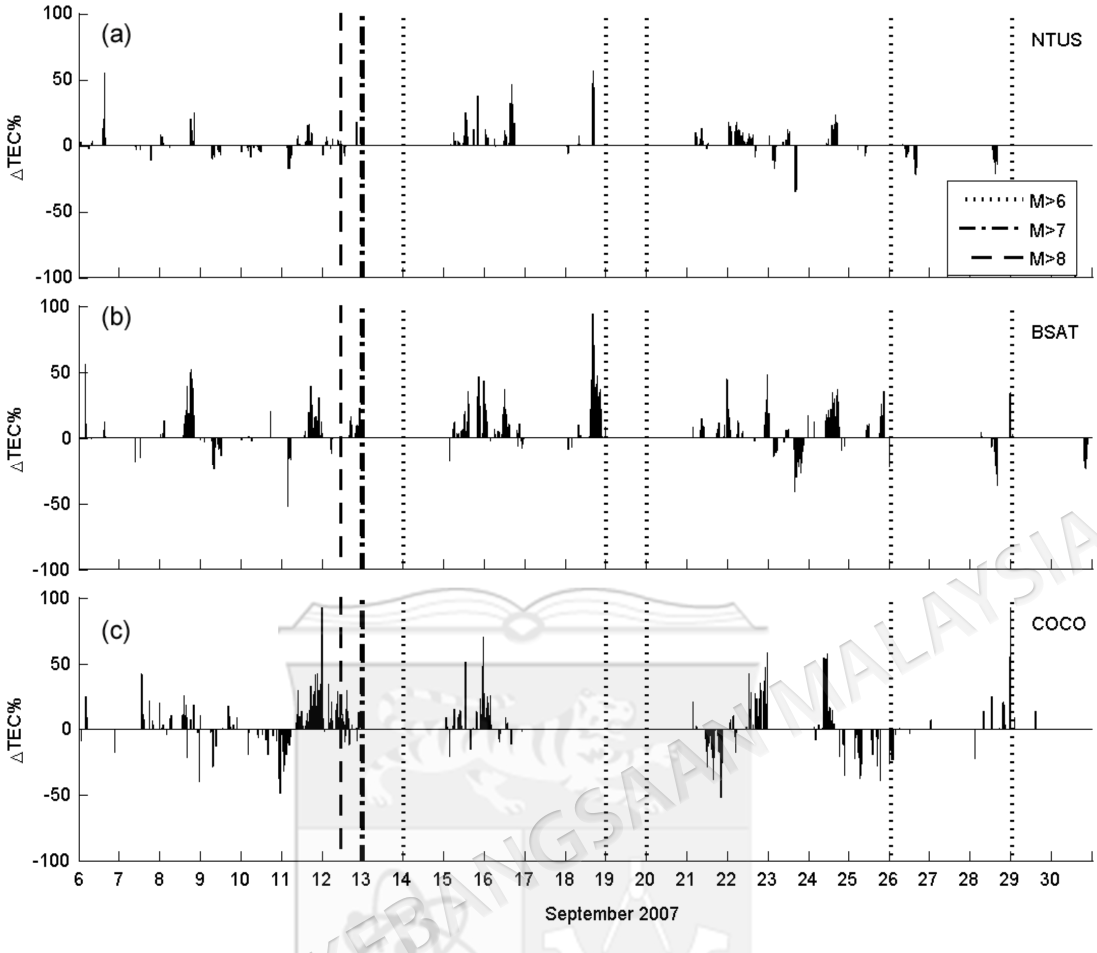

Figure 6.5 The geomagnetic Dst index and the percentage of VTEC deviation between 6 and 30 September 2007 at three GPS stations.

b. Temporal pattern of ∆VTEC% detection

Figure 6.6 shows the geomagnetic and solar indices Dst and solar flux F10.7, the daily average of the positive and inverse negative ∆VTEC% and the total number of weighted daily positive and negative ∆VTEC% detections for seven stations during the period between July and December 2004. The horizontal dashed lines in Figures 6.6(a),(b),(e),(f) represent the threshold values of the Dst and F10.7 indices and number of positive and negative detections, respectively. As shown in Figures 6.6(c),(e), the daily average positive ∆VTEC% of about 5-27% and a total number of 93 positive detections were observed throughout the six month period. However, it can be seen that the total number of positive detections increases with increasing value of F10.7 and 15% (14/93) of the detections, which exceed the threshold value correspond to the peaks of F10.7. Meanwhile, the average negative ΔVTEC% in Figure 6.6(d) of about -5% are also detected with a total number of 92 detections throughout the observation period. In contrast to the positive ΔVTEC% detection, the total number of negative ΔVTEC% detection shows an increasing trend with the decreasing value of the F10.7 index.

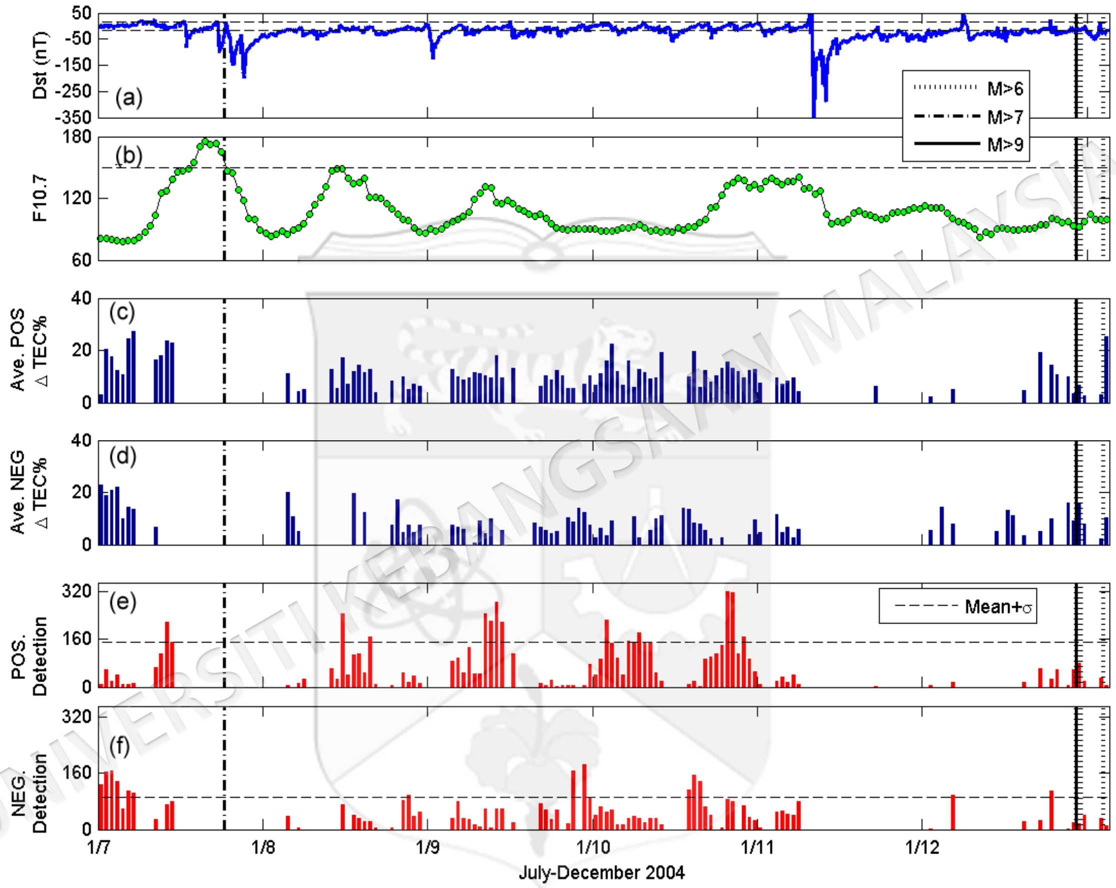

Figure 6.6 The (a) Dst and (b) F10.7 indices, the daily average (c) positive and (d) negative ΔVTEC% and the total number of (e) positive and (f) negative detections for seven GPS stations between July and December 2004 using the envelope method.

In order to investigate the dependence of the total number of ΔVTEC% detection to the solar flux F10.7 index, the relationship between these two parameters will be analyzed later in the section. For the period between July and December 2004, about 4-10% of the negative ΔVTEC% detections were observed during the period of 15 days before the earthquake events.

Figures 6.7 and 6.8 present the Dst and F10.7 indices, the daily average and the total number of weighted daily positive and negative ΔVTEC% detections for six stations during the periods between January and June 2005 and between July and December 2005, respectively. As shown in Figures 6.7(c)-(d), the average ΔVTEC% of about 12% and -15% were observed for positive and negative detections, respectively throughout the six month period, which corresponds to 66 detections for both positive and negative ΔTEC% as shown in Figure 6.6(e)-(f). Similar to the observation in Figure 6.6(e), the total number of positive detections was found to be linearly increasing with F10.7 and that 13% (9/66) of the detections, which exceed the threshold value correspond to the peaks of F10.7.

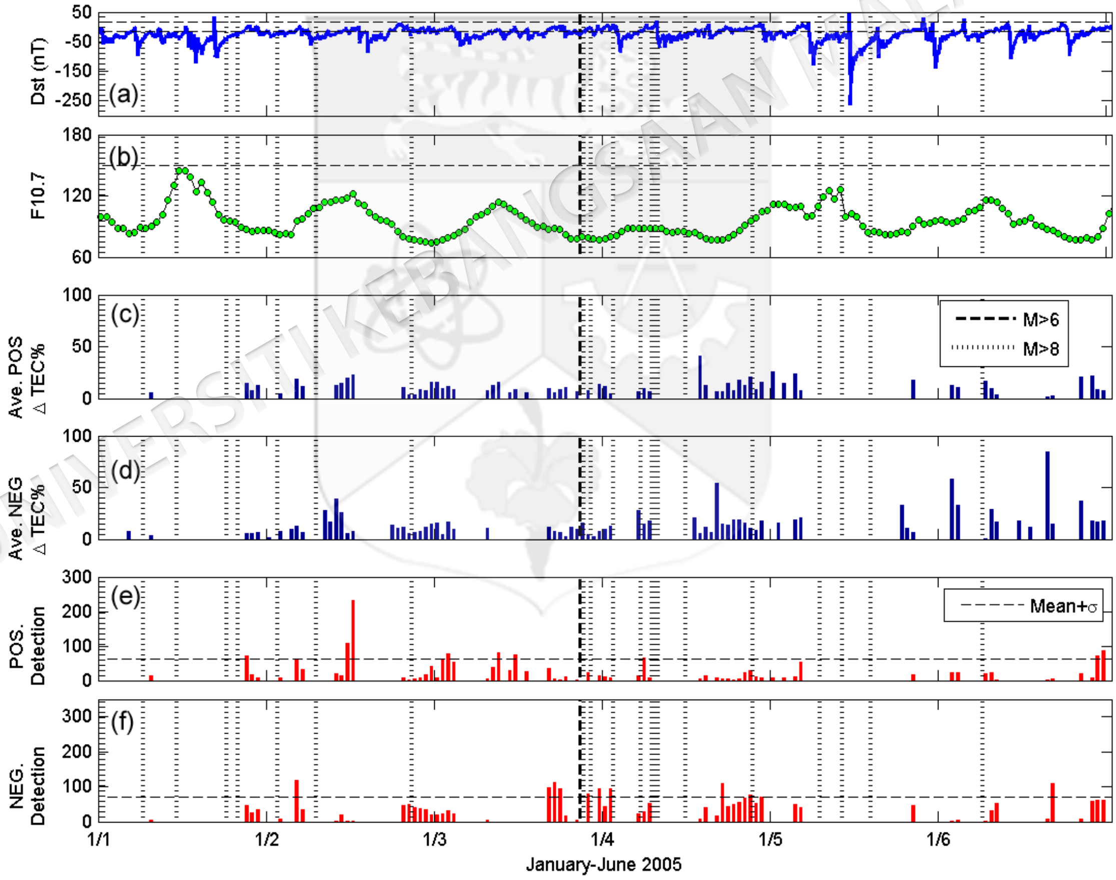

Figure 6.7 The (a) Dst and (b) F10.7 indices, the daily average (c) positive and (d) the inverse negative ΔVTEC% and the total number of (e) positive and (f) negative detections for seven GPS stations between January and June 2005 using the envelope method.

In Figure 6.7(f), it was observed that about 18% of the total number of negative ΔVTEC% detections exceed the threshold value and these values show no relation with the F10.7 index. As for pre-earthquake detection during the period between January and June 2005, about 51% (34/66) of the negative ΔVTEC% detections were observed within a week before the earthquake events.

As shown in Figure 6.8(d), an average negative ΔVTEC% of -17% was found during the period between July and December 2005 and this corresponds to 93 detections as shown in Figure 6.8(f). It was observed that about 17% of the pre-earthquake detections were found although most of the negative ΔVTEC% detections, which exceed the threshold value were observed during the absence of earthquakes, that is between August and November 2005.

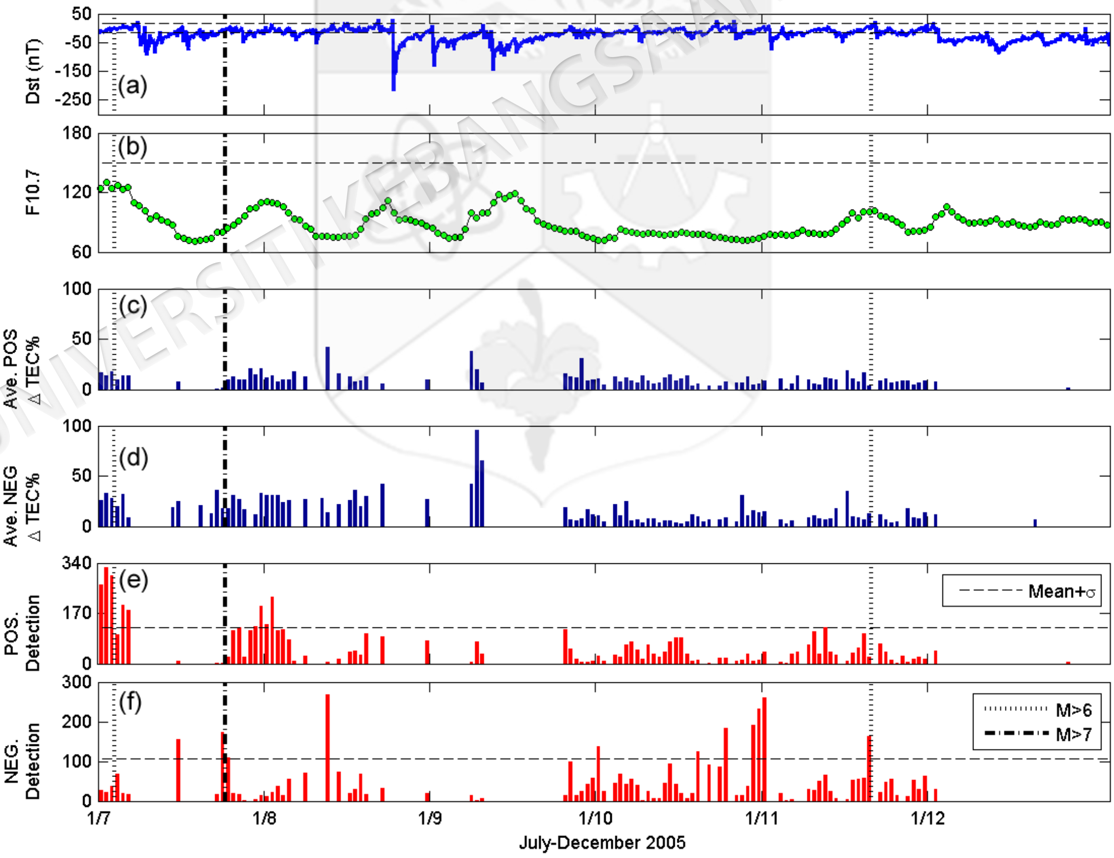

Figure 6.8 The (a) Dst and (b) F10.7 indices, the daily average (c) positive and (d) the inverse negative ΔVTEC% and the total number of (e) positive and (f) negative detections for seven GPS stations between July and December 2005 using the envelope method.

As shown in Figure 6.9(d), the average negative ΔVTEC% of about -8% was observed with a total number of 102 detections during the observation period from January to June 2006. Among these detections, about 14% were detected within a week before the events, although many of these detections were also found during the absence of earthquakes, especially in March, April and June 2006.

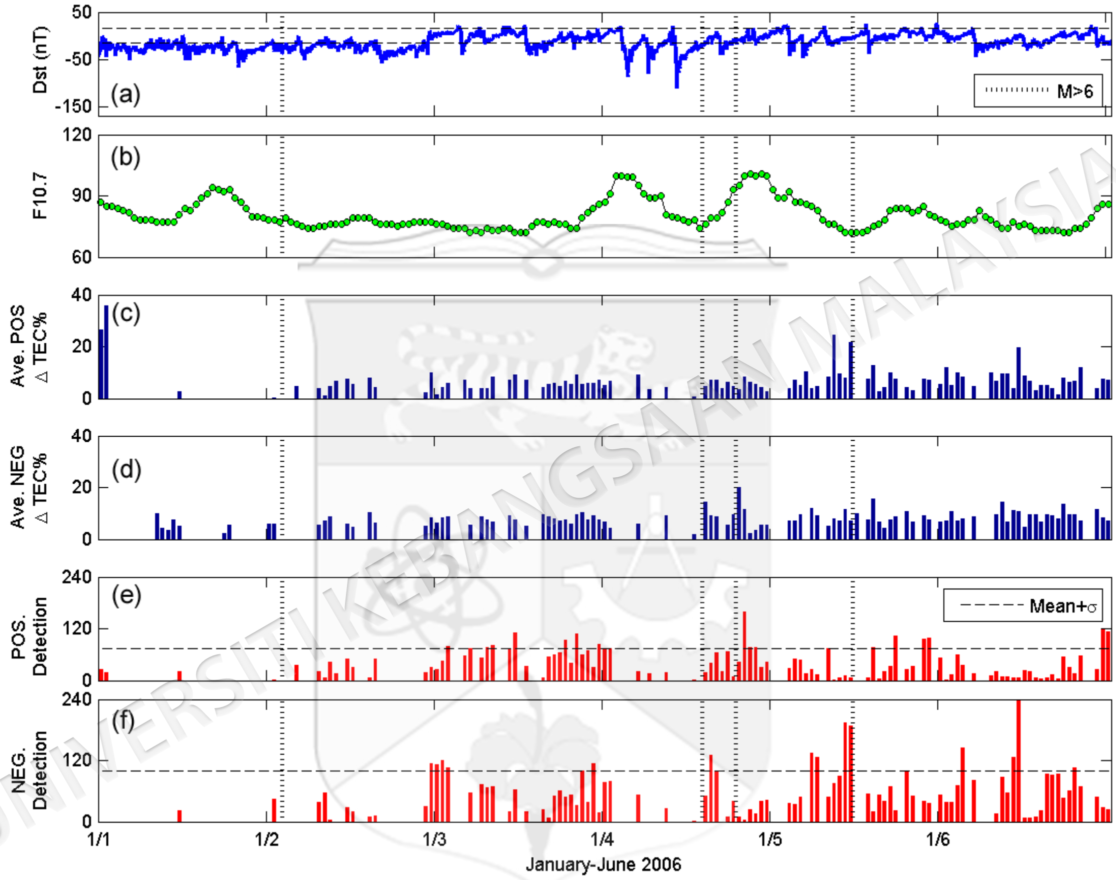

Figure 6.9 The (a) Dst and (b) F10.7 indices, the daily average (c) positive and (d) the inverse negative ΔVTEC% and the total number of (e) positive and (f) negative detections for seven GPS stations between January and June 2006 using the envelope method.

As shown in Figure 6.10(a)-(b), the period between 6 and 30 September 2007 corresponds to very quiet and low geomagnetic and solar conditions, respectively. During this period, the average of both positive and negative ΔVTEC% of about 12 and -12%, respectively show no relation with the changing values of either Dst or F10.7 index. In Figures 6.10(e)-(f), it is shown that all the 18 positive and negative

ΔVTEC% detections were found within a week before the events in September 2007. It was also observed that the total number of positive and negative detections increase as the event day approaches.

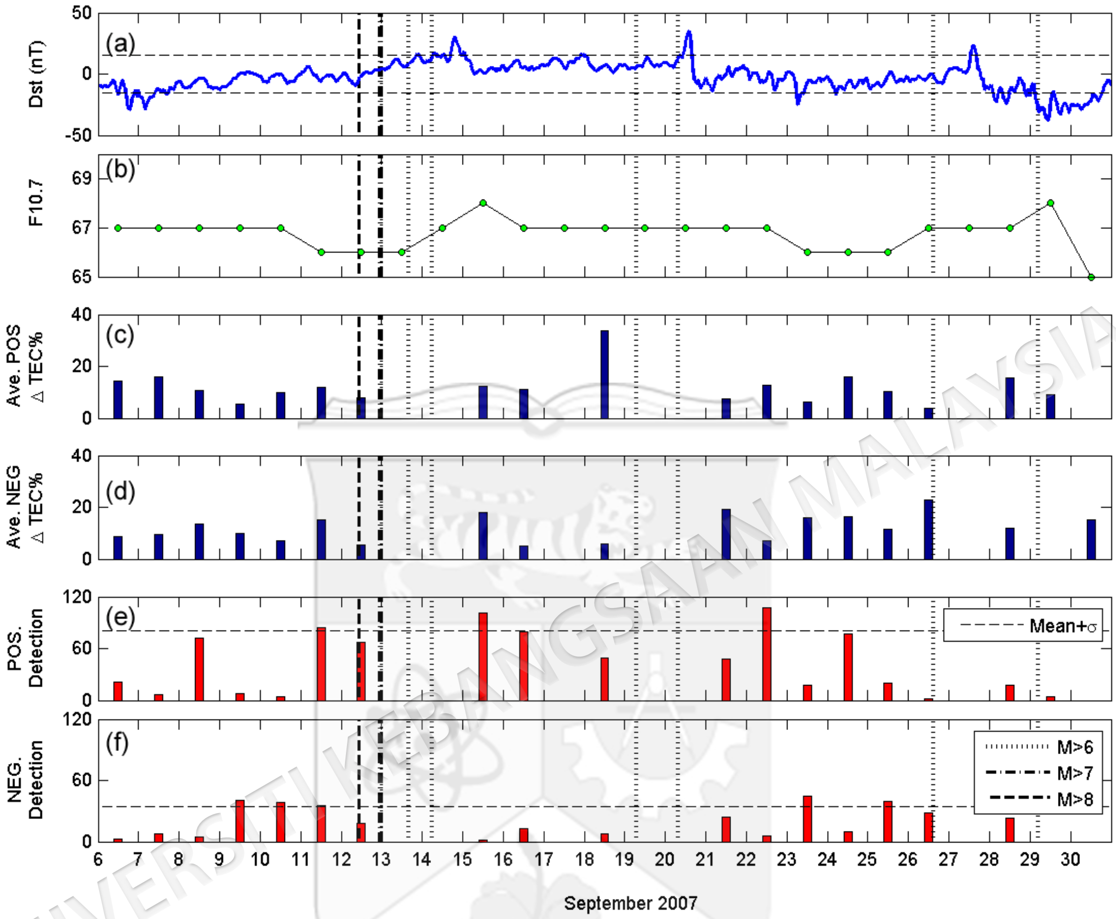

Figure 6.10 The (a) Dst and (b) F10.7 indices, the daily average (c) positive and (d) the inverse negative ΔVTEC% and the total number of (e) positive and (f) negative detections for three GPS stations between 6 and 30 September 2007 using the envelope method.

In order to determine whether the positive and negative ΔVTEC% detections during the entire studied period are caused by the earthquake preparation or solar-terrestrial phenomena, the relationship between these detections with the solar flux F10.7 is demonstrated. Figure 6.11 presents the scatter plot and linear regression of the total number of positive and negative ΔVTEC% detections versus F10.7 for the period of 7 days before earthquakes and non-earthquake period. In these figures, the red dots show the detections which exceed the threshold value. As shown in Figure 6.11(a)-(b), an increased linearly relationship was observed between the number of positive detections and F10.7 during both the pre-earthquake and non-earthquake periods. It was seen that the positive detections during the pre-earthquake period is weakly correlated with F10.7 with the correlation coefficient of (R = 0.29). Meanwhile, the correlation during the non-earthquake period (R = 0.46) is higher than the one observed during the pre-earthquake period with the number of positive detections, which exceed the threshold value increases as the F10.7 index increases. In Figures 6.11(c)-(d), the number of negative detections was found to be have almost no correlation (R = -0.08) with F10.7, while a negative linear relationship was observed during the non-earthquake period with a correlation coefficient of (R = -0.34). The result shows that the positive and negative detections observed before the strong earthquake events in Sumatra are lowly correlated with solar activity.

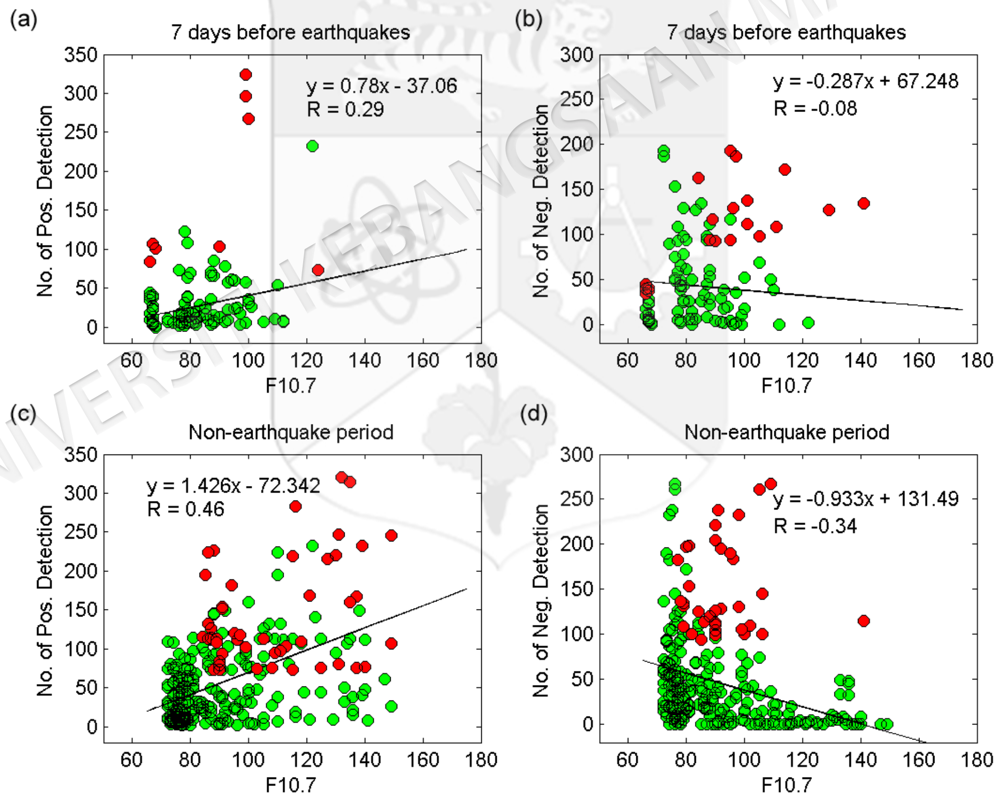

Figure 6.11 The relationship between total number of positive and negative detections and the solar flux F10.7 for pre-earthquake and non-earthquake periods.

6.2 CORRELATION ANALYSIS TECHNIQUE

As mentioned in Section 3.7.3, this method involves the correlation coefficients between one station in the earthquake preparation area and the other located outside of it. Due to lack of GPS measurements in the equatorial region, the daily correlation coefficients between the station located within 1000 km from the earthquake epicentre (PSKI, ARAU, BSAT, USMP, NTUS or UTMJ) and COCO station, which is located further than 1000 km are determined throughout the observation period. Figure 6.12 presents the geomagnetic Dst index and correlation coefficient for six GPS station pairs for the period between July and December 2004. In Figures 6.12(b)-(g), the solid and dashed blue horizontal lines represent the mean and threshold values of the correlation coefficient (Mean-σ), respectively during the six month interval, whereby σ is standard deviation of the correlation coefficient.

As shown in Figures 6.12(b)-(g), a total number of 80 correlation coefficient drops were found to fall below the threshold value throughout the six month period but only 11% (9/80) of them were observed about 15 days before the earthquake events. Most of the correlation coefficient drops such as those observed from the months of August to October 2004 do not coincide with the pre-earthquake periods. During this period, the correlation coefficients drop to values as low as 0 and similar to the observation of the envelope analysis, the correlation analysis technique also show strong seasonal variations. During the period prior to the M9.3, 26 December 2004 event, the first correlation coefficient drop was detected by the station pair COCO-BSAT, whereby BSAT is nearest station from the epicentre about 7 days before the event. This is followed correlation coefficient drops detected by other stations about 1-2 days before the event. It is interesting to find that these correlation coefficients decrease gradually with decreasing distance of the sensor station from the epicentre, which shows a localized seismo-ionospheric coupling behavior as described by Tsolis et al. (2009).

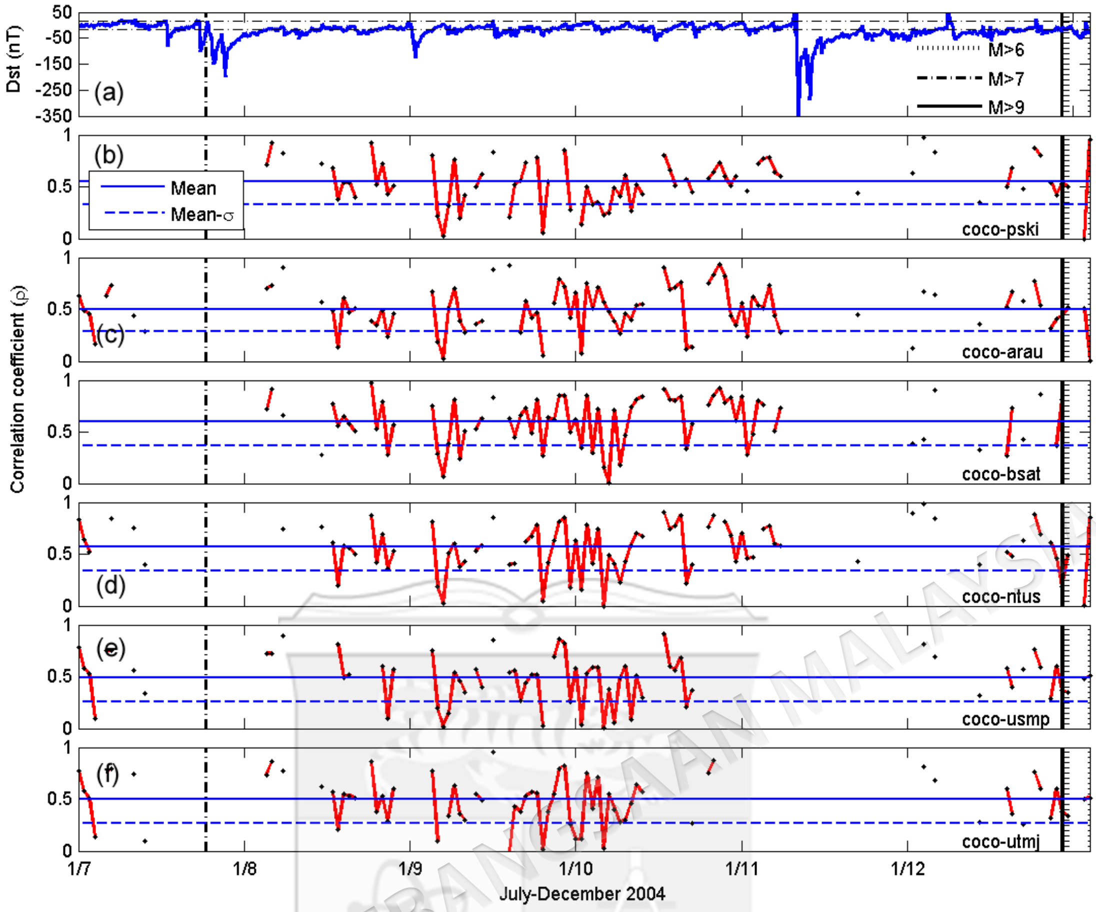

Figure 6.12 The geomagnetic Dst and correlation coefficient for six station pairs between July and December 2004. The solid and dashed blue horizontal lines show the mean and threshold value, respectively.

Figures 6.13 and 6.14 show the geomagnetic Dst and correlation coefficients for five GPS station pairs for the periods between January and June 2005 and July and December 2005, respectively. As shown in these figures, a total number of 58 and 84 correlation drops, which exceed their threshold values were detected during the first and second half of 2005, respectively. During these periods, it was observed that about 52% (30/58) and 14% (12/84) of these correlation drops exceed the associated threshold values for the first and second half of 2005, respectively within a week before the earthquake events. In Figures 6.13(b)-(f), it was found that the pre-earthquake correlation drops during the 5 and 26 February, 28 March and 28 April 2005 events decrease with decreasing distance of the sensor station from the epicentre. However, this trend was not observed during the period of July - December 2005 as presented in Figure 6.14(b)-(f), whereby most the significant correlation drops were detected between the months of August and October 2005 even during very quiet geomagnetic activity although no earthquake events took place during this period.

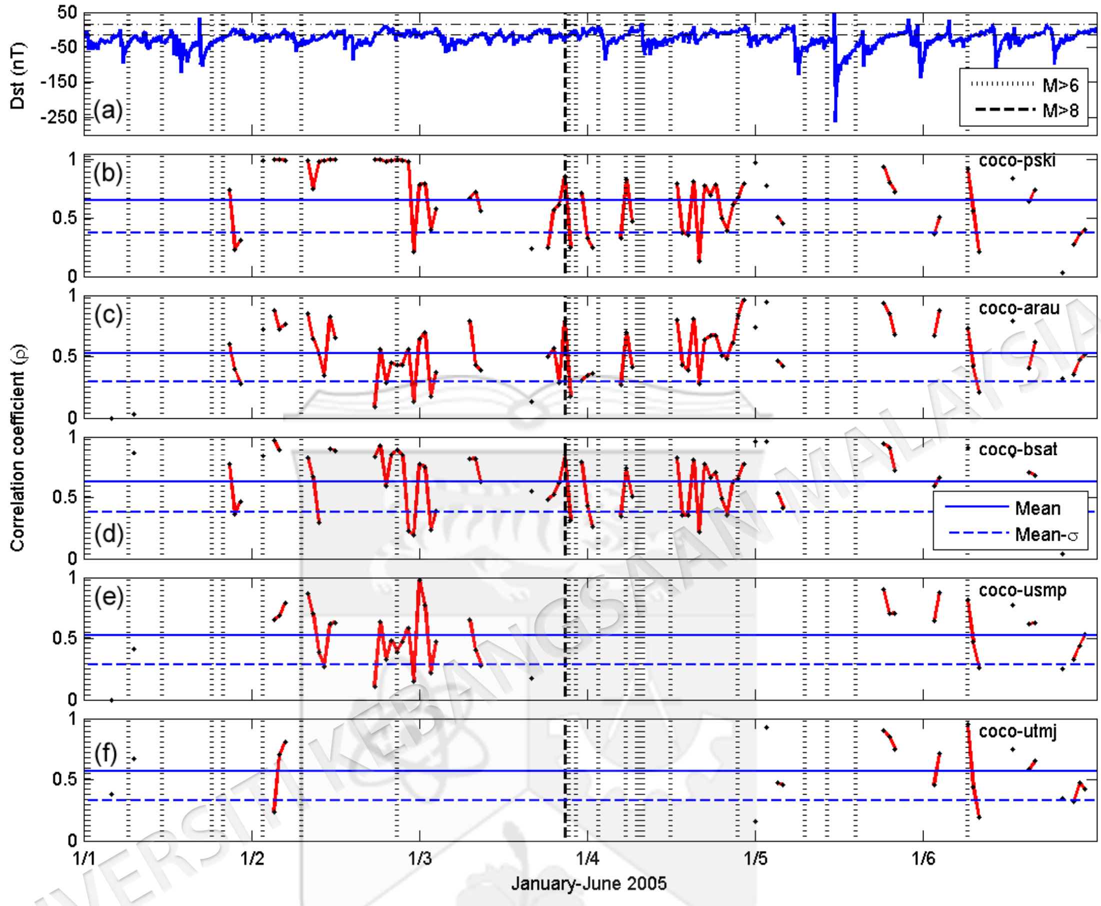

Figure 6.13 The geomagnetic Dst and correlation coefficients for five station pairs between January and June 2005.

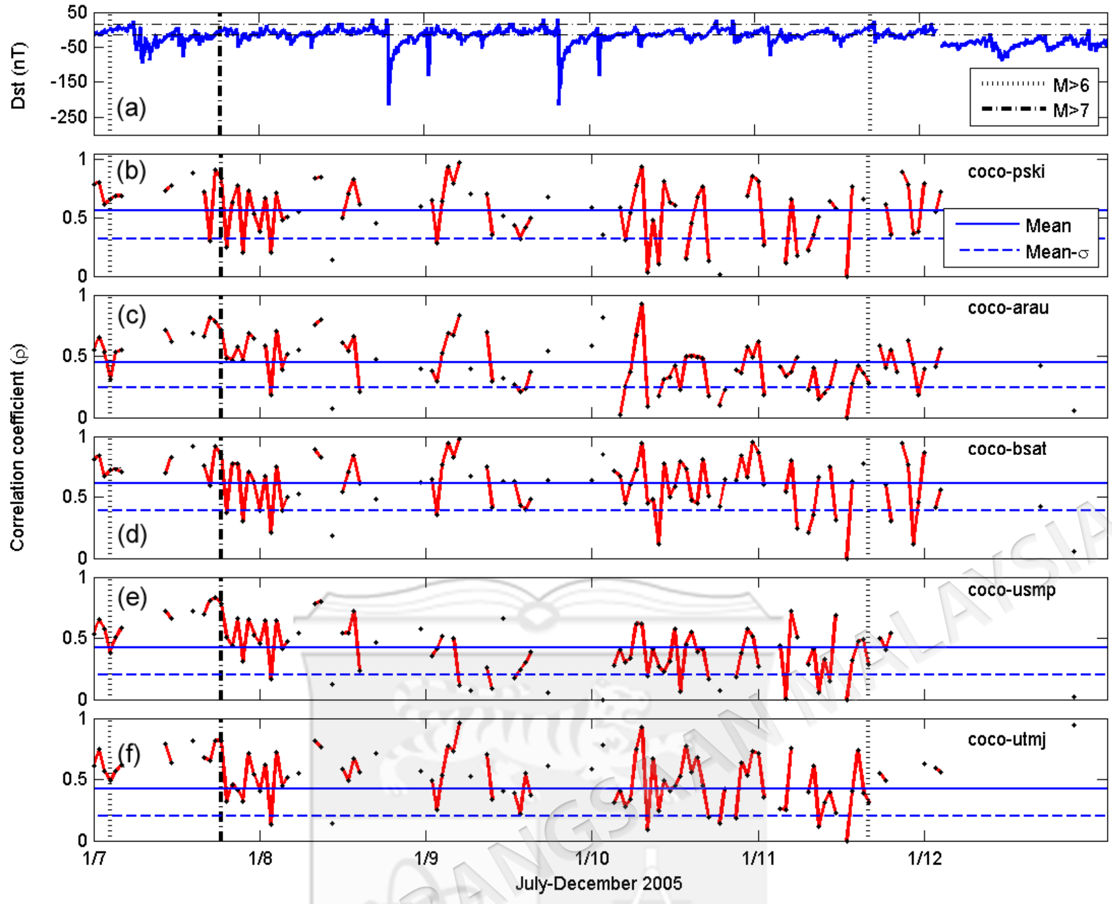

Figure 6.14 The geomagnetic Dst and correlation coefficient for five station pairs between July and December 2005.

The correlation coefficient analysis during the period of January - June 2006 is presented in Figure 6.15. As shown in Figures 6.15(b)-(f), about 76 correlation coefficient drops were observed to fall below the threshold value, in which only 9% (7/76) coincide with the pre-earthquake periods (within a week before the events). Similar to the observation using the envelope method in Figures 6.4 and 6.9, many of the significant correlation drops were also found during the absence of earthquakes, especially in March, April and June 2006. Nonetheless, the pre-earthquake correlation drops of the 25 April and 26 May 2006 events were found to be decreasing with the decreasing distance of the sensor station from the epicentre.

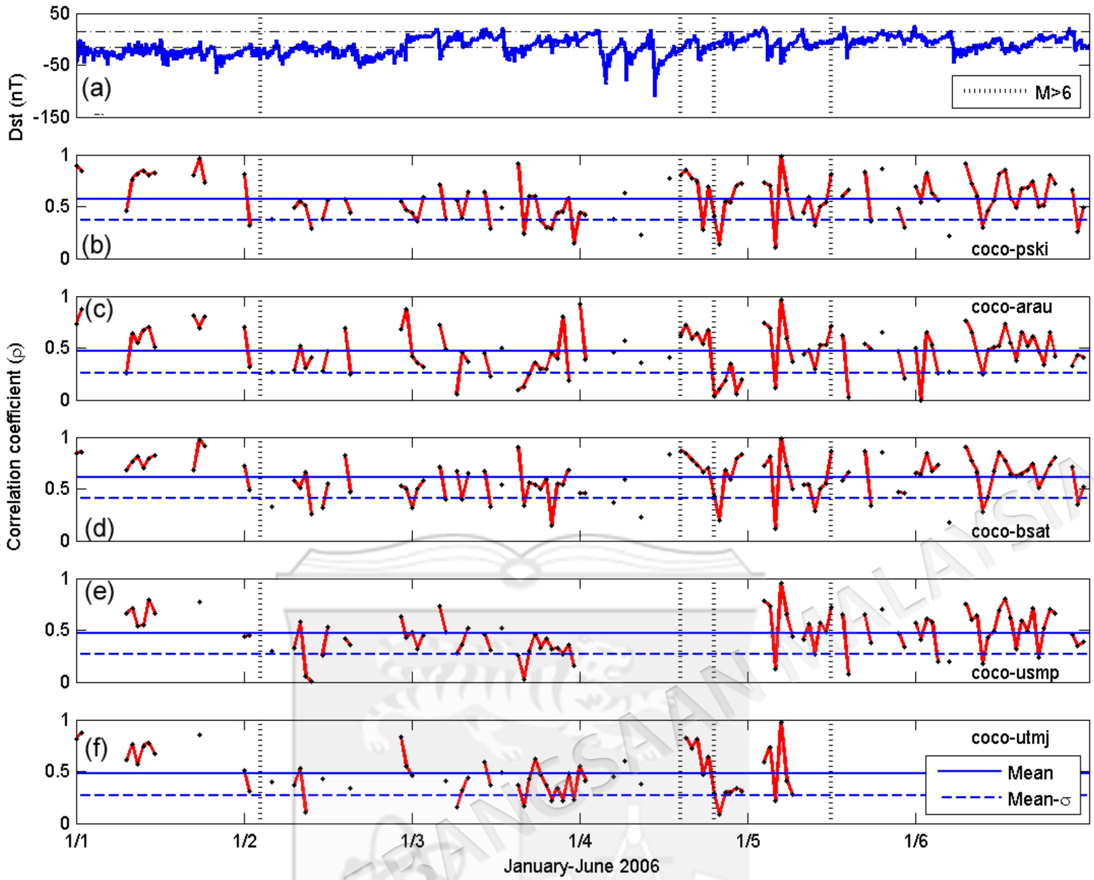

Figure 6.15 The geomagnetic Dst and correlation coefficients for five station pairs between January and June 2006.

In Figure 6.16(b)-(d), it can be seen that among 18 correlation coefficient drops, which exceed their threshold value, 17 of them were observed within 1-7 days before the events during September 2007 and this corresponds to a value of 94%. During this period, it can be seen that these pre-earthquake correlation drops for both the station pairs of COCO-BSAT and COCO-NTUS are much lower as compared to that of BSAT-NTUS. This is because BSAT and NTUS station are both positioned within the earthquake preparation area. Therefore, the seismo-ionospheric coupling effect felt by both stations are less compared to the station pair, with one of the stations positioned in the earthquake preparation area and the other outside of it as in the case of COCO-BSAT and COCO-NTUS. This observation shows that the choice of the station pair for this analysis is important in order to obtain better results.

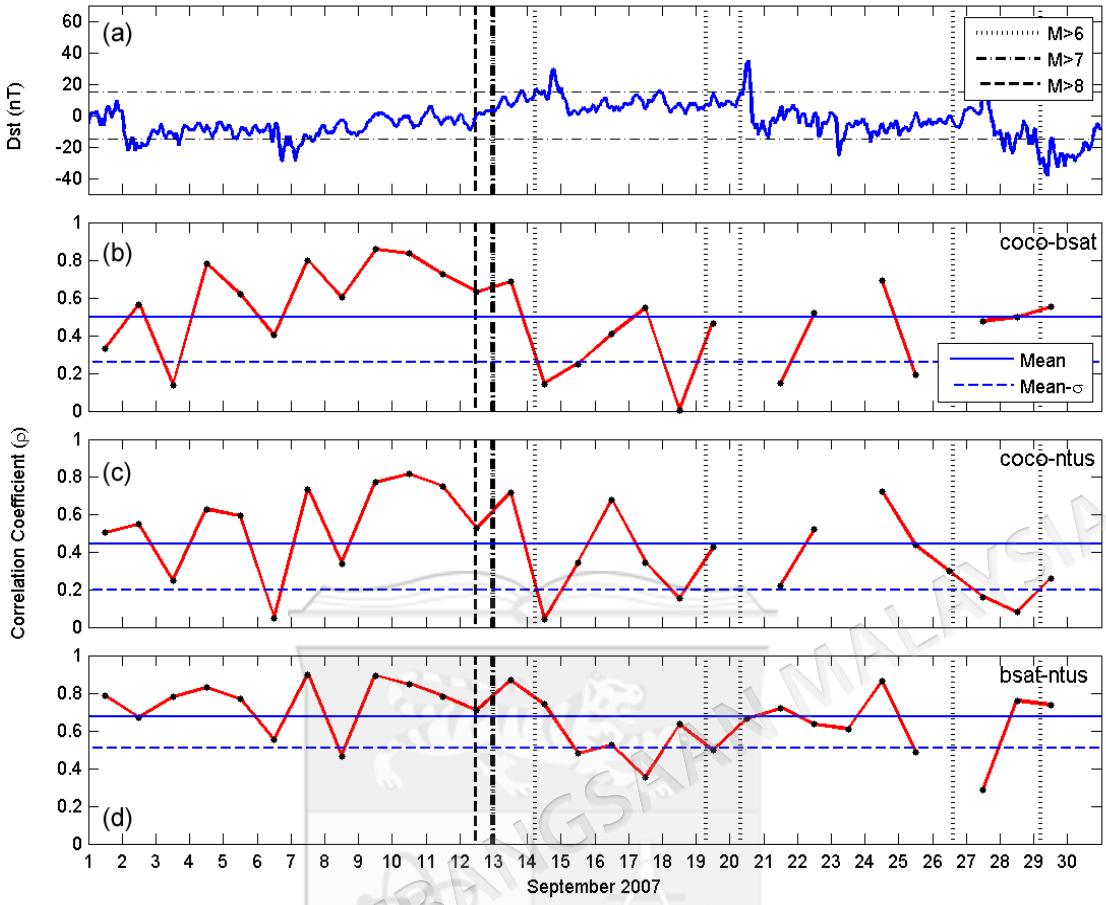

Figure 6.16 The geomagnetic Dst and correlation coefficients for two station pairs for the month of September 2007.

6.3 VTEC VARIABILITY INDEX TECHNIQUE

Figure 6.17 presents the geomagnetic Dst and the VTEC variability ($\Delta VTEC_{var}$) indices between COCO and five other GPS stations for the period between July and December 2004. In Figures 6.17(b)-(g), the dashed horizontal line shows the threshold value of (Mean+σ) during the six month interval, whereby σ is standard deviation of the VTEC variability index ($\Delta VTEC_{var}$). As shown in these figures, an enhancement of VTEC variability, which exceeds the threshold value was seen about 23 days before the 25 July 2004 event, while no enhancement was observed before the 26 December 2004 event although it was a major event. During the period between August and early November 2004, large enhancements in the $\Delta VTEC_{var}$ index were observed but this period does not coincide with any earthquake event.

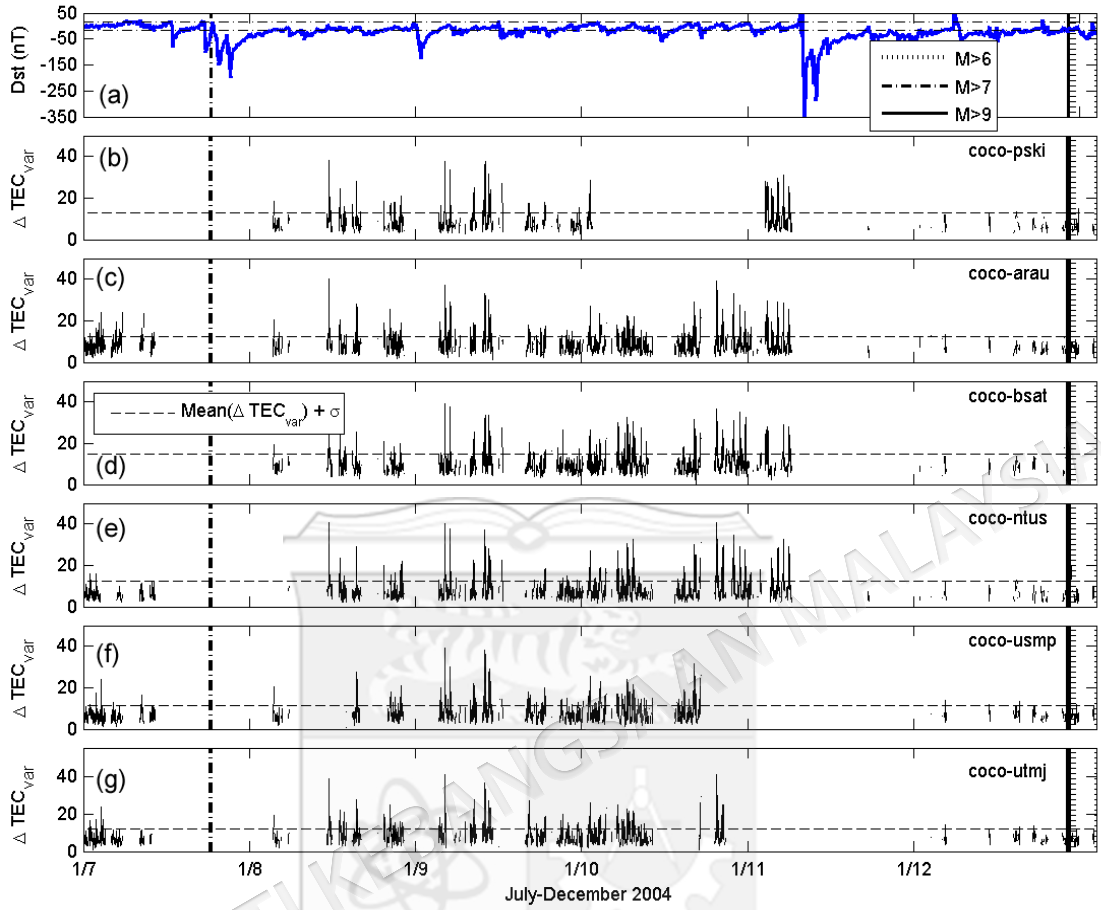

Figure 6.17 The Dst and VTEC variability indices of five GPS station pairs from July to December 2004.

Figures 6.18 and 6.19 present the Dst and $\Delta VTEC_{var}$ indices for the first and second half of 2005, respectively. As shown in Figures 6.18(b)-(f), no $\Delta VTEC_{var}$ index was observed prior to the events in January as the $\Delta VTEC_{var}$ values during this month were filtered out due to high geomagnetic activity (Dst < -50nT). In February 2005, the $\Delta VTEC_{var}$ enhancements, which exceed the threshold value were found a few days prior to the 26 February event. Larger $\Delta VTEC_{var}$ enhancements of up to 40 TECU were found during 1-6 days before the March and April events. These enhancements were detected simultaneously by four station pairs, which are COCO-PSKI, COCO-ARAU, COCO-BSAT and COCO-USMP. In Figure 6.19(b)-(f), the $\Delta VTEC_{var}$ index was found to exceed the threshold value throughout the entire period from July to December 2005 but no significant $\Delta VTEC_{var}$ enhancements were detected prior to the strong earthquake events.

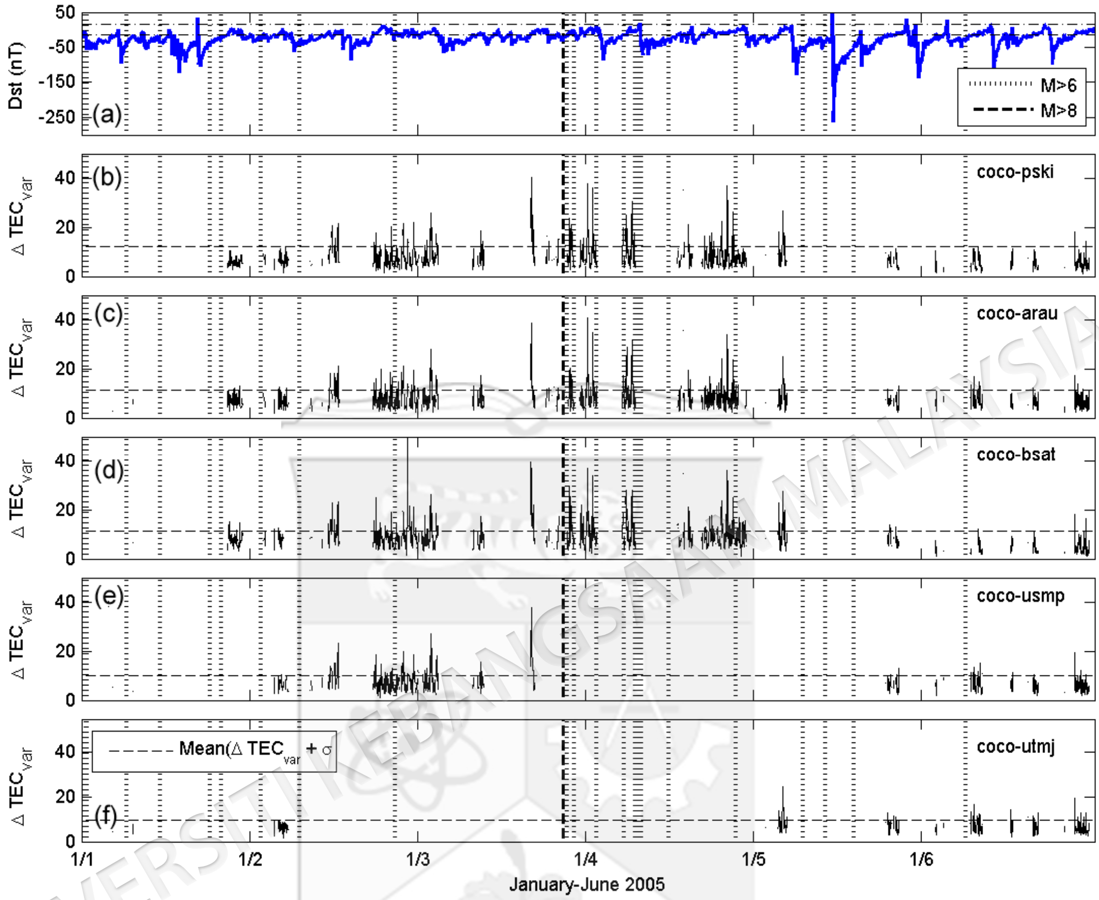

Figure 6.18 The geomagnetic Dst and VTEC variability indices of five GPS station pairs from January to June 2005.

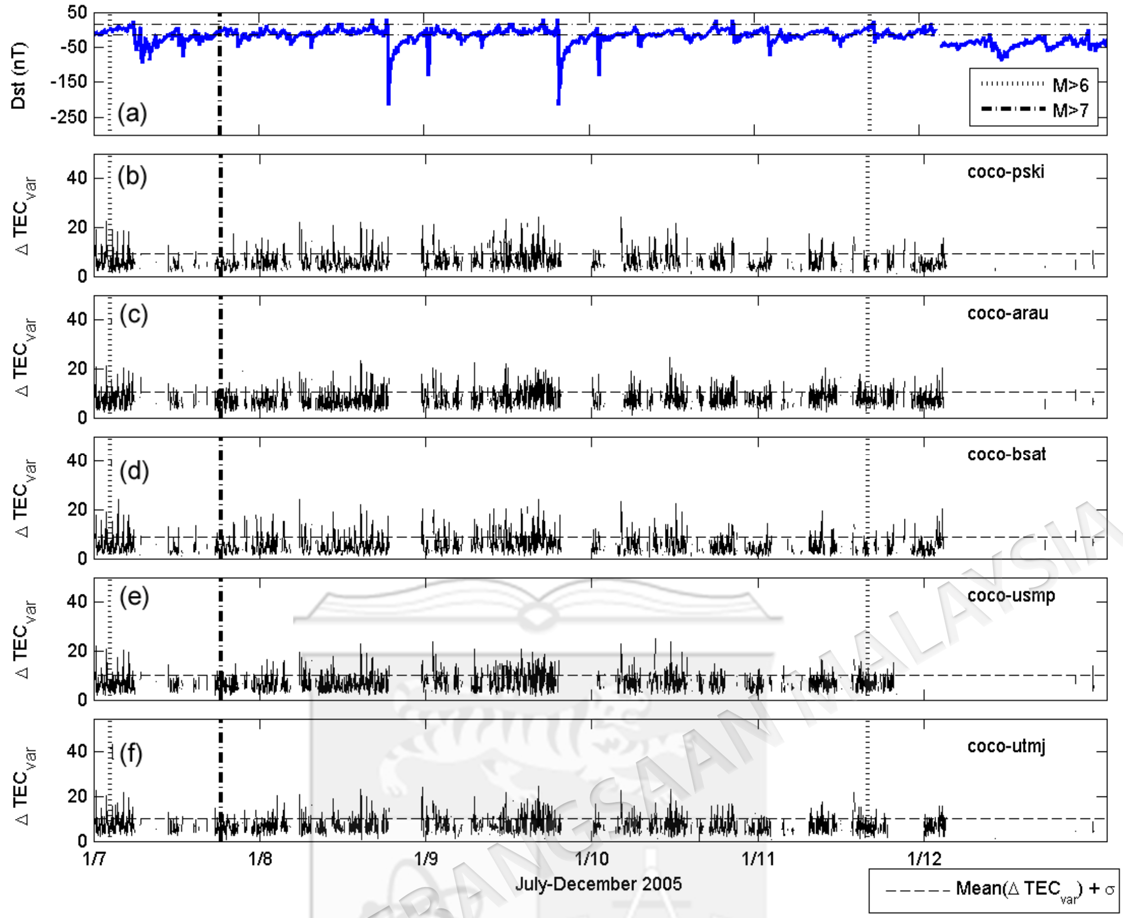

Figure 6.19 The geomagnetic Dst and VTEC variability indices of five GPS station pairs from July to December 2005.

The Dst and $\Delta VTEC_{var}$ indices for the period between January and June 2006 are shown in Figure 6.20. As shown in Figures 6.20(b)-(f), it can be seen that significant enhancements in the VTEC variability were observed about 16 days before the 19 April 2006 event by all station pairs. An enhancement in the $\Delta VTEC_{var}$ index was also seen a day before the before the 25 April 2006 event was it was only detected by the station pair COCO-PSKI, while such an enhancement was not detected by other station pairs. During about 3 days prior to the 16 May 2006 event, it was observed that the ΔTEC_{var} increases slightly and returns to its normal state after the event. Such an enhancement was prominently observed by station pairs COCO-PSKI and COCO-BSAT but was not seen at the remaining station pairs.

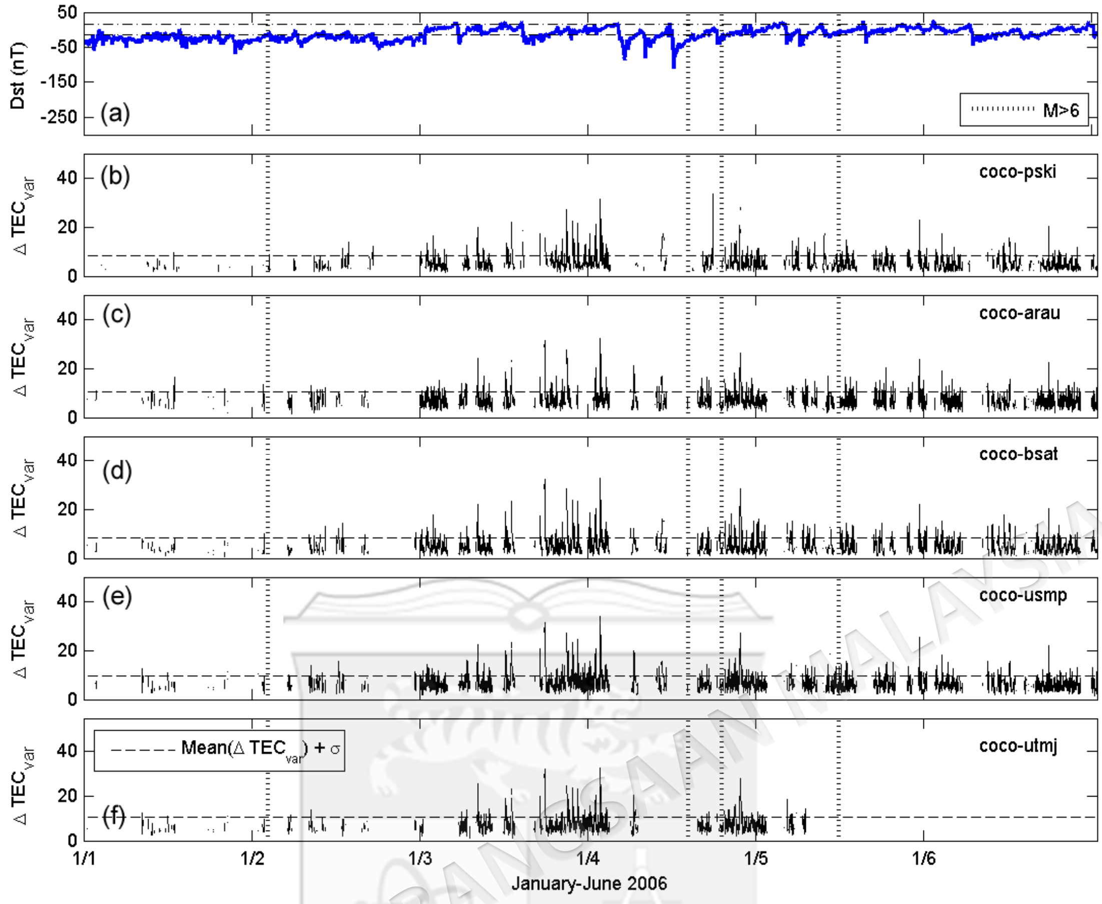

Figure 6.20 The geomagnetic Dst and VTEC variability indices between COCO and five other GPS stations from January to June 2006.

Figure 6.21 presents the Dst and $\Delta VTEC_{var}$ indices for the month of September 2007 at three station pairs. As shown the Figures 6.21(b)-(d), the $\Delta VTEC_{var}$ index for all station pairs was found to exceed the threshold value almost throughout the whole month of September 2007 but significant enhancements of about 10-17 TECU were detected during 1-11 days before the 9 events. It was found that the TEC variability at station pairs COCO-BSAT and BSAT-NTUS were higher than that at COCO-NTUS.

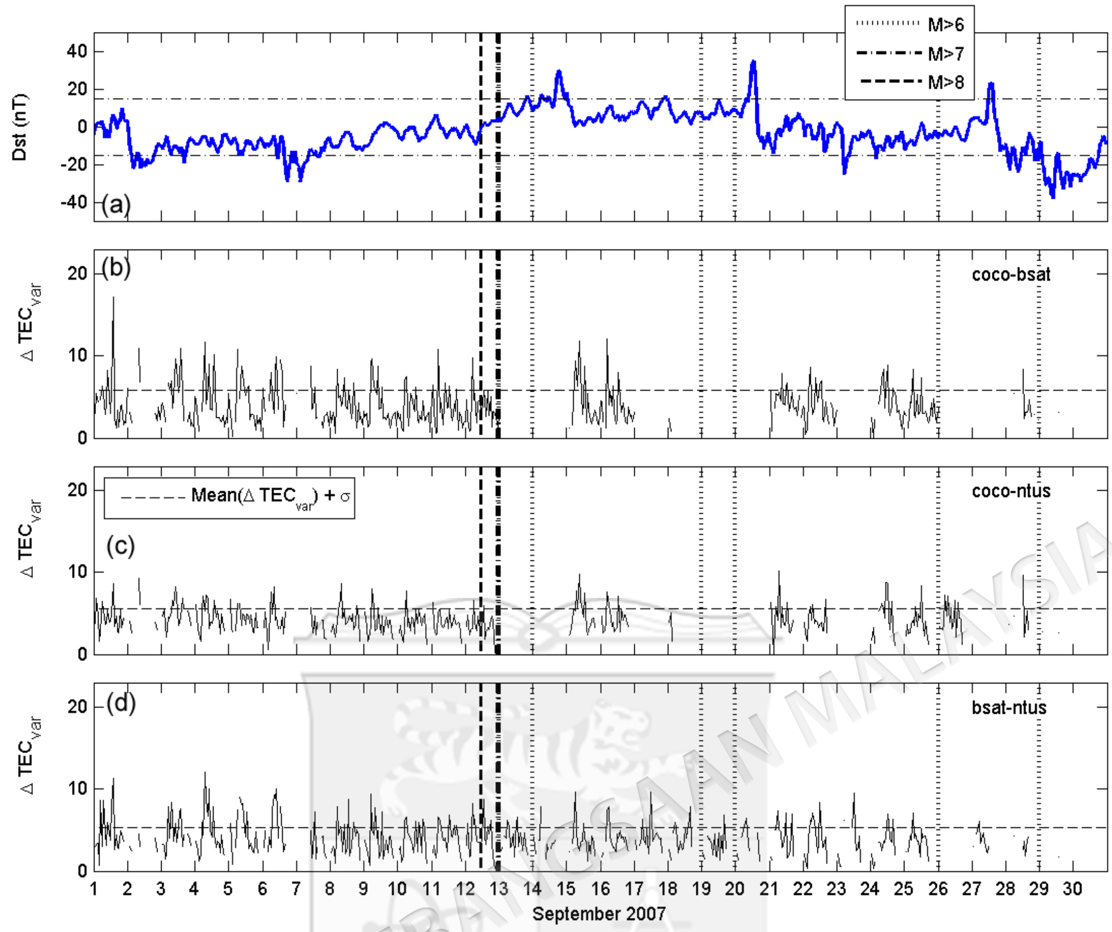

Figure 6.21 The geomagnetic Dst and VTEC variability indices for three station pairs during the month of September 2007.

6.4 SUMMARY AND CONCLUSION

The precursory effects in the GPS VTEC has been investigated using continuous measurements for the period of 25 months (July 2004 - June 2006 and September 2007) at seven GPS stations surrounding the epicentres of 57 strong earthquake events in Sumatra. The relationship between the occurrences of irregular VTEC variations and the equatorial latitude earthquake events based on long-term VTEC time series are analyzed for the first time using three different statistical analysis methods. The VTEC variations were analyzed under very low solar and geomagnetic activity conditions.

The three statistical analyses showed that anomalous VTEC variations were found throughout the entire observation period but very few temporal statistical correlations were found between the irregular VTEC and the occurrence of strong earthquakes in the Sumatra region during the studied period. The envelope and correlation analysis methods both showed a consistent trend in the detection of anomalous VTEC variations for earthquake events with magnitudes larger than 7.0 but this trend was not consistently observed in the VTEC variability index analysis. The number of the irregular VTEC detections during the pre-earthquake periods was found to be weakly correlated with the solar flux F10.7 variations. However, anomalous VTEC variations were also detected during non-earthquake periods with stronger amplitudes. These anomalous TEC variations do not only have semidiurnal periods, which reflect lunar tides but also show seasonal variations in solar activity.

The analysis of the long-term data set shows that it is always possible to find an anomalous VTEC variation during a week before an earthquake event by using all the three methods but with no correlation in the days with anomalous VTEC variation. However, these anomalous VTEC variations should not only be temporally correlated with earthquakes but also detected at a significant level simultaneously by several techniques in order to qualify as earthquake precursors. It is indeed a great challenge to predict earthquakes in the equatorial ionosphere as it is highly dynamic and unpredictable. Apart from the well-known solar weather, equatorial anomaly, diurnal, seasonal, lunar tides, there are many unknown physical processes that might occur in the equatorial ionosphere. The three statistical methods showed seasonal variations of VTEC detected at all stations. Therefore, the analyses of anomalous VTEC variations due to seasonal factors as well as other processes that are not related to the earthquake preparation are important and require further research in the future.

The results in this chapter present some of the difficulties associated with the search for ionospheric precursory signatures. It is difficult to separate the precursory signals from the background VTEC variability in the absence of a priori knowledge of the temporal and spatial structure of these ssignals. The long time series, spatially dense measurements and also the use of several statistical detection techniques are important to demonstrate the presence of earthquake precursors. The statistical analysis methods used in this chapter give estimates of the background VTEC variability and detection statistics. The results in this chapter also give an insight on the challenges in discriminating the non-seismic VTEC variations due to acoustic gravity waves and seasonal variations. The anomalous VTEC variations due to these factors should be discriminated by examining their periods.

Ionospheric measurements between ground-based GPS receivers and other ground or space-based electromagnetic measurements will help to understand the source of the observed signals. With these analyses combined in a future analysis of large earthquakes in well instrumented GPS areas such as the western U.S., Europe or Japan might still reveal convincing evidence for precursors. Although the results in this chapter do not corroborate with previous observations of ionospheric earthquake precursors, they do not disprove the possibility of precursory phenomena. The long-term statistical analysis of the VTEC measurements is indeed useful to provide the understanding of the physical process in the equatorial ionosphere as well as for the future application of the data for earthquake prediction modelling.

CHAPTER VII

CONCLUSION AND FUTURE WORK

7.1 CONCLUSION

This final chapter concludes the discussions in the previous chapters and also includes recommendations for the continuity of this project. The characterization, analysis and investigation of ionospheric disturbances before and during earthquake events over the Sumatra region measured by ground-based GPS, CHAMP satellite and ground-based magnetometer measurement techniques have been presented in this thesis. Generally, all three objectives have been accomplished and the outcomes are discussed as follows:

i. The first objective was to investigate the ionospheric and geomagnetic responses during the strong Sumatra earthquake events using GPS and magnetometer stations located in the near zone of the epicenters. These events were investigated during very low solar and geomagnetic activity. From the results of GPS VTEC, the VTEC variations showed directivity in the northeast direction of the epicenters only. VTEC variations were not observed in the east of the epicenters, as the ion mobility is not affected by the neutral wind perpendicular to the geomagnetic field lines. During the earthquake events, VTEC oscillations with periods of 5-8 minutes were observed about 10-27 minutes after the events and have horizontal propagation velocities of 912-1271 m/s. The results of geomagnetic field responses during earthquakes showed high frequency fluctuations shortly after the event, followed by a long period Pc5 pulsation occurring at about 11 min after the event. In addition to these disturbances, a Pc3 pulsation was also observed at about 8 minutes after the 26 December 2004 earthquake. The correlation between the GPS VTEC and magnetic disturbances were obtained using filtering techniques. The results showed that the filtered GPS VTEC and Pc5 pulsation were in good agreement.

ii. The second objective was to investigate the precursory signatures in the GPS VTEC and the electron density measurements onboard CHAMP satellite prior to strong earthquake events based on short-term analysis. The GPS VTEC results showed that positive as well as negative anomalies of up to 88% and 45% above and below their upper and lower bounds, respectively were observed about a few hours to 6 days before these events. These anomalies have duration of 1 - 5 hours and observed mostly during the daytime hours. From the analysis of the CHAMP electron density measurements, the EIA modification prior to the events was investigated. The results showed the modification of the EIA structure in the form of crests disappearance and amplification in the equatorial anomaly trough and crests regions during the daytime about a few hours to 6 days prior to some earthquake events. The GPS VTEC and electron density measurements show similar tendencies but both show variability in the equatorial anomaly trough and crest regions.

iii. The third objective was to investigate the long-term temporal and spatial correlation of the anomalous GPS VTEC variations and earthquake occurrences using three statistical analysis techniques. The analyses were conducted using continuous measurements for the period of 25 months (July 2004-June 2006 and September 2007) at seven GPS stations surrounding the epicenters of 57 strong earthquake events in Sumatra using the envelope, cross-correlation and VTEC variability analysis index techniques. The VTEC variations were analyzed during very low solar and geomagnetic activity conditions. The results of the envelope and correlation analysis methods both showed a consistent trend in the detection of anomalous VTEC variations for earthquake events with magnitudes larger than 7.0 but this trend was not consistently observed in the VTEC variability index analysis. The number of the irregular VTEC detections prior to earthquake events was found to be weakly correlated with the solar flux F10.7 variations. Anomalous VTEC variations were also detected during non-earthquake periods with stronger amplitudes especially during the equinox months showing seasonal dependence in solar activity.

It is also noteworthy to mention that there is no direct correlation between the three aforementioned measurement techniques for the ionospheric disturbances before and during earthquakes in Sumatra. The reason behind this is particularly due to the difference in parameters recorded by different instruments and also due to the altitude in which these measurements were recorded, i.e. GPS VTEC (400 km), CHAMP electron density (450 km) and magnetic field (120 km).

7.2 RESEARCH CONTRIBUTIONS

The major research contributions of the thesis include the following:

i. The research analyzed the correlation of the coseismic ionospheric disturbances between GPS VTEC and magnetic measurements during the occurrences of large earthquakes in Sumatra. This analysis has provided the further understanding about the propagation of coseismic ionospheric disturbances from ground level to the ionosphere. Furthermore, the CID monitoring will help the forecast of tsunami attacks and could serve as a part of an early tsunami warning system.

ii. This work has analyzed in detail the precursory signatures prior to several large earthquake events in Sumatra using ground-based GPS VTEC measurements from many stations and correlating them with satellite based data. The research enhances the understanding of the ionospheric dynamics in the equatorial anomaly trough and crest regions and their physical processes are of paramount importance for earthquake prediction modelling.

iii. The third contribution is the usage of several statistical analysis techniques to find the correlation between anomalous ionospheric variations and earthquake occurrences under very quiet geomagnetic and solar conditions. This study enhances the understanding about the seismo-ionospheric coupling phenomena and non-earthquake related processes that can occur even during very quiet geomagnetic and solar conditions. The work can help to improve the interpretation of seismo-ionospheric perturbations for earthquake prediction modeling.

7.3 RECOMMENDATIONS FOR FUTURE WORK

The research has also identified a number of issues and further improvement on the earthquake and Tsunami prediction analyses for the application of space warning and prediction that could be incorporated in future research. The following issues and directions are presented as follows:

i. In order to further understand the origin of the coseismic ionospheric disturbances, the implementation of the ray tracing method could help to trace the latitude and longitude of the earthquake epicentre.

ii. It is important to characterize the magnetic disturbances observed during earthquakes, understand their origin and to determine whether they are caused by external source or induced by earthquakes. This can be done by correlating ground-based magnetic field variations and pulsations with satellite-based magnetometer data.

iii. The study of pre-earthquake ionospheric perturbations over Sumatra can be extended by systematically combining ground-based VTEC measurements with other ground or satellite-based electromagnetic measurements such as the ULF, ELF and VLF signals. The comparison between the ground-based VTEC measurements and the Global ionospheric VTEC mapping (GIM VTEC) should also be conducted to investigate the spatial patterns of the ionospheric perturbation.

iv. In order to distinguish between pre-earthquake ionospheric perturbations from the non-earthquake related perturbations, the anomalous GPS VTEC variations measurements should be characterized by their periods by using fractal analysis. This study is important to discriminate seismo-ionospheric perturbations from non-seismic perturbations such as the ones caused by acoustic gravity waves.

v. The pre-earthquake and coseismic ionospheric disturbances over the Sumatra region need to be compared with those in the mid-latitudes and also high latitudes. Characterization and modelling of the seismo-ionospheric disturbances by categories of different earthquake magnitudes, geography (undersea, island or land) and also regions (mid and high latitude) should be conducted in order to enhance the understanding of these complicated phenomena.

vi. A more precise statistical method to discriminate anomalous pre-earthquake ionospheric precursors from those due to seasonal changes should be worked on. The analysis should also be correlated and verified with other statistical methods in order to really qualify as precursors.

vii. Development of a mathematical model for determining possible earthquake precursors at stations where real-time measurements are unavailable.

7.4 CONCLUDING REMARKS

To summarize it all, this research has successfully implemented the ground-based GPS VTEC, CHAMP satellite and ground-based magnetometer measurement techniques to study the ionospheric disturbances before and during earthquakes over

Sumatra. The impact of the ionosphere to strong earthquake occurrences is evident in the ionospheric E and F layers with established physical mechanism. On the other hand, the prediction of earthquakes is still a challenge. Although the long-term statistical analysis of GPS VTEC using several techniques does not show any convincing ionospheric precursors, this does not disapprove the possibility of earthquake prediction. For a more detail long-term analysis, the long periodic anomalies observed during non-earthquake periods require deeper understanding of the root cause. Earthquake prediction via space observation technique is still in its infancy hence needs to be further studied and improved. The knowledge gained in this work has indeed provided a better understanding of the lithosphere, atmosphere and ionosphere relationship as well as the dynamics of the equatorial ionosphere, which is vital for the improvement of earthquake prediction modelling.

APPENDIX A

RINEX OBSERVATION FILE

A1. GPS observation data file in RINEX format

```
   2.10              OBSERVATION DATA          G (GPS)                 RINEX VERSION / TYPE
teqc  2002Mar14                                20080214 06:41:07UT
CPGM / RUN BY / DATE
MSWin2000|IAx86-PII|bcc32 5.0|MSWin95/98/NT/2000|486/DX+  COMMENT
   2.11              OBSERVATION DATA        G (GPS)                   COMMENT
teqc  2007Jun25                               20070928 05:07:05UTC

COMMENT
MSXP|IAx86-PII|bcc32 5.0|MSWin95->XP|486/DX+                        COMMENT
teqc  2007Jun25                             20070927 03:00:01UTC COMMENT
BIT 2 OF LLI FLAGS DATA COLLECTED UNDER A/S CONDITION       COMMENT
TRS                                                          MARKER NAME
Base                                                         MARKER NUMBER
-Unknown-        -Unknown-                                   OBSERVER / AGENCY
00021125         TRIMBLE 4000SSI           NP 7.29 / SP 3.07  REC # / TYPE / VERS
02201071         TRM29659.00                                 ANT # / TYPE
 -1131050.5623  6236311.4463   711749.5171                   APPROX POSITION XYZ
      0.1740       0.0000       0.0000                       ANTENNA: DELTA H/E/N
   1    1                                                    WAVELENGTH FACT L1/2
   7   L1   L2   C1   P2   D1   S1   S2                      # / TYPES OF OBSERV
  30.0000                                                    INTERVAL
Forced Modulo Decimation to 30 seconds                       COMMENT
 SNR is mapped to RINEX snr flag value [1-9]                 COMMENT
  L1: 3 -> 1; 8 -> 5; 40 -> 9                                COMMENT
  L2: 1 -> 1; 5 -> 5; 60 -> 9                                COMMENT
Forced Modulo Decimation to 30 seconds                       COMMENT
  2006    1    1    0    0   0.0000000    GPS                TIME OF FIRST OBS
                                                             END OF HEADER
 06  1  1  0  0  0.0000000  0  6G20G16G 1G19G 3G23
 6330185.27845     5539008.30245  22667403.3394     22667408.8904     -2449.0864
       9.0004           9.2504
 1186847.53342     718413.48245      24014330.5324   24014334.1114     -3579.7974
       4.7504           5.2504
 2553208.13645     9660996.00345    22351337.7944   22351343.5174     -3782.3974
       9.2504           10.2504
 -7233198.05546    -5405473.31946   20664666.0444   20664669.1744      367.1654
      15.7504           22.7504
 -3005907.91746    -2187277.18946   20521050.9234   20521056.2894     -2252.2524
      16.7504           19.5004
 -11126265.93746 -7625511.69946   21009572.7834   21009574.3054      978.8004
      16.0004           19.2504
```

APPENDIX B

MAP OF EARTHQUAKE EPICENTERS AND GPS RECEIVER STATIONS

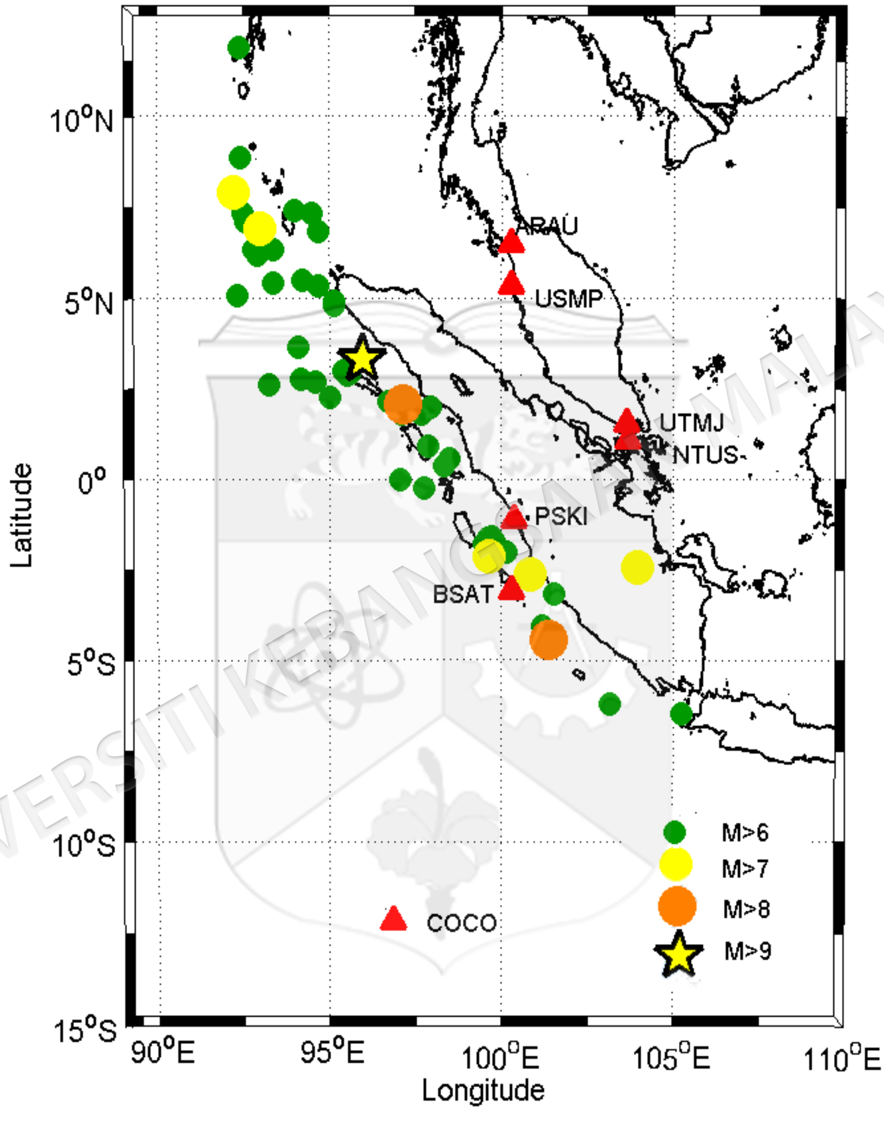

Figure B1 Geographic locations of the 57 earthquake epicenters of magnitude M > 6.0 during the period of 2004-2007 (star and circle) and GPS receiver stations (triangle).

APPENDIX C

DETAILS OF EARTHQUAKE EPICENTER

Table C1 The time, geographic coordinates, depth of earthquakes with M > 6 in Sumatra that occurred during the period of July 2004 – June 2006 and September 2007 (NEIC 2010).

No.	Date	Time	Latitude	Longitude	Depth	Magnitude
1	25.7.2004	14:35:19	-2.43	103.98	582	7.3
2	26.12.2004	0:58:53	3.3	95.98	30	9.1
3	26.12.2004	1:21:20	6.34	93.36	30	6.1
4	26.12.2004	1:22:25	7.42	93.99	30	6
5	26.12.2004	1:25:48	5.5	94.21	30	6.1
6	26.12.2004	2:00:40	6.85	94.67	30	6
7	26.12.2004	4:21:29	6.91	92.96	39	7.2
8	26.12.2004	9:20:01	8.88	92.38	16	6.6
9	26.12.2004	15:06:33	3.65	94.09	17	6
10	26.12.2004	19:19:55	2.79	94.16	30	6.1
11	27.12.2004	9:39:06	5.35	94.65	35	6.1
12	31.12.2004	2:24:00	7.12	92.53	14	6.1
13	31.12.2004	12:04:57	6.2	92.91	11	6
14	1.1.2005	6:25:44	5.1	92.3	11	6.7
15	2.1.2005	19:08:07	7.34	94.46	55	6.1
16	4.1.2005	15:35:56	6.36	92.79	30	6.4
17	9.1.2005	22:12:56	4.93	95.11	40	6.1
18	15.1.2005	13:47:05	-6.46	105.24	58	6
19	24.1.2005	4:16:47	7.33	92.48	30	6.3
20	26.1.2005	22:00:42	2.7	94.6	22	6.2
21	5.2.2005	4:03:13	2.26	94.99	30	6
22	9.2.2005	13:27:25	4.8	95.12	44	6
23	26.2.2005	12:56:52	2.91	95.59	36	6.8
24	28.3.2005	16:09:36	2.09	97.11	30	8.6
25	28.3.2005	18:30:44	0.92	97.87	36	6.1
26	30.3.2005	16:19:41	2.99	95.41	22	6.3
27	3.4.2005	0:59:21	0.37	98.32	30	6
28	3.4.2005	10:56.0	2.02	97.94	36	6.3
29	8.4.2005	5:48:37	-0.22	97.73	20	6.1
30	10.4.2005	10:29:11	-1.64	99.61	19	6.7
31	10.4.2005	11:14:19	-1.71	99.78	30	6.5
32	10.4.2005	17:24:39	-1.59	99.72	30	6.4

Continue...

Continued...

33	11.4.2005	6:11:11	2.17	96.76	24	6.1
34	16.4.2005	16:38:03	1.81	97.66	31	6.4
35	28.4.2005	14:07:33	2.13	96.8	22	6.2
36	10.5.2005	1:09:05	-6.23	103.14	17	6.3
37	14.5.2005	5:05:18	0.59	98.46	34	6.7
38	18.5.2005	11:37:41	5.44	93.36	2	6.1
39	19.5.2005	1:54:52	1.99	97.04	30	6.9
40	8.6.2005	6:28:10	2.17	96.72	23	6.1
41	5.7.2005	1:52:02	1.82	97.08	21	6.7
42	24.7.2005	15:42:06	7.92	92.19	16	7.2
43	3.2.2006	20:34:10	11.86	92.37	19	6.1
44	19.4.2006	20:36:46	2.64	93.23	17	6.2
45	25.4.2006	18:26:17	1.99	97.00	21	6.3
46	16.6.2006	15:28:25	0.009	97.05	12	6.8
47	19.11.2005	14:10:13	2.16	96.79	21	6.5
48	12.9.2007	11:10:26	-4.44	101.37	34	8.5
49	12.9.2007	23:49:03	-2.62	100.84	35	7.9
50	13.9.2007	2:30:03	-1.69	99.67	28	6.5
51	13.9.2007	3:35:28	-2.13	99.63	22	7
52	13.9.2007	16:09:16	-3.17	101.52	53	6
53	14.9.2007	6:01:32	-4.07	101.17	23	6.4
54	19.9.2007	7:27:50	-2.75	100.89	35	6
55	20.9.2007	8:31:14	-2.00	100.14	30	6.7
56	26.9.2007	15:43:01	-1.79	99.49	26	6.1
57	29.9.2007	5:37:07	2.9	95.52	35	6

APPENDIX D

LIST OF PUBLICATIONS

D1. CONFERENCE PROCEEDINGS

1. Hasbi, A.M., Mohd Ali, M.A. & Misran, N. & Pulinets, S. 2007. Variations of ionospheric total electron content during the M=9.0 Northern Sumatran Earthquake of 26 December 2004 over Malaysia, Singapore and Sumatra. *CD-Proceedings of the Joint International Symposium & Exhibition on Geoinformation and GPS/GNSS 2007*, Johor Bahru, Johor, Malaysia, 5-7 November 2007.

2. Hasbi, A.M., Mohd Ali, M.A. & Misran, N. 2007. Ionospheric TEC and Scintillation during the 15-16 May 2005 Major Storm over Equatorial Anomaly Region at ARAU. *CD-Proceedings of the 2007 Asia-Pacific Conference on Applied Electromagnetics,* Malacca, Malaysia, 4-6 December 2007.

3. Hasbi, A.M., Mohd Ali, M.A. & Misran, N. 2008. TEC irregularity, scintillation and geomagnetic variations associated with the 28 March 2005 Sumatran earthquake. *Presented at the 12th Ionospheric Effects Symposium,* Old Town Alexandria, Virginia, USA, 13-15 May 2008.

4. Hasbi, A.M., Mohd Ali, M.A., Misran, N., Yumoto, K., Otadoy, R.E.S. & Mcnamara, D.J. 2008. Ionospheric and magnetic field effects observed during the 2005 geomagnetic storms in the South-East Asian sector. *Presented at the 12th International Symposium of Equatorial Aeronomy,* Crete, Greece, 18-24 May 2008.

5. Hasbi, A.M., Mohd Ali, M.A. & Misran, N. 2008. Investigation of ionospheric total electron content during earthquakes in Sumatra July 2004 – June 2006. *CD-Proceedings of the Engineering Postgraduate Conference (EPC) 2008,* Residence Hotel, Kajang, Selangor, Malaysia, 21-22 October 2008.

6. Hasbi, A.M., Momani, M.A., Mohd Ali, M.A. & Misran, N. 2009. Ionospheric and magnetic disturbances during earthquakes over Sumatra 2004-2007. *Proceedings of the Seminar Penyelidikan ANGKASA*, pp. 21-27, Pulau Tioman, Pahang, Malaysia, 6-8 August 2009.

7. Hasbi, A.M., Momani, M.A., Mohd Ali, M.A. & Misran, N. 2009. The Relationship between ionospheric and magnetic disturbances during the 28 March 2005 Sumatra earthquake. *CD-Proceedings of the International Conference on Space and Communication 2009*, Port Dickson, Negeri Sembilan, 25-26 October 2009.

8. Hasbi, A.M., Mohd Ali, M.A., Momani, M.A. & Misran, N. 2010. Ionospheric Variations Associated with Earthquake Preparation over Sumatra, *CD-Proceedings of the Seminar Penyelidikan Siswazah Angkasa 2010*, Hulu Langat, Selangor, 23-25 June 2010.

D2. JOURNAL

1. Hasbi, A.M., Momani, M.A., Mohd Ali, M.A., Misran, N., Shiokawa, K., Otsuka, Y. & Yumoto, K**.** 2009. Ionospheric and Geomagnetic Disturbances during the 2005 Sumatran earthquakes. *Journal of Atmospheric and Solar-Terrestrial Physics* 71(17-18): 1992-2005.

2. Hasbi, A.M., Mohd Ali, M.A., .Momani, M.A. & Misran, N. 2011. Ionospheric variations before some large earthquakes over Sumatra. *Natural Hazards and Earth System Sciences*. 11: 1-15.

D3. AWARD

1. Space Publication Prize 2010. First prize for the category of Professional Research Paper entitled: *Ionospheric and Geomagnetic Disturbances during the 2005 Sumatran earthquakes.* Agensi Angkasa Negara (ANGKASA), Putrajaya.